This is to certify that the
thesis entitled

ELASTIC MODULUS AND BIAXIAL FLEXURAL STRENGTH OF THERMALLY FATIGUED HOT PRESSED LAST AND LASTT THERMOELECTRIC MATERIAL

presented by

Andrew Q. Morrison

has been accepted towards fulfillment
of the requirements for the

M.S. degree in Materials Science Engineering

Eldon D. Case
Major Professor's Signature

November 23, 2010
Date

MSU is an Affirmative Action/Equal Opportunity Employer

ELASTIC MODULUS AND BIAXIAL FRACTURE STRENGTH OF THERMALLY FATIGUED HOT PRESSED LAST AND LASTT THERMOELECTRIC MATERIALS

By

Andrew Q. Morrison

A THESIS

Submitted to
Michigan State University
In partial fulfillment of the requirements
For the degree of

MASTER OF SCIENCE

Materials Science Engineering

2010

Abstract

ELASTIC MODULUS AND BIAXIAL FRACTURE STRENGTH OF THERMALLY FATIGUED HOT PRESSED LAST AND LASTT THERMOELECTRIC MATERIALS

By

Andrew Q. Morrison

An application area for thermoelectric materials is the harvesting of waste heat from heat sources. Such applications can lead to thermal fatigue of the thermoelectric materials due to the thermal transients that arise during the heat-up and cool-down of the heat source. Thermal fatigue can in turn result in the accumulation of macrocrack and/or microcrack damage in the thermoelectric elements. For this study, two PbTe based thermoelectric materials, n-type LAST (Lead-Antimony-Silver-Tellurium) and p-type LASTT (Lead-Antimony-Silver-Tellurium-Tin) were thermally fatigued for up to 200 thermal cycles between 50°C and 400°C. All LAST specimens had surface inclusion that averaged 50-70 microns in diameter and spalled during thermal cycling; also 21 of 90 LASTT specimens had blisters on average of 7.5 mm in diameter and 2.5 mm in height as a result of thermal cycling. LAST and LASTT specimens had a relatively constant Young's modulus and Poisson's ratio, with a Young's modulus decrease no greater than 1 GPa and the largest decrease in the Poisson's ratio of 2.2% over 200 thermal cycles. A LASTT fracture strength band between 25 MPa and 40 MPa occurred for specimens fatigued up to 200 thermal cycles, where a band of fracture strengths between 15 MPa and 38 MPa occurred for LAST specimens. The LAST and LASTT specimens appeared to be unaffected by microcracking during the thermal fatigue cycling.

Acknowledgments

I would like to express my utmost gratitude to Dr. Eldon Case for his support and help during my time at Michigan State University, especially during my time as a graduate student.

Fei Ren (Michigan State University, East Lansing, MI) for his prior work and fabrication of the Large and Small thermal fatigue chambers. For his design and test methods of the ring-on-ring biaxial fracture testing apparatus. Also for his initial work testing LAST and LASTT disk specimens.

Daniel C. Kleinow (Michigan State University, East Lansing, MI) for his initial work with thermal cycling plate-shaped LAST and LASTT specimens in the Small thermal fatigue chamber.

Jennifer Ni (Michigan State University, East Lansing, MI) for her help with learning to use the Resonant Ultrasound Spectroscopy equipment and software. I would like to thank her for time and skill in performing all the Scanning Electron Microscopy used in this thesis.

Alexander J. Baumann (Michigan State University, East Lansing, MI) for help with cycling, imaging and performing resonant ultrasound spectroscopy of LAST and LASTT plate-shaped small thermal fatigue chambers. Also for his help in counting pit and inclusion evolution on LAST specimens during thermal cycling.

Terry J. Hendricks (Pacific Northwest National Laboratory, Corvallis, OR) for his leadership and oversight of the project.

Charles Cauchy and James Barnard at Tellurex Corporation (Traverse City, MI) for supplying all the LAST and LASTT specimens used in this study.

TABLE OF CONTENTS

List of Tables ix

List of Figures xi

1. INTRODUCTION 1
1.1. Thermoelectric Effect 1
1.2. Thermoelectric Material Background 2
1.3 Figure of Merit, ZT 6
1.4 Thermoelectric Material Grain Size 8
1.5. Temperature Effects on the Thermoelectric Coefficient of Brittle Conductive Materials 9
1.6. Possible Methods of Improving Brittle Conductive Materials 12
1.7. Microcracking in Brittle Conductive Materials 13
1.8. Thermally Induced Microcracks 14
1.9. Electrically Induced Microcracking 16
1.10. Microcracking Caused by Crystallographic or Phase Transformation 17
1.11. Microcracks due to Thermal Shock and Fatigue 19
1.12. Advantages of Microcracking 21
1.13. Microcrack Healing 23
1.14. Microcrack Summary 24
1.15. Spinodal Decomposition 25
1.16. Fracture Strength and Elastic Moduli 28

2. EXPERIMENTAL PROCEDURES 32
2.1. Material and Specimen Preparation 32
2.2. Microstructural Characterization 34
2.3. Large Thermal Fatigue Chamber 37
2.3.1. Large Thermal Fatigue Chamber Overview 37
2.3.2. Hot Side Alumina Refractory Brick 39
2.3.3. Hot Side Fiberglas Base Plate Assembly 41
2.3.4. Large Chamber Hot Plate Assembly 44
2.3.5. Hot Side Thermocouple Attachment 46
2.3.5.1. Fiberglas Thermocouple Lead Holes 46
2.3.5.2. Hot Plate Thermocouple Attachment 47
2.3.5.3. Hot Side Thermocouple and Thermocouple Lead Soldering 50
2.3.6. Cold Side Thermocouple Attachment 51
2.3.6.1. Cold Plate Thermocouple Attachment 51
2.3.6.2. Cold Side Thermocouple and Thermocouple Lead Soldering 53
2.3.7. Thermal Chamber Backside Thermocouple, Electrical, and Bubbler Tube Feed Through 54
2.3.7.1. Thermocouple Feed Through 54

2.3.7.2. Hot Plate Electrical Feed-Through 56
2.3.7.3. Bubbler Tube Feed-Through 57
2.3.8. Cold Plate Chiller Chamber Feed-Through 58
2.3.8.1. Cold Plate Chiller Large Thermal Fatigue Chamber Inlet 58
2.3.8.2. Cold Plate Chiller Large Thermal Fatigue Chamber Outlet 59
2.3.9. Fibrous Zirconia Specimen Insulation 60
2.3.9.1. Fibrous Zirconia Geometry 60
2.3.9.2. Positioning of LAST and LASTT Specimens on Hot Plate with Fibrous Zirconia Insulation 62
2.3.10. Loading of Hot Side Assembly into Large Thermal Fatigue Chamber 64
2.3.11. Purging the Large Thermal Fatigue Chamber 67
2.3.11.1. Vacuum Pump Connection to Large Thermal Fatigue Chamber 67
2.3.11.2. Vacuum Pumping and Argon Purging the Large Chamber 68
2.3.11.3. Connection of the Large Thermal Fatigue Chamber to a Bubbler 69
2.3.11.4. The Large Thermal Fatigue Bubbler 70
2.3.11.5. Argon Gas Flow Rate to the Large Thermal Fatigue Chamber 71
2.3.12. Large Thermal Chamber Temperature Control 72
2.3.12.1. Thermocouple Controller and Thermocouple Meter 72
2.3.12.2. Large Thermal Chamber Heating Profile 75
2.3.12.3. Large Thermal Chamber Thermocouple Meter 76
2.3.13. Completion of a Thermal Cycle Experiment 77
2.4. Small Thermal Fatigue Chamber 78
2.4.1. Small Thermal Chamber Overview 78
2.4.2. Hot Side Refractory Brick Assembly 79
2.4.3. Hot Side Fiberglas Base Plate Assembly 81
2.4.4. Small Chamber Hot Plate Assembly 87
2.4.5. Hot Side Thermocouple Attachment 88
2.4.5.1. Hot Plate Thermocouple Attachment 88
2.4.5.2. Hot Side Thermocouple and Thermocouple Lead Soldering 90
2.4.6. Cold Side Thermocouple Attachment 91
2.4.6.1. Cold Plate Thermocouple Attachment 91
2.4.6.2. Cold Side Thermocouple and Thermocouple Lead Soldering 94
2.4.7. Cold Plate Stand 96
2.4.8. Small Thermal Chamber Base 99
2.4.8.1. Small Thermal Chamber Plexiglas Base Plate 99
2.4.8.2. Small Chamber Base Plate Vacuum Pump and Argon Gas Feed-Through 102
2.4.8.3. Small Chamber Base Plate Cold Plate Chiller Line Feed-Through 105
2.4.8.4. Small Chamber Base Plate Bubbler Line Feed-Through 108
2.4.8.5. Small Chamber Base Plate Electrical and Thermocouple Lead Through 110
2.4.9. Small Thermal Chamber Temperature Control 111
2.4.9.1. Thermocouple Meter and Thermocouple Controller 111
2.4.9.2. Small Thermal Fatigue Chamber Heating Profile 114
2.4.10. Fibrous Zirconia Test Specimen Insulation 115

2.4.11. Preparing for Thermal Cycling in Small Chamber 117
2.4.11.1. Loading Hot Side Assembly into Small Chamber 117
2.4.11.2. Purging the Small Thermal Fatigue Chamber 119
2.4.11.3. Starting the Small Thermal Fatigue Chamber Cycling 121
2.4.11.4. Completion of a Thermal Cycling Experiment 122
2.5. Elastic Modulus Measurements (RUS) 123
2.5.1. Preparation of Specimen Elastic Modulus Testing 123
2.5.2. Resonant Ultrasound Spectroscopy 124
2.5.2.1. Overview 124
2.5.2.2. Resonant Ultrasound Spectroscopy Transducers 126
2.5.2.3. Resonant Ultrasound Spectroscopy Transducer Arrangement 128
2.5.2.4. Resonant Ultrasound Spectroscopy Program 131
2.5.2.5. Resonant Ultrasound Spectroscopy Spectrum Data 133
2.5.2.6. RUS Analysis using RPModel 134
2.6. Fracture Testing 135
2.6.1. Biaxial Fracture Testing Ring-on-ring Introduction 135
2.6.2. Overview of Biaxial Flexural Ring-on-ring Assembly 137
2.6.3. Ring-on-ring Support Fixture 140
2.6.4. Ring-on-ring Loading Fixture 142
2.6.5. Ring-on-ring Load Rod 144
2.6.6. Ring-on-ring Support Gasket 145
2.6.7. Ring-on-ring Sample Teflon Tape 147
2.6.8. Ring-on-ring Cage Assembly 149
2.6.9. Ring-on-ring Cage Assembly Loading in the Instron Machine 151
2.6.9.1. Ring-on-ring Instron Software 151
2.6.9.2. Ring-on-ring Cage Loading in Instron 152
2.6.10. Post Biaxial Flexural Testing Valid and Invalid Fractures 155

3. RESULTS AND DISCUSSION 161
3.1.1. Grain Size of LAST and LASTT 161
3.1.2. LAST Surface Inclusion and Pitting 167
3.1.3. LASTT Disk Specimen Blistering 189
3.2. Elastic Modulus Measurements in LASTT and LAST Specimens 195
3.2.1. Young's Modulus of LAST and LASTT Specimens 198
3.2.1.1. Initial LAST Specimens' Young's Modulus 198
3.2.1.2. Reformulated LAST Specimen's Young's Modulus 200
3.2.1.3. LASTT Specimen's Young's Modulus 202
3.2.2. Poisson's Ratio of LAST and LASTT Specimens 204
3.2.2.1. Initial LAST Specimen's Poisson's Ratio 204
3.2.2.2. Reformulated LAST Specimen's Poisson's Ratio 206
3.2.2.3. LASTT Specimen's Poisson's Ratio 208
3.3. Fracture Strength of As-received and Thermally Fatigued LAST and LASTT 210
3.3.1. Fracture Strength 210
3.3.1.1. Fracture Strength of As-received and Thermally Fatigued LASTT 211
3.3.1.2. Fracture Strength of As-received and Thermally Fatigued LAST 214

3.3.2. Weibull Statistics for As-received LAST and LASTT 217
3.3.2.1. Weibull Statistics for As-received LASTT 218
3.3.2.2. Weibull Statistics for As-received LASTT 220
3.3.2.3. Comparative Weibull Statistics for As-received LAST and LASTT 222
3.4 Specimen Surface Finish and Impact on this Study 225

4. SUMMARY AND CONCLUSION 226

5. FUTURE WORK 231

Appendix A. Standard Operation Procedure for Large Thermal Fatigue Experiment with the Prototype Thermal Fatigue Chamber (Fei Ren)This standard operating procedure gives the ability to properly load and operate the large thermal fatigue chamber used in the thermal cycling of the wafer LAST and LASTT specimens. 233

Appendix B. Standard Operation Procedure for Thermal Fatigue Experiment with the Prototype Thermal Fatigue Chamber (Dan Kleinow and Fei Ren 12-16-2008). This standard operating procedure gives the ability to properly load and operate the small thermal fatigue chamber used in the thermal cycling of the parallelepiped LAST and LASTT specimens..... 244

Appendix C. Bluehill ROR-BFT Test Protocol Software Standard Operating Procedure (SOP) for the proper programming, loading and testing methods for Ring-on-ring fracture testing. The Appendix has the step by step process for programming the computer used to run the Instron machine with the ring-on-ring apparatus, as well as the testing procedures to properly prepare and run the Instron and Bluehill safely. 251

Appendix D. Ring-on-ring biaxial flexural data for all LASTT specimens tested. The Tables in this appendix contain all measurements and validity for all LASTT specimens tested for 0, 30, 60, 90, 120, 150, and 200 thermal fatigue cycle using ring-on-ring technique. A brief description for specimens with an invalid or premature fracture can be found under the specimens corresponding table..... 254

Appendix E. Ring-on-ring biaxial flexural data for all Reformulated LAST specimens tested. The Tables in this Appendix contain all size and strength measurements and validity for all LAST specimens tested for 0, 30, 60, 90, 120, 150, and

200 thermal fatigue cycle using ring-on-ring technique. A brief description for specimens with an invalid or premature fracture can be found under the specimens corresponding table.....263

References 271

List of Tables

Table 3.1.1.1. The average grain size for as-received LAST and LASTT specimen determined using scanning electron microscope images and the line-intercept method. It was determined that the LAST samples had a unimodal grain size, where the LASTT tended to show a bimodal grain size 166

Table 3.2.1. With respect to the number of thermal fatigue cycles, N, the initial (N=0), the final (N=200), the mean, the maximum, and the minimum values of the Young's modulus, E, for each of the twelve elasticity/thermal fatigue specimens included in this study 196

Table 3.2.2. With respect to the number of thermal fatigue cycles, N, the initial (N=0), the final (N=200), the mean, the maximum, and the minimum values of the Poisson's ratio, υ, for each of the twelve elasticity/thermal fatigue specimens included in this study 197

Table D1. P15: As-received 254

Table D2. P28: As-received 255

Table D3. P15: 30 Thermal Fatigue Cycles 256

Table D4. P28: 60 Thermal Fatigue Cycles 257

Table D5. P25:90 Thermal Fatigue Cycles 258

Table D6. P28/32: 90 Thermal Fatigue Cycles 259

Table D7. P26: 120 Thermal Fatigue Cycles 260

Table D8. P32: 150 Thermal Fatigue Cycles 261

Table D9. P28: 200 Thermal Fatigue Cycles 262

Table E1. N39: As-received 263

Table E2. N39: As-received 264

Table E3 N39: 30 Thermal Fatigue Cycles 265

Table E4. N41: 60 Thermal Fatigue Cycles 266

Table E5. N38/39: 90 Thermal Fatigue Cycles.....267

Table E6. N38: 120 Thermal Fatigue Cycles.....268

Table E7. N37/38: 150 Thermal Fatigue Cycles.....269

Table E8. N37: 200 Thermal Fatigue Cycles.....270

List of Figures

Figure 2.1.1. Example of disk-shaped specimen of LAST and LASTT used in large thermal fatigue chamber 33

Figure 2.1.2. Example of LAST and LASTT rectangular parallelepiped sample used in Small Thermal fatigue chamber 33

Figure 2.3.1. Alumina refractory brick with heater section removed and electrical lead holes drilled through it. Side B-# is used to designate the sides of the refractory brick to assist in the explanation of the construction of the alumina brick 40

Figure 2.3.2. Alumina refractory brick with heater sitting in cavity, flush with cavity walls 40

Figure 2.3.3. Fiberglass base plate with electrical and thermocouple lead holes drilled through it. The fiberglass plate also shows the refractory brick attachment screws. Side F-# is used to designate the sides of the fiberglass base plate to assist in the explanation of the construction of the plate 42

Figure 2.3.4. Fiberglass base plate with alumina refractory brick zirconia insulation separator and electrical leads. Side I-# is used to designate the sides of the zirconia insulation separator to assist in the explanation of the construction of the insulation sheet 43

Figure 2.3.5. Alumina refractory brick in place on fiberglass base plate with electrical leads running up through pre-drilled holes 45

Figure 2.3.6. Large thermal fatigue chamber hot plate stage configuration of the lab jack, Plexiglas base plate, refractory brick and hot plate. Holes were drilled through the Plexiglas base plate and the thermocouple leads were fed through the holes to keep them from moving or becoming caught when the stage was adjusted 45

Figure 2.3.7. Large chamber heater positioned in the porous alumina refractory brick with the four k-type thermocouples cemented on. Side H-# is used to designate the sides of the hot plate to assist in the location of the thermocouple attachments to the hot plate 49

Figure 2.3.8. Large thermal fatigue chamber copper cold plate mounted inside of thermal chamber with four k-type thermal couples attached. Side C-# is used to designate the sides of the cold plate to assist in the location of the thermocouple attachments to the cold plate . 52

Figure 2.3.9. Back of the large thermal fatigue chamber showing the bubbler gas line connection, water chiller inlet and outlet for the cold plate, the hot plate electrical feed thru, and the cold side and hot side thermocouple feed thru 55

Figure 2.3.10. Pre-cut fibrous zirconia insulation sheet used to insulate sides of specimens during thermal cycling placed over on to the large thermal chamber refractory brick and heater configuration 61

Figure 2.3.11. Large thermal fatigue chamber hot plate set-up and pre-cut fibrous zirconia insulation with 10 samples in place for cycling. The insulation accomodates a sample configuration of two rows of five, the insulation also helps to keep the samples from shifting while the hot plate stage is loaded into the chamber 63

Figure 2.3.12. The hot plate assembly after it had been loaded into the large thermal fatigue chamber and raised by the lab jack to allow the specimens to contact the hot and cold plate 65

Figure 2.3.13. Schematic drawing of the large thermal fatigue chamber internal and rear assembly [Drawing by Fei Ren] 65

Figure 2.3.14. The clear Plexiglas front cover with o-ring in place on the large thermal fatigue chamber and firmly held in place and sealed by 6 hex bolts 66

Figure 2.3.15. Front view of the sealed large thermal fatigue chamber with the sample stage in place and the thermocouple meter and temperature controller prepared for cycling 73

Figure 2.3.16. The thermal cycling profile for the large thermal fatigue chamber. It took one hour to complete one thermal cycle of 50-400 °C 74

Figure 2.4.1. Alumina refractory brick with cavity removed and lead wire holes drilled for placement and attachment of the hot plate. Two holes drilled for connection with the fiberglass board are visible as well. Side B-# is used to designate the sides of the refractory brick to assist in the explanation of the construction of the alumina brick 80

Figure 2.4.2. Small thermal fatigue chamber hot plate set up within the refractory alumina brick with attached thermocouple 80

Figure 2.4.3. Fiberglass base plate attached to lab jack with alumina refractory brick attachment bolts. Side F-# is used to designate the sides of the fiberglass base plate to assist in the explanation of the construction of the plate 83

Figure 2.4.4. Underside of the refractory brick (opposite side of heater) showing the section removed, in the black oval, for the electrical lead wire to lie between the refractory brick and fiberglass base plate without tilting the heater during thermal cycling..... 84

Figure 2.4.5. Zirconia insulation used to separate the fiberglass base plate from direct contact with the alumina refractory brick during heating. Side I-# is used to designate the sides of the zirconia insulation separator to assist in the explanation of the construction of the insulation sheet 85

Figure 2.4.6. Heater assembly of lab jack, fiberglass base plate, zirconia insulation separator and refractory brick with heater electrical lead wires. Heater assembly ready for hot plate attachment 86

Figure 2.4.7. Top view of small thermal chamber set-up, showing the vacuum and bubbler tubes inlets, heater power cord feed thru, the thermocouple feedthru from the floor mat, as well as the cold plate water chilling inlet and outlet tubes..... 92

Figure 2.4.8. Small Thermal Chamber Cold Plate (sample contact side) with thermocouple and thermocouple lead attached. Side C-# is used to designate the sides of the cold plate to assist in the location of the thermocouple attachments to the cold plate..... 93

Figure 2.4.9. Back side of the small thermal fatigue chamber set-up with the sample stage, with a view of the hot and cold plate thermocouples and the thermocouple leads, also the electrical feed thru for the hot plate 95

Figure 2.4.10. Small Thermal Fatigue Chamber Cold Plate installed on cold plate stand using attached threaded rods. Side F-# is used to designate the sides of the cold stand fiberglass base plate to assist in the explanation of the construction of the plate..... 98

Figure 2.4.11. Left side of the small thermal fatigue chamber showing the configuration of the 100 cm gasket ring riveled to four L-brackets held to the chamber floor using a nut and bolt design, used in vacuum sealing the glass bell jar prior to thermal cycling. 100

Figure 2.4.12. Top View of the Small thermal chamber Plexiglas and rubber mat base plate with the cold side assembly in position for thermal testing. Side P-# is used to designate the sides of the small thermal chamber Plexiglas base plate to assist in the explanation of the construction of the plate 101

Figure 2.4.13. Front view of the small thermal fatigue chamber with a clear view of the vacuum/argon tube connections on the chamber floor. Side P-# is used to designate the sides of the small thermal chamber Plexiglas base plate to assist in the explanation of the construction of the plate 103

Figure 2.4.14. Underside view of small thermal fatigue Plexiglas base plate Argon gas and vacuum pump hose connection 104

Figure 2.4.15. Side P-C side view (Figure 2.4.12.) of small thermal fatigue Plexiglas base plate Chiller water inlet and outlet hoses and connections 107

Figure 2.4.16. Side P-B of Figure 2.4.12. showing the bubbler hose connection to the small chamber floor. Also shown is the Hot plate electrical lead and the hot and cold side thermocouple lead outlet 109

Figure 2.4.17. Small thermal fatigue chamber set-up and connected to the Argon tank, the bubbler, and the water chiller. This also shows the chambers thermocouple controller and temperature controller reading 112

Figure 2.4.18. The thermal cycling profile for the small thermal fatigue chamber. It took 38 minutes to perform one thermal fatigue cycle of 50-400°C 113

Figure 2.4.19. Pre-cut fibrous zirconia insulation placed on top of the small thermal fatigue chamber hot plate and refractory brick set-up, with a sample area rectangle removed, as shown in the black circle. This insulation was used to insulate the two samples during thermal cycling 116

Figure 2.4.20. Hot plate apparatus raised by lab-jack and in contact with cold plate prior to tightening the bell jar 118

Figure 2.5.1. The resonant ultrasound spectroscopy tripod arrangement used to test the small thermal fatigue chamber specimens. There is one drive transducer and two pickup transducers 125

Figure 2.5.2. The resonant ultrasound spectroscopy tripod arrangement showing the rounded rubber transducer tips which contact the specimen during the testing 127

Figure 2.5.3. Resonant ultrasound Spectroscopy tripod arrangement with a sample in place for testing. The drive transducer was placed at the edge of the sample along the width of the parallelepiped sample, while the pickup transducers were placed under the samples opposite two corners. Side S-# is used to designate the sides of the test sample in respect to the samples position on the RUS transducers 129

Figure 2.5.4. Side view of the resonant ultrasound spectroscopy tripod arrangement with a parallelepiped sample in place for testing from figure 2.5.3. It should be noted that the sample only sits at the tip of the transducer and should not be in contact with the transducers metal housing 130

Figure 2.5.5. Example of a section of RUS spectrum data with distinctive peaks 132

Figure 2.6.1. Schematic of the ring-on-ring apparatus used to perform the biaxial fracture testing. The ring-on-ring apparatus is used in a commercial testing machine (Model 4206 Instron Corporation, Norwood, MA) to perform biaxial flexural testing. The device consists of five separate parts working in sequence; the load rod and ball, load fixture, support fixture, support platen/rod, and the support gasket. (image by Fei Ren) 136

Figure 2.6.2. Ring-on-ring cage sections used to house the LAST and LASTT large thermal fatigue samples during biaxial flexural testing. This cage is composed of the support gasket, load fixture, and support fixture 138

Figure 2.6.3. The load fixture top and load rod were designed to assist in the proper loading of the specimen during testing. The alignment of the hemispherical cavity and the ball bearing assisted in applying the loading force to the center of the cage, distributing the force evenly through the loading ring to the sample. This even spread of force is achieved by the ball bearing in the loading rod and the hemispherical cavity machined into the top of the load fixture. The hemispherical cavity will require the ball bearing to only apply force in a vertical axis, if there is any horizontal force then the ball bearing will continue to move to the bottom of the sphere with an applied horizontal force because of the low amount of friction between the two materials 139

Figure 2.6.4. Ring-on-ring support fixture side view of the support fixture base, support ring platform, and the support ring. The ROR support fixture also had three guide pins in place to ensure stability and alignment between the load and support rings during testing 141

Figure 2.6.5. Load ring showing the three holes in which the guide pins use to align the load fixture and support fixture 143

Figure 2.6.6. Ring-on-ring support fixture with the support gasket placed over the support ring to decrease the friction between the sample and the support ring during loading which could lead to low or invalid fracture strengths 146

Figure 2.6.7
Figure 2.6.8
Figure 2.6.9
Figure 2.6.10
Figure 2.6.11
Figure 2.6.
Figure 2.6
Figure 2.
Figure 2

Figure 2.6.7. Ring-on-ring support fixture and gasket with a large thermal fatigue chamber specimen set in place on top of the gasket in the center of the fixture. This image is a succession of Figure 2.6.5. prior to testing 148

Figure 2.6.8. Ring-on-ring cage setup with a large thermal fatigue specimen in place and support gasket sandwiched between the aligned support and load rings. The specimen was centered equidistant from each support leg on the support fixture, allowing for the specimen to be relatively centered within the loading apparatus ... 150

Figure 2.6.9. Ring-on-ring cage and loading rod positioned and centered on a compression plate within the Instron machine and ready for biaxial flexural testing 154

Figure 2.6.10. LASTT specimen P14-19 (as-received) showing a valid low energy ring-on-ring fracture. (47 MPa) 157

Figure 2.6.11. LAST specimen N39-28 (as-received) showing a valid low energy ring-on-ring fracture. (9.1 MPa) 157

Figure 2.6.12. LASTT specimen P15-60 (30 cycles) showing a valid medium energy ring-on-ring fracture. (32.2 MPa) 158

Figure 2.6.13. LASTT specimen P28-10 (60 cycle) showing a valid medium energy ring-on-ring fracture. (33.7 MPa) 158

Figure 2.6.14. LASTT specimen P15-34 (as-received) showing a valid high energy ring-on-ring fracture. (38.1 MPa) 159

Figure 2.6.15. LASTT specimen P26-36 (120 cycles) showing a valid high energy ring-on-ring fracture. (47.8 MPa) 159

Figure 2.6.16. LASTT specimen N38-9 (as-received) showing an invalid ring-on-ring fracture. The crack most likely propagated through the sample because of an edge flaw shown with the black arrow. 160

Figure 2.6.17. LASTT specimen P14-26 (as-received) showing an invalid ball-on-ring fracture. The crack most likely propagated through the sample because of an edge flaw shown with the black arrow 160

Figure 3.1.1.1a. LAST as-received specimen N39-10 fracture surface using a scanning electron microscope used to determine the average grain size (31.35 micron/grain) through the line-intercept method. 162

Figure 3.1.1.1b. LAST as-received specimen N39-15 fracture surface using a scanning electron microscope used to determine the average grain size (31.35 micron/grain) through the line-intercept method. 163

Figure 3.1.1.2a. LASTT as-received specimen P28-31 fracture surface using a scanning electron microscopy image of the fracture surface. This shows the bimodal grain size found in the LASTT material of larger grains (15.57 microns/grain) in a matrix of much smaller grains (3.375 micron/grain) 164

Figure 3.1.1.2b. LASTT as-received specimen P28-30 fracture surface using a scanning electron microscopy image of the fracture surface. This shows the bimodal grain size found in the LASTT material of larger grains (15.57 microns/grain) in a matrix of much smaller grains (3.375 micron/grain) 165

Figure 3.1.2.1. SEM backscattered electron image of inclusions in as-received (not thermally cycled) LAST specimen N38-10 of surface inclusions (black ovals). As was the case for other as-received LAST specimens, no surface pits are evident on the as-received specimen surface..... 172

Figure 3.1.2.2. SEM secondary electron images of surface pitting in LAST specimen N38-9 after thermal cycling in the large specimen chamber for 150 cycles. The pits (dashed circles) in this micrograph have an average diameter of about 150-200 microns. In addition, small, intact inclusions are also visible on the surface that are as large as approximately 50 microns across (black oval) 173

Figure 3.1.2.3a. Surface of LAST specimen N37-21 in contact with the **cold plate**, showing surface pitting and inclusions after 200 thermal cycles 174

Figure 3.1.2.3b. Surface of LAST specimen N37-21 in contact with the **hot plate**, showing surface pitting and inclusions after 200 thermal cycles ... 174

Figure 3.1.2.4a Inclusion and pit counts versus thermal cycling for LAST sample N39-46 cycled in the small thermal fatigue chamber (N=20). The inclusions and pits were counted from three random areas of each sample for each cycle of the thermal fatigue cycling. The total number of surface inclusions from the three areas were added together, as were the total number of surface pits for each cycle. The total number of surface pits and surface inclusions were then divided by three to give an average for each thermal fatigue cycle 175

Figure 3.1.2.4b. Inclusion and pit counts versus thermal cycling for LAST sample N39-49 cycled in the small thermal fatigue chamber (N=20). The inclusions and pits were counted from three random areas of each sample for each cycle of the thermal fatigue cycling. The total number of surface inclusions from the three areas were added together, as were the total number of surface pits for each cycle. The total number of surface pits and surface inclusions were then divided by three to give an average for each thermal fatigue cycle 176

Figure 3.1.2.4c. Sum of Inclusion and Pit Count versus number of thermal fatigue cycles from 0-20 cycles 177

Figure 3.1.2.5a. LAST specimen N39-46, as-received specimen, with inclusions ranging from roughly 20-200 microns observed using optical microscopy 178

Figure 3.1.2.5b. The surface of LAST specimen N39-46 after 5 thermal cycles. Both inclusions and surface pits are evident 179

Figure 3.1.2.5c. The surface of LAST specimen N39-46 after 10 thermal cycles. Microcracking (within black circle) is observed around the inclusion 180

Figure 3.1.2.5d. A higher magnification view of N39-46 after 10 thermal cycles, the arrows highlight microcrack damage surrounding the inclusion caused by thermal expansion anisotropy due to the different thermal expansion coefficients of the inclusion and the LAST matrix 181

Figure 3.1.2.5e. N39-46 after 12 thermal cycles. The dashed circle shows similar fracture damage surrounding the pit as is found within the matrix surrounding the inclusion in the solid black circle to the right. The inclusion in the white circle can be seen in Figure 3.1.2.5f having suffered further damage during thermal cycling 182

Figure 3.1.2.5f. N39-46 after 15 thermal cycles. Following the lower left inclusion in Figure 3.1.2.5e, it is noticed that spalling occurred at the bottom edge of the inclusion in the white circle within 3 cycles 183

Figure 3.1.2.6a. For as-received LAST specimen N38-10 with an inclusion (dark area) within a lighter-appearing matrix. Light and dark areas are due to atomic number contrast in the SEM 184

Figure 3.1.2.6b. EDS image of as-received LAST specimen N38-10 with silver rich area within inclusion 185

Figure 3.1.2.6c. EDS image for as-received LAST specimen N38-10 with an antimony rich area. The antimony rich region is disjoint from silver-rich regions shown in part (b)..... 186

Figure 3.1.2.6d. An EDS image of as-received specimen, N38-10, with a uniform distribution of tellurium in the inclusion, except within silver rich area of Figure 3.1.2.6b..... 187

Figure 3.1.2.6e. EDS image of as-received N38-10 specimen indicating the inclusion is lead poor while the surrounding LAST matrix has a uniform and higher concentration of lead..... 188

Figure 3.1.3.1. The surface of specimen P26-50 in contact with the **cold plate**. Specimen P26-50 blistered after 120 cycles. The blister dimensions were 1 cm in diameter and 5 mm in height as measured from the original sample surface..... 191

Figure 3.1.3.2. The surface of specimen P26-50 in contact with the **hot plate**. Specimen P26-50 blistered after 120 cycles. The blister dimensions were approximately 8 mm in diameter and 3 mm in height as measured from the original surface of the specimen..... 191

Figure 3.1.3.3. The surface of specimen P32-11 in contact with the **cold plate**. Specimen P32-11 blistered after 150 cycles. The blister dimensions were approximately 7 mm in diameter and 2 mm in height as measured from the original sample surface..... 192

Figure 3.1.3.4. The surface of specimen P32-14 in contact with the **hot plate**. Specimen P32-14 blistered after 150 cycles. The blister dimensions were approximately 6 mm in diameter and 2 mm in height as measured from the original sample surface..... 192

Figure 3.1.3.5a. The surface of specimen P25-31 in contact with the **cold plate** after ring-on-ring fracture testing, which blistered after 90 cycles. The blister dimensions are 1 cm in diameter and 1 mm in height from the original specimen surface 193

Figure 3.1.3.5b. Interior view of specimen P25-31 on the side which was in contact with the **cold plate**, showing a large void area within the sample with a rough wall compared to the smoother surface of the sample along the fracture, designated by the black circle, which occurred in the sample during blistering after 90 cycles 193

Figure 3.1.3.5c. Interior view of specimen P25-31 on the side which was in contact with the **hot plate**, showing the underside of the void area within the sample which caused the surface to dimple. The inner surface of the internal void was considerably rougher compared to the smooth surface of the sample along the fracture, designated by the black circle, which occurred in the sample during blistering after 90 cycles 194

Figure 3.2.1.1. Resonant Ultrasound Spectroscopy (RUS) measurements of the Young's modulus as a function of the number of thermal fatigue cycles for initial n-type (LAST) samples, cycled in the small thermal fatigue chamber 199

Figure 3.2.1.2. Resonant Ultrasound Spectroscopy (RUS) measurements of the Young's modulus as a function of the number of thermal fatigue cycles reformulated for n-type (LAST) samples, cycled in the small thermal fatigue chamber 201

Figure 3.2.1.3. Resonant Ultrasound Spectroscopy (RUS) measurements of the Young's modulus as a function of the number of thermal fatigue cycles for p-type (LASTT) samples, cycled in the small thermal fatigue chamber 203

Figure 3.2.2.1. Resonant Ultrasound Spectroscopy (RUS) measurements of the Poisson's ratio as a function of the number of thermal fatigue cycles for initial n-type (LAST) samples, cycled in the small thermal fatigue chamber 205

Figure 3.2.2.2. Resonant Ultrasound Spectroscopy (RUS) measurements of the Poisson's ratio as a function of the number of thermal fatigue cycles for reformulated n-type (LAST) samples, cycled in the small thermal fatigue chamber 207

Figure 3.2.2.3. Resonant Ultrasound Spectroscopy (RUS) measurements of the Young's modulus as a function of the number of thermal fatigue cycles for p-type (LASTT) samples, cycled in the small thermal fatigue chamber 209

Figure 3.3.1. Ring on Ring (ROR) fracture strength as a function of the number of thermal fatigue cycles for p-type LASTT cycled in the large thermal fatigue chamber. For the numbers in parentheses near the plotting symbols (i,j), the first number "i" indicates the number of valid fractures obtained and the second number "j" indicates the number of specimens fractured for the given thermal shock treatment..... 212

Figure 3.3.2. For the ROR fracture data shown in Figure 3.3.1, the coefficient of variation (standard deviation divided by the mean strength) versus the number of thermal fatigue cycles for the p-type LASTT specimens thermally cycled in the large thermal fatigue chamber 213

Figure 3.3.3. Ring on Ring (ROR) fracture strength as a function of the number of thermal fatigue cycles for LAST cycled in the large thermal fatigue chamber. For the numbers in parentheses near the plotting symbols (i,j), the first number "i" indicates the number of valid fractures obtained and the second number "j" indicates the number of specimens for fractured for the given thermal shock treatment..... 215

Figure 3.3.4. For the ROR fracture data shown in Figure 3.3.3, the coefficient of variation (standard deviation divided by the mean strength) versus the number of thermal fatigue cycles for the LAST cycled specimens thermally cycled in the large thermal fatigue chamber. 216

Figure 3.3.5. The Weibull modulus of the as-received high lead LAST N39 specimens show a distinct high strength and low strength trend. The low strength Weibull modulus had a variable distribution of 1.4407 with a characteristic strength of 19.8 ± 10 MPa. The high strength Weibull modulus had a variable distribution of 8.2196 with a characteristic strength of 36.7 ± 3.6 MPa 219

Figure 3.3.6. The Weibull modulus of the as-received LASTT P15 and P28 specimens show a distinct high strength and low strength trend. The low strength Weibull modulus had a variable distribution of 2.0775 with a characteristic strength of 17.9 ± 6.9 MPa. The high strength Weibull modulus had a variable distribution of 8.2196 with a characteristic strength of 32.7 ± 4.5 MPa 221

Figure 3.3.7. The weibull analysis compares both high lead LAST and LASTT as-received specimens. It is seen that there is a similar strength distribution for the LAST and LASTT samples. The fractions in the parentheses indicate the number of valid fractures in each group over the initial sample size during ring-on-ring testing 223

Figure 3.3.8. The weibull analysis shows only the high strength high lead LAST and LASTT as-received specimens. It is seen that there is a similar strength distribution for the LAST and LASTT samples. The fractions in the parentheses indicate the number of valid fractures in each group over the initial sample size during ring-on-ring testing 224

Figure A1. Front View of the thermal fatigue chamber system 234

Figure A2. Schematic of the thermal fatigue chamber 236

Figure A3. Schematic of large thermal chamber cold plate for construction by MSU physics shop 237

Figure A4. Detailed schematic of large chamber cold plate 238

Figure B1. Small thermal fatigue chamber with cold plate chiller and thermocouple controller and thermocouple meter 251

Figure B3. Schematic of the thermal fatigue system 254

1.1 Thermoelectric Effect

There are three distinct thermal electric effects, which can arise in a brittle thermoelectric due to an applied temperature gradient, electrical field, or both. The thermoelectric effects are known as the Seebeck coefficient, Peltier effect, and Thompson effect; and all pertain to the fundamental functioning of modern day thermoelectric materials [Li 2006]. Brittle thermoelectric materials are generally semiconductor compounds, and are being pursued for the conversion of waste heat to electricity, or the exchange of electric current to run refrigerant free cooling devices. Whether the thermoelectric device is for electricity or temperature control, the understanding of the Seebeck and Peltier thermoelectric effects and the relation to the effectiveness and efficiency of thermoelectric devices is important.

Thermoelectric coefficients are the basic building blocks for the theory of thermoelectric devices. Manipulation of the thermoelectric coefficients can produce a more effective and a more efficient device [Pollock 1991]. The understanding of a materials response to thermoelectric coefficients can help with increasing the power output of semiconductive material during development. A higher Seebeck coefficient can help in the manipulation of a semiconductors figure of merit (ZT), resulting in a greater efficiency of heat to energy, or vice versa [Nolas 2001].

1.2 Thermoelectric Material Background

The Seebeck coefficient was first discovered in 1822 and pertains to the conversion of heat directly to electricity without the need for moving parts [Pollock 1991]. The thermoelectric conversion method of electrical production is commonly performed using heavily doped, or extrinsic semiconductors, such as Lead-Telluride or Gallium-Arsenic compounds. Such an energy device could prove most useful in an automotive setting, for instance using the exhaust or engine heat lost through burning fuel to power electrical components within the vehicle. Increased efficiency of TE semiconductors could reduce and even eliminate the need of electric power produced by a vehicles alternator, helping to reduce fuel usage [Kasap 2006].

A basic Seebeck effect thermal generator consists of an n-type and p-type thermocouple connected electrically in series and thermally in parallel. The semiconductors are connected using an ohmic contact, a contact with a negligibly small voltage drop between the materials [Sze 2007]. The Seebeck effect occurs when a temperature gradient develops an open circuit voltage between two dissimilar metals when the two junction points of the n- and p-type semiconductors are maintained at different temperatures [Kasap 2006, Li 2006].

The Seebeck coefficient is given as $S = \Delta V/\Delta T$ (for all temperatures), where ΔV is the potential difference voltage and ΔT is the difference in the temperature in the conductors junction. The sign of the Seebeck coefficient depends on the potential of the thermoelectric device's cold side with respect to the hot side. Electrons diffuse from the hot side to the cold side whether the Seebeck is negative or positive. The absolute

Seebeck coefficient is negative of more electrons are collected on the cold side than holes [Kasap 2006, Mikami 2009].

The Peltier effect was discovered in 1834, shortly after the Seebeck effect. With a great enough efficiency, Peltier thermoelectric devices could be used in place of harmful refrigerants and noisy compressor pumps in appliances and even in upcoming electric cars. The Peltier effect occurs in materials using a similar setup as the Seebeck coefficient. The Peltier effect is when heat is absorbed or liberated at a junction of two materials when an electrical current flows through the junction. The Peltier effect creates a thermal gradient through the module with an electric current [Li 2006, Nolas 2001]. The Thomson effect is merely the combination of both an applied electric current and a thermal gradient in the same direction on a semiconductor, ultimately causing a heating or cooling effect depending on their direction [Li 2006].

For thermoelectric materials to be seen as viable in today's world there are several important factors that include the material's Seebeck coefficient, electrical conductivity, thermal conductivity and absolute temperature. The Seebeck coefficient is the ratio between the electric field and the temperature gradient and allows one to determine whether the majority charge carriers are electrons or holes. If the thermal conductivity within the material is small, and the electrical conductivity is large, a much higher Seebeck is produced. If the thermal conductivity is high and the heat flow in the material does not increase there will be a very small thermal gradient throughout the material, the voltage would drop as the charge carriers carry heat through the semiconductor for a degenerately doped semiconductor. Whereas, for a non-degenerately doped semiconductor at high temperatures, thermal vibrations of atoms will be so severe that

bonds between atoms in the material will begin to break and an electron or hole will be released and thermally excited across the band gap. The increase in the electron concentration from the valence band to the conduction band will be mainly due to thermal generation and will generate and equal concentration of holes in the valence band. The semiconductor will perform as if it were intrinsic [Kasap 2006].

Thermoelectric materials have temperature dependent properties. As the temperature increases on one side of the device, the thermal gradient between the hot and cold side increases. The increased thermal gradient will increase the Seebeck effect, to a point. At a high enough temperature (depending on the material), a thermal gradient becomes increasingly difficult to maintain through the material. At a high enough temperature the thermal gradient of the material can reach a thermodynamic equilibrium, slowing and even stopping the current flow completely [Sze 1981].

Extrinsic semiconductors are similar to intrinsic semiconductors, except defects are purposely introduced into the material to induce additional electron or hole states [Jiles 1994]. An n-type (negative) semiconductor is one in which there are more electrons in the conduction band than there are holes in the in the valence band. A p-type (positive) semiconductor is one in which added impurities in the material remove electrons from the valence band creating more holes than electrons in the conduction band. Electrons can be thermally activated from the 'donor' levels in the band gap into the conduction band, which results in electrical conduction. . Alternatively, electrons may also be thermally stimulated from the valence band into the 'acceptor' levels in the band gap, causing hole conduction in the valence band [Kittel 2005, Jiles 1994, Kasap 2006] . When the temperature of one end of a thermocouple is raised, the electrons

become excited and diffuse towards the cold end, leaving a positive potential (holes) at the heated side. In the development of brittle and non-brittle semiconductors alike, the dopant levels, which add electron and hole states to the material, are important for a high Seebeck effect [Mikama 2009].

1.3 Figure of Merit, ZT

The figure of merit, ZT, is a material constant, which is proportional to the efficiency of the thermoelectric couple with the n and p-type semiconductors [Martin 2009]. The figure of merit (ZT), used to determine the performance of thermoelectric materials , is given as $ZT= S^2\sigma T/\kappa$; where S, σ, T and κ are the Seebeck coefficient, electrical conductivity, absolute temperature, and thermal conductivity [Takahashi 2010, Salvador 2009] respectively. A large figure of merit is necessary for a "good" thermoelectric material, but it becomes difficult to increase the ZT as it is not possible to maximize the three transport properties of the expression in unison. The electrical and thermal conductivity of a material are related for a thermoconductor. When the electrical conductivity is large for a conductor, the thermal conductivity also increases. This electrical/thermal conductivity relation is caused by the transport of the electrical charge in the material as well as heat carried by lattice phonons. However, materials that tend to have a high electrical conductivity generally have a low Seebeck coefficient [Kanatzidis 2003].

The Z can be separated into two categories, a power factor of $S^2\sigma$ which is dominated by charge carriers, and κ which is dominated by phonons. In this setup it can be assumed that a material with a high electron density will also have a high electrical conductivity, but this will lower the Seebeck coefficient due to the decrease in electrical potential within the material making it act more like a metal [Gogotsi 2006]. Maximization of the Seebeck coefficient can be done by reducing the carrier concentration in the material, but in doing so this will lower the electrical conductivity as

the carrier concentration and electrical conductivity are directly proportional. The figure of merit for thermoelectric semiconductors generally decreases with an increase in temperature. The decrease in ZT at an elevated temperature can be attributed to the increase in phonon scattering and the increase in electron and hole density which affect the Seebeck coefficient, thermal conductivity and electrical conductivity [Harris 2008].

The average ZT for a modern bulk thermoelectric material is ~1, but individual thin film materials have been known to exhibit ZT of around ~ 2 to 3. The larger figure of merit in thin films can be attributed in part to the material's grain sizes.

1.4 Thermoelectric Material Grain Size

Grain sizes for thin film semiconductors are typically less than 1 micron in size , giving the material a lower thermal conductivity and a higher electrical conductivity than larger grained polycrystalline semiconductors [Sootsman 2009, Kasap 2006]. The difference between bulk materials and thin film materials is due to the ability of the grain boundaries to scatter phonons within the material [Liao 2010]. The more grain boundaries present in the material, the more likely the phonon is impeded, ultimately reducing the thermal contribution of lattice and atom vibrations [Sootsman 2009].

The Seebeck coefficient is directly affected by a material's ability to transport electrons with an increase in temperature [Pollock 1991]. Electrical and thermal transport both involve electron transport and electron scattering, and in order to gain a high ZT there is a need for a reduction in phonon transport, this reduction has been obtained by using nanoscaled materials. By reducing the grain size in the material a quantum size effect emerges which enhances electron transport due to an increased electron density at the band edge, while also slowing phonon transport with the increase in the surface and grain boundary scattering [Ozin 2009]. In other words, the efficiency is greater for a material that retains a larger current over a given thermal gradient, which can be further maximized with the addition of dopants and grain size considerations [Liao 2010, Takahashi 2010]. The grain/temperature/dopant relationship is important in the development of extrinsic (generally brittle) semiconductor devices.

1.5 Temperature Effects on the Thermoelectric Coefficient of Brittle Conductive Materials

Thermoelectric materials have become a very sought after energy solution in recent history, though it was discovered over a hundred years ago [Pollock 1991]. The development of efficient modules is an important next step in developing alternative energies. Thermoelectric modules can enhance the use of the worlds' energy potential, specifically in dealing with wasted heat energy, and reduce the use of harmful chemicals. With the basic knowledge of how extrinsic semiconductors work and the role the Seebeck coefficient has in the increase in thermoelectric efficiency, an understanding of temperature effects and material constraints on thermoelectric devices in real world applications is key in developing functional devices.

The Seebeck Coefficient generally reaches a maximum at lower temperatures (600 ^{0}C) for brittle thermoelectrics, after which point it abruptly drops back towards zero with an increase in temperature. The study by Mikami 2009 for Sb-doped Heusler Fe_2VAl alloys showed that the initial Seebeck coefficient is effected by thebnad-like shift of the Fermi level in the band gap towards the conduction band with the increase of electrons through doping, but ultimately there is a common decrease around 300 K. According to Makami et. al., "The absolute value of S is inversely proportional to the number of carriers. Therefore, the decrease in the S value at higher temperatures can be attributed mainly to the increase in the number of thermally excited carriers across the pseudogap" [Mikami 2009 (446-447)].

The trend of temperature dependent hole-electron pairing in thermoelectric

materials was also noted in Takahashi 2010, in work with silicon and manganese doped $Ru_{1-x}Fe_xAl_2$. The initial carrier concentration of the material was increased by the addition of Mn and Si doping. As with Mikami [Makami 2009], Takahashi's Mn doped samples showed the intrinsic carrier concentrations began to dominate around 600 K. As the intrinsic carriers dominate, the electron and hole concentrations approach an equal value, which in turn removes the ability to generate the electric potential with temperature difference. A temperature equilibrium in a thermoelectric device means a thermal gradient cannot exist [Takahashi 2009]. The Si doped material begins with a negative S and turns positive after around 700 K, due to the hole excitation with the increase in temperature.

The Seebeck coefficient is affected by the microstructure [Salvador 2009]. Salvador worked with nanostructured TAGS (Tellurium-Antimony-Germanium-Silver), drastically increasing the material's efficiency by lowering the thermal conductivity and increasing the electrical conductivity by increasing the GeTe ratio. Salvador designed the TAGS material with a nano-microstructure with one conduction band and two valence bands. At elevated temperatures the TAGS has two valence bands, due to the increase in GeTe, that compete against a much smaller contribution from the conduction band, and as the material cooled one of the bands becomes dominant. [Salvador 2009]. With Salvadors' design [Salvador 2009] it is possible to not only run a TAGS thermoelectric device at temperatures over 600 K, but the Seebeck coefficient continuously increases with the increase in temperature. The TAGS nanostructured essentially has two valence bands competing with a smaller contribution from the conduction band in comparison to traditionally hot pressed TAGS powder which only has one valence band and one

conduction band [Salvador 2009].

1.6 Possible Methods of Improving Brittle Conductive Materials

Materials with nanosized grains have high interfacial energy barriers between grains which leads to an increased Seebeck coefficient and a decrease in the thermal conductivity. Grain boundaries impede the flow of heat through the material by scattering phonons through the grain boundaries [Martin 2009]. Sootsman et. al. stated that "draw backs in thin films such as their cost, scale-up and processing difficulties have prompted the exploration of new methods to prepare bulk nanostructured materials", along with strength, module design, and optimization of the materials ZT. [Sootsman 2009].

The development of materials that will function at elevated temperatures without a decrease in the Seebeck coefficient is important. A thermoelectric semiconductors survival at high temperatures can be developed through the increase and decrease of dopant levels, as well as decreasing the average grain size in the material. An effort between nanostructural aspects and material composition/doping considerations may maximize the Seebeck coefficient for the prospective temperature ranges of brittle semiconductor devices [Sootsman 2009].

1.7 Microcracking in Brittle Conductive Materials

Microcrack damage within brittle conductive materials influence mechanical, thermal and electrical properties [Case 2002]. Microcracks interact with a brittle material in either a negative or positive manner. [Case 2002]. Micro damage can be induced by microstructure, impact loading, and thermal stresses. Material flaws and microconstiuents (grains size, composition) may work separately or conjoined to induce microcracks [Green 1983]. Significant changes occur in the Young's modulus, E, Poisson's ratio, ν, fracture toughness, K_C, as well as the thermal and electrical conductivity of a microcracked sample compared to those of a microcrack-free brittle conductive specimens [Case 2002]. The principle mechanisms of microcracking help us understand how materials are affected and suggest methods of avoiding damage or employing the damage to a material's advantage.

1.8 Thermally Induced Microcracks

Thermally created microcracks result from thermal expansion anisotropy, thermal expansion mismatch, and thermal fatigue/shock. Internal material mechanisms create stresses within the material, leading to microcracking [Yamai 1993].

A critical grain size for microcracking in a material results from an energy balance between the residual elastic strain energy and the energy needed to create fracture surfaces. As grain size increases, the volume and surface area increases, as well as elastic strain energy. A larger grain size in turn creates more energy to propagate a crack [Green 1983]. For grains larger than the critical grain size, there is enough stored elastic strain energy to propagate a crack. Thermal expansion anisotropy occurs in single and polycrystalline materials when randomly aligned grains ($GS>GS_c$) expand or contract unequally along the XYZ axes. Microcracking can arise when randomly oriented grains have differing thermal expansion coefficients along their axes. Differing thermal expansions lead to stresses at grain boundaries, which result in cracking [Barsoum 2003].

Yamai *et al.* [Yamai 1993] showed that the Young's modulus of the $CaZr_4(PO_4)_6$ ceramic is very dependant on microcracking. The Young's modulus was measured in relation to grains size. The grain size was carefully controlled with sintering time and temperature. The Young's modulus and the material strength decreased for grains larger than the critical grain size. The coefficient of thermal expansion became negative with the increased microcracking. With the increased microcrack damage the material was unable to withstand plastic deformation without the propagation of cracks due to the applied stress. Increased microcrack damage lowers strength. Microcracks break atomic

bonds and damage grain boundaries [Yamai 1993].

Thermal expansion mismatch is similar to TEA, but thermal expansion mismatch occurs in multiphase systems. Rather than the thermal expansion coefficients differing along the single phase crystallographic axes, the difference occurs due to differing thermal expansions between two distinctly separate phases [Case 2002]. Schilling *et al.* [Schilling 1991] reported that during the laser ablation of $Yba_2Cu_3O_x$ superconducting thin films, thermal expansion mismatch between the $Yba_2Cu_3O_x$ film and the Si substrate created a high density of microcracks, which decreased the superconductivity of the film. The resistance curve for three different substrates (prepared at 685°C, 727°C, and 775°C), shows the electrical resistivity increases with increasing temperature due to the differing thermal expansions of the substrate and the film [Schilling 1991]. Microcracking impedes electrical conduction in the material due to the electron barrier caused by the crack [Schilling 1991].

Thermal expansion mismatch resulted in a decrease in hardness of brittle materials. Hardness is the measurement of a material's resistance to plastic deformation; H values are high for ceramics and brittle conductors. For $LaNbO_4$- based ceramics used for solid oxide fuel cells and hydrogen sensors, a mismatch between the materials created microcrackings, which lead to low microindentation hardness. Material with a grain size greater than the critical grain size suffered more severe thermal expansion mismatch causing large residual stresses. Microcracking may occur at both the indentation corners of the nanoindent, as well as running transgranularly down the indentation impression, indicating that there was very little elastic deformation, [Mikkelbost 2009].

1.9 Electrically Induced Microcracking

Microcracking in brittle conductive materials can also be electrically induced, by placing piezoelectric ferroelectric materials such as $BiTiO_3$ and poled lead titanate zirconate under a high electric field. Cracks grow perpendicular to the applied electric field. Combined materials with differing thermal expansion coefficients and crystal structure create strain mismatch that leads to differences in the electric field resulting in stresses that lead to crack propagation [Westram 2009].

Chung *et al.* [Chung 1989] observed that the electrically induced microcracks grew with an increase in the poling field. Electrically induced microcracks do not occur or propagate at grain boundaries; cracks are instead transgranular (across the grain). Electrically induced microcracks were also found to occur in materials, such as poled lead zirconate titanate, with a tetragonal crystal structure. The microcrack density depends on the grain size of the material; larger grains in the material have higher elastic strain energies than smaller grains. The applied electric or poling field to a large grained material induces more strain energy on the material, resulting in microcracking [Chung 1989]. A main crack can grow and propagate in a low electric field where microcracks will impede the crack growth. However, for a high electric field there is little time for the growth of the microcracks and the main crack will dominate cracking [Fang 2004].

1.10 Microcracking Caused by Crystallographic or Phase Transformation

Crystallographic/phase transformation can result in microcrack damage within a brittle material since a change from one crystal structure to another usually is accompanied with a volume change. Transformations can be induced in a material through temperature changes (such as thermal cycling) or the addition of compositional impurities during processing. VO_2-based ceramics are used for current limiters [Ivon 1997] because of the crystallographic transformation induced when thermally cycled through a metal-semiconductor transition temperature. The phase transition induces interfacial stresses from the volume change, which ultimately causes microcracks to form. The electrical resistivity increases with the increase in microcrack density, the microcracks hinder the electrical current [Ivon 1997]. Also crystallographic transformation can occur during processing.

Barbier et al. [Barbier 1992] researched $TiC_{1-x}N_x$-ZrO_2 used for cutting tools and wear resistant materials machined using electric discharge machining due to the materials high melting point, high hardness, and good thermal and electrical conductivity. The zirconia in $TiC_{1-x}N_x$-ZrO_2 was found to transform from a tetragonal to monoclinic crystal structure at a high enough nitrogen composition. A crystallographic transformation in the $TiC_{1-x}N_x$-ZrO_2 resulted in microcracks, which blocked electron passage [Barbier 1992]. With an increase of microcracks in the titanium carbonitride-zirconia material, phase transformation reversibility (monoclinic Zirconia back to a tetragonal structure) within the material began to decrease. Microcracking was found to

lower the residual stresses in the material, removing the driving force for the phase transformation (lowers the strain within the microstructure induced by the phase transformation) [Liu 1994].

1.11 Microcracks due to Thermal Shock and Fatigue

Thermal shock induces stresses in a material with the application of large temperature gradients. Thermal shock can result in cracking in a material as a result of a rapid change in temperature, generally occurring in only one thermal cycle. For thermal shock, there is a minimum temperature difference needed to microcrack the material. The temperature change rate necessary to thermally shock a material is material dependent. A temperature increase above the critical minimum thermal shock temperature will result in a higher microcrack density within a material [Case 2002].

While studying the affects of thermal shock on aluminum titanate ceramics (used as thermocouples for non-ferrous metallurgy), grain size and temperature are directly related to the development of microcracks [Matsudaira 2009]. When the material is quenched from its heated state the microcracking occurs at the grain boundaries as a result of thermal expansion anisotropy for grain size critical, degrading the flexural strength of the material [Matsudaira 2009]. The aluminum titanate was also cyclically loaded after it was quenched to show the drastic effect of the induced microcracks [Matsudaira 2009]. The aluminum titanate fatigued because microcrack flaws were introduced to the material, and with the repeated mechanical loading, the cracks propagated [Matsudaira 2009].

Thermal fatigue is the progressive increase of residual stresses in a material from the cyclic heating and cooling of the material [Case 2002]. Residual stresses increase within the material during each thermal cycle and eventually lead to microcracking. An increase in the microcrack density, due to the build up of residual stresses within a

thermally cycled sample, may result in catastrophic failure. The increase in microcrack damage during thermal cycling may be tracked in the decrease of the mechanical properties of the material, such as Young's modulus. It is understood that with the increase in the residual stress damage, the Young's modulus will decrease [Case 2002].

1.12 Advantages of Microcracking

Though microcracks are generally seen as detrimental to the mechanical, thermal, and electrical properties of conductive thermoelectric, microcracking may increase the fracture toughness. Fracture toughness is a materials resistance to crack growth [Barsoum 2003]. For ceramic materials there is generally little crack tip plasticity. Once a crack size reaches the critical flaw size it must release energy to stabilize, which means that the crack propagates until it is energetically stable again [Barsoum 2003]. For a brittle conductive material the crack generally arises as a crack tip opening load, which is the dominant loading for materials that are weak in tension [Barsoum 2003].

Fracture toughness can be increased by manipulating the crack path and mode during crack elongation, from a mode of least resistance to one of sliding or shearing (more energy required) [Liu 1994]. Crack deflection can be achieved with grain boundaries, second-phase particles, and other induced microstructural flaws. Grain boundaries and second-phase particles cause the crack to twist or tilt from a pure direction due to a lower energy than the flaw, causing a rise in the applied stress necessary to grow the crack, inversely shrinking the stress intensity factor [Liu 1994].

Transformation toughening or phase/crystallographic transformation may occur as long as the transformation zone is in direct contact with the crack-tip area [Soboyejo 1995]. Some materials will actually undergo a transformation (i.e. tetragonal-to-monolithic for molybdenum disilicide composites) to increase the residual stresses around it to be higher than that of the crack-tip, resulting in a compressive stress, which deters the crack movement [Soboyejo 1995]. Transformation toughening is the product

of crystallographic change resulting in a volume change, but instead of creating microcracks it is used to slow them. Transformation toughening was shown to occur in molybdenum disilicide composites, but could be considered in the development of conductive brittle materials due to crack development during basic operations [Soboyejo 1995].

1.13 Microcrack Healing

Microcracking has a profound effect on brittle materials. There is the ability, however, to reverse microcracking in some materials [Case 1983]. A reversal of the microcracks in the material is referred to as microcrack healing and is attributed to the ability to increase the materials mechanical properties with the decrease in the microcrack density [Case 1983]. Microcrack healing, for most materials, takes place at a temperature well below the melting point of the material.

Low temperature crack healing is a function of the size of the crack. Since the crack size is on a small scale compared to the material bulk, there is not much diffusion within the material necessary to repair the flaw [Case 1983]. An evolution of damage occurs from microcrack healing as residual stresses increase in the material. Unfortunately diffusion crack healing results in voids and dislocations. Voids and dislocations do not allow the full regeneration of the mechanical, thermal, and electrical properties the material possessed before the microcracks were induced [Case 1983].

Thermally annealing a material to heal microcracks at temperatures of 0.6 melting temperature and above can result in an increase in grain size and even the possibility of pore growth, both of which can lead to more severe material problems [Case 1983].

1.14 Microcracking Summary

Microcrack damage results from residual stresses that occur in a brittle material through thermal expansion anisotropy, thermal expansion mismatch and phase transformations. Microcracking lowers aspects of material properties, such as the elastic modulus, hardness, thermal and electrical conductivity. A decrease in the mechanical properties in a material due to microcracking creates issues for brittle conductive materials being able to perform in a device without failure or fatigue. Though there are methods to slow or repair microcrack damage (crack healing, crack blunting), avoiding microcracking is more beneficial in a material. The avoidance of increased residual strain assists in reducing the microcracking of brittle thermoelectric materials. Knowledge and understanding of brittle thermoelectric material traits and flaws will only help in the development of better and more effective materials.

1.15 Spinodal Decomposition

Spinodal decomposition is a phenomenon which occurs in a wide range of materials from metal alloys, polymer blends and ceramics. Spinodal decomposition is an irreversible process that occurs in a material in which the transition of a liquid or solid solution is caused by a sinusoidal fluctuation in the concentration of the components [Schaftenaar 2008]. Unlike diffusion transport transitions in a material caused by the nucleation and growth from a composition concentration peak, spinodal decomposition, which occurs out of thermodynamic equilibrium, is caused from local fluctuations in the concentration of the component [Schaftenaar 2008].

A basic form of spinodal decomposition is that of the demixing of a system composed of component A and component B. As the heated mixture of A-B atoms is cooled the atoms will separate into phase rich areas of component A and component B for spinodal decomposition, where a stable solution will become thermodynamically stable through the diffusion of components A and B to create a homogeneous material [Porter 2004]. To cause spinodal decomposition during material processing a material in a single phase region is quickly quenched into an unstable region in the miscibility gap [Schaftenaar 2008, Porter 2004]. Small fluctuations in the composition create A-rich and B-rich regions which cause the total free energy to decrease; this causes an 'up-hill' diffusion to occur. Normal diffusion or 'downhill' diffusion is the diffusion of a higher concentration to a lower concentration, where 'uphill' diffusion is the diffusion of low concentration to a higher concentration [Favvas 2008].

The free energy of the system is lowered without the creation of phase boundaries, which in turn means there is no activation energy barrier to overcome. The removal of the activation barrier energy means there is no need for a nucleation stage. During the uphill diffusion, the boundaries between the two phases sharpen due to interdiffusivity (short range diffusion) [Flake 2008]. The interdiffusivity of the A and B atoms up the diffusion gradient into A-rich and B-rich bands is caused by a gradient energy driven by the increase in the number of unlike nearest neighbors in a solution containing composition gradients compared to a homogeneous solution [Porter 2004]. The material will become energetically stable through diffusing the dislike A and B atoms away from each other and into like atom rich regions, but the diffusion of the particles is limited [Porter 2004]. The regions are separated due to incoherent regions causing an increase in the lattice strain between the A and B rich areas [Campbell 2008].

The segregation of atoms in spinodal decomposition can have positive effects on the mechanical, electrical and thermal properties of materials. The spinodal structure works favorably in the production of permanent magnetic materials such as Cu-Ni-Fe [Sinha 2003]. Spinodal decomposition also has played a role in enhacing the thermoelectric properties of $Pb_{1-x}Sn_xTe$–PbS. The ordered separation of the material can be done on a nanoscale level of PbTe-rich region and PbS-rich regions. The thermal conductance through the material is disrupted due to the nanostructure-induced acoustic impedance mismatch between the PbTe-rich and PbS-rich regions. The incoherent regions between the two phases act like a grain boundary in the material. The incoherent region between the regions is not large enough, however, to impede electron mobility. The material thermoelectric efficiency was increased through spinodal decomposition

[Androulakis 2007].

1.16 Fracture Strength and Elastic Moduli

Fracture strength (σ_f) is a measure of the stress required to fracture a body. The fracture strength in a material is dependent on several factors; the one that will be focused on will be that of grain size. Grain size can have a large impact on the fracture strength of a material, where the fracture strength is roughly proportional to the reciprocal square root of the grain size [Barsoum 2003]

$$\sigma_f = B/GS^{1/2} \quad (1)$$

where GS is the grain size, and B is a material dependent property. It was determined that there are generally two grain size regimes that exist around a grain size transition (GS_{Trans}) which can range from a few microns or less depending on the material and the application [Lawn 1993, Barsoum 2003].

For a grain size larger than the grain size transition, the fracture strength is a function of the grain size and generally decreases with the increase in grain size. For a grain size smaller than the grain size transition, the fracture strength is not significantly affected. The difference in the grain size/fracture strength relationship can be attributed to the flaw populations within the material [Barsoum 2003].

Flaws in a material such as macro and microcracks, processing damage and accidental damage through handling or use can attribute to a decrease the fracture strength of a material depending on the grain and flaw size. If a materials grain size is

larger than the grain size transition, the largest flaw (known as the critical or strength controlling flaw) scales with the grain size. Once the grain size has passed the grain size transition the fracture strength of the material is hindered by grain boundary flaws, and the flaw population induced by processing can be viewed as background flaws. However, when the grain size of the material is less than the grain size transition processing flaws play a much larger role in the mechanical properties. For a material with a grain size under the grain size transition the processing-induced flaws dominate the fracture strength. The flaws in the material become the largest flaws in the material with the decrease in grain size, which means the fracture strength is no longer a function of grain size [Barsoum 2003].

In this study, the Ring-on-Ring (ROR) or equibiaxial configuration [ASTM C 1499] was selected for the strength testing. The Ring-on-Ring configuration decreases the likelihood of failures from flaws located along the specimen edges, since the stress intensity factor tends to be high in the vicinity of sharp corners [Wachtman 2009]. For example, specimens tested in uniaxial bend tend to fail from edge flaws [Wachtman 2009] while for the ring on ring configuration the stresses are lower along the specimen circumference, making failures from edge flaws less likely.

Not all mechanical properties are a function of grain size, as is the case with the elastic modulus (E), except when grain-size-dependent microcracking is present [Rice 2000]. Elastic modulus measurements (Young's modulus, and Poisson's ratio) allow one to non-destructively monitor the accumulation of thermal fatigue damage in a specimen [Lee 1989; Lee 1990; Lee 1992; Case 1993; Wilson 1993; Case 1995]. Also, the Young's modulus and Poisson's ratio are required in order to construct a stiffness

matrix for the finite element method evaluation of stress and strain [Kaliakin 2002].

Models for the microcrack-induced decrement in Young's modulus, E, have been proposed by Laws and Brockenbrough [Laws 1987] and Budiansky and O'Connell [Budiansky 1976] such that with an accumulation of microcrack damage, where

$$E = E_0(1 - f(\nu)\varepsilon) \tag{2}$$

where E = the Young's modulus of the microcracked body, E_0 is the Young's modulus of the uncracked material, $f(\nu)$ is a function of the microcrack alignment and the Poisson's ratio, ν, and ε is the crack damage parameter [Laws 1987]. For randomly oriented microcracks the crack damage parameter, ε, is in turn given by [Laws 1987]

$$\varepsilon = \frac{2}{\pi}\left(\frac{\langle A^2 \rangle}{\langle P \rangle}\right)\Lambda \tag{3}$$

where $\langle A^2 \rangle$ is the mean square of the crack surface area, $< P >$ is the mean crack perimeter, and Λ is the volumetric crack number density (the number of cracks per unit volume). If the simplifying assumption is made that the microcracks are planar and circular with all cracks having the same radius a, then ε becomes $\langle a^3 \rangle \Lambda$. Thus the thermal fatigue induced decrement in elastic modulus depends on an "ensemble average" of the microcrack damage, but is biased toward the larger cracks by the third moment of the crack radius, $<a^3>$ that appears in the crack damage parameter [Laws 1987; Budiansky 1976].

$$E = E_0\left(1 - \frac{2fc(\nu)\langle a^3\rangle - 1}{\pi}\right) \tag{4}$$

Measurements of microcracked materials have demonstrated that as the crack damage parameter increases, the Young's modulus decreases [Case 1993a, Kim 1993a, Kim 1993b]. The microcrack damage in brittle materials such as semiconductors and ceramics can be induced by a variety of physical mechanisms, including thermal expansion anisotropy in a single phase material [Bradt 1978, Case 1981], thermal expansion mismatch in a multi-phase material [Davidge 1968, Luo 1997, Todd 2004], thermal shock [Bradt 1993, Ohira 1988, Hasselman 1969] and thermal fatigue damage [Lee 1990, Chiu 1992, Case 2002, Case 1993b].

2.1 Materials and specimen preparation

The n-type initial LAST materials ($Ag_{0.86}Pb_xSbTe_{20}$), n-type reformulated LAST materials ($Ag_{0.86}Pb_ySbTe_{20}$) and the p-type LASTT materials ($Ag_{0.9}Pb_9Sn_9Sb_{0.6}Te_{20}$) studied were processed by Tellurex Corporation (Traverse City, MI). Two specimen geometries, circular disks (Figure 2.1.1.) and rectangular parallelepiped plates (Figure 2.1.2.) were examined. Both the disk and plate-shaped specimens were powder processed by Tellurex Corporation from cast ingots of LAST and LASTT. Tellurex Corporation then hot pressed the resulting powders to form dense specimens. The as-received (by MSU) circular disks had an average diameter of 25 mm and an average thickness of 2.5 mm. The as-received rectangular parallelepiped plates were on average 12 mm long, 10 mm wide and 2.5 mm thick.

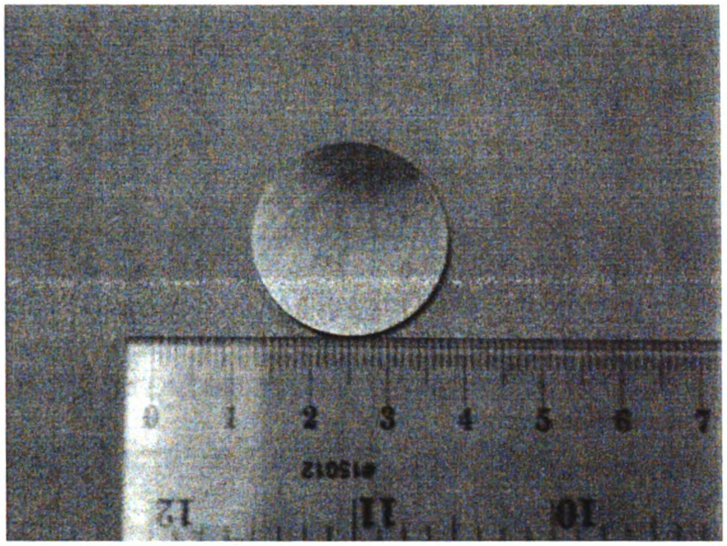

Figure 2.1.1. Example of disk-shaped specimen of LAST and LASTT used in large thermal fatigue chamber.

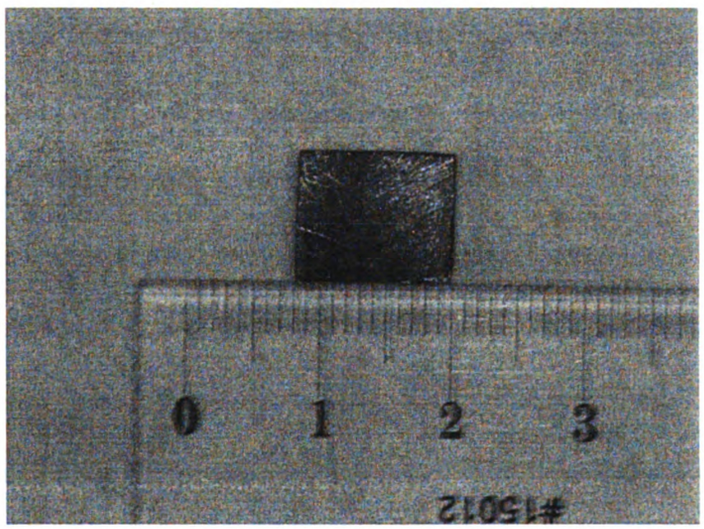

Figure 2.1.2. Example of LAST and LASTT rectangular peallelpiped sample used in Small Thermal fatigue chamber.

2.2 Microstructural characterization

For selected LAST and the LASTT specimens, the fracture surfaces and external surfaces of both as-received and thermally fatigued specimens were examined by optical microscopy and by scanning electron microscopy (JEOL 6400, JEOL Ltd., Japan) using a working distance of 15 mm and an accelerating voltage of 15 kV. The electrical conductivities of both the LAST and the LASTT specimens were sufficiently high so that no conductive coatings were needed for the specimens examined in the SEM in this study. All SEM images included in this thesis were provided by Jennifer Ni.

In addition to the SEM images, inclusions and surface pitting in the LAST specimen surfaces were examined using a Nikon Epiphot 200 (Tokyo, Japan) equipped with the imaging program IQ Materials v2 (Media Cybernetics, Sydney Australia).

Inclusions and surface pitting in the LAST specimen surfaces were examined using a Nikon Epiphot 200 (Tokyo, Japan) equipped with the imaging program IQ Materials v2 (Media Cybernetics, Sydney Australia).

Micrographs were viewed using GIMP 2.6 (GNU Image Manipulation Program) graphics editor. The rough size of the inclusions and pits was measured using the "Ellipse Select Tool", and the "Size:" dropdown menu in the toolbar was set to "mm", and the scale bar was measured to obtain a conversion factor. The micrographs were then sharpened to increase visibility using "Sharpen" located in "Enhance" under the "Filters" menu.

1) Measure area of each inclusion/pit

a. Inclusions were harder to count in the extremes of the cycle count (very beginning and very end). Determining inclusions—if looking at the micrographs for too long, counting the smallest of inclusions leads your eyes to neighboring imperfections, and after a while, every minute fault is counted, and no work can get done. A choice was then somewhat arbitrarily made between what was too small to be an inclusion and what was the smallest to be classified as an inclusion.

b. Pits were sorted from pores and "gouges" with the following rules—

    i. Pits

        1. irregularly shaped
        2. if the bottom was visible AND it was irregularly shaped
        3. surface damage surrounded the pit candidate
        4. some of the inclusions did not fire off completely, so if about 50% of an inclusion was gone, the remaining piece of the inclusion and the pit left were entirely counted as a pit

    ii. Gouges

        1. pits were discarded as "gouges" and not counted for if the pit was at the end, or beginning of a large scratch; it cannot be deciphered if the damage was from the scratch or from a lost inclusion.

2. i.e 5cycles 5x1 – at the mid bottom, there are two holes—the most southern one was counted as a pit, and the hole to the north east was classified as a gouge and not counted)

iii. Pores

1. Keep a very circular shape
2. have no cracking or surface damage around them
3. seem to be "bottomless" since they are not shallow ditches left behind from a surface inclusion
4. if the bottom was visible, but was circular shaped, it was counted as a pore.

2.3. Large Thermal Fatigue Chamber

2.3.1. Large Thermal Fatigue Chamber Overview

The steel chamber itself that was used for the basis of the large thermal fatigue chamber (used for the LAST and LASTT thermal cycling) was fabricated and assembled by the Michigan State University Physics Shop approximately twelve years prior to the start of the thermal fatigue work described here. (The chamber initially provided a roughening pump level of vacuum for sonic resonance measurements of elastic modulus performed by Professor Case's group).

The chamber was an 11 cm diameter steel pressure vessel tube with 0.7 cm thick walls. The chamber was 24.5 cm in length with a 7.5 cm x 20 cm x 0.3 cm thick stainless steel plate silver soldered to the bottom of the inside of the tube to allow for a level floor within the chamber to work on. The back wall of the chamber was a solid steel plate attached with eight hex bolts and was the inlet for the electrical, thermocouple, gas, and water feed–through (When the chamber was initially fabricated, the back wall of the had been silver soldered in place, but during the conversion of the chamber into a thermal fatigue chamber, the physics shop cut off the back plate in order to place vacuum feed throughs in the back plate). There was a t-valve at the top of the chamber, to which was attached a pressure gauge and the inlet lever for the argon flow tube. A steel ring, 11 cm in diameter, 2.7 cm wide and 0.3 cm thick was soldered to the front of the chamber as a faceplate to attach a cover. The front cover was an 11 cm diameter, 2 cm thick piece of Plexiglas, which held to the faceplate using six hex bolts. Within the large thermal chamber there was a copper cold plate cooled by a solid-state chiller. A hot plate stage

assembly consisted of the sample hot plate, and alumina refractory brick, a sheet of fiberglass and a lab jack.

2.3.2. Hot Side Alumina Refractory Brick Assembly

A porous alumina refractory brick (18 cm x 10 cm x 3.5 cm) was used as the heater housing (Figure 2.3.1). A 15.5 cm x 7.5 cm x 0.5 cm section was removed from the brick face using a single-edged razor blade. The outline of the area was scribed into the alumina brick with the razor, and then the razor was placed at an angle and used to chisel out the alumina. The cavity in the alumina brick was created to allow the 300-watt, 120 V resistance heater (Tempco MSH00048 K 08-14, Electric Heater Corporation, Wood Dale, MA) to sit flush with the brick's surrounding edges (Figure 2.3.2.). Two 1 cm diameter holes were drilled through the brick, one hole was 3.5 cm from Side B-B and the other 1 cm diameter hole was 3.5 cm from Side B-D, and both of the 1 cm holes were located 4.5 cm from Side B-A (Figure 2.3.1., Side B-# designates the sides of the refractory brick to assist in the explanation of the construction of the alumina brick). The holes were drilled to allow the 18 gauge insulated electric leads (CSA Type LL81924 SJT 18AWG FT2 Wire, Hewlett Packard, Palo Alto, CA) to connect to the heater (Figure 2.3.1).

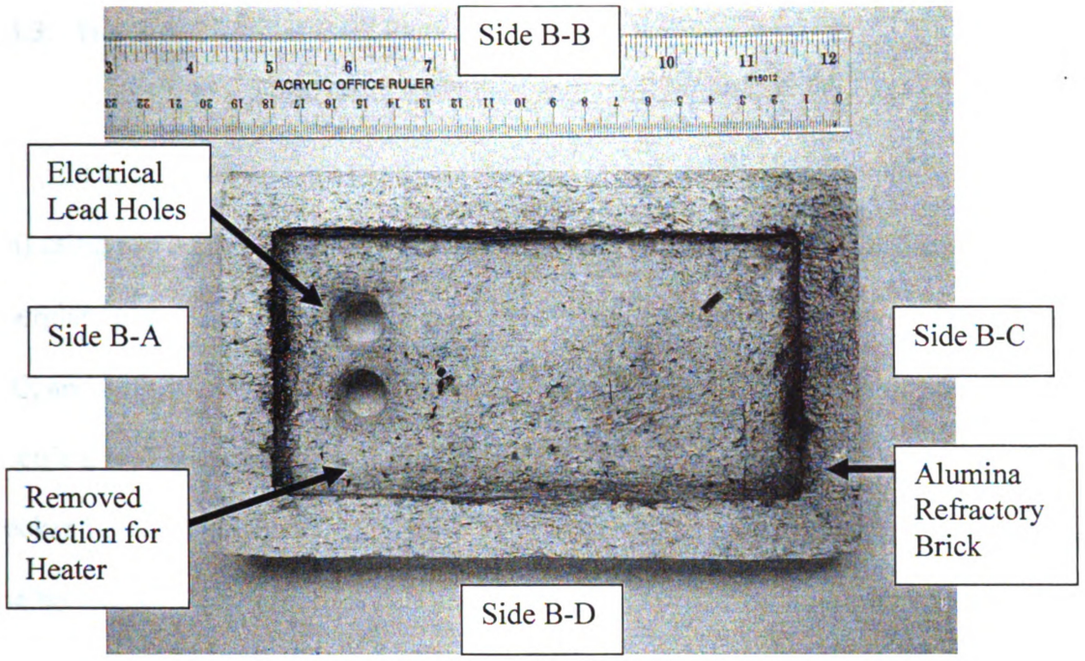

Figure 2.3.1. Alumina refractory brick with heater section removed and electrical lead holes drilled through it. Side B-# is used to designate the sides of the refractory brick to assist in the explanation of the construction of the alumina brick.

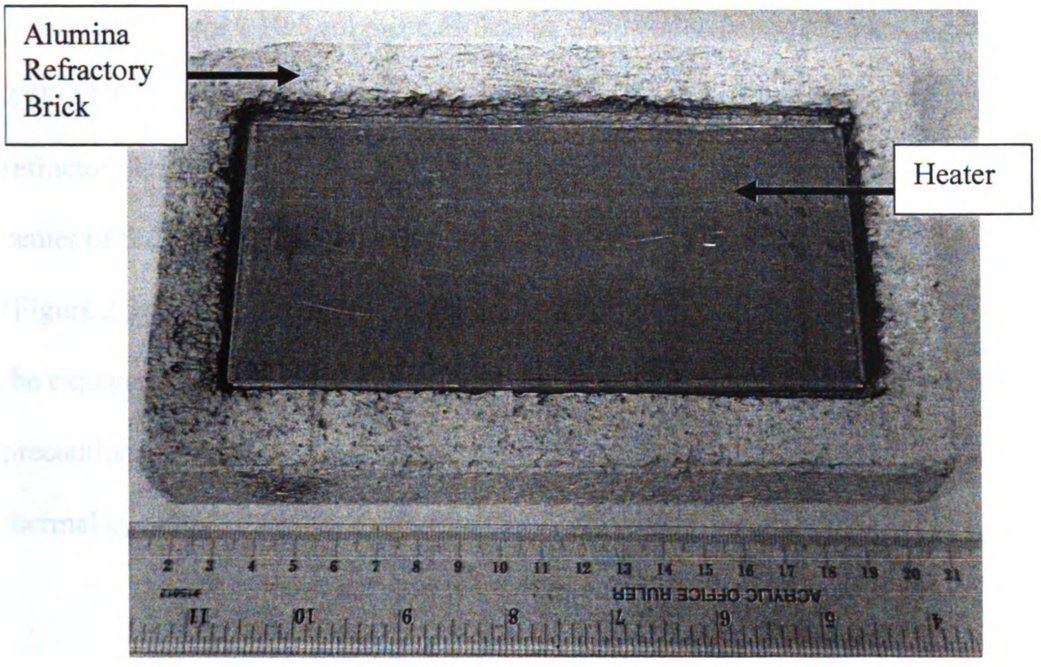

Figure 2.3.2. Alumina refractory brick with heater sitting in cavity, flush with cavity walls.

2.3.3. Hot Side Fiberglas Base Plate Assembly

The brick sat on top of and was attached to a fiberglass plate (19 cm x 12 cm x 0.5 cm) using two 3 cm x 0.2 cm bolts. The bolts were fixed to two holes drilled through the fiberglass plate, one bolt was 2 cm from Side F-A and the other bolt was 2 cm from Side F-C, and both bolts were 6 cm from Side F-B (Figure 2.3.3). Two 1 cm diameter electrical lead holes were also drilled through the fiberglass plate, using a Black and Decker 1.3 cm drill with a 0.6 cm drill bit. The two holes were drilled through the brick, one hole was 3.5 cm from Side F-B and the other 1 cm diameter hole was 3.5 cm from Side F-D, and both of the 1 cm holes were located 4.5 cm from Side F-A (Figure 2.3.3., Side F-# designates the sides of the fiberglass base plate to assist in the explanation of the construction of the plate).

A 15.5 cm x 10.5 cm piece of fibrous zirconia insulation (Zircar Corporation, ZYF-A2.13, Florida, NY) was cut to fit between the fiberglass base plate and alumina refractory brick (Figure 2.3.4.). The insulation had two 1 cm x 1 cm squares cut at the center of Side I-A and I-C edges to accommodate the refractory brick attachment screws (Figure 2.3.4., Side I-# designates the sides of the zirconia insulation separator to assist in the explanation of the construction of the insulation sheet). The zirconia insulation was a precautionary barrier between the heated refractory brick and the fiberglass plate during thermal cycling.

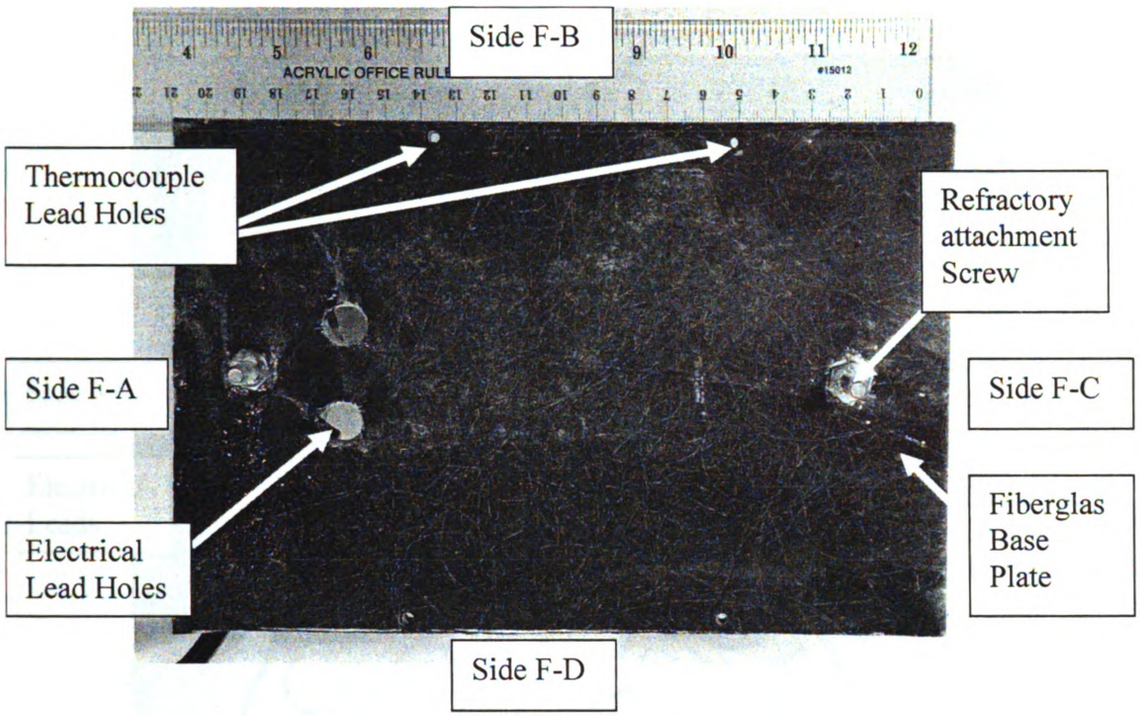

Figure 2.3.3. Fiberglass base plate with electrical and thermocouple lead holes drilled through it. The fiberglass plate also shows the refractory brick attachment screws. Side F-# is used to designate the sides of the fiberglass base plate to assist in the explanation of the construction of the plate.

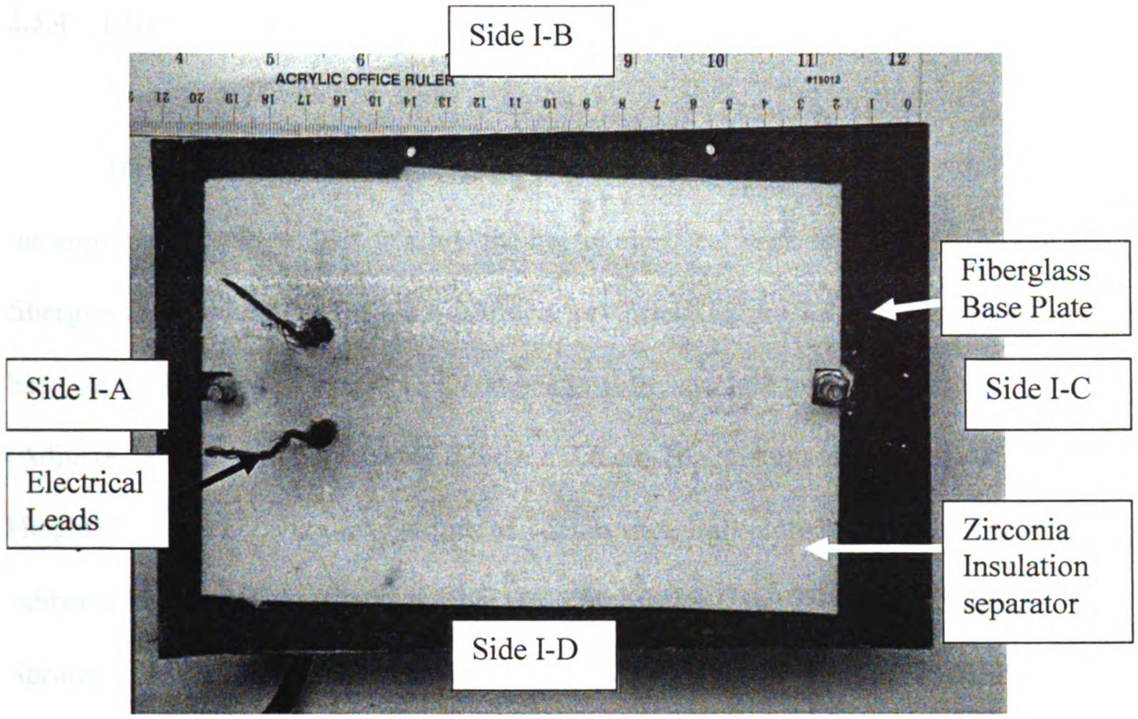

Figure 2.3.4. Fiberglass base plate with alumina refractory brick zirconia insulation separator and electrical leads. Side I-# is used to designate the sides of the zirconia insulation separator to assist in the explanation of the construction of the insulation sheet.

2.3.4. Large Chamber Hot Plate Assembly

The holes drilled in the fiberglass plate were aligned with the holes drilled within the alumina refractory block to allow the heater electrical leads to run through both the fiberglass base board and the alumina refractory brick (Figure 2.3.5.). The fiberglass base plate, alumina refractory brick and heater were attached to a scissor lab jack (Adjustable-Height Support Stand 7.6 cm x 7.6 cm Top, 6.4 cm to 12.7 cm Adjustable Height) using two 7.6 cm long stripes of 1.9 cm wide light-duty polyethylene foam rubber adhesive double-sided adhesive tape (McMaster-Carr, 7598A912, Santa Fe Springs, CA) attached to the front and back edge of the top of the support stand (Figure 2.3.6.).

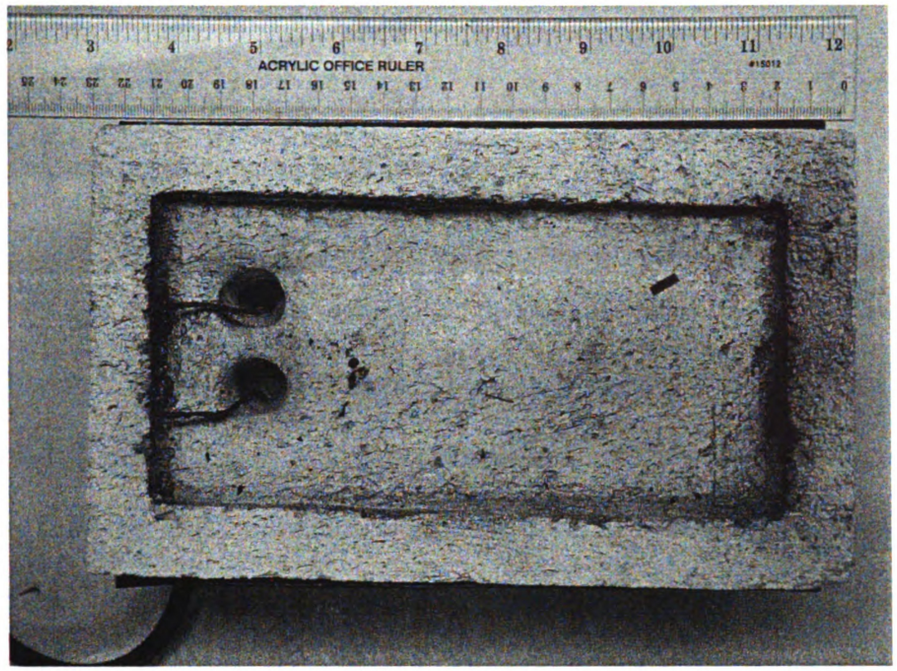

Figure 2.3.5. Alumina refractory brick in place on fiberglass base plate with electrical leads running up through pre-drilled holes.

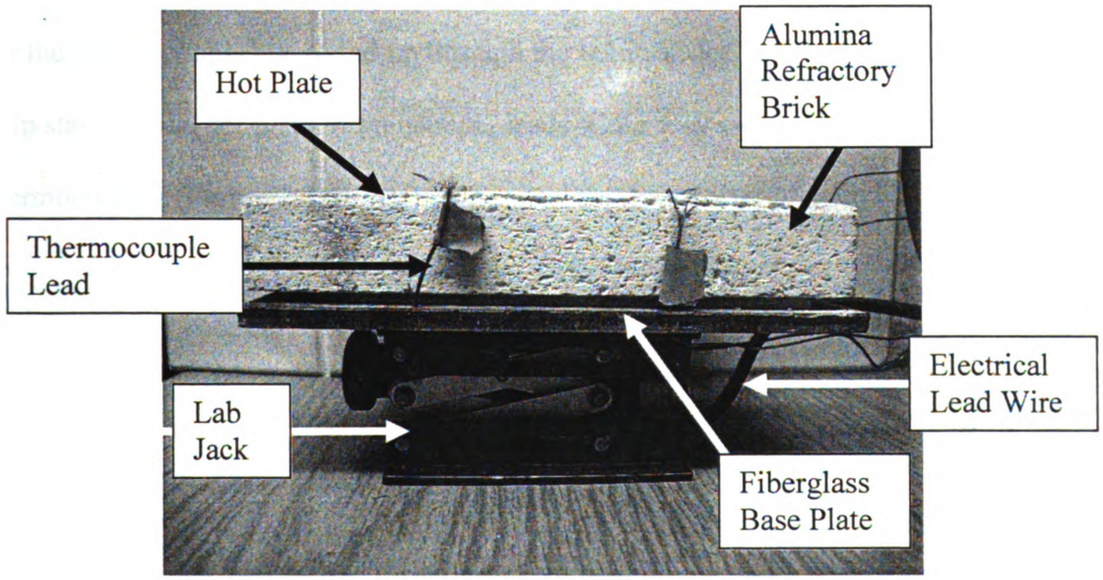

Figure 2.3.6. Large thermal fatigue chamber hot plate stage configuration of the lab jack, Plexiglas base plate, refractory brick and hot plate. Holes were drilled through the Plexiglas base plate and the thermocouple leads were fed through the holes to keep them from moving or becoming caught when the stage was adjusted.

2.3.5. Hot Side Thermocouple Attachment

2.3.5.1 Fiberglas Thermocouple Lead Holes

Four 2 mm diameter holes were drilled through the fiberglass plate to hold the four hot plate thermocouple leads (Figure 2.3.3). Two holes were made 0.5 cm from the edge of Side F-B, one hole was 5 cm from Side F-A and the other hole was 5 cm from Side F-C. The other two 2 mm holes were made 0.5 cm from the edge of Side F-D, one hole was 5 cm from Side F-A and the other hole was 5 cm from Side F-C (Figure 2.3.3, Side F-# designates the sides of the fiberglass base plate to assist in the explanation of the construction of the plate). The four type K, fluorinated ethylene propylene insulated 20 gauge solid thermocouple lead wires (McMaster-Carr, 3870K62, Santa Fe Springs, CA) for the thermocouples were fed up through the holes drilled in the fiberglass base plate to help stabilize the hot plate thermocouple leads while they were attached to the k-type thermocouples (Figure 2.3.6).

2.3.5.2. Hot Plate Thermocouple Attachment

The thin film CO2 k-type thermocouples (Omega Engineering Inc, Stanford, CT) were attached to the hot plate using a high-temperature cement (Omega Engineering Inc, OMEGA CC High Temperature Cement, Stanford, CT). The heater surface was hand polished using a 400 grit sandpaper (Leco, St. Joseph, MI) to remove an industrial finish which did not allow the high-temperature cement to adhere. The high-temperature cement comes in a powder and binder, which must be mixed.

Using a 30 ML mixing cup and a 15 cm applicator wooden stick (Puritan, Guilford, Maine) approximately 3 ML of powder was mixed with 1 ML of binder. The cement was mixed into a homogenous mixture with no clumps of powder. The mixture needed a higher viscosity than water; the mixture had to be spread able but not have a tendency to run on a flat surface. A high viscosity in the cement ensured that there was a proper coating of the cement over the thermocouple, which ensured a good bond between the thermocouple and the hot plate.

Using the wooden applicator a drop of the cement mixture (>5 ML) was spread in a 1 cm x 1 cm square onto the cleaned surface of the heater. The adhesive was applied four times (once per thermocouple), 3.5 cm from each corner, two pads along Side H-A and two along Side H-C. This initial dry coat layer of high-temperature cement kept the thermocouple from having direct contact with the heater surface. Direct contact with the heater surface is to be avoided due to the danger of shorting out thermocouples readings. The end of each thermocouple was then placed onto the cement pad. Again, using the wooden applicator, approximately 0.5 ML of cement was placed on top of the

thermocouple and the cement was then allowed to set in room air for 24 hours (Figure 2.3.7).

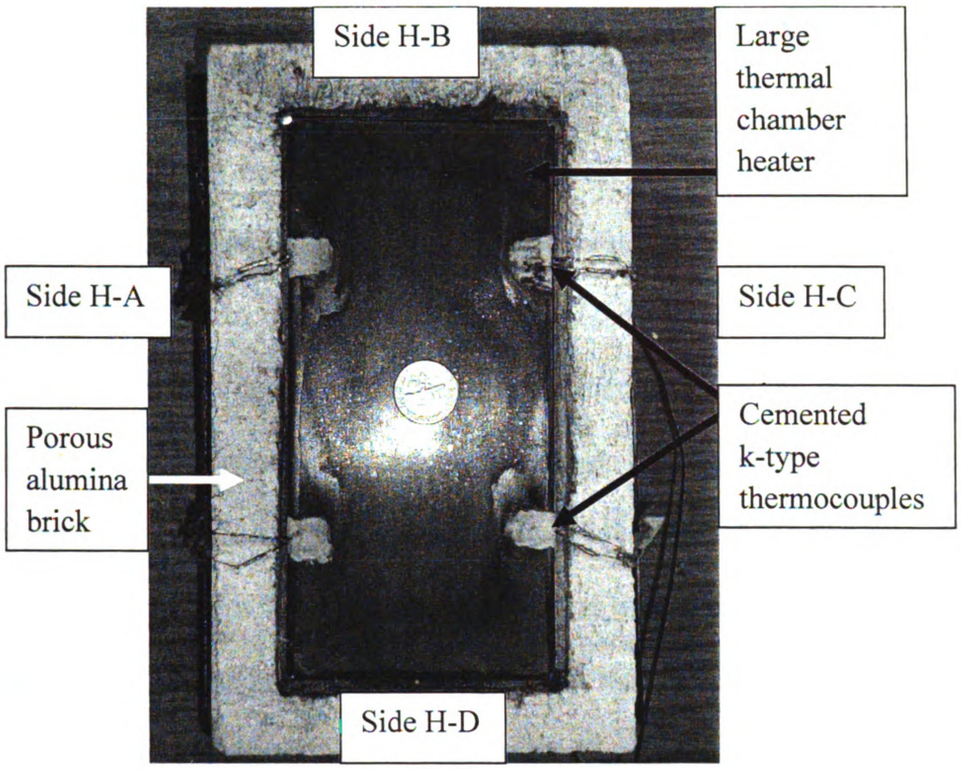

Figure 2.3.7. Large chamber heater positioned in the porous alumina refractory brick with the four k-type thermocouples cemented on. Side H-# is used to designate the sides of the hot plate to assist in the location of the thermocouple attachments to the hot plate.

2.3.5.3. Hot Side Thermocouple and Thermocouple Lead Soldering

Once the cement had cured, the thermocouples were cut to 2 cm in length, and sanded with 400 grit sandpaper until there were visible scratches. The sanding was performed to remove a coating material on the surface of the thermocouples that would not adhere to the solder melt during the soldering of the thermocouple and the thermocouple lead. The fiberglass insulated, 24 gauge, type K stranded thermocouple (McMaster-Carr, 6579T42, Santa Fe, CA) leads that were fed through the fiberglass plate had about 2 cm of fiberglass wire covering removed using wire cutters. The thermocouples were connected to the thermocouple leads that were fed through the fiberglass base plate using a 40-watt Radio Shack soldering station with 0.032 diameter, 8.0 oz, 60/40 Radio Shack solder and Radio Shack non-spill paste rosin soldering flux (Figures 2.3.6. and 2.3.7.).

2.3.6. Cold Side Thermocouple Attachment

2.3.6.1. Cold Plate Thermocouple Attachment

A water-cooled cold plate 15.2 cm x 8.9 cm x 0.7 cm was fabricated at the Michigan State University Physics Shop using a 15.2 cm x 10.2 cm x 1.9 cm copper block with 1 cm diameter copper tubing running through the block (Appendix A). Prior to being installed into the thermal fatigue chamber, four thermocouples were attached to the cold plate. Before the thermocouples were attached to the cold plate the copper surface of the plate was wiped clean using a Kimwipe (Kimberly-Clark Co., Neenah, WI) to remove any debris that would keep the thermocouple cement from adhering to the cold plate surface.

The thin film CO1 k-type thermocouples (Omega Engineering Inc, Stanford, CT) were attached to the hot plate using the same cement as with the hot plate thermocouple connection in Section 2.3.5.2. The same amount and application procedure was followed for the cold side cement. The thermocouples were placed at different locations on the cold plate in comparison to the hot plate thermocouples. The adhesive was applied four times (once per thermocouple), 3.5 cm from each of the cold plates corners, two pads along Side C-A and two pads along Side C-C (Figures 2.3.7 – 2.3.8., Side C-# designates the sides of the cold plate to assist in the location of the thermocouple attachments to the cold plate).

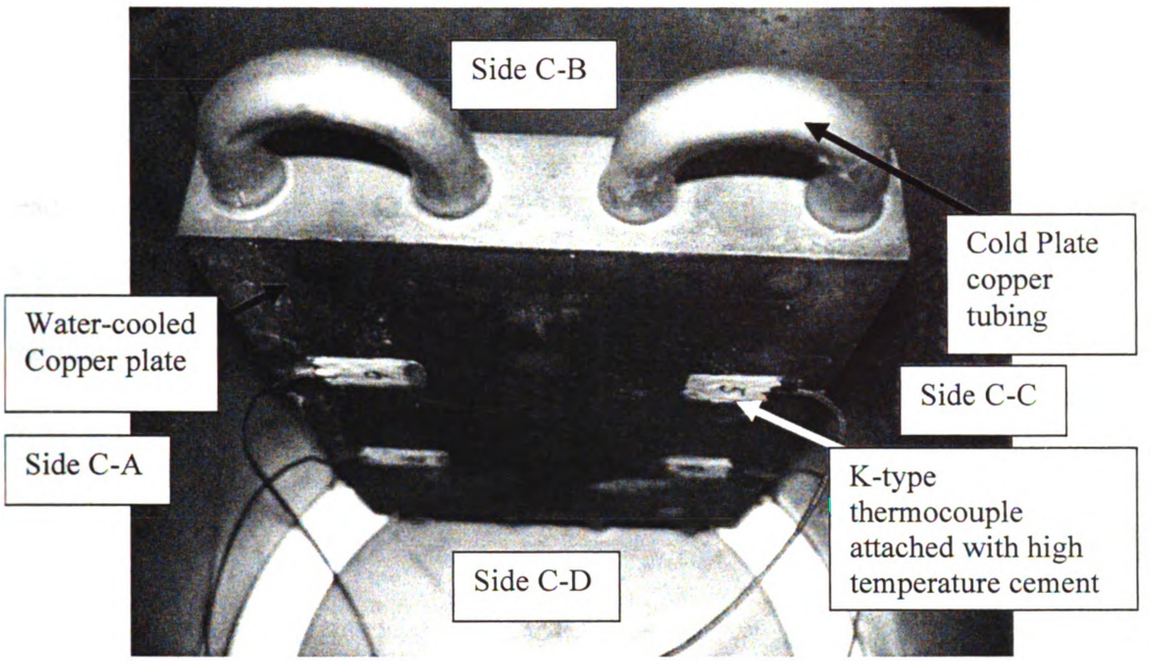

Figure 2.3.8. Large thermal fatigue chamber copper cold plate mounted inside of thermal chamber with four k-type thermal couples attached. Side C-# is used to designate the sides of the cold plate to assist in the location of the thermocouple attachments to the cold plate.

2.3.6.2. Cold Side Thermocouple and Thermocouple Lead Soldering

The procedure of preparing and soldering the thermocouples and thermocouple leads was the same followed in Section 2.3.5.3 for the hot plate thermocouples (Figure 2.3.8). Once the thermocouples were soldered the cold plate was placed into the large thermal chamber.

2.3.7. Thermal Chamber Backside Thermocouple, Electrical, and Bubbler Tube Feed Through

2.3.7.1. Thermocouple Feed-through

The eight thermocouple leads necessary to connect the thermocouples to their respective controllers were feed through the back of the large chamber wall using vacuum seal feed-through plugs (Omega Engineering, PFTFS-8K, Stanford, CT, Figure 2.3.9). The fiberglass insulated, 24 gauge, type K stranded thermocouple (McMaster-Carr, 6579T42, Santa Fe, CA) feed thru wires were then connected to the soldered thermocouple leads usingBe/Cu connectors for 0.1 cm diameter wire, with a maximum of 10 Amperescapacity (Kurt J. Lesker, FTAIBC041, Clairton, PA).

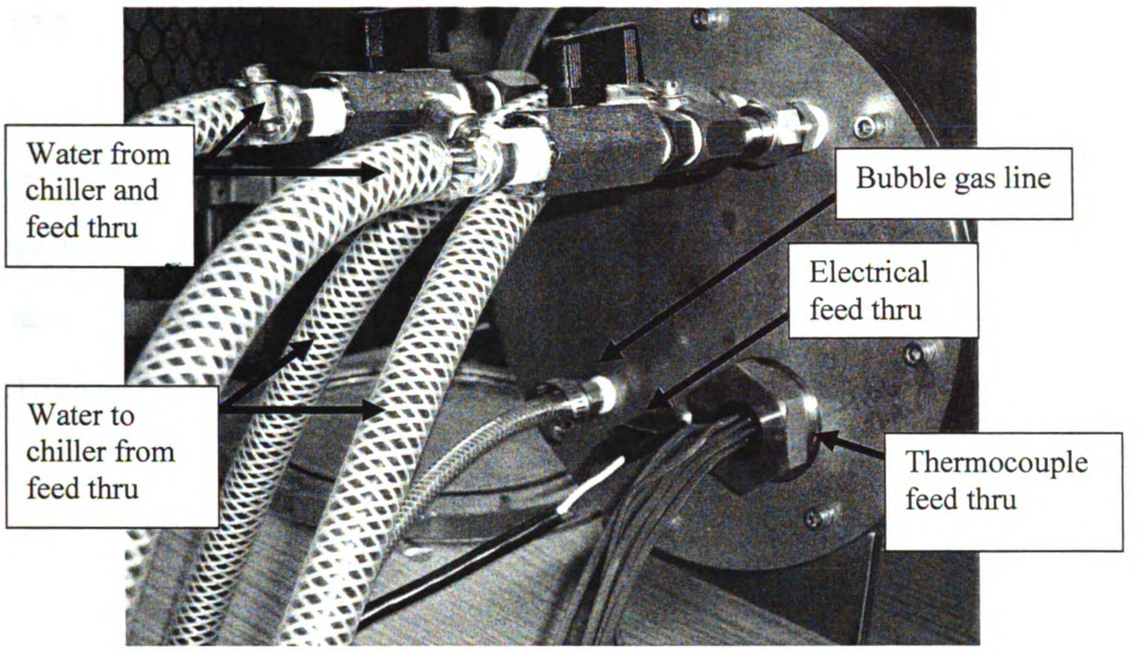

Figure 2.3.9. Back of the large thermal fatigue chamber showing the bubbler gas line connection, water chiller inlet and outlet for the cold plate, the hot plate electrical feed thru, and the cold side and hot side thermocouple feed thru.

2.3.7.2. Hot Plate Electrical Feed-Through

The 60 cm long hot plate electrical wire was connected through the back of the large thermal chamber as well using a two pin, 3A, 500V feed-through which then connected to another 60 cm long piece of 18 gauge, insulated wire (CSA Type LL81924 SJT 18AWG FT2 Wire, Hewlett Packard, Palo Alto, CA, Figure 2.3.8).

2.3.7.3. Bubbler Tube Feed-Through

A 140 cm long piece of 6.35 mm diameter, 14 bar Flexeel polyurethane tubing (Freelin-Wade Co, McMinnville, OR) was attached to the back wall of the large thermal chamber using a type 303 SS multi-barbed tube fitting adapter for 6.35 mm diameter tube inner diameter male pipe (McMaster-Carr, 5670K84, Santa Fe, CA). The other end of the flexeel tubing running from the back of the large chamber was fitted with a chrome plated brass quick disconnect tube coupling socket for a 6.35 mm inner diameter tube (McMaster-Carr, 5478K718, Santa Fe, CA). The quick disconnect allowed easy exchange between the bubbler and the vacuum pump, as both the bubbler and pump linked to the large chamber using the same hose (Figure 2.3.9).

2.3.8. Cold Plate Chiller Chamber Feed Through

2.3.8.1. Cold Plate Chiller Large Thermal Fatigue Chamber Inlet

The cold plate had a 140 cm long inlet hose connected from the chiller to the back of the large chamber wall. Smoothbore high-purity clear Tygon high-pressure tubing (1 cm ID, 1.6 cm OD, 0.3 cm wall thickness, McMaster-Carr, 5624K12, Santa Fe, CA) was used for the chiller tubing. A Type 303 SS multi-barbed tube-fitting tee for 1.6 cm tube ID (McMaster-Carr, 5670K32, Santa Fe, CA) separated the inlet hose into two 40 cm lengths of hose. The inlet hoses were then connected to a brass ball valve with a Yor-Lok fitting, for a 1.6 cm Tube OD (McMaster-Carr, 4112T37, Santa Fe, CA) using a Type 303 SS multi-barbed tube fitting adapter for 1.6 cm tube ID x 0.6 cm male Pipe (McMaster-Carr, 5670K85, Santa Fe, CA).

The brass ball valves were then attached to steel compression tube fitting adapters for a 1 cm tube OD to 0.6 cm diameter NPTF male pipe (McMaster-Carr, 52215K445, Santa Fe, CA). The compression adapters were attached to a standard brass compression tube fitting tube support for 0.6 cm tube OD (McMaster-Carr, 50915K243, Santa Fe, CA) and standard brass compression tube-fitting nut for 0.6 cm tube OD. The compression tube and the fitting nut fit onto a precision threaded type 316 SS pipe fitting 0.6 cm x 0.6 cm pipe size, 3.75 cm in length, hex nipple (McMaster-Carr, 48805K81, Santa Fe, CA) which was threaded into the back of the large chamber wall, connecting to the cold plate (Figure 2.3.9). All hoses were clamped using 316 SS worm-drive hose and tube clamps, with a 0.6 cm clamp diameter (McMaster-Carr, 5011T141, Santa Fe, CA).

2.3.8.2. Cold Plate Chiller Large Thermal Fatigue Chamber Outlet

The cold plate outlet had two outlet tubes converge back to one tube. The tubes to the chiller were also Smoothbore high-purity clear Tygon high-pressure tubing (1 cm ID, 1.6 cm OD, 0.3 cm wall thickness, McMaster-Carr, 5624K12, Santa Fe, CA). The chiller return lines first ran from a precision threaded type 316 SS pipe fitting 0.6 cm x 0.6 cm pipe size, 3.75 cm in length, hex nipple (McMaster-Carr, 48805K81, Santa Fe, CA) which was threaded into the back of the large chamber wall and were held using the worm drive hose clamps. The 40 cm hoses connected to a Type 303 SS multi-barbed tube-fitting tee for 1.6 cm diameter tube ID (McMaster-Carr, 5670K32, Santa Fe, CA) that channeled the two outlet hoses to a single hose. The single hose from the stainless steel tee was clamped with the worm driven hose clamp and connected directly to the chiller (Figure 2.3.9).

2.3.9. Fibrous Zirconia Specimen Insulation

2.3.9.1. Fibrous Zirconia Geometry

A 13 cm x 5 cm rectangular segment was removed from the center of a fibrous zirconia ceramic blanket material 15.5 cm x 10 cm x 0.3 cm (Zircar Corporation, ZYF-A2.13, Florida, NY). The cut zirconia ceramic blanket material was then placed on top of the alumina refractory brick (Figure 2.3.10). The edges of the fiber cover the hot side thermocouples while allowing access to the hot plate surface.

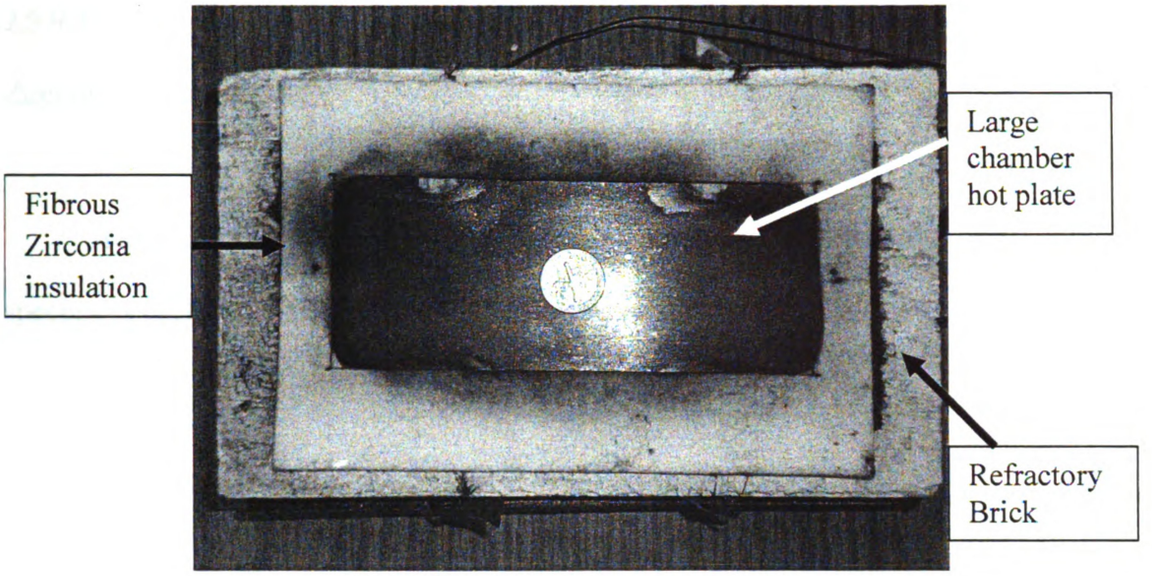

Figure 2.3.10. **Pre-cut fibrous zirconia insulation sheet used to insulate sides of specimens during thermal cycling placed over on to the large thermal chamber refractory brick and heater configuration.**

2.3.9.2. Positioning of LAST and LASTT Specimens on Hot Plate with Fibrous Zirconia Insulation

Ten plate-shaped specimens were placed onto the plate in two rows of 5 specimens each and surrounded with the fibrous zirconia insulation (Figure 2.3.11).

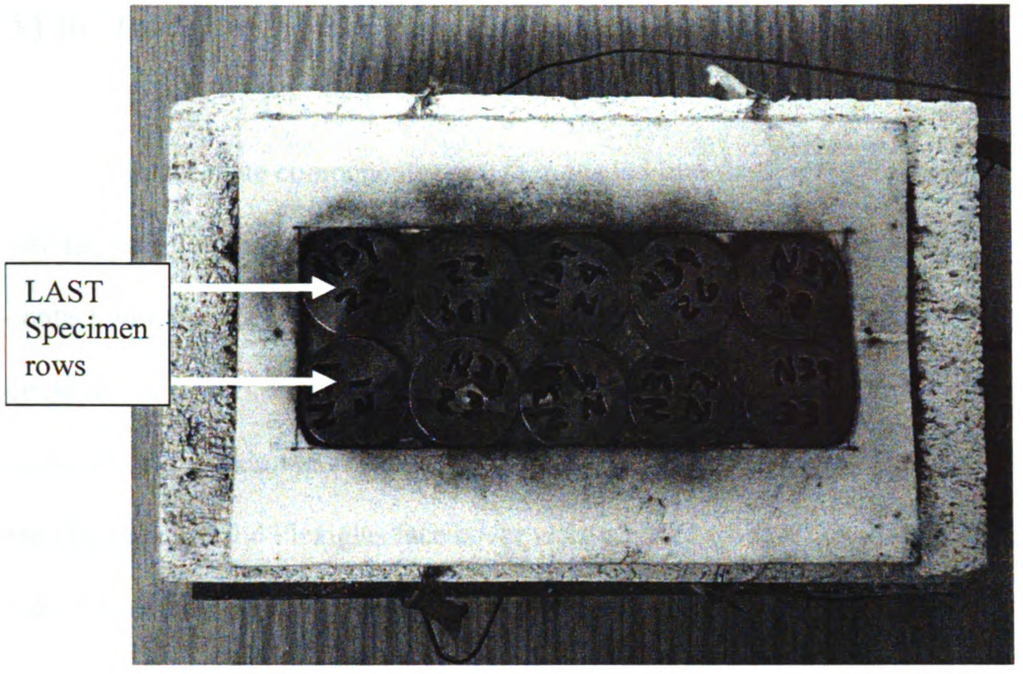

Figure 2.3.11. Large thermal fatigue chamber hot plate set-up and pre-cut fibrous zirconia insulation with 10 samples in place for cycling. The insulation accomodates a sample configuration of two rows of five, the insulation also helps to keep the samples from shifting while the hot plate stage is loaded into the chamber.

2.3.10. Loading of Hot Side Assembly into Large Thermal Fatigue Chamber

The hot plate components were then loaded into the front of the pressure vessel. The lab jack was raised using a screw knob until the specimens were sandwiched in firm contact with the hot and cold plate (Pressure was applied until the knob on the lab jack could not be tightened any further using only thumb and pointer fingers, Figure 2.3.12, and a schematic side view of the loaded large chamber, Figure 2.3.13). The front face of the chamber and the Plexiglas face cover were cleaned using a kimwipe (Kimberly-Clark Co., Neenah, WI), ensuring no debris between the o-ring of the plastic face and the front of the chamber (Figure 2.3.14). While using a gloved hand, a thin layer of Dow Corning high vacuum grease (Dow Corning, Midland, MI) was applied along the rubber gasket seal of the chamber's faceplate. The faceplate was attached to the chamber using six 2.0 cm x 0.2 cm hex bolts spaced equidistant around the chamber's front perimeter (Figure 2.3.14). The screws were only hand tightened initially to hold the plate in place.

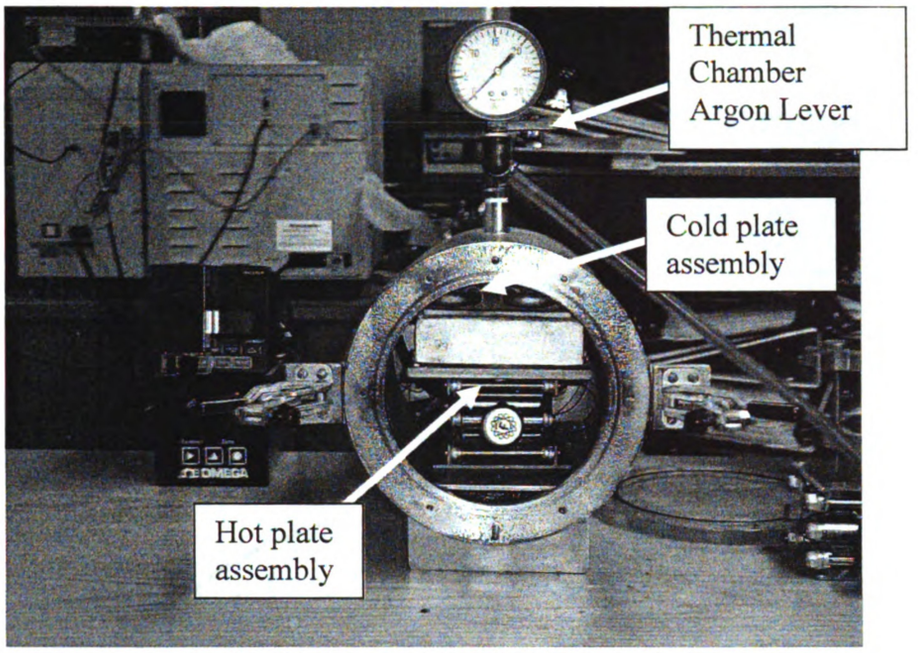

Figure 2.3.12. The hot plate assembly after it had been loaded into the large thermal fatigue chamber and raised by the lab jack to allow the specimens to contact the hot and cold plate.

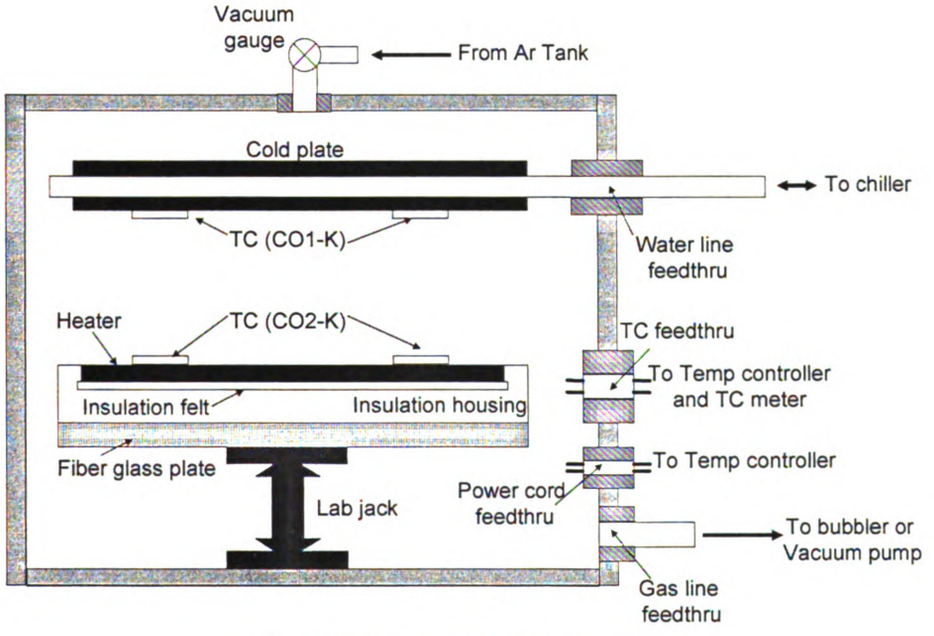

Figure 2.3.13. Schematic drawing of the large thermal fatigue chamber internal and rear assembly [Drawing by Fei Ren].

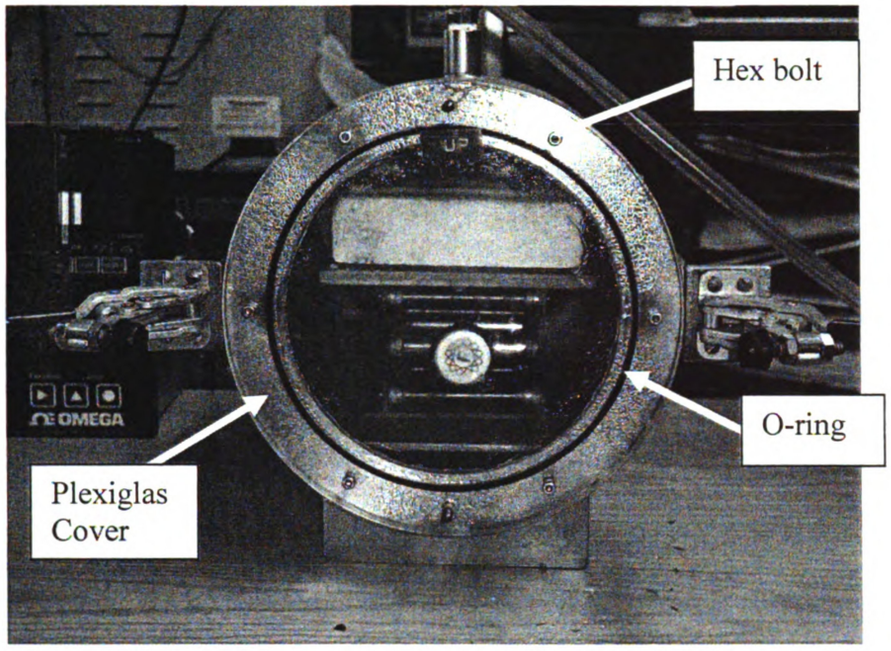

Figure 2.3.14. The clear Plexiglas front cover with o-ring in place on the large thermal fatigue chamber and firmly held in place and sealed by 6 hex bolts.

2.3.11. Purging the Large Thermal Fatigue Chamber

2.3.11.1. Vacuum Pump Connection to Large Thermal Chamber

A roughening vacuum pump (UlvacKikoInc, GHD-030, Japan) was attached to a 140 cm long piece of 6.35 mm diameter, 14 bar Flexeel polyurethane tubing (Freelin-Wade Co, McMinnville, OR) which was connected to a chrome plated brass quick disconnect tube coupling plug for a 6.35 mm inner diameter tube (McMaster-Carr, 5478K148, Santa Fe, CA). The coupling plug of the vacuum tubing was then plugged into the quick connect tube coupling socket which ran from the back of the large thermal chamber.

2.3.11.2. Vacuum Pumping and Argon Purging the Large Chamber

Ensuring that all valves to the chamber were closed, the chamber was pumped down, and the six hex bolts on the faceplate were fully tightened using an Allen wrench to create an airtight seal. The chamber was evacuated until the fatigue chamber gauge reached and held at 206.8 KPa (Figure 2.3.12). An airtight seal between the chamber and the faceplate was indicated if the gauge held at 206.8 KPa with the vacuum off for approximately 30 seconds. The valve connecting the thermal fatigue chamber to the 99.9% purity, 10 cubic meter argon tank (Airgas, Independence, OH) was then opened to purge the system. Argon gas was allowed to flow into the large chamber until the chamber gauge read zero KPa. The chamber was then purged two more times.

2.3.11.3. Connection of the Large Thermal Chamber to a Bubbler

After the final argon gas purge, the chamber coupling plug was disconnected from the vacuum and connected to a coupling socket. The coupling socket was connected to a 100 cm longpiece of flexeel hose; the other end of the hose was placed into a container called a bubbler.

2.3.11.4. The Large Thermal Chamber Bubbler

The bubbler used for the large thermal chamber was a 250 mL UN-compliant plastic shipping bottle (McMaster-Carr, 42305T35, Santa Fe Springs, CA). A bubbler is a beaker or bucket that uses water to help indicate a flow of argon gas through the chamber when the open-ended tube from the small chamber was placed under the water. The bubbler also helps to equalize the chamber with argon and not oxygen. The water will be pulled up the tubing towards the chamber instead of air, keeping an inert atmosphere thermal chamber.

The bubbler bottle was weighted using a mixture of small rocks and epoxy that were allowed to harden at the bottom of the bottle, which filled approximately 1/4 of the container. Water was then added until 3/4 of the bubbler container was filled. The bubbler was used to indicate that there was a flow of inert gas flowing through the chamber during the experiment.

2.3.11.5. Argon Gas Flow Rate to the Large Thermal Chamber

The argon flow was adjusted using a lever handle brass Yor-Lok tube fitting tee for 1 cm Tube outer diameter (McMaster-Carr, 5272K252, Santa Fe, CA) attached to a miniature brass ball valve 1 cm Yor-Lok tube (McMaster-Carr, 4112T37, Santa Fe, CA) which ran the argon from the tank into the top of the large chamber (Figure 2.3.8). Using the lever, the gas pressure was adjusted to allow the release of approximately 5 bubbles per second or greater within the bubbler.

2.3.12. Large Thermal Chamber Temperature Control

2.3.12.1. Thermocouple Controller and Thermocouple Meter

The cold plate was cooled using a solid state chiller (Teca Corporation, Ameritemp Solid State Chiller, Model TLC 700, Chicago, Il) was set to 38.5°C to achieve a cold-side temperature of 40°C. The temperature control for the thermal fatigue chamber was regulated using the UP550E temperature controller (Yokogawa Electric Corporation, Sugarland, Texas), connected to only one thermocouple on the hot plate (the thermocouple chosen for the large chamber was the thermocouple located on the hot plate on Side H-A, closest to Side H-B, Figure 2.3.7 and Figure 2.3.15). The other seven thermocouples were connected to a CN612TC1 (Omega Engineering Inc, Stanford, Maine) thermal couple meter (Figure 1.3.15.). The temperature controller was run using the computer program Green Series Model LL 100 (Yokogawa Electric Corporation, Sugarland, Texas). Using the program, the hot side of the chamber was set to cycle between 50-400°C for a pre-selected number of cycles (Figure 2.3.16). Each cycle for the large thermal fatigue chamber took approximately 60 minutes to complete.

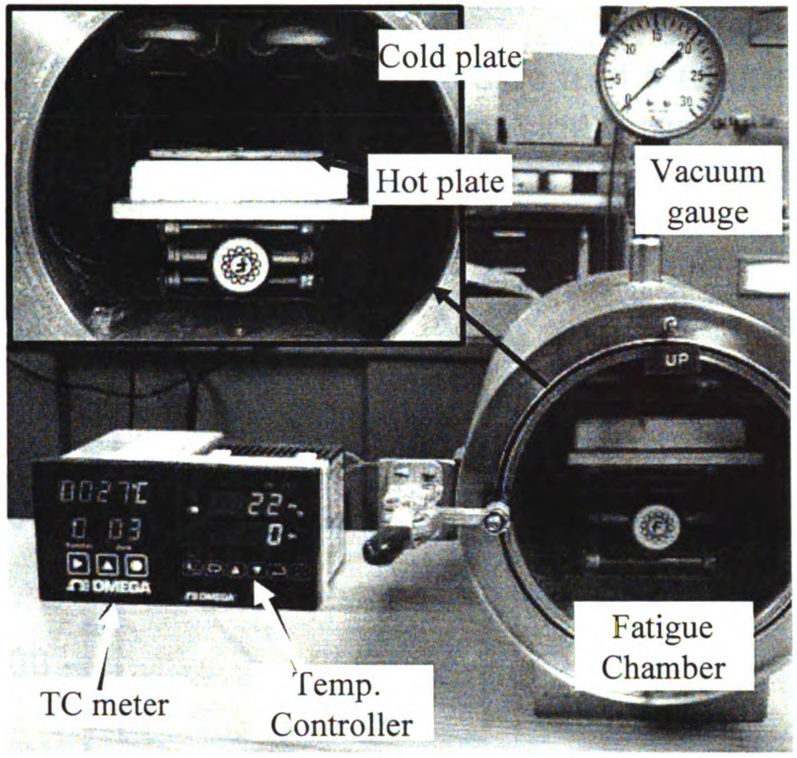

Figure 2.3.15. Front view of the sealed large thermal fatigue chamber with the sample stage in place and the thermocouple meter and temperature controller prepared for cycling.

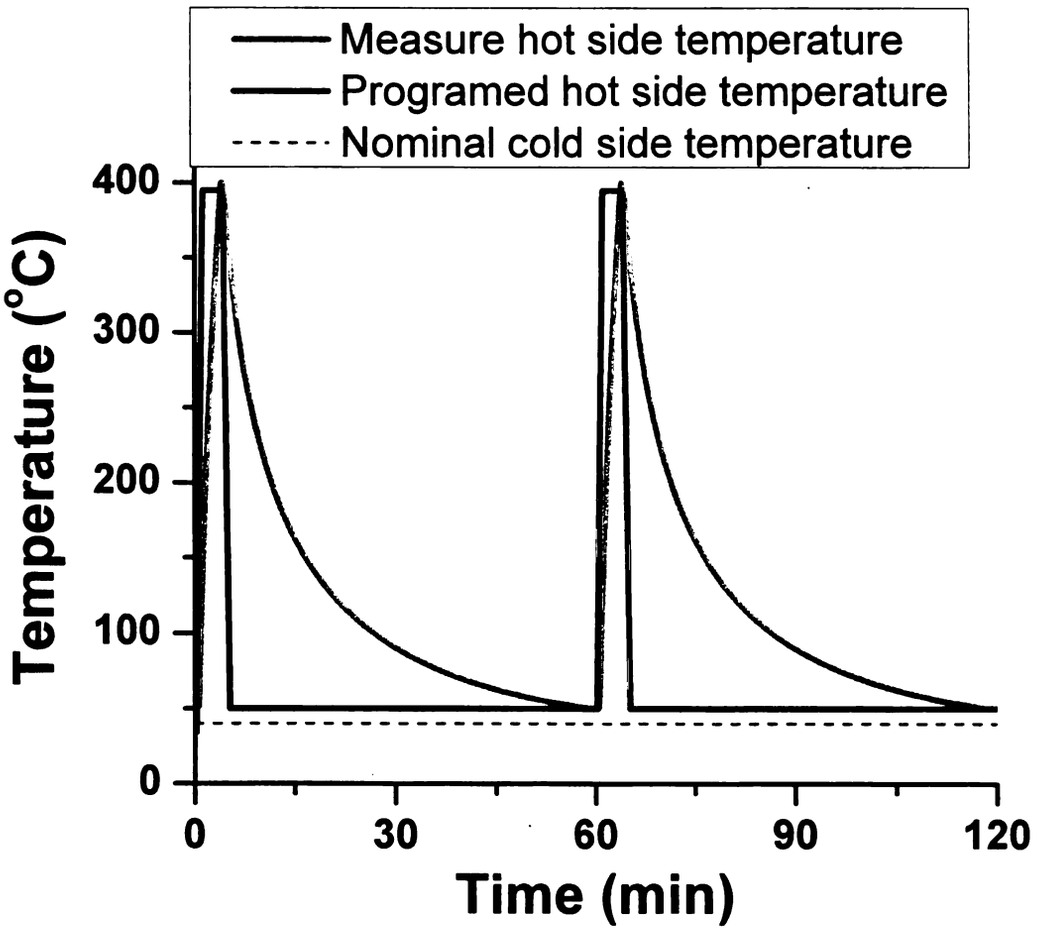

Figure 2.3.16. The thermal cycling profile for the large thermal fatigue chamber. It took one hour to complete one thermal cycle of 50-400 °C.

2.3.12.2. Large Thermal Chamber Heating Profile

The heating profile was determined by programming the heating ramp, hold, and cooling temperature and time to heat the specimens from 50 to 400°C as quickly as possible without holding the samples at an elevated temperature for an extended period of time. Once the 400°C temperature was reached, the thermocouple meter shut off the power to the heater and the samples began to cool to 50°C. The purpose for avoiding an isothermal hold at the maximum temperature of 400°C was to keepa thermal gradient through the material a predetermined number of times. An isothermal hold at 400°C would cause the hot plate and cold plate sides of the test specimens to reach the same temperature. In the large chamber it took 6 minutes to heat 10 samples from 50 to 400°C at a ramp rate of 5°C/minute.

2.3.12.3. Large Thermal Chamber Thermal Couple Meter

The CN612TC1 thermal couple meter Omega CN606/612 scanner software (Omega Engineering Inc, Stanford, Maine) recorded a time/temperature profile of the hot plate to determine whether or not the samples were evenly heated over the entire length of the heater. CN606/612 software recorded real time temperature reading for the seven thermocouples attached to the thermal couple meter during thermal cycling. The Scanner software allowed the comparison of the cold plate and hot plate temperature profiles during thermal cycling. Comparing of the thermocouple profiles helped in the determination that the heating over the entire heater surface was relatively the same during thermal cycling.

2.3.13. Completion of a Thermal Cycling Experiment

When a given experiment was complete, the argon gas tank cylinder valve was closed, shutting of the argon gas flow to the thermal chamber. The thermal chamber argon valve at the top of the chamber was also closed (Figure 2.3.12.). The bubbler hose was then disconnected from the large chamber by ejecting its coupling plug from the chambers coupling socket hose. Finally the power was shut off to the solid-state chiller. The thermal cycling profile data collected by the CN606 and Green Series software was saved to a desktop folder for archiving. All power to the thermal chamber was shut off to avoid electrocution dangers. The screws holding the chambers front plate were removed and the chamber cover was removed. The lab jack was lowered and the hot plate stage was carefully removed from the chamber to avoid any tension to the thermocouples or the thermocouple leads, which could disconnect or tear the thermocouples from the leads or the hot plate. The samples were then removed from the hot plate surface.

2.4. Small Thermal Fatigue Chamber

2.4.1. Small Thermal Chamber Overview

The small thermal fatigue chamber was a 30.5 cm x 30.5 cm x 2 cm sheet of clear Plexiglas with a rubber sheet gasket and a 26 cm diameter x 29 cm tall high-pressure glass bell jar as a pressure vessel. The chamber was equipped with a 75 Watt, 120 V, resistance heater (RH68777, Fast Heat, Inc., Elmhurst, IL) and a 15.2 cm x 8.9 cm x 1.3 cm water-cooled copper cold plate (McMaster Carr, Chicago, IL). The small thermal fatigue chamber used a fibrous zirconia insulation (Zircar Corporation, Florida, NY) to insulate the side of the specimens during thermal cycling. The specimens and the ceramic insulation were then sandwiched between the hot plate and the cold plate, creating a temperature gradient through the specimen thickness. The cold plate temperature was maintained at 40°C, while the hot plate temperature was cycled between 50°C and 400°C for a preselected number of thermal cycles. The small chamber was sealed, evacuated with a mechanical pump and purged three times with argon gas. The thermal fatigue testing was performed in a flowing argon environment to minimize oxidation of the specimens. The cold plate was cooled to using a constant temperature water bath (Fisher Scientific Inc., Isotemp Constant Temperature Circulator Model 800, Pittsburg, PA).

2.4.2. Hot Side Refractory Brick Assembly

A porous alumina refractory brick (11.5 cm x 7 cm x 2.5 cm) was used as the heater housing (Figure 2.4.1). A 10.3 cm x 3.7 cm x 0.5 cm section was removed from the brick face using a generic straight edge razor. The outline of the area was scribed into the alumina brick with the razor, and then the razor was placed at an angle of between approximately 30 degrees and 50 degrees chisel out the alumina. The cavity in the alumina brick was created to allow the 75-watt, 120 V resistance heater (Lytron Corporation, Woburn, MA) to sit flush with the brick's surrounding edges (Figure 2.4.2., Side B-# designates the sides of the refractory brick to assist in the explanation of the construction of the alumina brick). A 1.5 cm diameter hole was drilled through the brick 3.5 cm from Side B-A of the alumina brick, and down the center of the brick (3.5 cm from Side B-B of the brick) using a Black and Decker 0.5 inch drill with a 0.25 inch drill bit. Another 1.5 cm through hole was drilled 2 cm from the center of the initial 1.5 cm diameter hole; this hole was also located along the center of the alumina brick (Figure 2.4.1.).

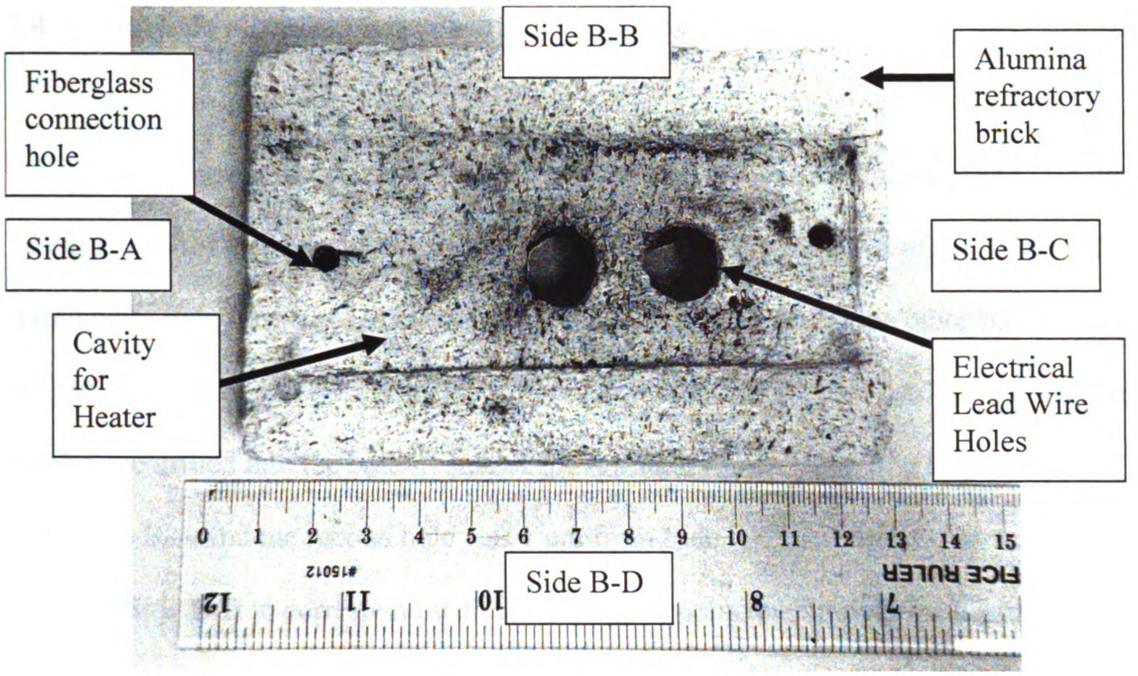

Figure 2.4.1. Alumina refractory brick with cavity removed and lead wire holes drilled for placement and attachment of the hot plate. Two holes drilled for connection with the fiberglass board are visible as well. Side B-# is used to designate the sides of the refractory brick to assist in the explanation of the construction of the alumina brick.

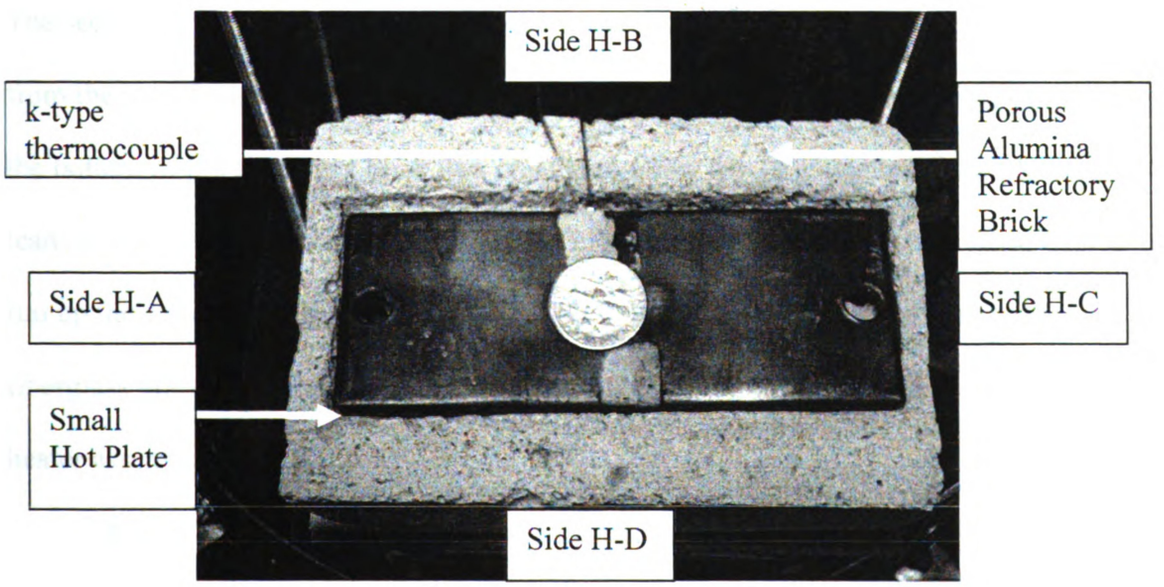

Figure 2.4.2. Small thermal fatigue chamber hot plate set up within the refractory alumina brick with attached thermocouple.

2.4.3. Hot Side Fiberglass Base Plate Assembly

The refractory brick sat on top of and was attached to a fiberglass plate (11.5 cm x 18 cm x 0.5 cm) using two 3 cm x 0.2 cm bolts. The bolts were fixed to two holes drilled through the fiberglass plate, one bolt was 1 cm from Side F-A and the other bolt was 1 cm from Side F-C, and both bolts were 5 cm from Side F-B (Figure 2.4.3.). Two 0.5 cm holes were drilled into the bottom side of the refractory brick. The first hole was 1 cm from Side B-A and the second hole was 1 cm from Side B-C, and both holes were 3.75 cm from Side B-B to correspond with the fiberglass bolts to help with the heaters stability (Figure 2.4.3.). Side F-# designates the sides of the fiberglass base plate to assist in the explanation of the construction of the plate. Side B-# designates the sides of the refractory brick to assist in the explanation of the construction of the alumina brick.

A section of the underside of the brick was removed using a straight edge razor. The section removed was a 2 cm x 3.75 cm rectangular section, 1 cm in depth, which ran from the two electrical lead holes to the edge of the brick (Figure 2.4.4.). The cavity on the bottom of the refractory brick was created to allow the 18 gauge insulated electric leads (CSA Type LL81924 SJT 18AWG FT2 Wire, Hewlett Packard, Palo Alto, CA) to run up the 1.5 cm lead holes while also keeping the refractory brick flush with the fiberglass plate. The electrical lead wire connected to the underside of the heater in the heater assembly (Figure 2.4.4.).

A 11.5 cm x 7.5 cm piece of fibrous zirconia insulation (Zircar Corporation, ZYF-A2.13, Florida, NY) was cut to fit between the fiberglass base plate and alumina refractory brick (Figures 2.4.5. and 2.4.6.). The insulation had two 1 cm x 1 cm squares

cut at the center of Side I-A and I-C edges to accommodate the refractory brick attachment screws (Figure 2.4.5., Side I-# designates the sides of the zirconia insulation separator to assist in the explanation of the construction of the insulation sheet). The zirconia insulation was a precautionary barrier between the heated refractory brick and the fiberglass plate during thermal cycling.

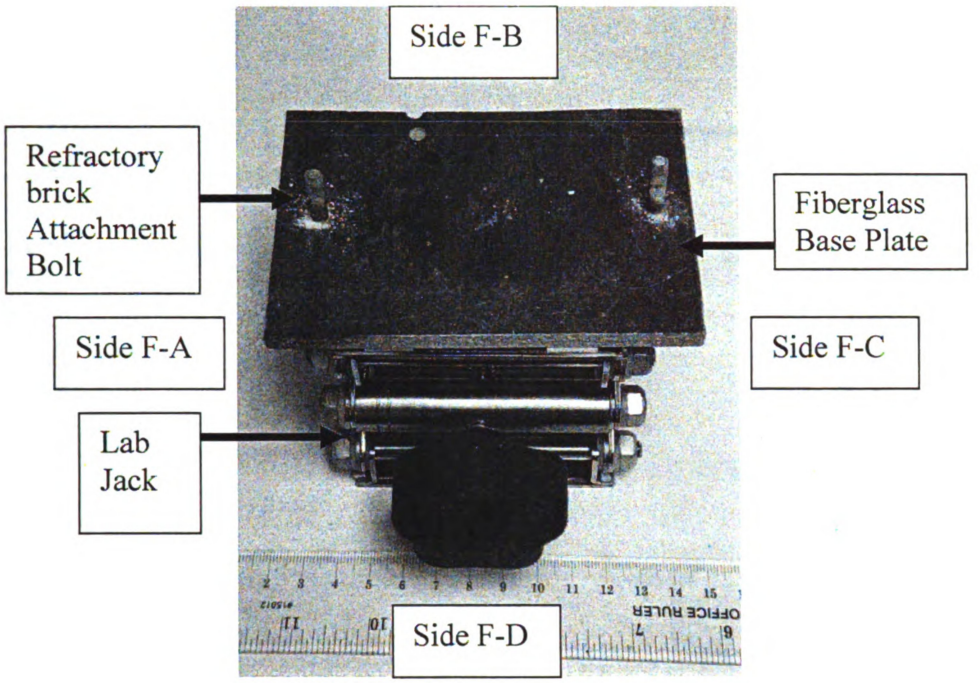

Figure 2.4.3. Fiberglass base plate attached to lab jack with alumina refractory brick attachment bolts. Side F-# is used to designate the sides of the fiberglass base plate to assist in the explanation of the construction of the plate.

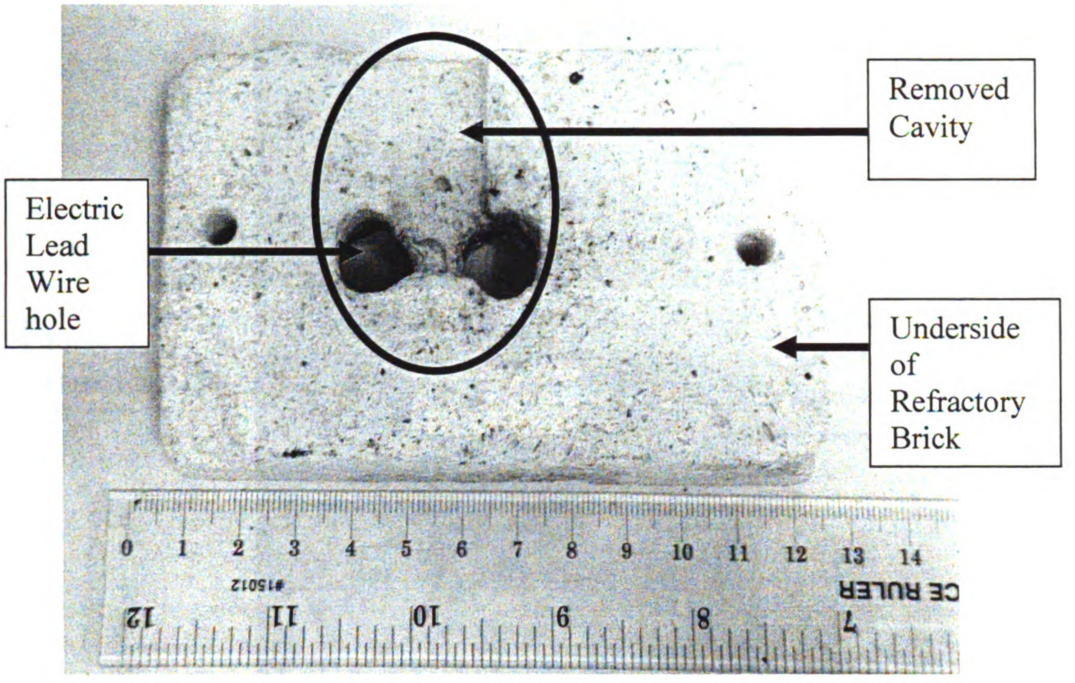

Figure 2.4.4. Underside of the refractory brick (opposite side of heater) showing the section removed, in the black oval, for the electrical lead wire to lie between the refractory brick and fiberglass base plate without tilting the heater during thermal cycling.

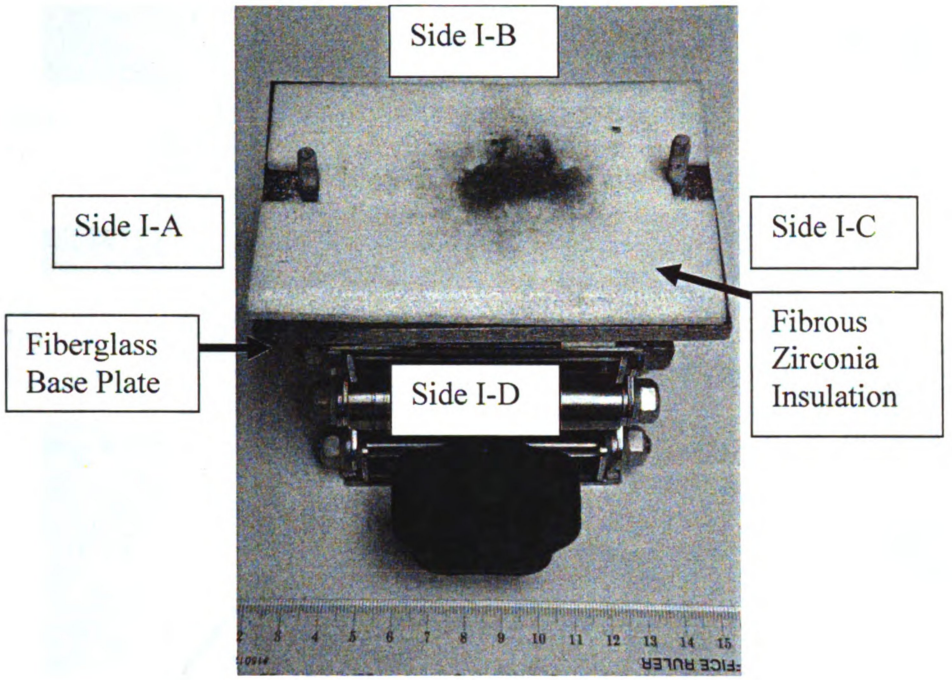

Figure 2.4.5. Zirconia insulation used to separate the fiberglass base plate from direct contact with the alumina refractory brick during heating. Side I-# is used to designate the sides of the zirconia insulation separator to assist in the explanation of the construction of the insulation sheet.

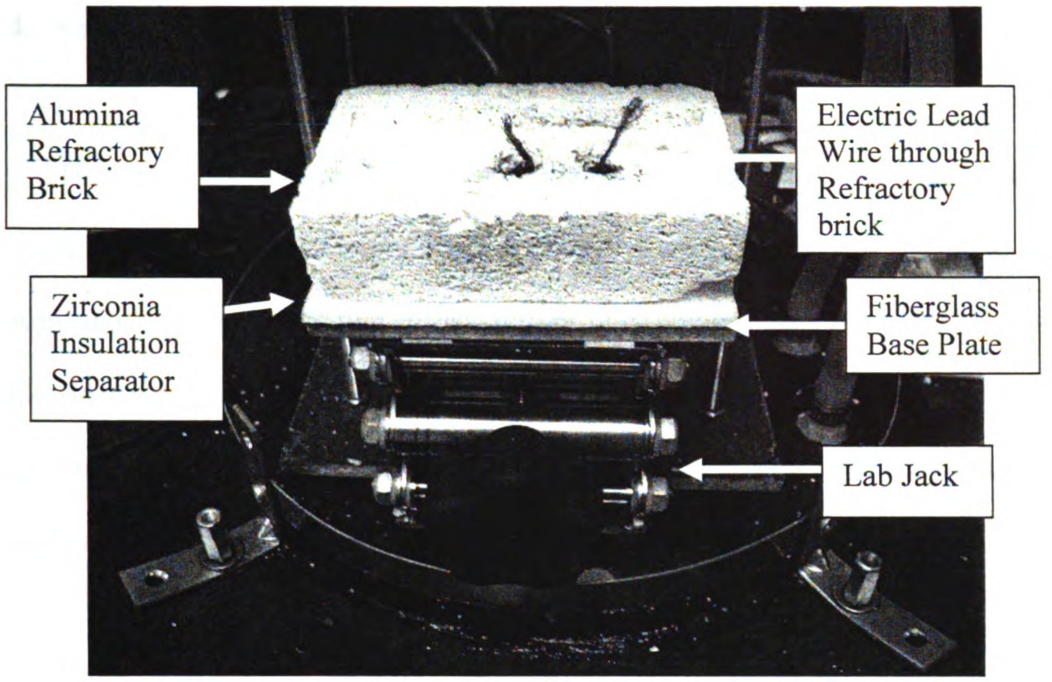

Figure 2.4.6. Heater assembly of lab jack, fiberglass base plate, zirconia insulation separator and refractory brick with heater electrical lead wires. Heater assembly ready for hot plate attachment.

2.4.4. Small Chamber Hot Plate Assembly

The fiberglass base plate, alumina refractory brick and heater were attached to a scissor lab jack (Adjustable-Height Support Stand 7.6 cm x 7.6 cm Top, 6.4 cm to 12.7 cm Adjustable Height) using two stripes of light-duty polyethylene foam rubber adhesive double-sided adhesive tape (McMaster-Carr, 7598A912, Santa Fe Springs, CA). The stripe of tape was 7.6 cm long and 1.9 cm wide and was attached to the front and back edge of the top of the support stand (Figure 2.4.6.).

2.4.5. Hot Side Thermocouple Attachment

2.4.5.1. Hot Plate Thermocouple Attachment

The thin film CO2 k-type thermocouple (Omega Engineering Inc, Stanford, CT) was attached to the hot plate using a high-temperature cement (Omega Engineering Inc, OMEGA CC High Temperature Cement, Stanford, CT). The heater surface was hand polished using a 400 grit sandpaper (Leco, St. Joseph, MI) to remove an industrial finish on the hot plate which does not allow the cement to adhere to the hot plate. The high-temperature cement comes as separate powder and binder phases, which must be mixed to form the cement.

Using a 30 ML mixing cup and 15 cm applicator wooden stick (Puritan, Guilford, Maine), approximately 1 mL of powder was mixed with 0.3 mL of binder. The cement's powder and binder phases were mixed to produce a homogenous mixture with no clumps of powder. The mixture needed a higher viscosity than water since the mixture had to be spread able but not have a tendency to run on a flat surface. A high viscosity in the cement ensured that there was a proper coating of the cement over the thermocouple, which ensured a good bond between the thermocouple and the hot plate.

Using the wooden applicator, a drop of the cement mixture (>5 mL) was spread in a 1 cm x 1 cm square onto the cleared surface of the heater. The adhesive was applied along the edge of Side H-B, 5 cm from Side H-A (Figure 2.4.2.) Side H-# designates the sides of the hot plate to assist in the location of the thermocouple attachments to the hot plate. This initial dry coat layer of high-temperature cement kept the thermocouple from

having direct contact with the heater surface. Direct contact with the heater surface was avoided due to the danger of shorting out the thermocouples. The end of each thermocouple was then placed onto the cement pad. Again, using the wooden applicator, approximately 0.5 mL of cement was placed on top of the thermocouple and the cement was then allowed to set in room air for 24 hours (Figure 2.4.2.).

2.4.5.2. Hot Side Thermocouple and Thermocouple Lead Soldering

Once the cement had cured, the thermocouple was cut to a length of 4 cm and then sanded with 400 grit sandpaper until there were visible scratches along the leads of the thermocouple. The sanding removed a coating material on the surface of the thermocouples that did not adhere to the solder melt during the soldering of the thermocouple and the thermocouple lead. A fiberglass insulated, 24 gauge, type K stranded thermocouple (McMaster-Carr, 6579T42, Santa Fe, CA) was used for what. About 2 cm of the fiberglass insulation was removed from the thermocouple wire using generic wire cutters. The thermocouple was then connected to the thermocouple lead using a 40-watt Radio Shack soldering station with 0.032 mm diameter, 8.0 oz, 60/40 Radio Shack solder and Radio Shack non-spill paste rosin soldering flux (Figure 2.4.2.).

2.4.6. Cold Side Thermocouple Attachment

2.4.6.1. Cold Plate Thermocouple Attachment

A water-cooled cold plate 15 cm x 9 cm x 1 cm was fabricated at the Michigan State University Physics Shop using a multipurpose aluminum (Alloy 6061) 30.5 cm x 10.2 cm x 0.6 cm block (McMaster-Carr, 8975K425, Santa Fe, CA) with 1 cm diameter copper tubing running through the block (Figure 2.4.7.).

The cold plate had one CO1 k-type thermocouple (Omega Engineering Inc, Stanford, CT) attached to it, prior to being installed into the thermal fatigue chamber. The aluminum surface of the plate was wiped clean using a Kimwipe (Kimberly-Clark Co., Neenah, WI) to remove any debris that would keep the thermocouple cement from adhering to the cold plate surface. The thin film CO1 k-type thermocouple (Omega Engineering Inc, Stanford, CT) was attached to the cold plate using the same method as with the hot plate thermocouple of Section 2.4.5.1.

The high-temperature cement was mixed as described in Section 2.4.5.1 for the hot plate thermocouple; except only1 ML of powder was mixed with 0.3 ML of binder for the cement ratio. The mixed cement was applied to the cold plate by following the hot plate instructions of Section 2.4.5.1., except the adhesive was applied once along Side C-B, 3.5 cm from Side C-A (Figure 2.4.8., Side C-# designates the sides of the cold plate to assist in the location of the thermocouple attachments to the cold plate).

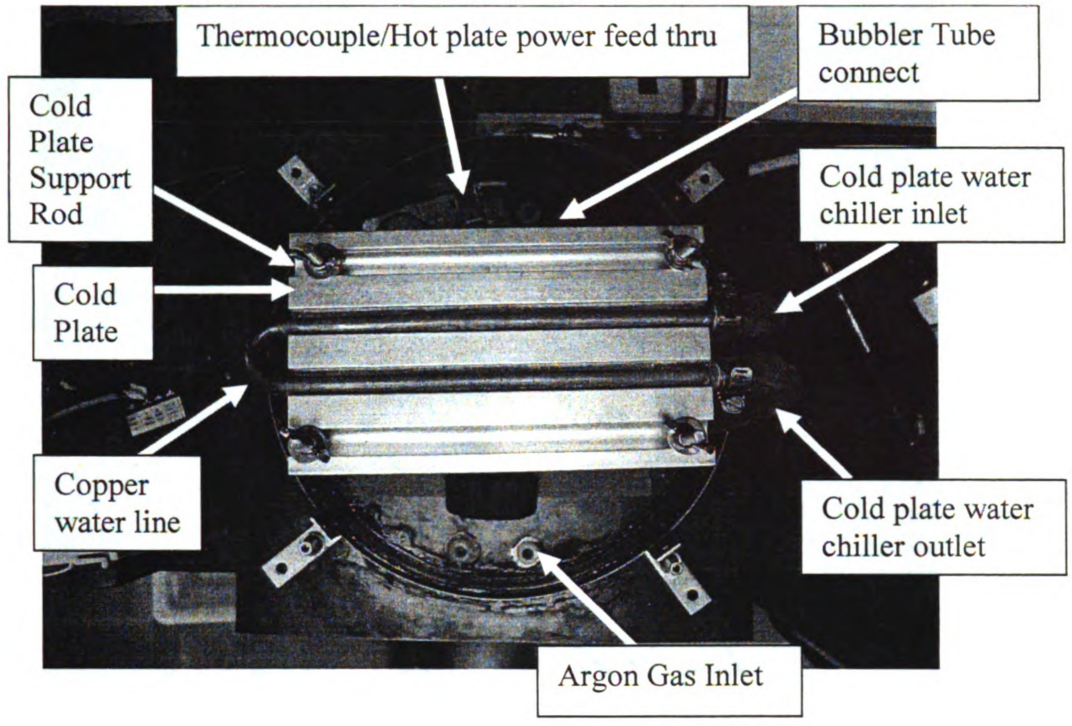

Figure 2.4.7. Top view of small thermal chamber set-up, showing the vacuum and bubbler tubes inlets, heater power cord feed thru, the thermocouple feedthru from the floor mat, as well as the cold plate water chilling inlet and outlet tubes.

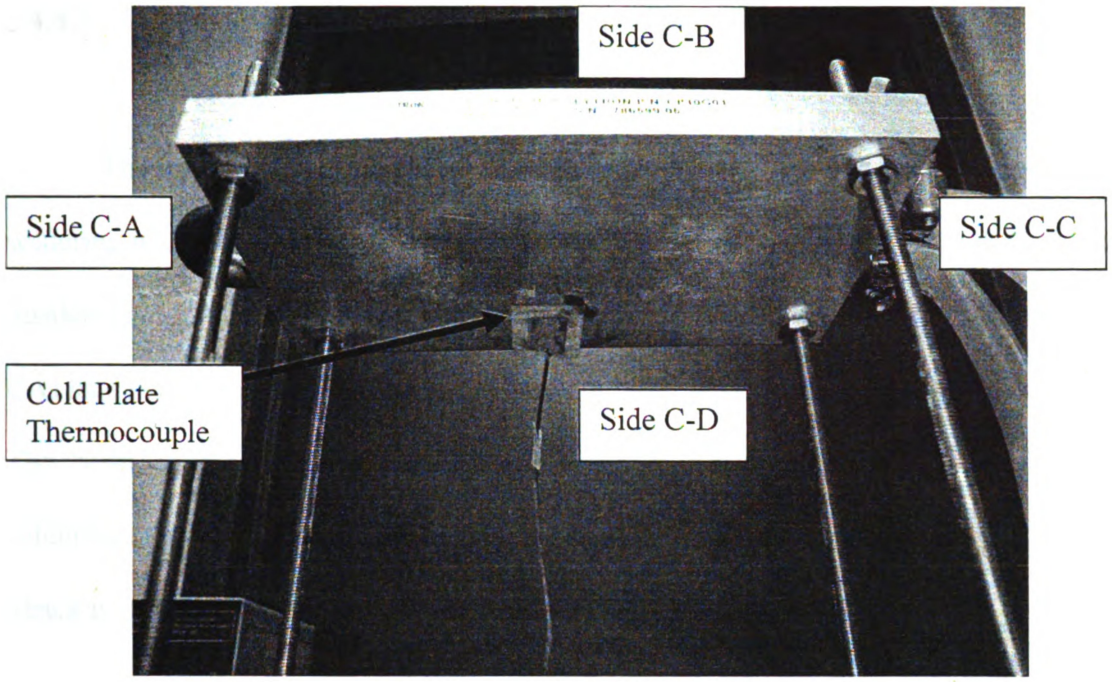

Figure 2.4.8. Small Thermal Chamber Cold Plate (sample contact side) with thermocouple and thermocouple lead attached. Side C-# is used to designate the sides of the cold plate to assist in the location of the thermocouple attachments to the cold plate.

2.4.6.2. Cold Side Thermocouple and Thermocouple Lead Soldering

The initial preparation of the cold plate thermocouple and thermocouple lead for soldering was the same procedure used for the hot plate in Section 2.4.5.2. A fiberglass insulated, 24 gauge, type K stranded thermocouple (McMaster-Carr, 6579T42, Santa Fe, CA) lead had about 2 cm of fiberglass wire covering removed using generic wire cutters. The thermocouple was connected to the thermocouple lead using a 40-watt Radio Shack soldering station with 0.032 cm diameter, 8.0 oz, 60/40 Radio Shack solder and Radio Shack non-spill paste rosin soldering flux (Figures 2.4.8. – Figure 2.4.9.).

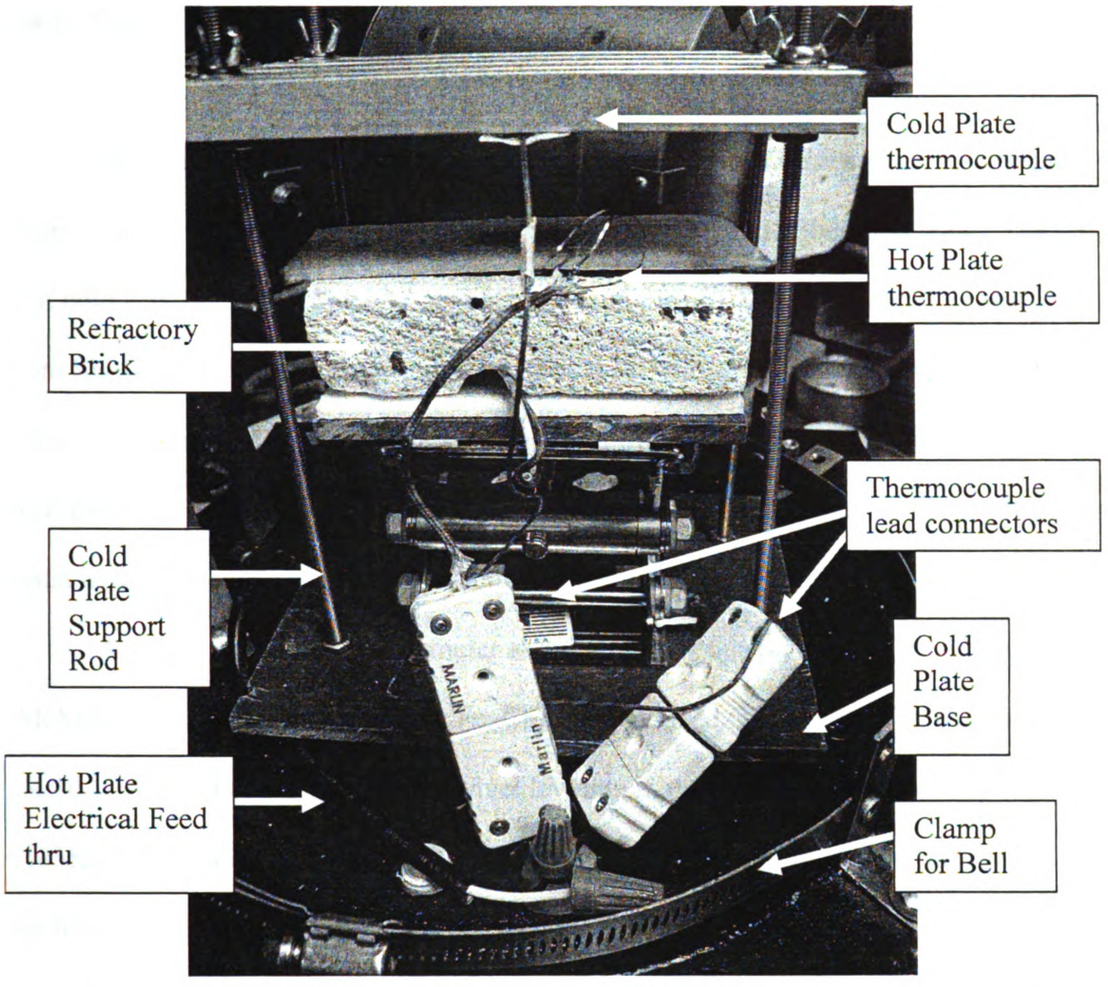

Figure 2.4.9. Back side of the small thermal fatigue chamber set-up with the sample stage, with a view of the hot and cold plate thermocouples and the thermocouple leads, also the electrical feed thru for the hot plate.

2.4.7. Cold Plate Stand

The cold plate stand initially consisted of a 17.5 cm x 13.5 cm x 0.5 cm fiberglass plate (Figure 2.4.10.). Four 1 cm holes were drilled through the fiberglass plate. The first hole was 2 cm from Side F-A and 3.5 cm from Side F-D. The second hole was 2 cm from Side F-A and 3.5 cm from Side F-B. The third hole was 2 cm from Side F-C and 3.5 cm from Side F-D. The fourth hole was 2 cm from Side F-C and 3.5 cm from Side F-B (Figure 2.4.10., Side F-# designates the sides of the cold stand fiberglass base plate to assist in the explanation of the construction of the plate).

A 20.3 cm long, 0.6 cm diameter aluminum alloy 6061-T6 fully threaded stud (McMaster-Carr, 93225A886, Santa Fe, Ca) was then feed through each hole (Figure 2.4.10.). A 0.6 cm diameter thread swivel leveling mount foot (McMaster-Carr, 6103K65, Santa Fe, CA) was attached to each of the threaded rods, on the underside of the fiberglass plate for stability. A 0.6 cm diameter generic hex nut was then threaded down each rod on the upper side of the fiberglass plate, until it firmly held the fiberglass plate onto the threaded feet (Figure 2.4.8.).

Another 0.6 cm diameter generic hex nut was threaded down each rod, 3.3 cm from the top. The cold plate was machined with four 1 cm holes drilled through it. The first hole was located 0.75 cm from Side C-A and 1.25 cm from Side C-B. The Second 1 cm hole was drilled 0.75 cm from Side C-C and 1.25 cm from Side C-B. The third hole was made 0.75 cm from Side C-C and 1.25 cm from Side C-D. The final 1 cm hole drilled in the cold plate was 0.75 cm from Side C-A and 1.25 cm from Side C-D (Figure 2.4.7. and Figure 2.4.9., Side C-# designates the sides of the cold plate to assist in the

location of the thermocouple attachments to the cold plate). The 1 cm holes in the cold plate were to accommodate for the threaded rods the cold side stand used as legs (Figure 2.4.8.). The four rods were then fed through the four holes in the cold plate until the cold plate was resting on the hex nuts that were previously threaded on the rods. Four generic 0.6 cm washers and wing nuts were then used to hold the cold plate in place against the hex bolts (Figure 2.4.7.).

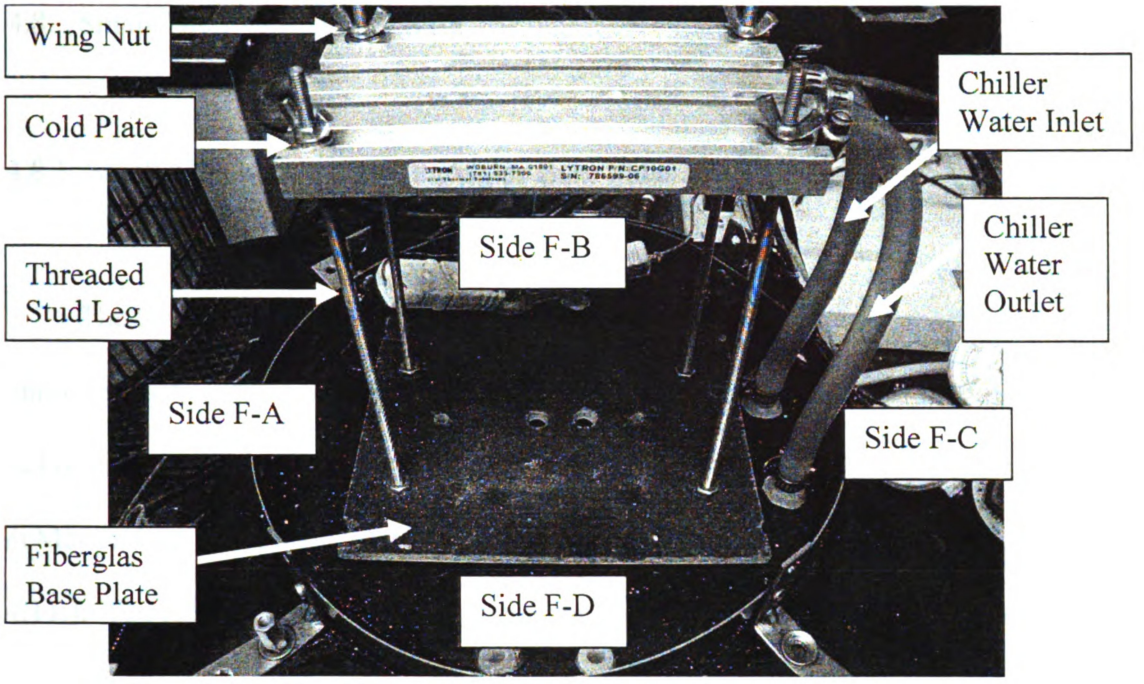

Figure 2.4.10. Small Thermal Fatigue Chamber Cold Plate installed on cold plate stand using attached threaded rods. Side F-# is used to designate the sides of the cold stand fiberglass base plate to assist in the explanation of the construction of the plate.

2.4.8. Small Thermal Chamber Base

2.4.8.1. Small Thermal Chamber Plexiglas Base Plate

The base of the small thermal chamber in which all heating and cooling components sat on during thermal cycling began initially as a 30.5 cm x 30.5 cm x 2 cm sheet of clear Plexiglas. A 30.5 x 30.5 x 0.3 cm oil-resistant vinyl rubber sheet (McMaster-Carr, 8513K44, Santa Fe, CA) was laid on top of the Plexiglas (Figure 2.4.11.). The rubber sheet acted as a gasket for the chamber when it was vacuum-sealed during testing.

Four 0.5 cm holes were drilled through both the Plexiglas base and the rubber mat 7 cm from each corner (Figure 2.4.11. and Figure 2.4.12.). The rubber mat was then held in place over the Plexiglas base by placing a 2.5 cm long zinc-plated alloy steel10-32 thread socket head cap screw (McMaster-Carr, 90128A947, Santa Fe, CA) through the underside of each 0.5 cm hole drilled in the Plexiglas and rubber mat. The ends of the four bolts were above the surface of the rubber mat and a steel L-bracket 5.1 cm in length and 1.6 cm in width (McMaster-Carr, 1556A13, Santa Fe, CA) was place onto each bolt and a 1.9 cm long 10-32 thread grade 2 zinc-plated steel coupling nut (McMaster-Carr, 90264A430, Santa Fe, CA) was threaded to the bolt (Figure 2.4.11.).

A 1.3 cm wide 316 SS worm-drive hose and tube clamp with a 91-114 cm clamp diameter range was riveted one time to each of the l-brackets in a circle configuration (Figures 2.4.9. and 2.4.11.).

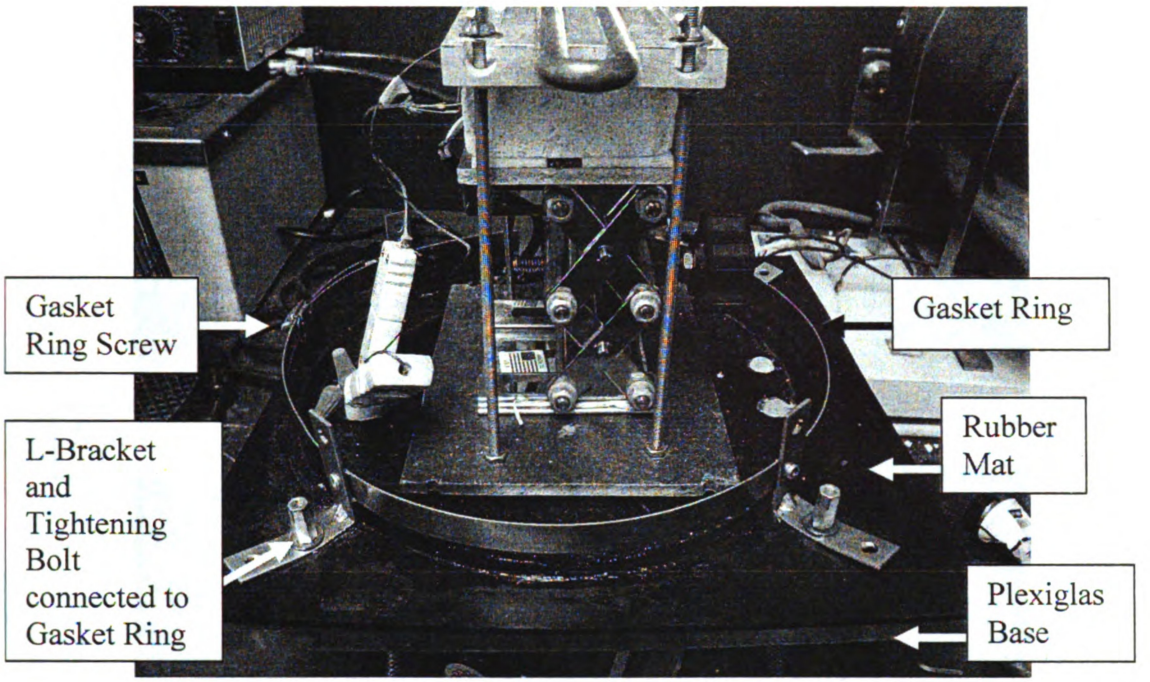

Figure 2.4.11. Left side of the small thermal fatigue chamber showing the configuration of the 100 cm gasket ring riveled to four L-brackets held to the chamber floor using a nut and bolt design, used in vacuum sealing the glass bell jar prior to thermal cycling.

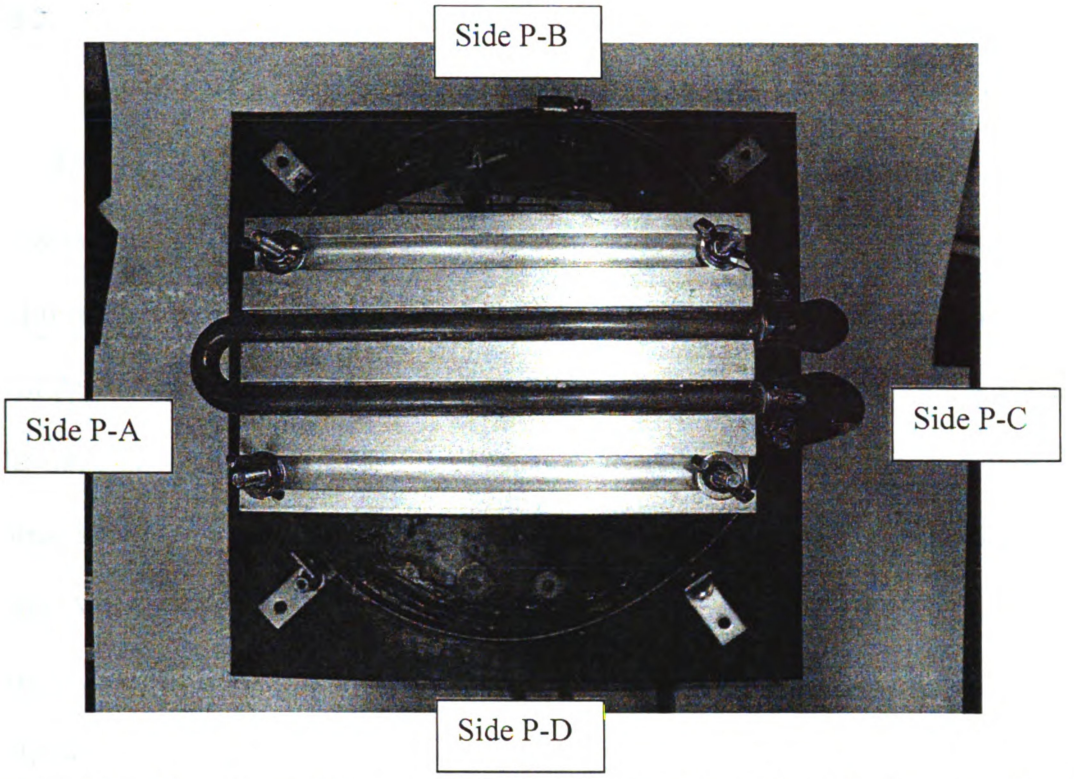

Figure 2.4.12. Top View of the Small thermal chamber Plexiglas and rubber mat base plate with the cold side assembly in position for thermal testing. Side P-# is used to designate the sides of the small thermal chamber Plexiglas base plate to assist in the explanation of the construction of the plate.

2.4.8.2. Small Chamber Base Plate Vacuum Pump and Argon Gas Feed Through

Five holes were drilled through the Plexiglas base and rubber mat, all of the holes were within the perimeter of the hose clamp connected to the l-brackets. The first hole was 1.6 cm in diameter and was located 5 cm from the Side P-D and 13 cm from the Side P-C of the Plexiglas base (Figure 2.4.12. and Figure 2.4.13., Side P-# designates the sides of the small thermal chamber Plexiglas base plate to assist in the explanation of the construction of the plate.). A 1.3 cm ID tube durable nylon multi-barbed tube-fitting adapter (McMaster-Carr, 5372K114, Santa Fe, CA) was inserted into the bottom of the Plexiglas base, with the barbed adapter facing towards the floor (Figure 2.4.14.). The adapter was connected to a 30 cm long piece of 6.35 mm, 14 bar Flexeel polyurethane tubing (Freelin-Wade Co, McMinnville, OR). The opposite end of the Flexeel tubing was then connected to a chrome plated brass quick disconnect tube coupling socket for a 6.35 mm inner diameter tube (McMaster-Carr, 5478K718, Santa Fe, CA). The quick disconnect allowed easy exchange between the bubbler and the vacuum pump, as both the bubbler and pump linked to the large chamber using the same hose.

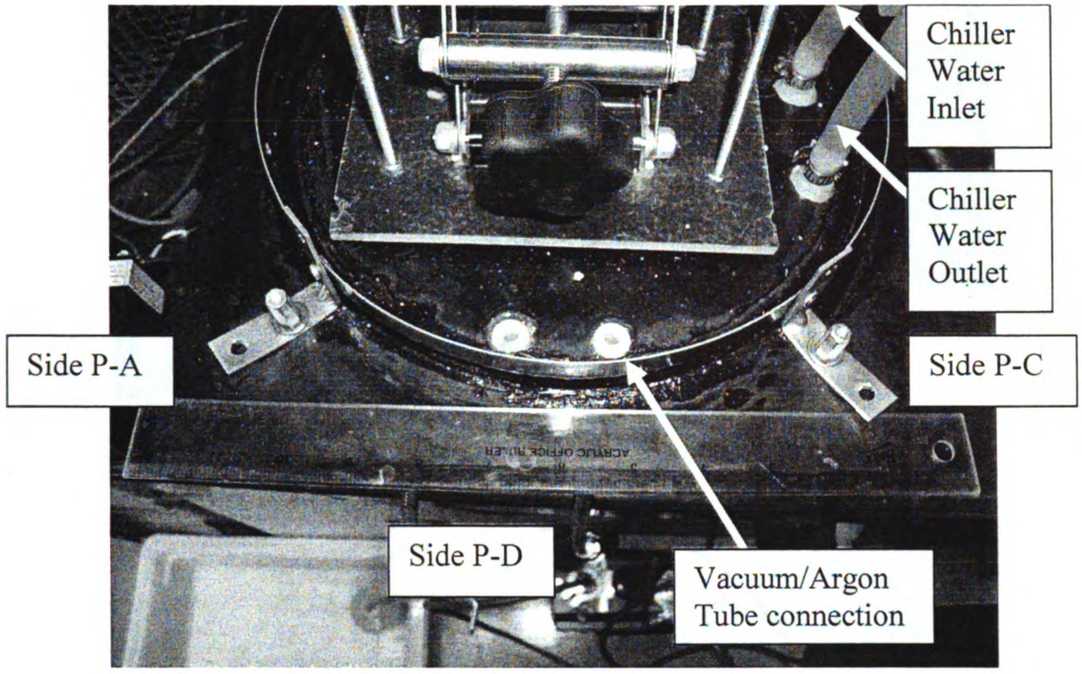

Figure 2.4.13. Front view of the small thermal fatigue chamber with a clear view of the vacuum/argon tube connections on the chamber floor. Side P-# is used to designate the sides of the small thermal chamber Plexiglas base plate to assist in the explanation of the construction of the plate.

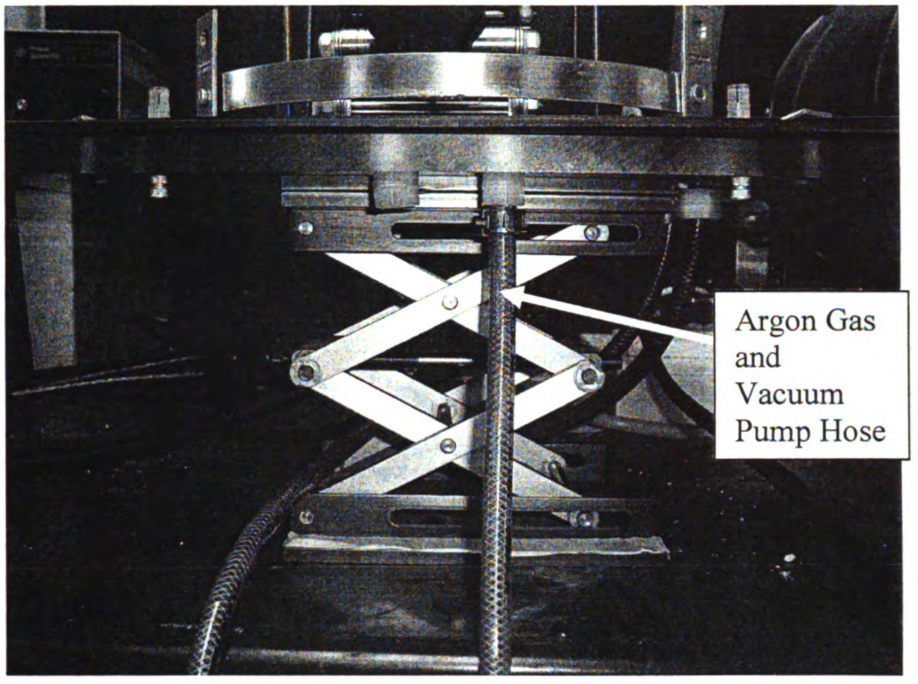

Figure 2.4.14. Underside view of small thermal fatigue Plexiglas base plate Argon gas and vacuum pump hose connection.

2.4.8.3. Small Chamber Base Plate Cold Plate Chiller Line Feed Through

Two 1.6 cm holes were located 4.5 cm from Side P-C of the Plexiglas base, one 12.5 cm from Side P-D and the other 12.5 cm from Side P-B (Figure 2.4.12., Side P-# designates the sides of the small thermal chamber Plexiglas base plate to assist in the explanation of the construction of the plate.). A 0.6 cm ID durable nylon single-barbed tube fitting coupling (McMaster-Carr, 2974K127, Santa Fe, CA) was inserted into the top face of each hole in the Plexiglas base and a 1.3 cm OD durable white nylon compression tube fitting nut (McMaster-Carr, 50775K371, Santa Fe, CA) screwed onto the 1.3 cm threaded end of the adapter on the underside of the Plexiglas base.

The barbed adapters were connected to pieces of laboratory clear Tygon PVC tubing 1.3 cm ID, 1.6 cm OD (McMaster-Carr, 5554K18, Santa Fe, CA), with 1.6 cm worm-drive hose clamps (McMaster-Carr, 5388K14, Santa Fe, CA) ensuring a leak free connection (Figure 2.4.15.). The Tygon tubing then connected to the copper tubing of the cold plate, one for the chiller inlet and the other for the chiller outlet (Figure 2.4.10.). A 45 cm long piece of 6.35 mm, 14 bar Flexeel polyurethane tubing was then inserted into each of the compression nuts of the cold plate adapters, while the open other end of the tubing was connected to a chrome plated brass quick disconnect tube coupling plug for a 6.35 mm inner diameter tube (McMaster-Carr, 5478K148, Santa Fe, CA).

The coupling plugs linked to chrome plated brass quick disconnect tube-coupling socket for a 6.35 mm inner diameter tubes (McMaster-Carr, 5478K718, Santa Fe, CA). Each of the quick disconnects connected to another 40 cm long of Flexeel tubing that attached to the constant temperature water bath (Fisher Scientific Inc., Isotemp Constant

Temperature Circulator Model 800, Pittsburg, PA), which ran the cooling of the cold plate.

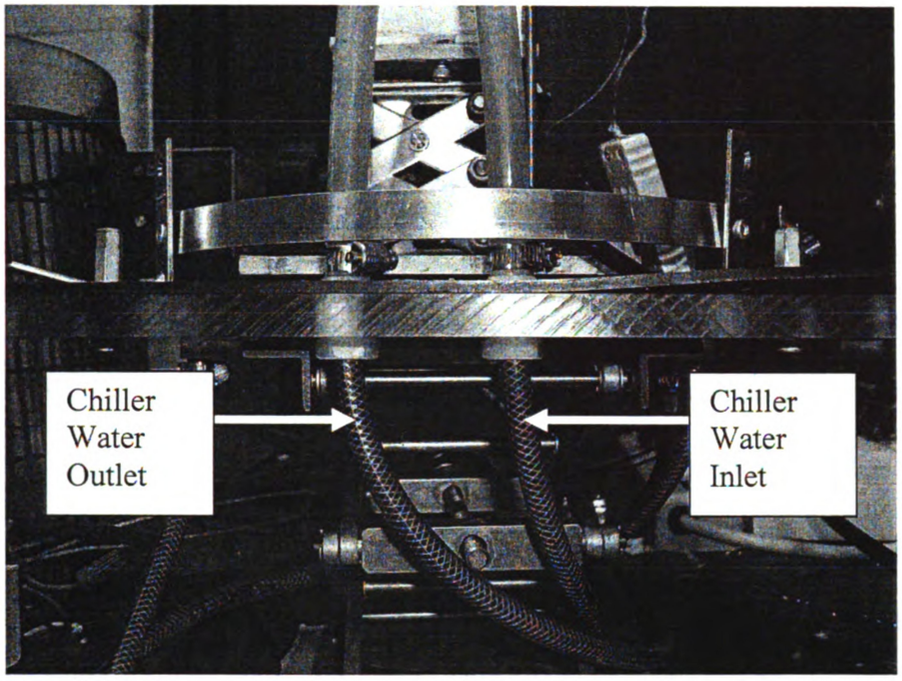

Figure 2.4.15. Side P-C side view (Figure 2.4.12.) of small thermal fatigue Plexiglas base plate Chiller water inlet and outlet hoses and connections.

2.4.8.4. Small Chamber Base Plate Bubbler Line Feed Through

A 1.3 cm hole drilled in the Plexiglas base was located 4.5 cm from Side P-B, and 15.5 cm from Side P-C (Figure 2.4.12. and Figure 2.4.13, Side P-# designates the sides of the small thermal chamber Plexiglas base plate to assist in the explanation of the construction of the plate). A 1.3 cm ID tube nylon multi-barbed tube-fitting adapter (McMaster-Carr, 5372K114, Santa Fe, CA) was inserted into the bottom of the Plexiglas base, with the barbed adapter facing towards the floor (Figure 2.4.16.). The adapter was connected to a 40 cm long piece of 6.35 mm, 14 bar Flexeel polyurethane tubing (Freelin-Wade Co, McMinnville, OR). The Flexeel tubing connected to a brass ball valve with Yor-Lok fittings for a 1 cm outer diameter tube (McMaster-Carr, 4112T37, Santa Fe, CA). The ball valve connected to a 65 cm length of Flexeel tubing, which in turn ran to a 250 mL UN-compliant plastic shipping bottle bubbler (McMaster-Carr, 42305T35, Santa Fe Springs, CA).

A bubbler is a beaker or bucket that uses water to help indicate a flow of argon gas through the chamber when the open-ended tube from the small chamber was placed under the water. The bubbler also helps to equalize the chamber with argon and not oxygen. The water will be pulled up the tubing towards the chamber instead of air, keeping an inert atmosphere within the bell jar. The bubbler bottle was weighted using a mixture of small rocks and epoxy that were allowed to harden at the bottom of the bottle, which filled approximately 1/4 of the container. Water was then added until 3/4 of the bubbler container was filled. The bubbler was used to indicate that there was a flow of inert gas flowing through the chamber during the experiment.

Hyp
mal
tem

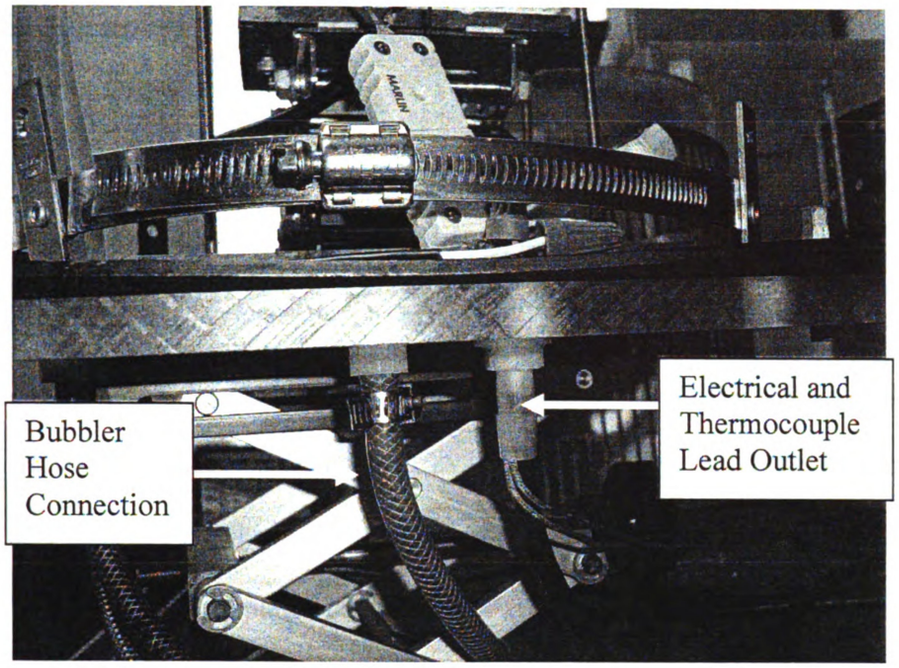

Figure 2.4.16. Side P-B of Figure 2.4.12. showing the bubbler hose connection to the small chamber floor. Also shown is the Hot plate electrical lead and the hot and cold side thermocouple lead outlet.

2.4.8.5. Small Chamber Base Plate Electrical and Thermocouple Lead Through

The last 1.3 cm hole drilled in the Plexiglas base was located 4.5 cm from Side P-B, and 15.5 cm from Side P-A (Figure 2.4.12., Side P-# designates the sides of the small thermal chamber Plexiglas base plate to assist in the explanation of the construction of the plate). A nylon single-barbed tube fitting adapter for a 1 cm ID tube x 1.3 cm diameter NPT male pipe (McMaster-Carr, 2974K135, Santa Fe, CA) was inserted into the underside of the Plexiglas hole, with the 1 cm adapter tube facing downward (Figure 2.4.16.). The 18-gauge hot plate electrical lead wire, the cold plate thermocouple lead wire and the hot plate thermocouple lead wire were fed through the adapter hole, allowing some extra length of wire (10 cm) as slack for movement of the hot side assembly. The adapter was then filled with roughly 10 ml of Loctite® epoxy (McMaster-Carr, Loctite® Epoxy Adhesive #1324007, Fast Cure, 1 Ounce Syringe, 7556A33, Santa Fe, CA), encasing the leads and potting them in the adapter to create an airtight seal for the thermal chamber. The epoxy took approximately one hour to fully harden around the lead wires.

2.4.9. Small Thermal Chamber Temperature Control

2.4.9.1. Thermocouple Meter and Thermocouple Controller

The cold plate was cooled using a constant temperature water bath (Fisher Scientific Inc., Isotemp Constant Temperature Circulator Model 800, Pittsburg, PA) that was set to 38°C to achieve a cold-side temperature of 40°C. The temperature control for the thermal fatigue chamber was regulated using the CN8201-R1-C2 temperature controller (Omega Engineering Co., Stamford, Connecticut), connected to the hot plate thermocouple and electrical lead (Figure 2.3.17). The cold plate thermocouple lead was connected to a CN72033 (Omega Engineering Inc, Stamford, Maine) thermal couple monitor (Figure 2.4.17.). The temperature controller was run using the computer program Multi-Comm CN8200.MCS (Omega Engineering Co., Stamford, Connecticut). Using the program, the hot side of the chamber was set to cycle between 50-400°C for a pre-selected number of cycles, a heating profile can be seen in Figure 2.3.18. Each cycle for the large thermal fatigue chamber took approximately 40 minutes to complete.

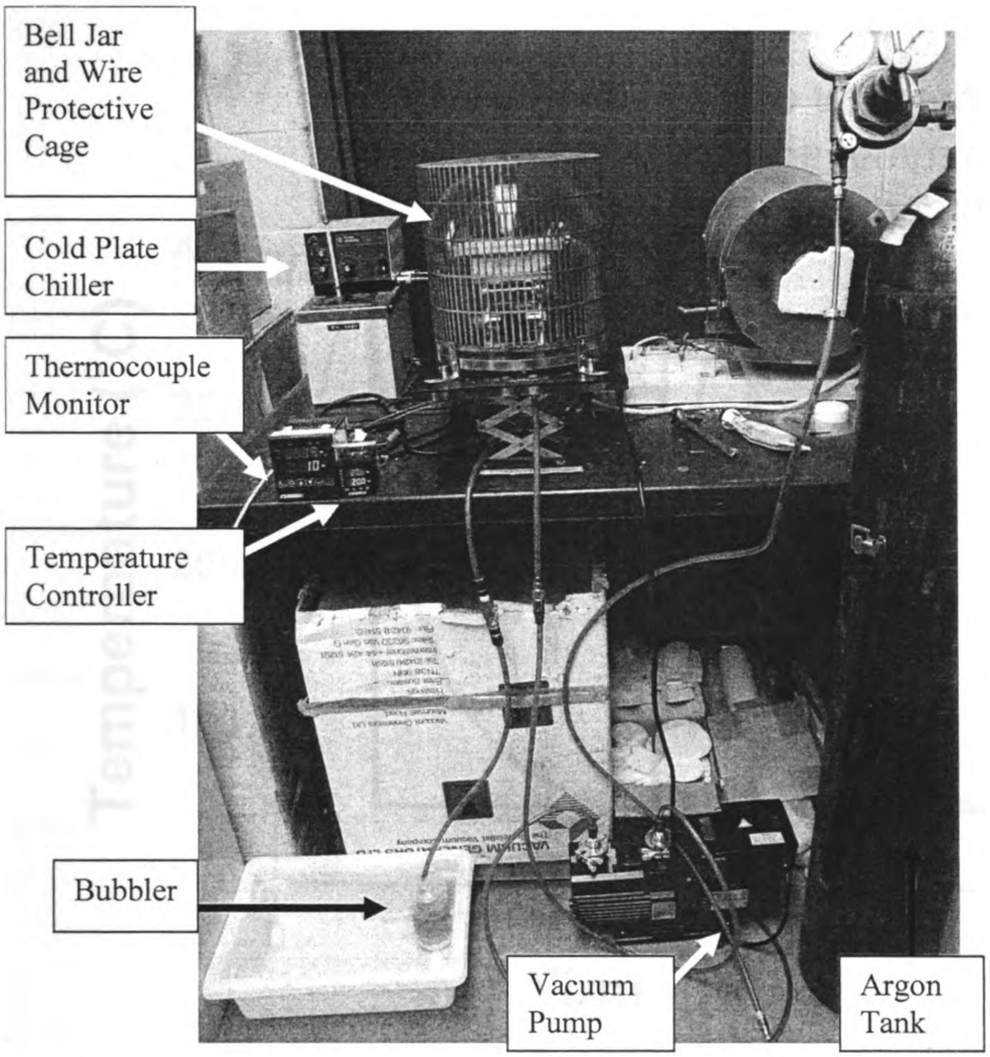

Figure 2.4.17. Small thermal fatigue chamber set-up and connected to the Argon tank, the bubbler, and the water chiller. This also shows the chambers thermocouple controller and temperature controller reading.

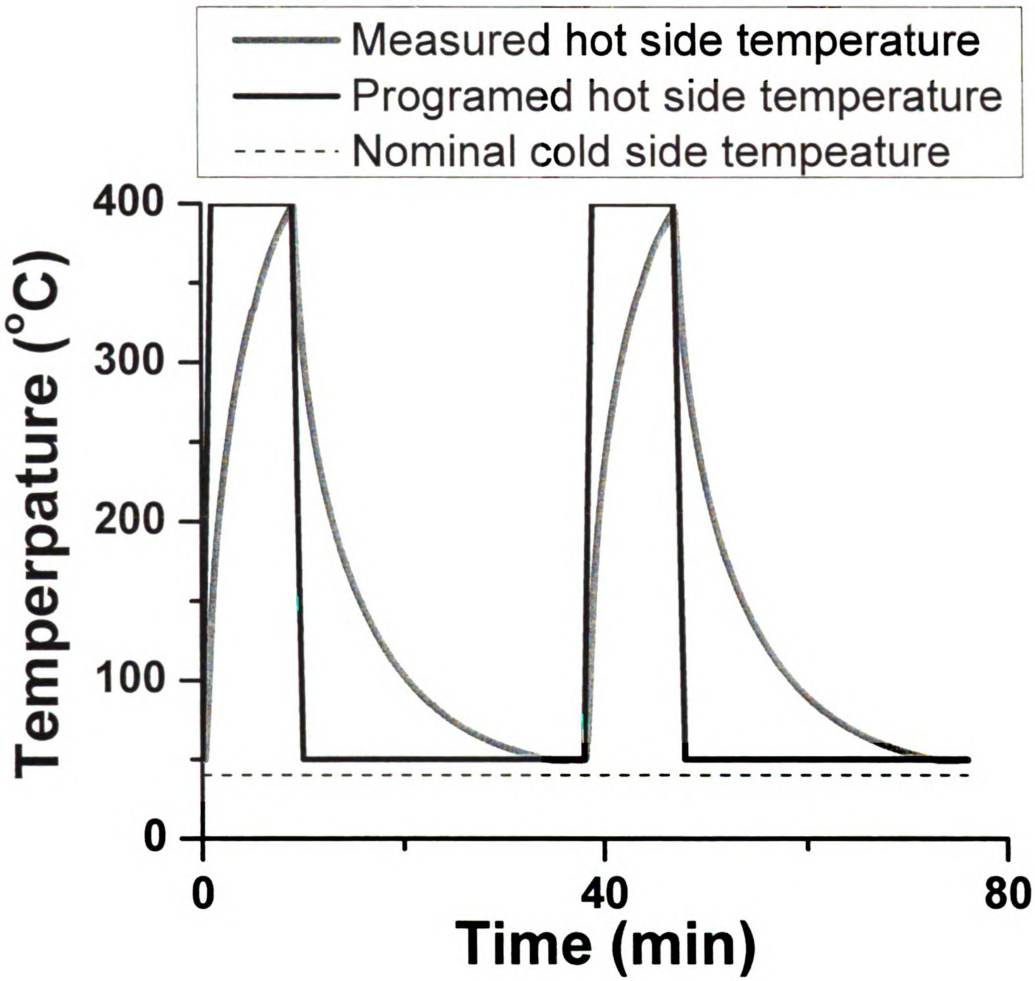

Figure 2.4.18. The thermal cycling profile for the small thermal fatigue chamber. It took 38 minutes to perform one thrmal fatigue cycle of 50-400°C.

2.4.9.2. Small Thermal Fatigue Chamber Heating Profile

The heating profile was determined by programming the heating ramp, hold, and cooling temperature and time to heat the specimens from 50 to 400°C as quickly as possible without holding the samples at an elevated temperature for an extended period of time. Once the 400°C temperature was reached, the thermocouple meter shut off the power to the heater and the samples began to cool to 50°C. The purpose for avoiding an isothermal hold at the maximum temperature of 400°C was to keepa thermal gradient through the material a predetermined number of times. An isothermal hold at 400°C would cause the hot plate and cold plate sides of the test specimens to reach the same temperature. In the small chamber it took 2 minutes to heat 2 parallelepiped samples from 50 to 400°C at a ramp rate of 5°C/minute.

2.4.10. Fibrous Zirconia Test Specimen Insulation

A 2 cm x 1.5 cm rectangular segment was removed from the center of a fibrous zirconia ceramic blanket material 12.5 cm x 5 cm x 0.3 cm (Zircar Corporation, ZYF-A2.13, Florida, NY). The cut zirconia ceramic blanket material was then placed on top of the alumina refractory brick (Figure 2.4.19). The edges of the fiber cover the hot side thermocouples while allowing access to the hot plate surface. Two specimens would be placed into this rectangular section in the insulation during thermal cycling. The specimens had contact with both the cold plate and hot plate while the perimeter of the specimens was insulated.

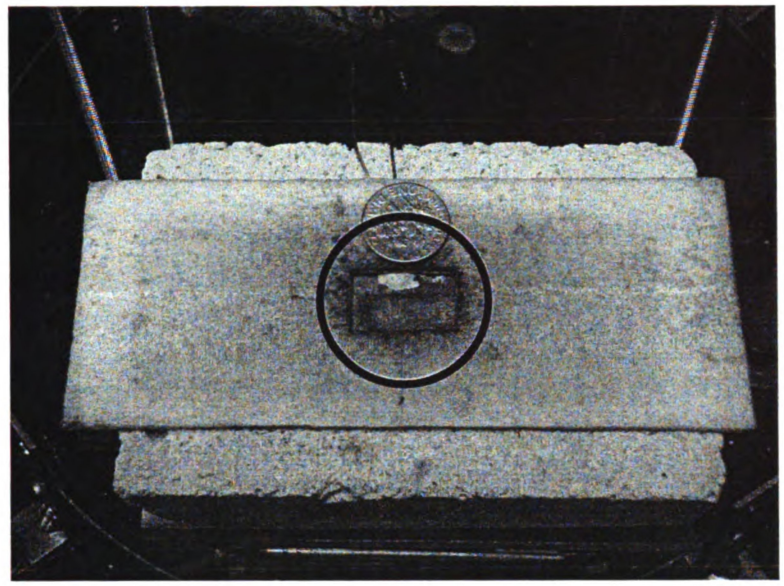

Figure 2.4.19. Pre-cut fibrous zirconia insulation placed on top of the small thermal fatigue chamber hot plate and refractory brick set-up, with a sample area rectangle removed, as shown in the black circle. This insulation was used to insulate the two samples during thermal cycling.

2.4.11. Preparing for Thermal Cycling in Small Chamber

2.4.11.1. Loading Hot Side Assembly into Small Chamber

The precut fibrous zirconia specimen insulation was placed on top of the alumina block and heater, covering the cemented thermocouple (Figure 2.4.19). Two parallelepiped samples were placed into the insulation cavity side by side. The hot side assembly was then placed on top of the cold side fiberglass base plate, underneath the cold plate in the cold plate stage set-up. The lab jack was raised using a screw knob until the specimens were sandwiched in firm contact with the hot and cold plate (Pressure was applied until the knob on the lab jack could not be tightened any further using only thumb and pointer fingers (Figure 2.4.20).

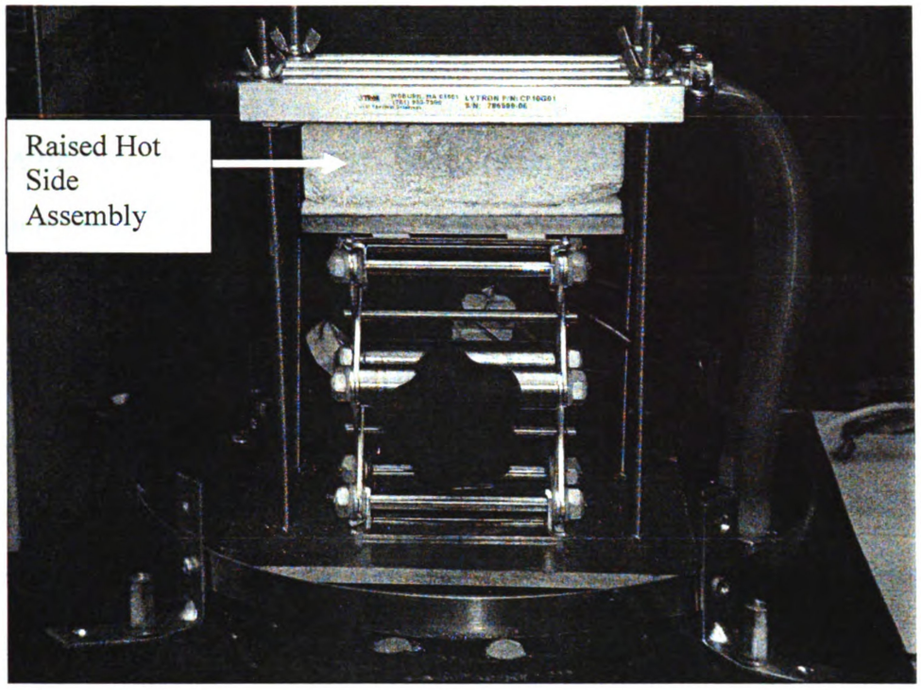

Figure 2.4.20. Hot plate apparatus raised by lab-jack and in contact with cold plate prior to tightening the bell jar.

2.4.11.2. Purging the Small thermal fatigue chamber

A roughening vacuum pump (UlvacKikoInc, GLD-040, Japan) was connected to the small thermal chamber via using the Flexeel polyurethane tubing connected to the quick disconnect tube coupling socket and plug (Figure 2.4.17.). A 26 cm diameter x 29 cm tall high-pressure glass bell jar was then set over the hot and cold side assembly. While using a gloved hand, a thin layer of Dow Corning high vacuum grease (Dow Corning, Midland, MI) was placed along the lip of the jar that contacted the rubber mat. The grease assisted in acquiring an airtight seal between the rubber mat and the bell jar. The bell jar sat on the inside of the worm-drive hose and tube clamp connected to the l-brackets at the perimeter of the small chamber Plexiglas base plate.

Before starting the vacuum pump, the ball valve for the bubbler line was closed and a metal wire protective cage was placed over the bell jar. If the bubbler ball valve were left open it would pull water from the bubbler and flood the small chamber. After the vacuum pump had been started, the worm driven clamp was tightened around the base of the bell jar using flat head screwdriver. Once the clamp was tighten as much as possible around the bell jar, the four hex bolts holding the L-brackets were tightened using an Alan wrench and a socket wrench. The vacuum pump was left running for 2 minutes (the pump would expel vapor from its exhaust hose).

The quick disconnect from the small chamber was unhooked from the vacuum and connected to a 99.9% purity, 10 cubic meter argon tank (Airgas, Independence, OH). The argon gas was used to purge the system. Argon gas flowed into the small chamber at a rate of no more than 10 kpa from the argon tank regulator. If the argon tank flow rate

was to great the seal between the bell jar and the mat, or the seal between the mat and the Plexiglas base plate would be compromised. The argon gas was flowed into the small chamber until the gas could not be heard flowing from the tank, about 1 minute. The chamber was then purged two more times.

Following the final argon purge the bubbler ball valve was slowly opened to allow a flow of argon gas through the small chamber and out the bubbler. There was a possibility of the small chamber still being in partial vacuum after purging, so by opening the bubbler valve slowly any water drawn up the bubbler tube towards the small chamber could be halted by closing the valve and increasing the flow rate of the argon tank. Using the bubbler ball valve, the gas pressure was adjusted to allow the release of approximately 5 bubbles per second or greater within the bubbler.

2.4.11.3. Starting the Small Thermal Fatigue Chamber Cycling

The CN8201-R1-C2 temperature controller and CN72033 Thermal Monitor were plugged in and the computer that ran the Multi-Comm software was turned on. Once the computer was ready, the Multi-Comm software was started. The desired number of thermal cycles was programmed into the computer and a folder on the desktop was chosen to record the heating and cooling data collected from the thermal monitor. The thermal monitor recorded the time and temperature of the hot plate every ten seconds to keep a record of the temperature profile for each thermal cycling test.

2.4.11.4. Completion of a Thermal Cycling Experiment

When a given experiment was complete, the argon gas tank cylinder valve was closed, and the argon tank hose was from the small chamber by ejecting its coupling plug from the chambers coupling socket hose. The bubble hose ball valve was closed and the hose was removed from the bubbler. Finally the power was shut off to the solid-state chiller. The thermal cycling profile data collected by the CN72033 and CN8201-R1-C2 software was saved to a desktop folder for archiving. All power to the thermal chamber was shut off to avoid electrocution dangers. The worm clamp was loosened from around the bell jar base, followed by the loosening of the L-bracket bolts. The bell jar was removed from the small chamber platform and stored in an area where it could not be damaged when not in use. The lab jack was lowered and the hot plate stage was carefully removed from the chamber to avoid any tension to the thermocouples or the thermocouple leads, which could disconnect or tear the thermocouples from the leads or the hot plate. The samples were then removed from the hot plate surface.

2.5 Elastic modulus measurements (RUS)

2.5.1. Preparation of Specimen Elastic Modulus Testing

Prior to thermal cycling, the disk and plate-shaped specimens of LAST and LASTT, the mass of each specimen was measured to within $\pm$ 0.0003 gram using an electronic balance (Adventurer AR2140, Ohaus Corp, Pine Brook, NJ) and the dimensions were measured to within $\pm$ 0.001 mm using electronic calipers (Mitutoyo CD-6"CSX, Kanagawa, Japan).

2.5.2. Resonant Ultrasound Spectroscopy

2.5.2.1. Overview

The Young's modulus, E, and Poisson's ratio, ν, were determined for the n-type LAST and p-type LASTT specimens via Resonant Ultrasound Spectroscopy (RUS) using a commercial unit (Quasar RUSpec, Quasar International, Albuquerque, NM). In the RUS technique, specimens were placed on a tripod arrangement of ultrasonic transducers (Figure 2.5.1). The tripod arrangement consists of three transducers: a single driver transducer in the tripod arrangement mechanically vibrated the specimen and the other two transducers of the tripod detected the specimen's mechanical response to the drive transducers mechanical vibration (Figure 2.5.1).

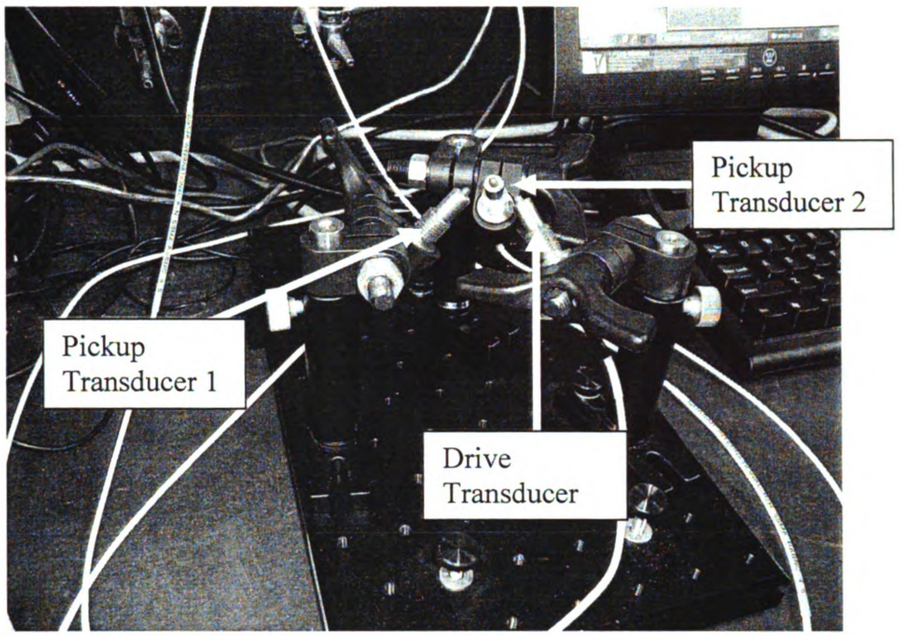

Figure 2.5.1. The resonant ultrasound spectroscopy tripod arrangement used to test the small thermal fatigue chamber specimens. There is one drive transducer and two pickup transducers.

2.5.2.2. Resonant Ultrasound Spectroscopy Transducers

Each of the three RUS transducers had a rounded rubber tip that the specimen sat on during testing (Figure 2.5.2). The transducers' rounded tips allowed for minimal contact with the specimen, so not to damp the mechanical vibration through the specimen. A rubber promoted grip between the specimen and the transducers so the samples would not vibrate off the transducers during testing and possibly become damaged (Figure 2.5.2).

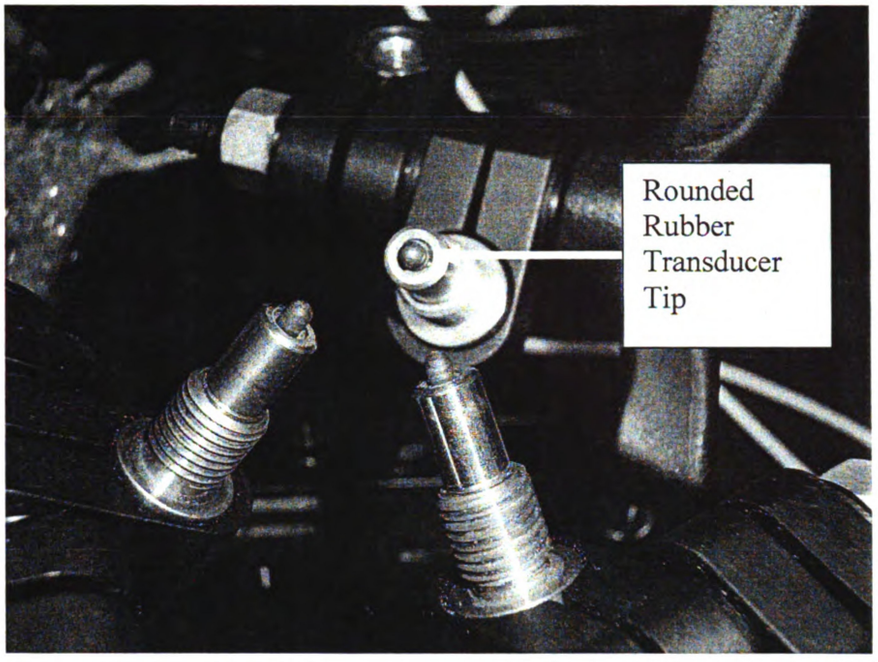

Figure 2.5.2. The resonant ultrasound spectroscopy tripod arrangement showing the rounded rubber transducer tips which contact the specimen during the testing.

2.5.2.3. Resonant Ultrasound Spectroscopy Transducer Arrangement

The resonant ultrasound spectroscopy transducers were arranged in a tripod formation when acquiring RUS spectrum data from the parallelepiped samples. The drive transducer was placed at the bottom edge of the parallelepiped sample along Side S-C. One of the pickup transducers was then placed under the corner of Side S-A and Side S-B, and the other pickup transducer was positioned under the corner of Side S-A and Side S-D (Figures 2.5.3-2.5.4, Side S-# is used to designate the sides of the test sample in respect to the samples position on the RUS transducers). The contact area between the transducers and the bulk of the sample was minimized in order to decrease the load the sample placed on the transducers. A smaller load on the transducers increased the vibration intensity that could be passed into the specimen and picked up by the transducers.

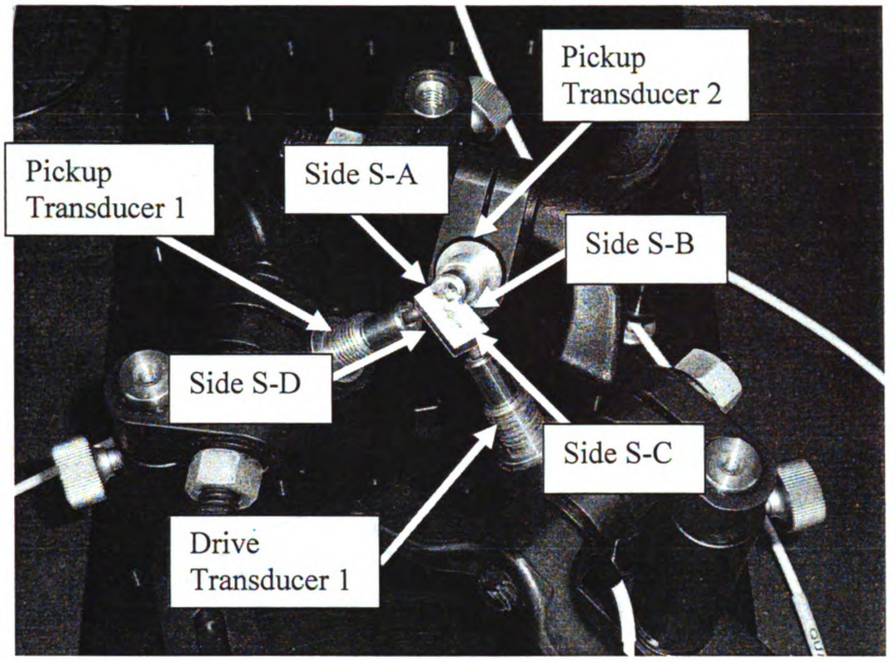

Figure 2.5.3. Resonant ultrasound Spectroscopy tripod arrangement with a sample in place for testing. The drive transducer was placed at the edge of the sample along the width of the parallelepiped sample, while the pickup transducers were placed under the samples opposite two corners. Side S-# is used to designate the sides of the test sample in respect to the samples position on the RUS transducers.

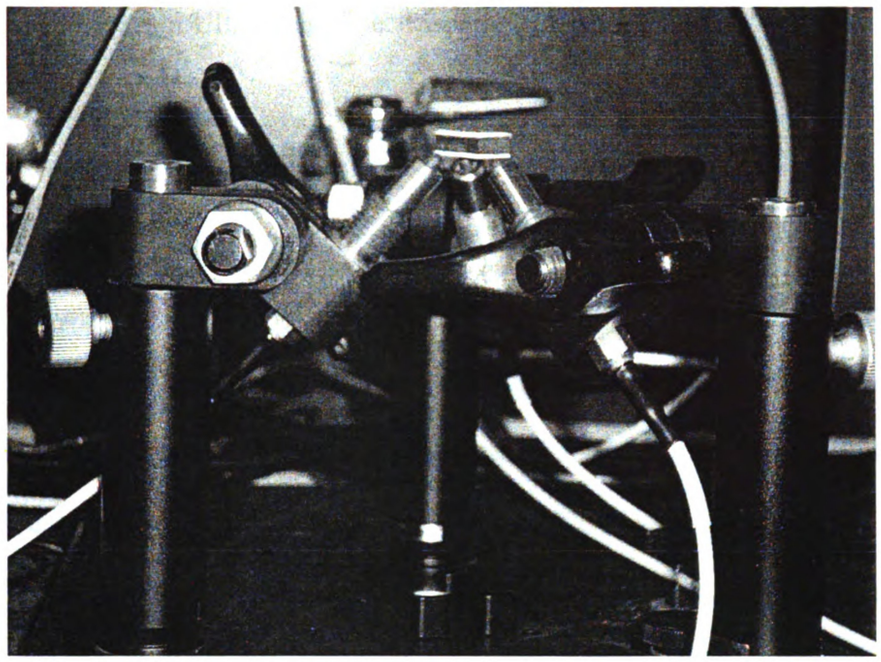

Figure 2.5.4. Side view of the resonant ultrasound spectroscopy tripod arrangement with a parallelepiped sample in place for testing from figure 2.5.3. It should be noted that the sample only sits at the tip of the transducer and should not be in contact with the transducers metal housing.

2.5.2.4. Resonant Ultrasound Spectroscopy Program

For the specimens included in this study, the sinusoidal driving signal was swept through a frequency range of approximately 20 kHz to 300 kHz with 10 Hz frequency increments (Figure 2.5.5). From the specimen mass, dimensions and the resonant frequency values, the Young's modulus and Poisson's ratio of the specimens were calculated using commercial RUS software, Quasar Galaxy RI2000 and RPModel software, Quasar International. The Quasar Galaxy RI2000 was used for the RUS analysis of disc-shaped specimens and the RPModel software was used for rectangular parallelepiped specimens.

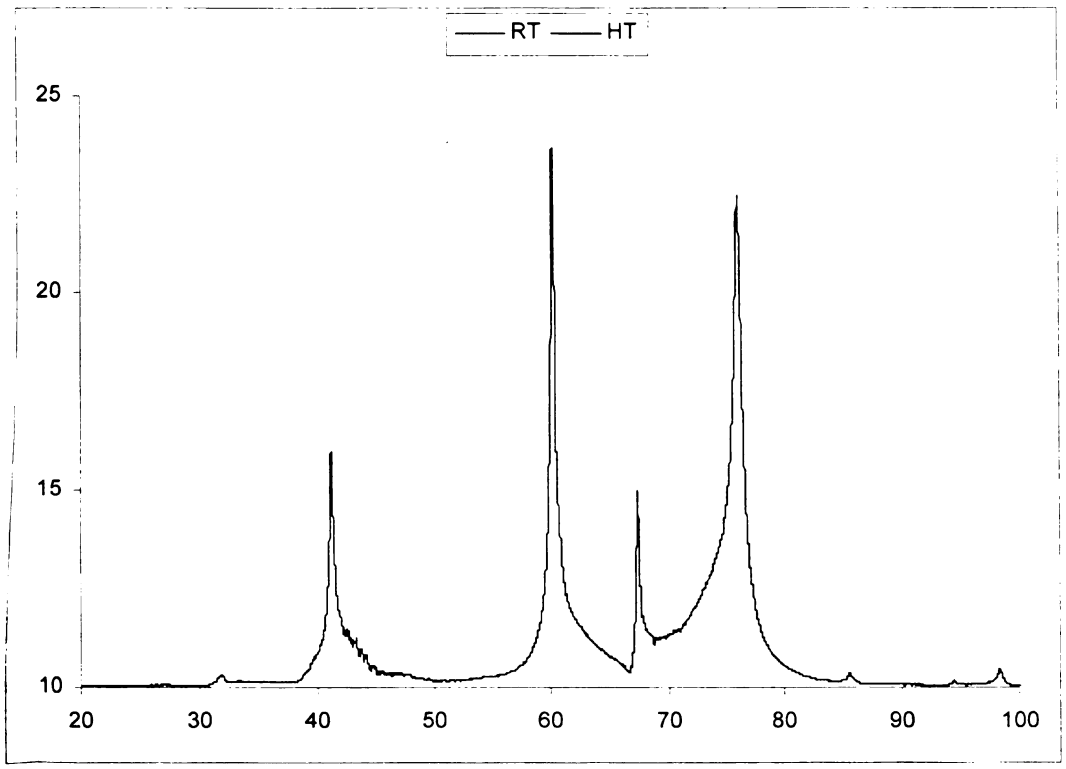

Figure 2.5.5. Example of a section of RUS spectrum data with distinctive peaks.

2.5.2.5. Resonant Ultrasound Spectroscopy Spectrum Data

When imparting the sinusoidal frequency sweep through the sample during testing the sample would respond to some frequencies more intensely than other, resulting in a peak. When the applied frequency matches one or more of the test materials resonant frequencies than the specimen would respond with a sharp, intense peak. Frequencies that did not match the materials frequency have relatively low intensities and could be negated in comparison to frequency matches. By locating the frequency peaks of the material after the RUS test, the resonant frequency of the material could be determined (Figure 2.5.5). A sample that happened to be incorrectly set on the transducers (transducers are in contact with the specimen face and not edges or corners) resulted in a decrease in the intensity of the resonant frequency peaks used to calculate the elastic moduli by dampening the transducers drive and pickup sensitivities [Migliori 1997].

2.5.2.6. RUS Analysis using RPModel

The RPModel software used the RUS frequency spectrum, the specimen's mass and dimensions to calculate the Young's modulus and Poisson's ratio. The RPModel program used the elastic constants c_{11} and c_{44} to help process the spectrum for the tested material. For the RPModel program an initial estimate of the materials theoretical Young's and Shear modulus were used to find c_{11} and c_{44}. With the LAST and LASTT materials, a spectrum was considered valid if there were between 20 and 40 distinctive acoustic resonance peaks to use with in the RPModel program. A mode of 40 peaks was chosen for RPModel [Migliori 1997].

A convergence rate of 0.5 was used with RPModel. A rate of convergence is the speed a sequence reaches its limit, and a rate of 1 or below was advised through the RUSpec manual. A larger rate of convergence (over 1) would cause the RUSpec program to overstep the materials resonant frequency minimum and improperly fit the analysis with the test data [Migliori 1997].

A polynomial order of 12 was used in RPModel. A polynomial order of 12 states that the highest exponential term calculated in the RPModel analysis will be of the twelfth degree. Once an RPModel frequency spectrum had been calculated, it was compared to the RUS spectrum. The comparison of the two spectrums resulted in a root mean squared (RMS) error between the calculated peaks and the peaks found during RUS. An RMS error under 0.3% for a given set of compared resonance peaks were accepted in the calculation of the elastic moduli [Migliori 1997].

2.6. Fracture testing

2.6.1. Biaxial Fracture Testing Ring-on-ring Introduction

Groups of up to 10 disc-shaped specimens at a time were thermally fatigued in the larger thermal fatigue chamber. The specimens were then fractured in a ring-on-ring configuration using a commercial testing machine (Model 4206 Instron Corporation, Norwood, MA) with a loading rate of 1 mm/minute (Figure 2.6.1.). The fracture strength, σ_f, was evaluated from the relationship [ASTM 1499]

$$\sigma_f = \frac{3F}{2\pi h^2}\left[(1-\nu)\frac{D_S^2 - D_L^2}{2D^2}(1+\nu)\ln\left(\frac{D_S}{D_L}\right)\right]$$

where F = the breaking load, h is the specimen thickness, ν = Poisson's ratio of the specimen, D_S = diameter of the support ring, D_L = the diameter of the loading ring and D = specimen diameter.

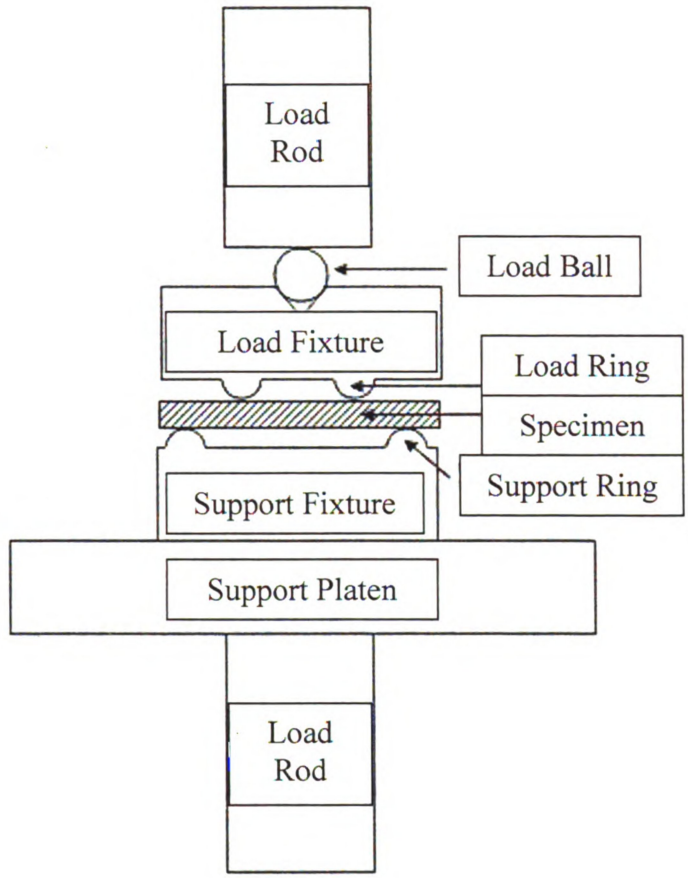

Figure 2.6.1. Schematic of the ring-on-ring apparatus used to perform the biaxial fracture testing. The ring-on-ring apparatus is used in a commercial testing machine (Model 4206 Instron Corporation, Norwood, MA) to perform biaxial flexural testing. The device consists of five separate parts working in sequence; the load rod and ball, load fixture, support fixture, support platen/rod, and the support gasket. (image by Fei Ren)

2.6.2. Overview of Biaxial Flexural Ring-on-ring Assembly

Fei Ren (Materials Science and Technology Division, Oak Ridge National Laboratory, Oak Ridge, TN 37831), the doctoral student initially tasked with testing the fracture strength of LAST and LASTT materials, drafted the plans for the ring-on-ring fixture used for biaxial flexural testing in this study, based on ASTM C1499 [ASTM 1499]. The Michigan State University Physics Shop fabricated the ring-on-ring loading fixture. The ring-on-ring apparatus used in loading LAST and LASTT large thermal fatigue samples during biaxial flexural testing was composed of a support gasket, load fixture, support fixture, and a load rod (Figure 2.6.2).

The support fixture, support gasket and load fixture were assembled as a ring-on-ring cage. The ring-on-ring cage housed the disk shaped specimen during testing. The cage also assisted in the alignment of the support ring and load ring on the specimen during loading using guide pins.

The ring-on-ring cage was loaded in an Instron machine with a load rod (Figure 2.6.3) during testing. The load rod and load fixture were designed to align during testing to distribute the applied load evenly throughout the load ring and onto the sample.

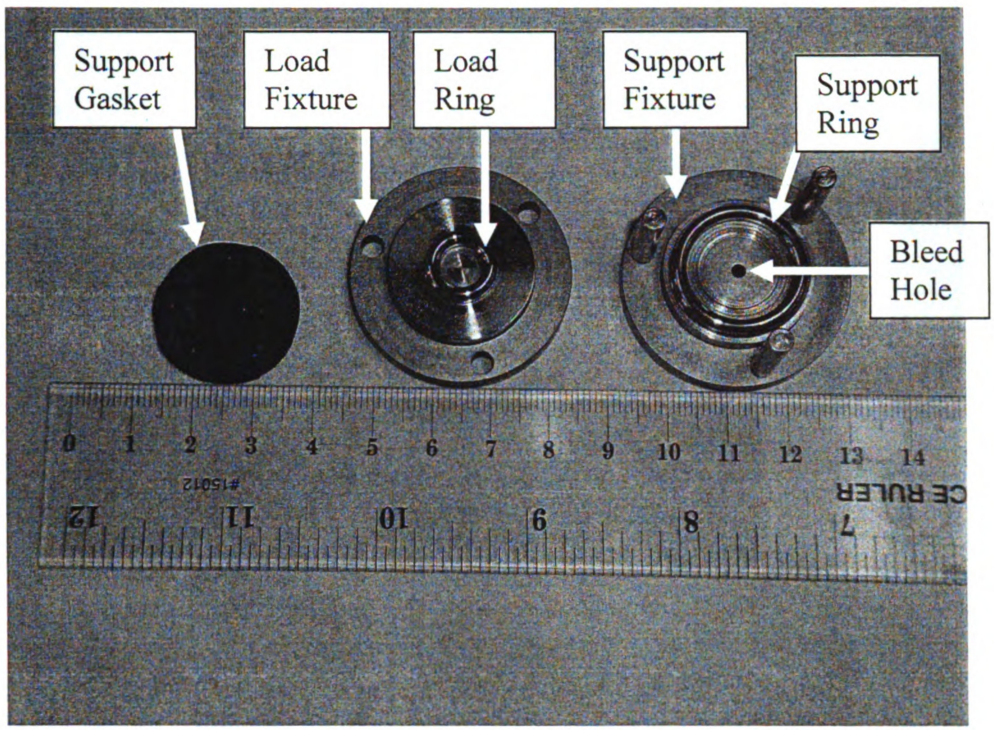

Figure 2.6.2. Ring-on-ring cage sections used to house the LAST and LASTT large thermal fatigue samples during biaxial flexural testing. This cage is composed of the support gasket, load fixture, and support fixture.

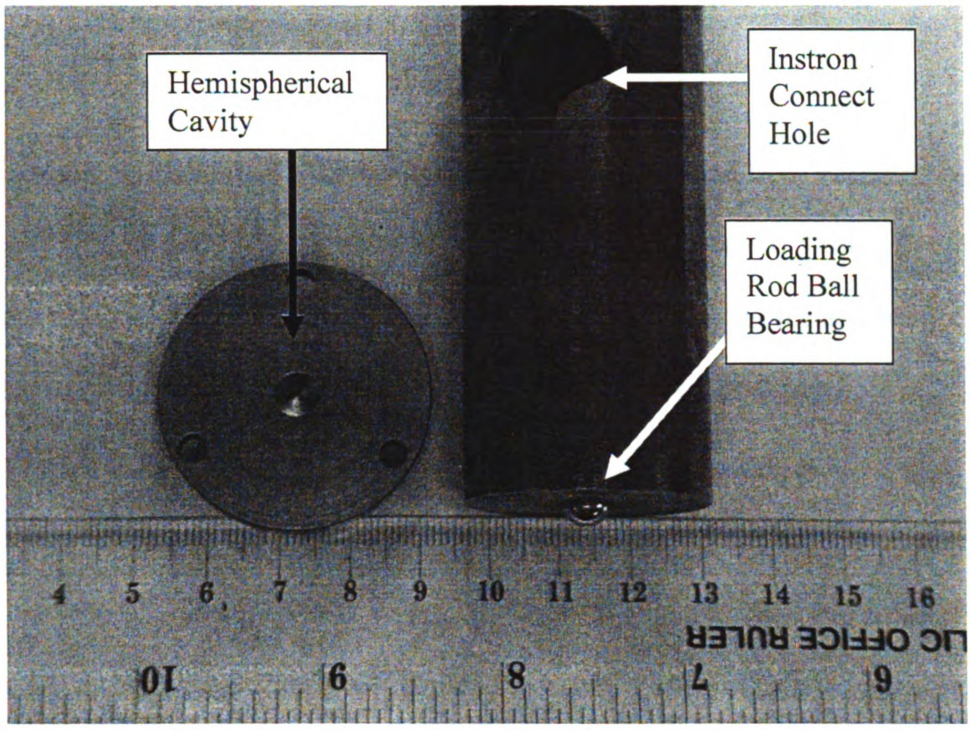

Figure 2.6.3. The load fixture top and load rod were designed to assist in the proper loading of the specimen during testing. The alignment of the hemispherical cavity and the ball bearing assisted in applying the loading force to the center of the cage, distributing the force evenly through the loading ring to the sample. This even spread of force is achieved by the ball bearing in the loading rod and the hemispherical cavity machined into the top of the load fixture. The hemispherical cavity will require the ball bearing to only apply force in a vertical axis, if there is any horizontal force then the ball bearing will continue to move to the bottom of the sphere with an applied horizontal force because of the low amount of friction between the two materials.

2.6.3. Ring-on-ring Support Fixture

The support fixture of the ring-on-ring fixture was milled from a single piece of mild steel. The support fixture base was 3.815 cm in diameter and 0.5 cm in height. A 2.5 cm diameter, 0.4 cm high cylindrical support ring platform was located between the fixture base and the ring (Figure 2.6.2 and Figure 2.6.4.). The support ring was 2.26 cm outer diameter, 0.26 cm in height and 0.26 cm thick. The face of the support ring, which contacted the specimen, had a rounded lip. The radius cross section of the support ring lip was between 0.13 cm and 0.39 cm [ASTM C-1499] (Figures 2.6.2 and 2.6.4.). In addition, a 0.25 cm air bleed hole was drilled through the support fixture to release any air that could be trapped in the cavity between the sample and the support ring bottom (Figure 2.6.2.). Three 0.4 cm diameter, 2.55 cm long guide pins were attached to the support fixture base equidistant from each other around the circumference of the support fixture base, 0.3275 cm from the outer perimeter of the base, Figure 2.6.4. The ROR support fixture guide pins were used to enhance stability and alignment between the load ring and support ring during biaxial flexure testing.

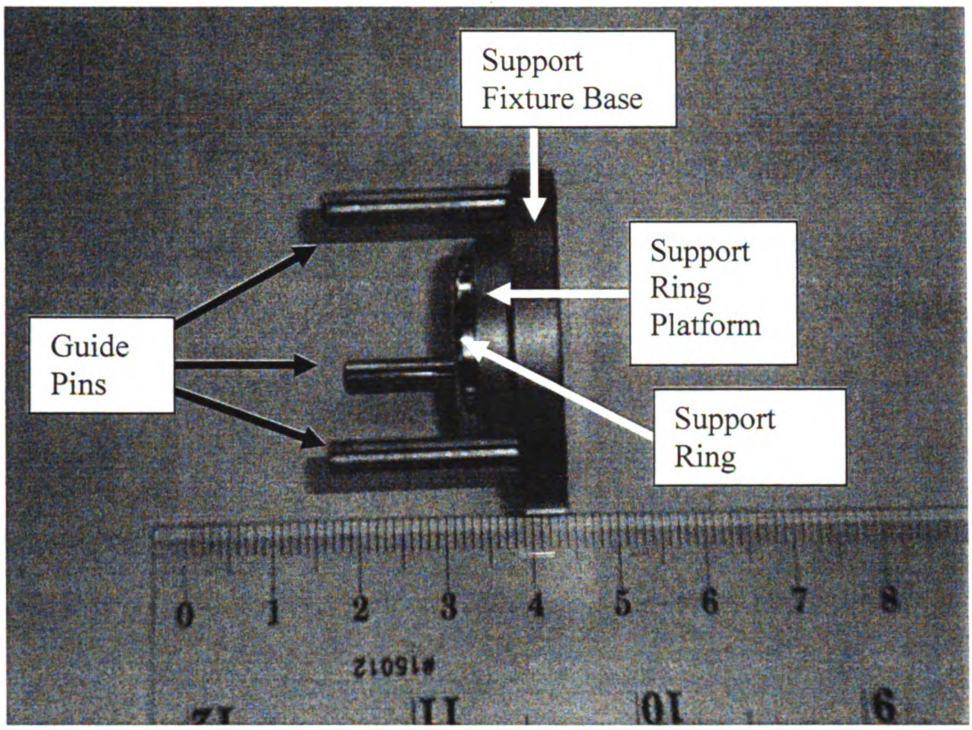

Figure 2.6.4. Ring-on-ring support fixture side view of the support fixture base, support ring platform, and the support ring. The ROR support fixture also had three guide pins in place to ensure stability and alignment between the load and support rings during testing.

2.6.4. Ring-on-ring Load Fixture

The load ring also was milled from a single piece of mild steel. The loading fixture base was 3.815 cm in diameter and 0.53 cm in height. A 2.5 cm diameter, 0.375 cm high cylindrical load ring platform was located between the fixture base and the ring (Figure 2.6.2 and Figure 2.6.5.). The outer diameter of loading ring was 1.245 cm, 0.265 cm in height and 0.26 cm thick. The face of the support ring, which contacted the specimen, had a rounded lip. The radius cross section of the load ring lip was between 0.13 cm and 0.39 cm [ASTM C-1499] (Figures 2.6.2. and 2.6.5.). Three 0.41 cm diameter holes were drilled through the loading fixture base equidistant from each other around the circumference of the base, 0.3275 cm from the edge of the base perimeter (Figure 2.6.5.). The ROR loading fixture holes were used in con junction with the support ring guide pins to ensure stability and alignment between the load and support rings during testing.

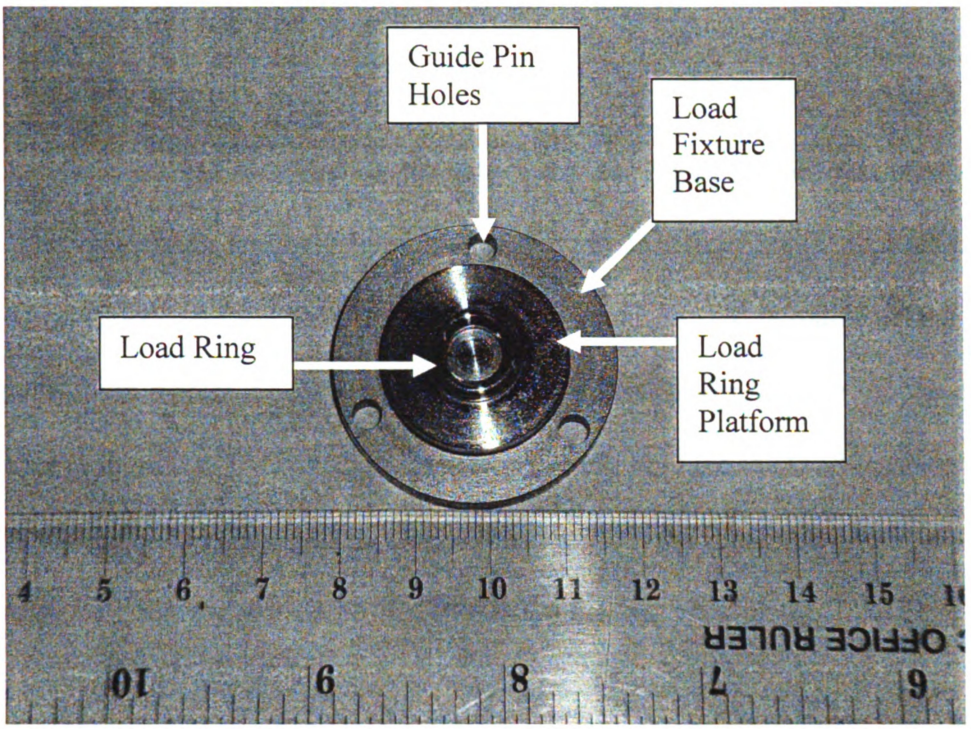

Figure 2.6.5. Load ring showing the three holes in which the guide pins use to align the load fixture and support fixture.

2.6.5. Ring-on-ring Load Rod

A mild steel load rod (manufactured by the MSU Physics Shop) was used in loading the ring-on-ring specimen apparatus with an Instron machine (Model 4206 Instron Corporation, Norwood, MA). The load rod was 3.385 cm in diameter and 7.5 cm in length. A 2 cm diameter hole was drilled through the cylinder, 2 cm from one edge of the cylinder (Figure 2.6.3.). The 2 cm hole was used to hold the load rod in place within the Instron machine. On the load rods opposite side from the Instron connect hole a 0.65 cm diameter ball bearing was embedded into the end of the rod, leaving 0.325 cm exposed (Figure 2.6.3.).

The ball bearing in the end of the load rod mated with a hemispherical cavity located in the loading fixture, on the opposite side of load ring. The hemispherical cavity was 3 cm in diameter x 3 cm in depth, located in the center of the loading ring fixture (Figure 2.6.3.). The load fixture top and load rod were designed to assist in the proper loading of the specimen during testing. The alignment of the hemispherical cavity and the ball bearing assisted in applying the loading force to the center of the cage, distributing the force evenly through the loading ring to the sample. The even spread of force is achieved by the ball bearing in the loading rod and the hemispherical cavity machined into the top of the load fixture. The hemispherical cavity required the ball bearing to only apply force in a vertical axis, if there was any horizontal force then the ball bearing would continue to move to the bottom of the sphere with any applied horizontal force because of the low amount of friction between the two materials.

2.6.6. Ring-on-ring Support Gasket

A 0.1 cm thick, 2.5 cm diameter support gasket of abrasion-resistant natural latex rubber (McMaster-Carr, 85995K21, Santa Fe, CA) was placed between the specimen and the support ring to reduce contact stresses and friction (Figure 2.6.6.). Since the ring-on-ring testing was performed on samples with as received surfaces, it could not be assured that the specimens' surfaces were within flatness tolerances. Non-flat specimens had the possibility of point or line contact stresses occurring during testing. The uneven loading caused by point and line stresses would lead to fractures in the specimen that were not true equibiaxial strengths [ASTM 1499].

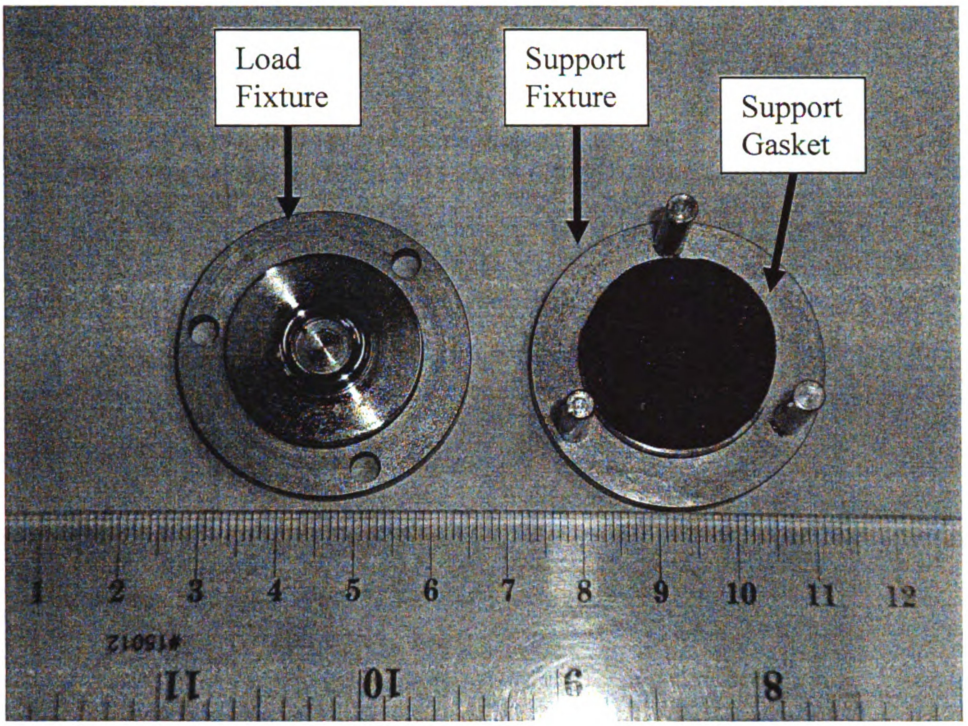

Figure 2.6.6. Ring-on-ring support fixture with the support gasket placed over the support ring to decrease the friction between the sample and the support ring during loading which could lead to low or invalid fracture strengths.

2.6.7. Ring-on-ring Sample Teflon Tape

Within the ring-on-ring support fixture a large thermal fatigue chamber specimen was set in place on top of the gasket in the center of the fixture (Figure 2.6.7). To reduce friction between the loading ring and the sample a Teflon® PTFE tape 25.4 cm diameter disc (McMaster-Carr, 7801A34, Santa Fe, CA) was placed on the sample (Figure 2.6.7.). The Teflon tape disc also helped keep the sample fragments together after fracture testing was complete.

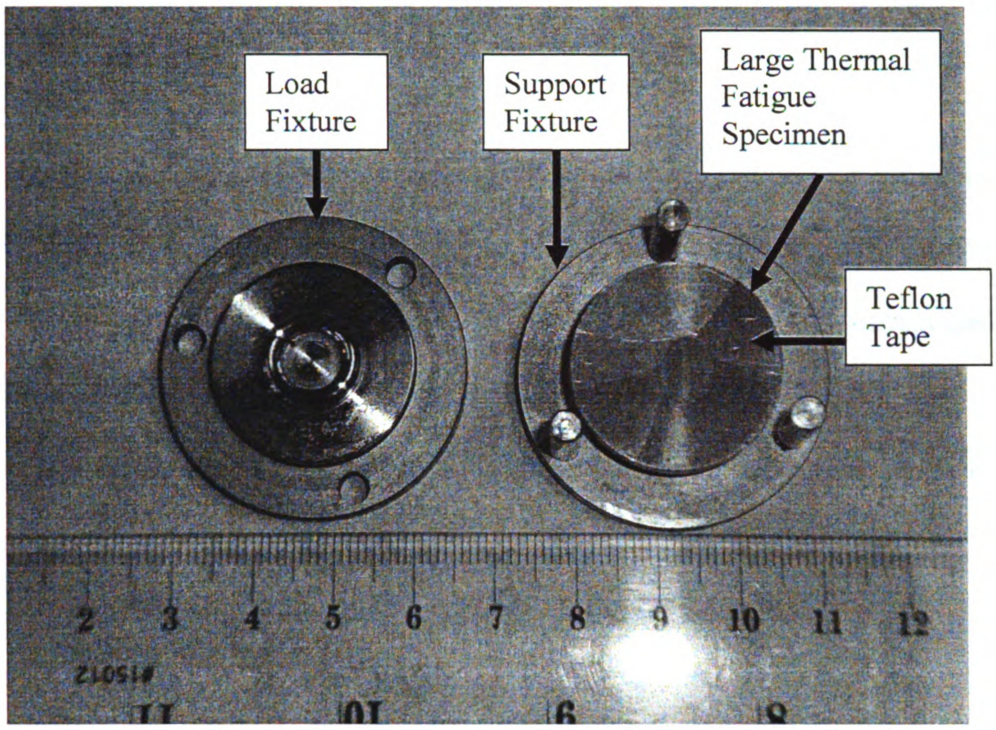

Figure 2.6.7. Ring-on-ring support fixture and gasket with a large thermal fatigue chamber specimen set in place on top of the gasket in the center of the fixture. This image is a succession of Figure 2.6.5. prior to testing.

2.6.8. Ring-on-ring Cage Assembly

Once the Teflon taped sample and support gasket were centered on the support ring the guide pins were lined up with the guide pin holes of the loading fixture, with the loading ring facing the sample. The large thermal fatigue specimen and support gasket were sandwiched between the aligned support and load rings (Figure 2.6.8.). The specimen was centered equidistant from each support leg on the support fixture, allowing for the specimen to be relatively centered on the support ring within the loading apparatus.

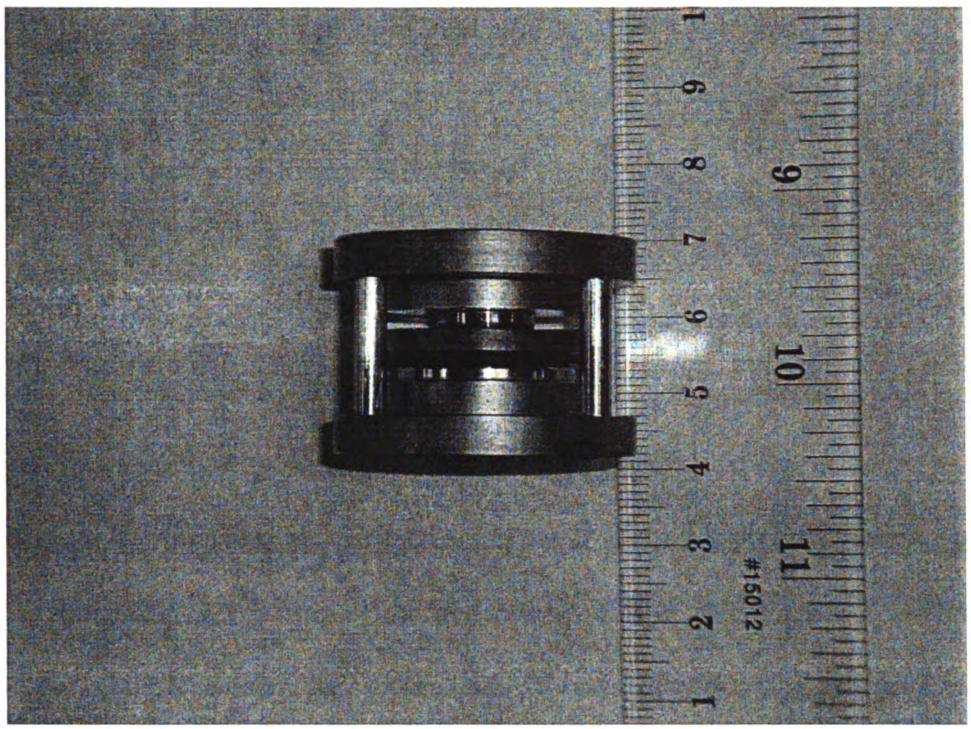

Figure 2.6.8. Ring-on-ring cage setup with a large thermal fatigue specimen in place and support gasket sandwiched between the aligned support and load rings. The specimen was centered equidistant from each support leg on the support fixture, allowing for the specimen to be relatively centered within the loading apparatus.

2.6.9. Ring-on-ring Cage Assembly Loading in the Instron Machine

2.6.9.1. Ring-on-ring Instron Software

The Instron operation program used for ring-on-ring testing was Bluehill Instron Version 1.1 (Instron Bluehill Software, Norwood, MA). A compression rate of 1 mm/minute was used during the biaxial flexural testing. Ring-on-ring testing generally consisted of ten samples that had been thermally cycled a predetermined number of times (up to 200 thermal cycles) before being fractured. A new data folder was created on the computer for each test to save the loading data for each specimen (the peak load before sample fracture in Newtons, and the displacement of the loading rod in millimeters) acquired from the Bluehill software.

2.6.9.2. Ring-on-ring Cage Loading in Instron

The ring-on-ring cage was centered on the Instron machines compression plate. The load rod was installed into the Instron loading ram and held in place with a 2 cm diameter, 10 cm long cylinder that fit through the load rod fixture hole (Figure 2.6.9.). The Instron machine and Instron computer were turned on. Once the computer was ready, the Bluehill Instron Version 1.1 program was opened. A preprogrammed test protocol labeled ROR-BFT (Fei Ren) was selected in the Bluehill software. A test protocol in the Bluehill software was a programmed set of guidelines that the Instron machine would follow during testing; loading, compression, compression rate (See Appendix C for a listing of the ROR-BFT test protocol used in this study). The ROR-BFT test protocol used during testing was set to compression with a loading rate of 1 mm/minute. After the test protocol was chosen a folder on the computer's desktop was selected to save the data collected from the Instron during testing. The Bluehill program was then ready to begin the ROR-BFT test.

The load rod was lowered toward the ring-on-ring cage at the Instron low speed setting, which was engaged by a switch on the machine. Lowering the load rod to the cage at a low speed helped to prevent a misalignment of the load rod and loading fixture or pre-loading of the sample. The load rod and the hemispherical cavity of the loading fixture were aligned by hand as the gap between the fixtures closed. Once the load rod ball began to enter the hemispherical cavity of the loading fixture, the ring-on-ring cage was moved in a circular motion on the compression plate while the load rod was still

lowering. The rotational movement of the ring-on-ring cage caused the Hemispherical cavity walls to contact the load ring ball bearing.

As the distance between the ball bearing and the bottom of the cavity decreased the cage movement was restricted. The rotational movement of the cage helped to align the cage and the load rod, as well as estimating the distance between contact of the ball bearing and the cavity floor. The load rod was lowered to the loading fixture until the ring-on-ring cage could no longer move, but without placing a significant load onto the specimen.

After the ring-on-ring cage and load rod were positioned properly within the Instron machine the Bluehill program was initiated. The program, when initiated the loading of the ring-on-ring cage. The loading of the specimen was stopped manually within the Bluehill program once the specimen had fractured. The Bluehill program produced a load/ displacement graph, as the specimen was loaded. The Bluehill graph helped to determine when the sample fractured, due to an instantaneous decrease in the loading on the sample once it had fractured. After the sample had fractured and the Bluehill program had been stopped, the Instron loading ram was raised off of the ring-on-ring cage. The sample was removed from the cage and another sample placed into the cage, this repeated until all specimens were tested.

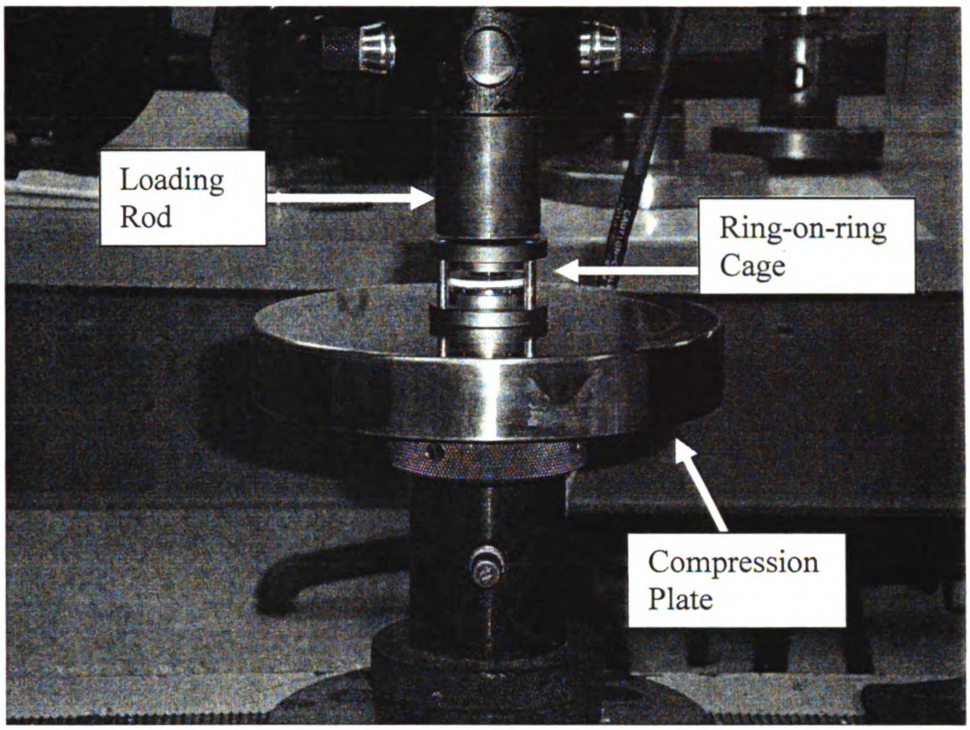

Figure 2.6.9. Ring-on-ring cage and loading rod positioned and centered on a compression plate within the Instron machine and ready for biaxial flexural testing.

2.6.10. Post Biaxial Flexural Testing Valid and Invalid Fractures

The fracture surface of each specimen was visually inspected post-fracture to determine whether or not the test was valid, since according to the ASTM standard for equibiaxial fracture, "for a properly conducted equibiaxial test, fracture should typically occur on the tensile surface within the diameter of loading ring" [ASTM 1499]. Thus, only fractures that initiated between the support and loading ring area were considered as valid tests (Figures 2.6.10-2.6.15.).

After the fracture test, an impression of the loading ring was present on the Teflon tape, which had been affixed to each of the ring-on-ring specimens. The impression from the loading ring was present on the Teflon tape helped to determine where the crack initiated.

The three types of valid fracture crack patterns are categorized by ASTM 1499 as: (1) low energy –low strength failure (Figures 2.6.10-2.6.11), (2) medium energy- medium strength failure (Figures 2.6.12-2.6.13), and (3) high energy- high strength failure (Figures 2.6.14-2.6.15). If a crack initiated from an edge flaw, such as a pre-existing crack or surface damage, then the fracture was deemed invalid (Figure 2.6.16.). The crack patterns shown in digital photographs given in this thesis as Figures 2.6.10 – 2.6.17, correspond very well to the set of schematic ring-on-ring test crack patterns given on page 767 of ASTM 1499, including the details of the crack patterns and the sorting of the test results into the relative levels of low, intermediate and high fracture strength. Fractures that traversed the diameter of the specimen, known as diametrial cracks, were most commonly due to internal damage or edge flaws likely acquired during

manufacturing (Figure 2.5.17.). Diametrial fractures occurred at low loads and were considered invalid as well [ASTM 1499].

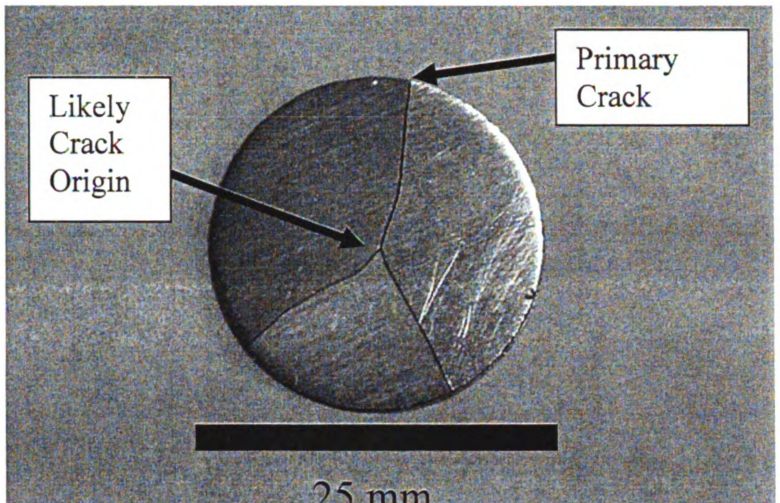

Figure 2.6.10. LASTT specimen P14-19 (as-received) showing a valid low energy ring-on-ring fracture. (47 MPa).

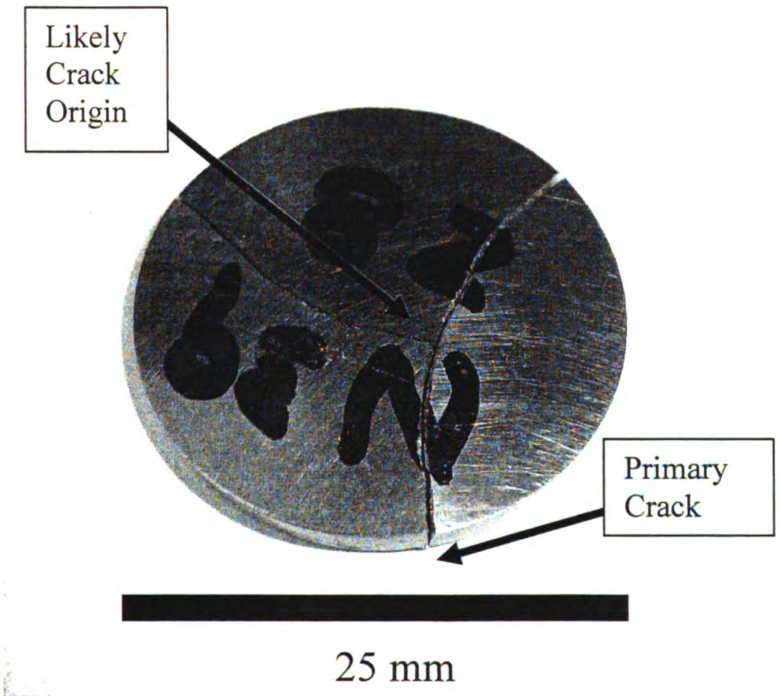

Figure 2.6.11. LAST specimen N39-28 (as-received) showing a valid low energy ring-on-ring fracture. (9.1 MPa).

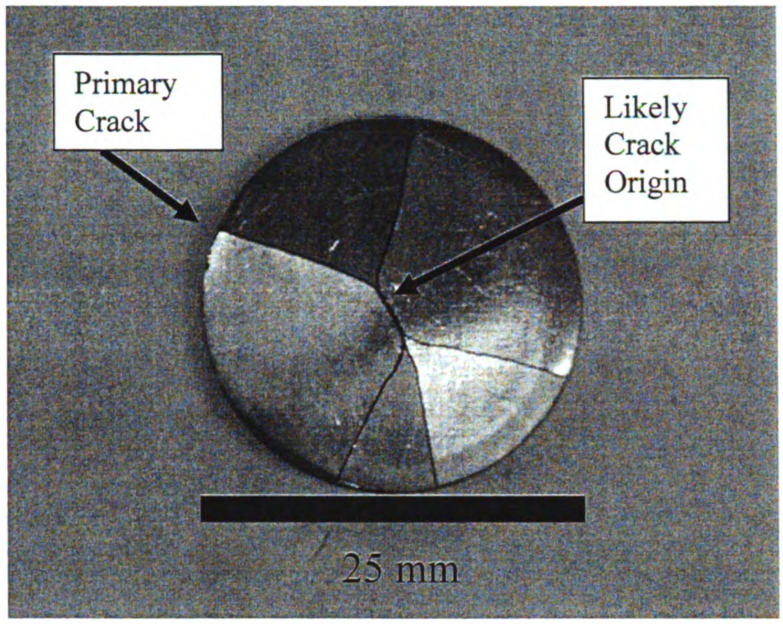

Figure 2.6.12. LASTT specimen P15-60 (30 cycles) showing a valid medium energy ring-on-ring fracture. (32.2 MPa).

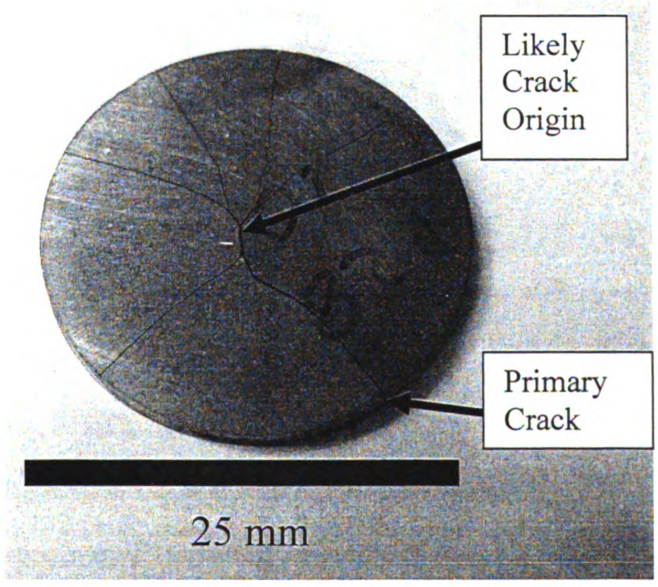

Figure 2.6.13. LASTT specimen P28-10 (60 cycle) showing a valid medium energy ring-on-ring fracture. (33.7 MPa).

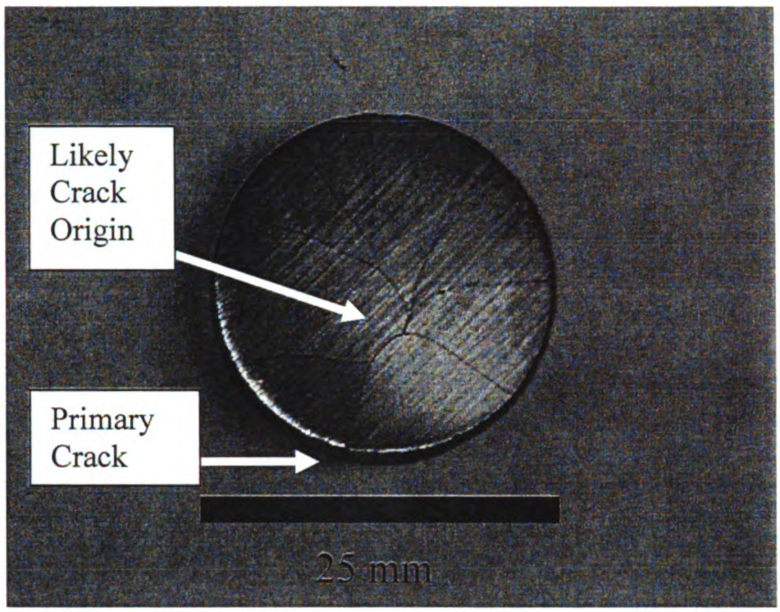

Figure 2.6.14. LASTT specimen P15-34 (as-received) showing a valid high energy ring-on-ring fracture. (38.1 MPa).

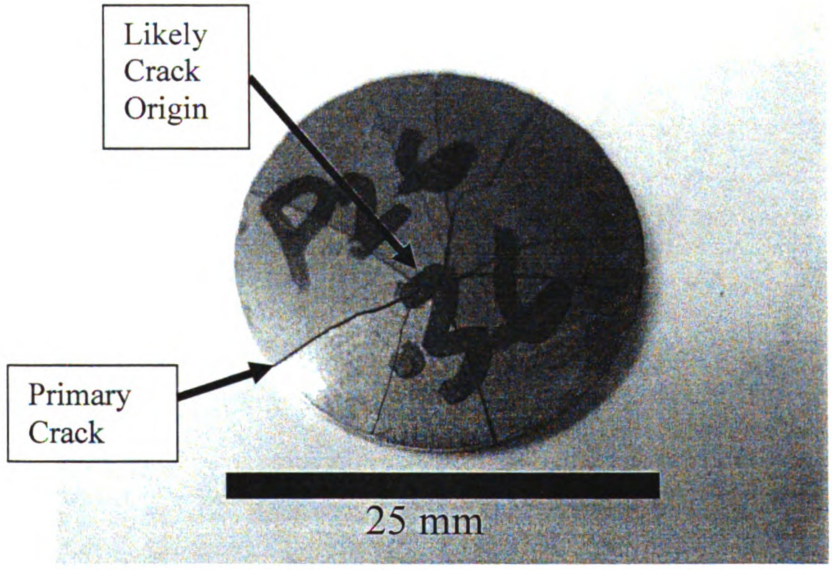

Figure 2.6.15. LASTT specimen P26-36 (120 cycles) showing a valid high energy ring-on-ring fracture. (47.8 MPa).

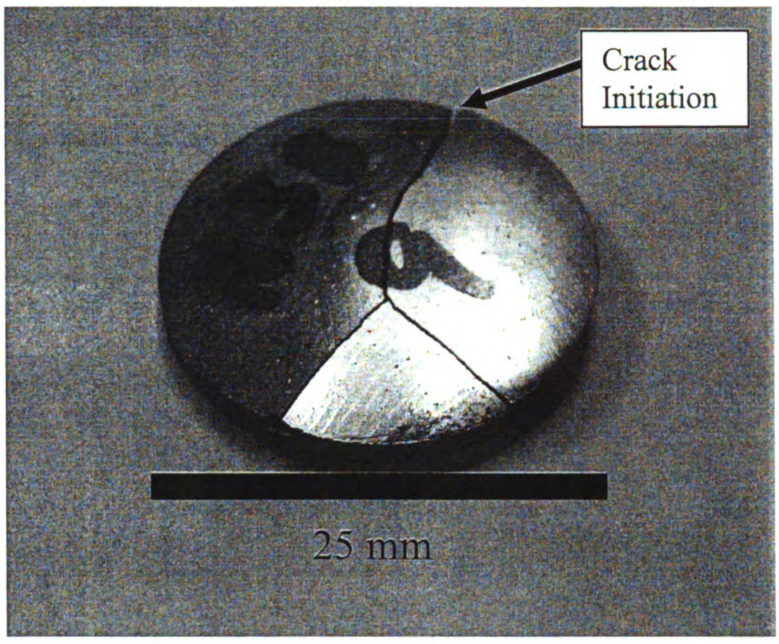

Figure 2.6.16. LASTT specimen N38-9 (as-received) showing an invalid ring-on-ring fracture. The crack most likely propagated through the sample because of an edge flaw shown with the black arrow.

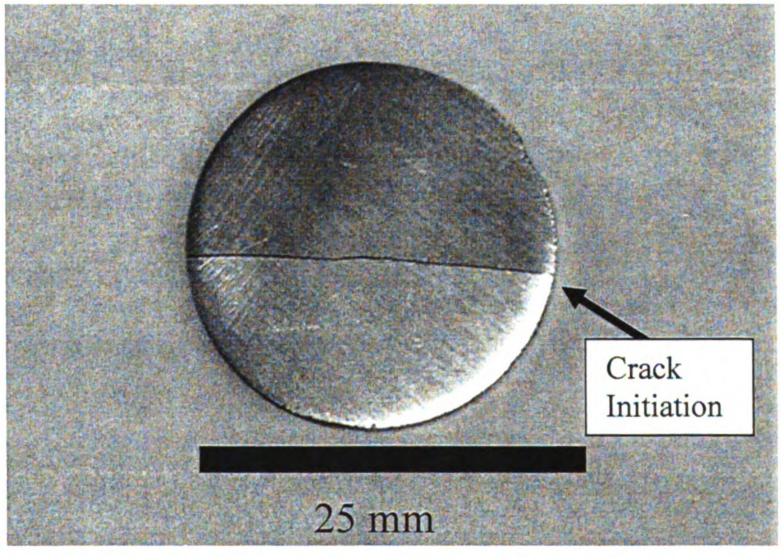

Figure 2.6.17. LASTT specimen P14-26 (as-received) showing an invalid ball-on-ring fracture. The crack most likely propagated through the sample because of an edge flaw shown with the black arrow.

3.1.1. Grain Size of LAST and LASTT

The grain size of the LAST and LASTT specimens was obtained from scanning electron microscopy micrographs of fracture surfaces of as-received specimen (All SEM images were taken by Jennifer Ni, analysis performed by Andrew Q. Morrison). The specimens used for grain size calculations were disk-shaped samples that had been previously fractured during biaxial flexural ring-on-ring testing. The grain sizes of the disks were calculated by performing the line-intercept method on the SEM micrographs. A stereographic projection factor of 1.5 was used to convert the average intercept length to an average grain size.

The average grain size average for the LAST as-received specimen was 31 microns (Table 3.1.1.1.). The LAST samples viewed with the SEM were had a relatively unimodal grain size. Though the average grain size of the LAST material was 31 microns/grain, grains from 10-100 microns across were observed (Figure 3.1.1.1a and Figure 3.1.1.1b).

The grain size distribution was bimodal for the as-received LASTT specimens (Figure 3.1.1.2a and Figure 3.1.1.2b). The LASTT samples had large grains of 16 microns across in a matrix of much smaller grains of 3.4 microns.

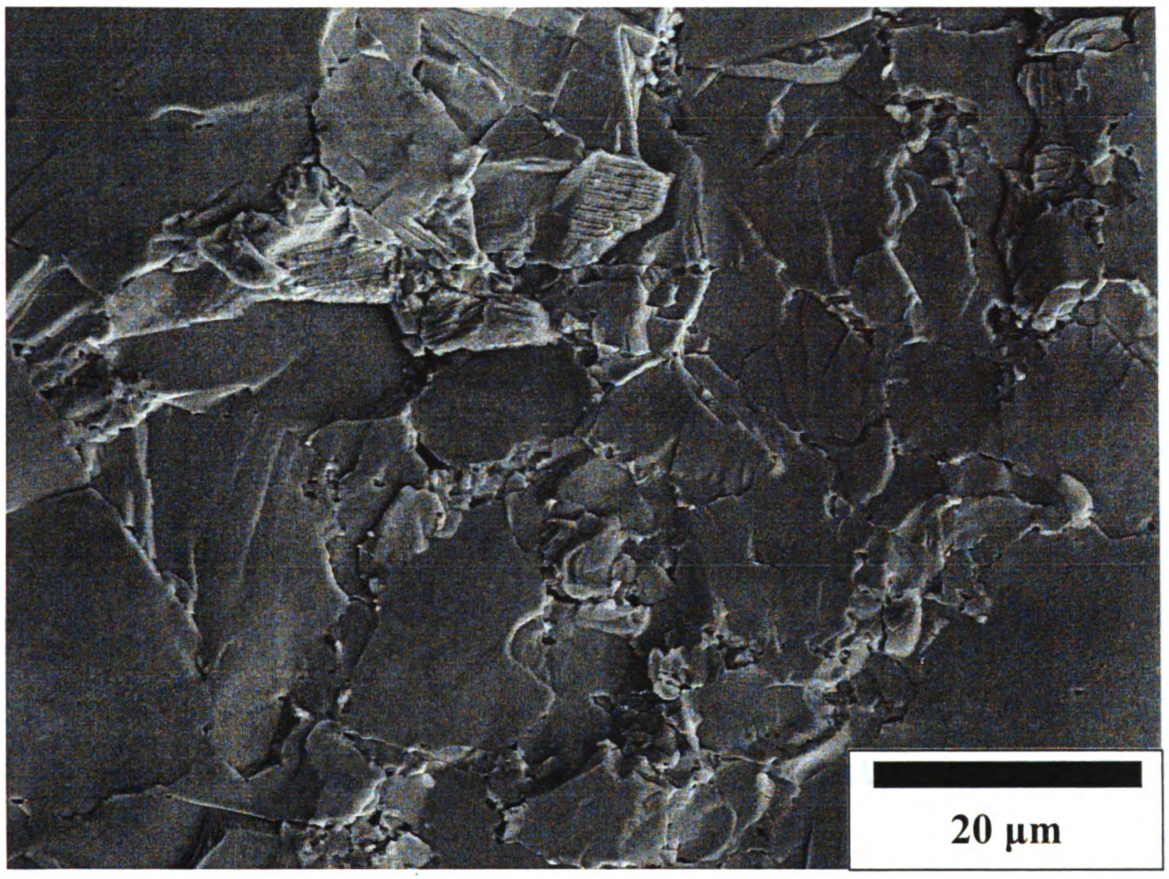

Figure 3.1.1.1a. LAST as-received specimen N39-10 fracture surface using a scanning electron microscope used to determine the average grain size (31.35 micron/grain) through the line-intercept method.

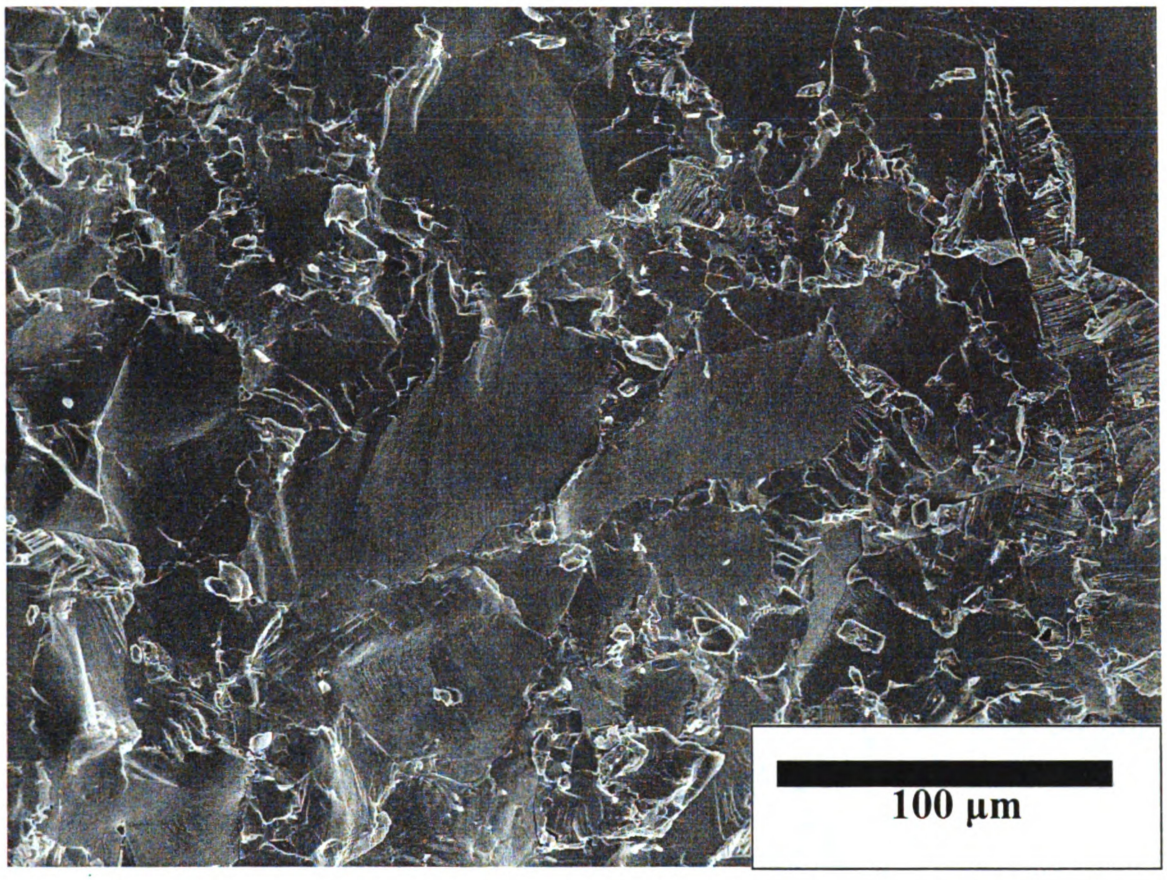

Figure 3.1.1.1b. LAST as-received specimen N39-15 fracture surface using a scanning electron microscope used to determine the average grain size (31.35 micron/grain) through the line-intercept method.

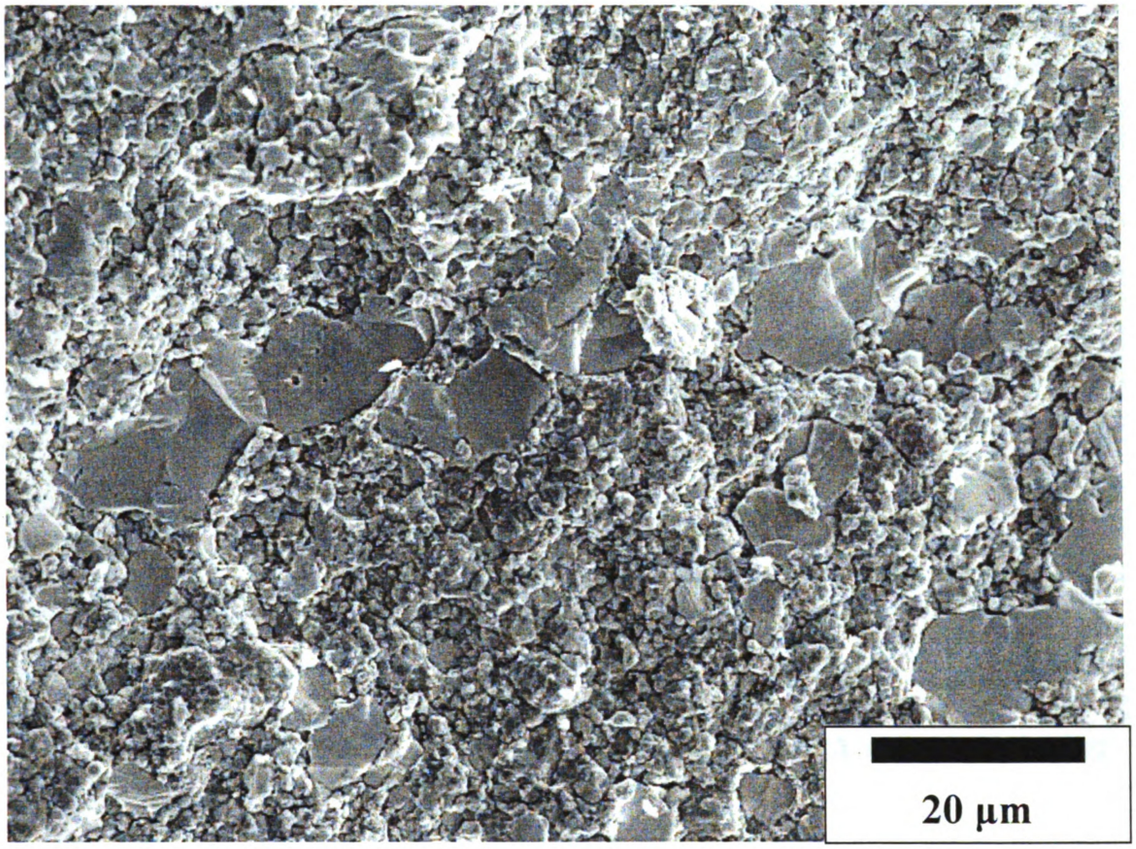

Figure 3.1.1.2a. LASTT as-received specimen P28-31 fracture surface using a scanning electron microscopy image of the fracture surface. This shows the bimodal grain size found in the LASTT material of larger grains (15.57 microns/grain) in a matrix of much smaller grains (3.375 micron/grain).

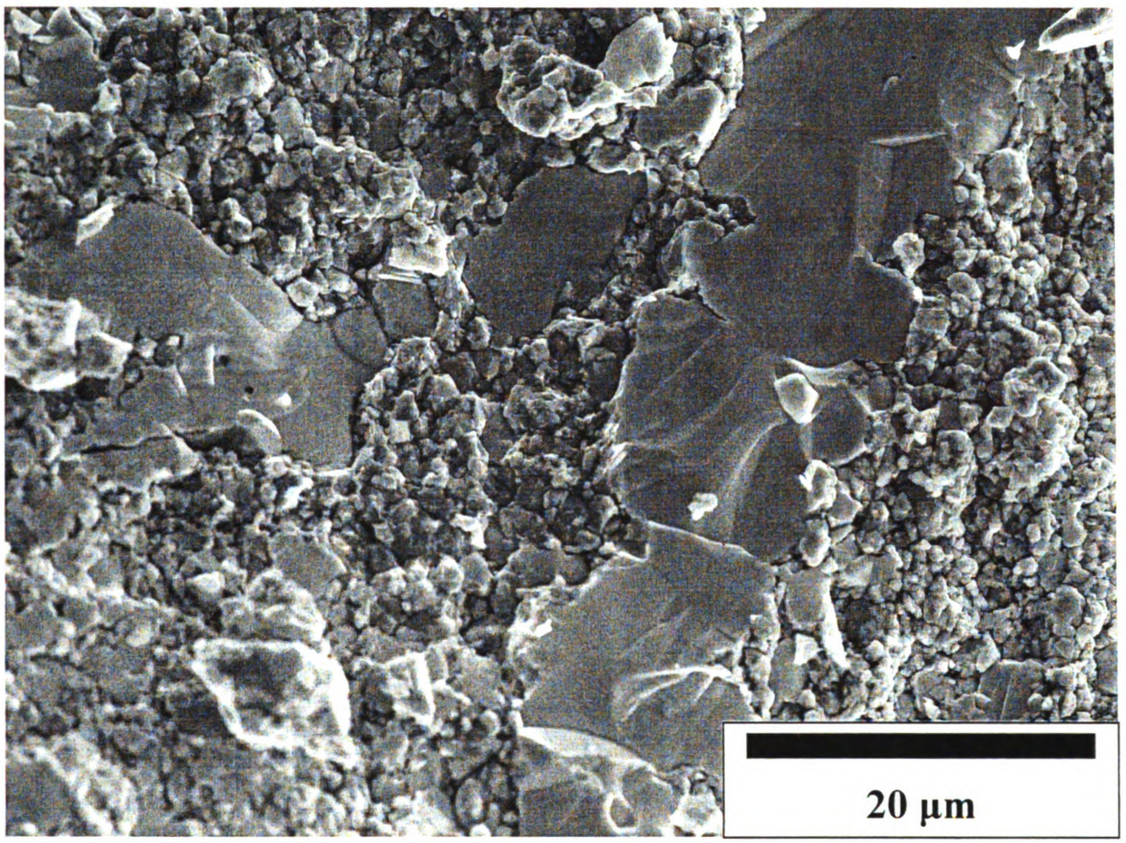

Figure 3.1.1.2b. LASTT as-received specimen P28-30 fracture surface using a scanning electron microscopy image of the fracture surface. This shows the bimodal grain size found in the LASTT material of larger grains (15.57 microns/grain) in a matrix of much smaller grains (3.375 micron/grain).

Table 3.1.1.1. The average grain size for as-received LAST and LASTT specimen determined using scanning electron microscope images and the line-intercept method. It was determined that the LAST samples had a unimodal grain size, where the LASTT tended to show a bimodal grain size.

Specimen	Grain Size Average (microns/grain)
LAST	31.35
LASTT (small)	3.375
LASTT (large)	15.57

3.1.2. LAST Surface Inclusions and Pitting

All as-received and thermally cycled reformulated LAST specimens examined microscopically and with the unaided eye showed surface inclusions (Figure 3.1.2.1.). The inclusions were shown to be disjointed regions of Silver and Antimony-Tellurium rich regions within the LAST matrix. The surface inclusions examined were typically 50-70 microns in diameter, but ranged from 20-200 microns across. However, no inclusions were observed on any of the LASTT specimen surfaces that were examined microscopically.

Following the thermal cycling of the LAST specimens, surface pitting was noticed on both (i) the surfaces of the plate-shaped LAST specimens used in the small thermal fatigue chamber for elastic moduli testing and (ii) the disk-shaped specimens used in the large thermal fatigue chamber for fracture testing (Figure 3.1.2.2.). Pits with diameters of 100 microns or larger were seen on the surface of the specimens and appeared to be homogeneously distributed over both the hot and cold faces of the thermally cycled specimens (Figures 3.1.2.3a and 3.1.2.3b). The pitting on the disk and plate LAST specimens was first noticed by unaided visual inspection of the surface as early as 20 thermal cycles. The surface pits had raised surface perimeters that were felt when handling the samples during testing.

The number of thermal cycles required for the on set of the surface pitting was not known or why the pits developed during the thermal fatigue testing of the LAST specimens. The initial hypothesis was that the pitting was caused by the spalling of the inclusions from the surface of the LAST specimens, starting between 10-20 thermal

cycles. To determine the origin and progression of the surface pitting, two LAST plate specimens (N39-46 and N39-49) were selected to be thermally cycled and visually inspected. Using the small thermal fatigue chamber, both LAST specimens were thermally fatigued where one thermal fatigue cycle was performed at a time. After each thermal cycle, the specimens were removed from the chamber, observed by optical microscopy and then thermally cycled again for a total of 20 thermal fatigue cycles.

For both LAST specimens N39-46 and N39-49, as the number of thermal fatigue cycles increased (i) the number of surface pits increased and simultaneously (ii) the number of inclusions decreased (Figure 3.1.2.4a and 3.1.2.4b). The inclusions and pits were counted from three randomly selected areas of each sample for each cycle of the thermal fatigue cycling. The total numbers of surface inclusions from the three areas were added together, to obtain a total number of surface pits for each cycle. The total number of surface pits and surface inclusions were divided by three to give an average for each of the thermal fatigue cycles. For samples N39-46 and N39-49, the average inclusion and pit count were summed together for each thermal cycle. The sum of the inclusion and pit count versus the cumulative number of thermal cycles showed that the sum stayed relatively constant with the increase in thermal cycling (Figure 3.1.2.4c). The constant sum of the inclusion/pit count indicated that there was a correlation between the pits and inclusions. Thus it appeared that the surface pits formed as a result of spalling of the inclusions off the specimen surface during thermal cycling.

Optical micrographs of the specimens taken after each thermal cycle support the concept that the surface pitting occurred by the spalling of surface inclusions (Figures 3.1.2.5a – 3.1.2.5f). The as-received specimens showed inclusions but no surface pitting

(Figure 3.1.2.5a). For the first two or three thermal cycles, there was little change in the specimen surfaces but after five thermal cycles surface pitting appeared (Figure 3.1.2.5b). As the number of thermal cycles increased to 10, the number density of surface pits increased (Figure 3.1.2.5c). Also, after 10 thermal cycles, microcracking occurred near the inclusion. (A microcracked region and an associated inclusion is enclosed by the black circle in Figure 3.1.2.5c). In a higher magnification view of the region, black arrows point to microcracking near the inclusion (Figure 3.1.2.5d). Damage continued to evolve at 12 and 15 thermal cycles (Figures 3.1.2.5e and 3.1.2.5f).

In order to identify the elemental chemical composition of the inclusions, Energy Dispersive X-ray Spectroscopy (EDS) elemental maps were collected for selected inclusions and the area surrounding the inclusion on the surface of the as-received specimen N38-10. The elemental maps (Figures 3.1.2.6a- 3.1.2.6e) indicate that the inclusion was partitioned into sub-regions of different chemical compositions. For example, the EDS analysis shows that for the inclusion shown in Figure 3.1.4a, there is an area rich in silver and poor in all other elements (Figure 3.1.2.6b) as well as a disjoint region in the same inclusion that was rich in antimony but poor in the other elements (Figure 3.1.2.6c). For the inclusion examined, the entire inclusion was lead poor (Figure 3.1.2.6d) but there were regions within the inclusion that were Te-rich (Figure 3.1.2.6e). It is not clear why these phase-segregated regions occurred in the LAST specimens, but no inclusions were observed in the LASTT.

It was assumed that the surface inclusions were caused in the LAST materials during powder processing. The inclusions are possibly partially reacted phases of the initial powders. Again the inclusions were shown to be disjointed regions of Silver and

Antimony-Tellurium rich regions within the LAST matrix. The inclusions may have occurred during mechanical alloying of the raw powders in a high-energy ball mill. The initial lead, silver, telluride and antimony powders are loaded together into the ball mill and the increased friction from milling causes the powders to react. As the powder is milled the increased friction causes the powders to weld and fracture repeatedly until the reaction is completed or the milling is stopped. It is assumed that the inclusions resulted from premature milling which left un-reacted powders in forms of inclusions.

Given that the phase-segregated regions occur, the differing composition within the inclusions likely lead to differing local thermal expansion coefficients. The thermal expansion coefficient of the inclusion would likely be different than that of the matrix. During heating and cooling, these differing thermal expansions would generate mechanical stresses that could lead to cracking near the inclusion and a subsequent spalling off of the inclusions to form the surface pits observed in thermally cycled LAST specimens.

In the thermally cycled LAST specimens, microscopic examination shows that populations of smaller inclusions (generally smaller than 100 microns across) are still intact after thermal cycling. This is also consistent with microcracking due to thermal expansion mismatch (TEA). For a given level of thermal expansion mismatch, there is a critical inclusion size below which microcracking is not induced by thermal expansion mismatch [Clevland 1978, Davidge 1968].

The Young's modulus and Poisson's ratio were relatively constant as a function of thermal cycling, which implies that the average microcrack "size" and number density

did not change appreciably as a function of the thermal fatigue. The effects of the specimen inclusions on the elastic moduli will be discussed further in Section 3.2.

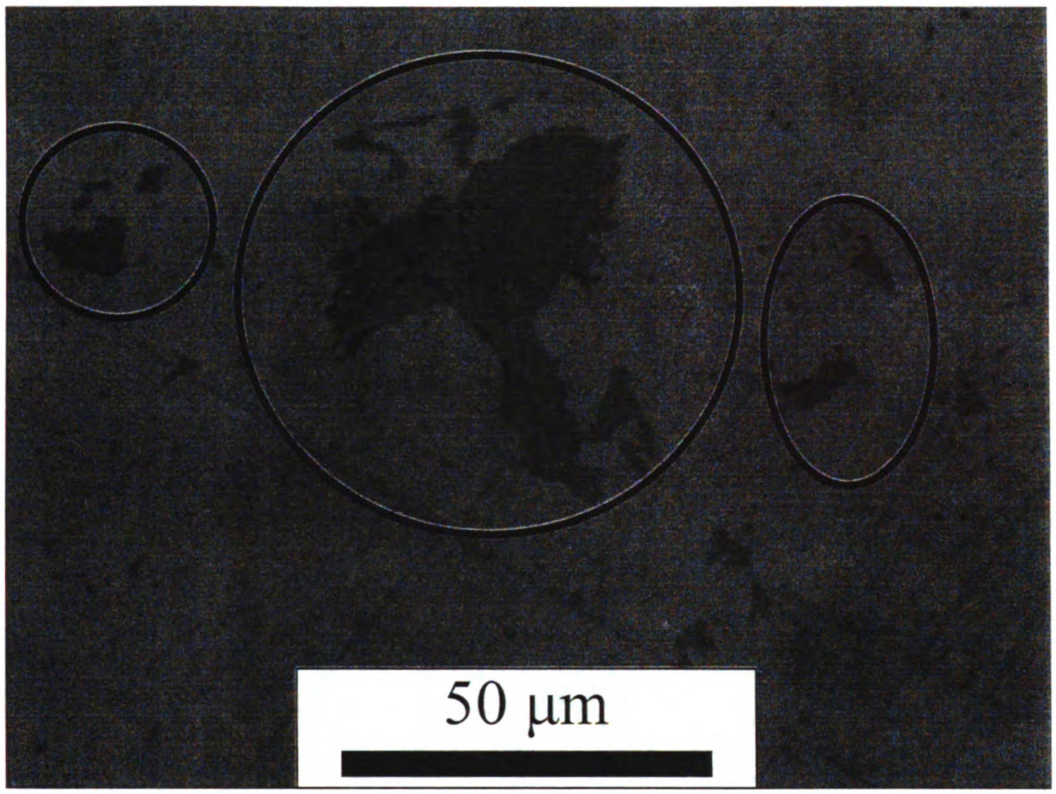

Figure 3.1.2.1. SEM backscattered electron image of inclusions in as-received (not thermally cycled) LAST specimen N38-10 of surface inclusions (black ovals). As was the case for other as-received LAST specimens, no surface pits are evident on the as-received specimen surface.

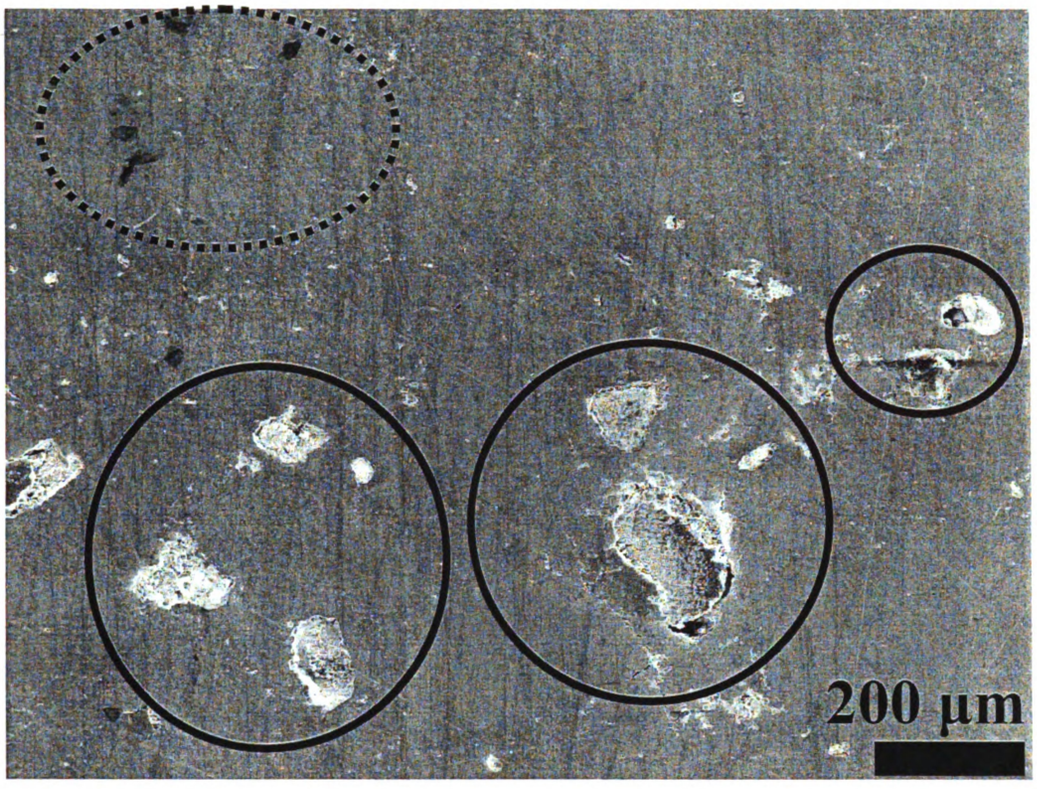

Figure 3.1.2.2. SEM secondary electron images of surface pitting in LAST specimen N38-9 after thermal cycling in the large specimen chamber for 150 cycles. The pits (dashed circles) in this micrograph have an average diameter of about 150-200 microns. In addition, small, intact inclusions are also visible on the surface that are as large as approximately 50 microns across (black oval).

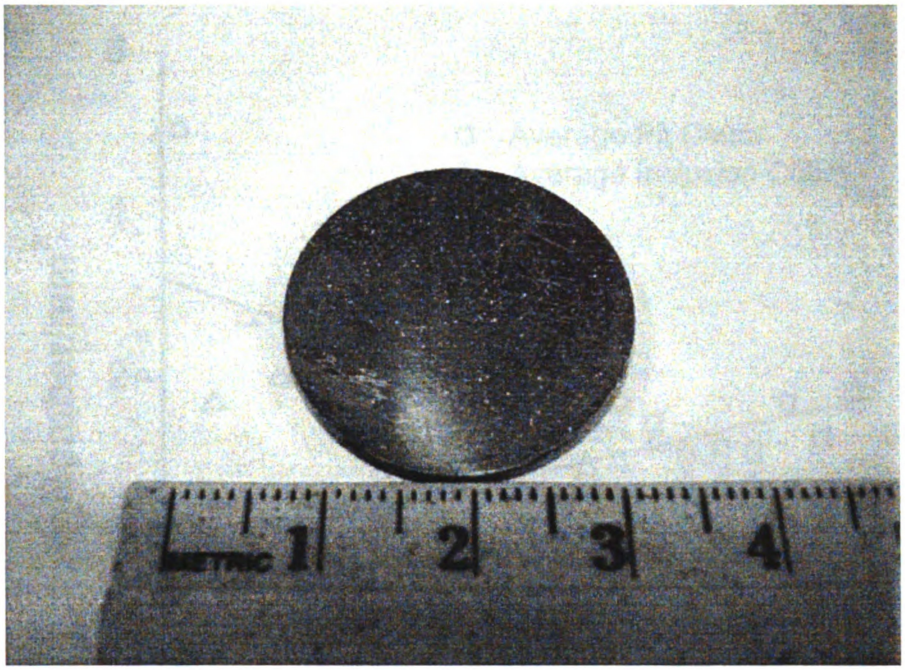

Figure 3.1.2.3a. Surface of LAST specimen N37-21 in contact with the **cold plate**, showing surface pitting and inclusions after 200 thermal cycles.

Figure 3.1.2.3b. Surface of LAST specimen N37-21 in contact with the **hot plate**, showing surface pitting and inclusions after 200 thermal cycles.

Inclusions and Pits versus number of thermal fatigue Cycles (N39-46)

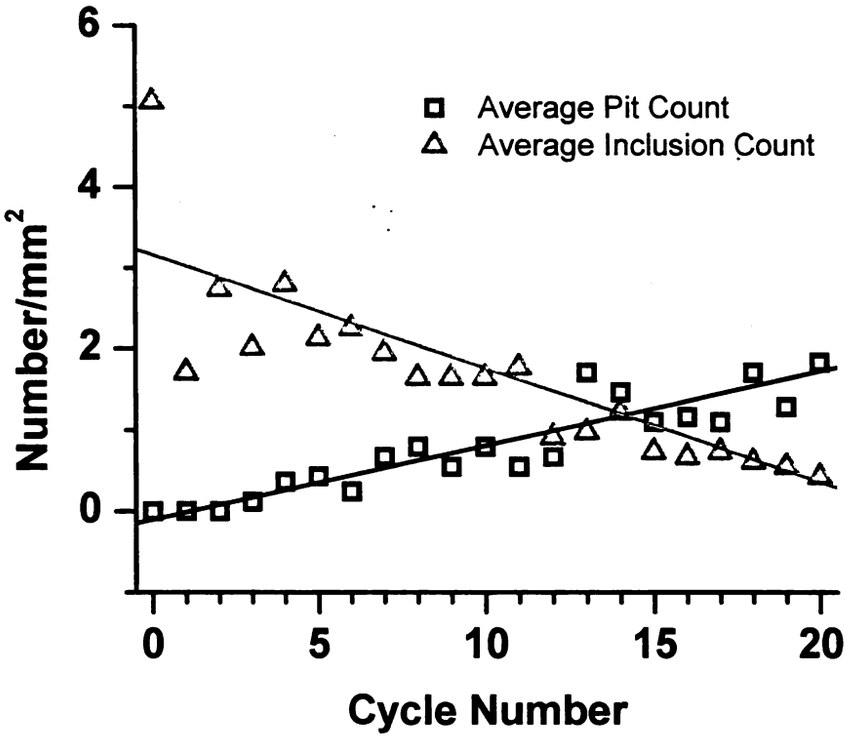

Figure 3.1.2.4a. Inclusion and pit counts versus thermal cycling for LAST samples N39-46 cycled in the small thermal fatigue chamber (N=20). The inclusions and pits were counted from three random areas of each sample for each cycle of the thermal fatigue cycling. The total number of surface inclusions from the three areas were added together, as were the total number of surface pits for each cycle. The total number of surface pits and surface inclusions were then divided by three to give an average for each thermal fatigue cycle.

Inclusions and Pits versus number of thermal fatigue cycles (N39-49)

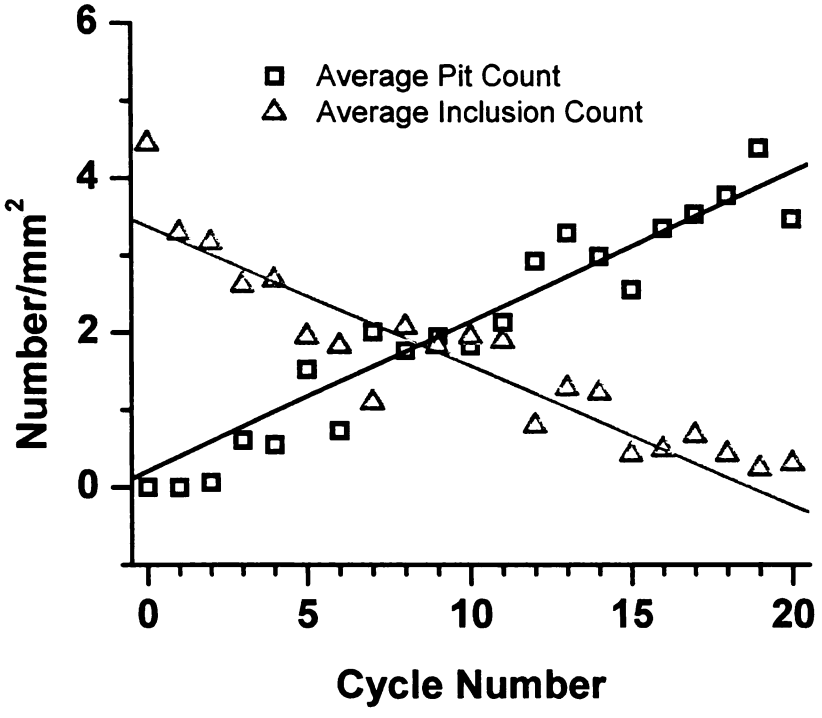

Figure 3.1.2.4b

Figure 3.1.2.4b. Inclusion and pit counts versus thermal cycling for LAST sample N39-49 cycled in the small thermal fatigue chamber (N=20). The inclusions and pits were counted from three random areas of each sample for each cycle of the thermal fatigue cycling. The total number of surface inclusions from the three areas were added together, as were the total number of surface pits for each cycle. The total number of surface pits and surface inclusions were then divided by three to give an average for each thermal fatigue cycle.

Sum of Inclusion and Pit Count versus number of thermal fatigue cycles

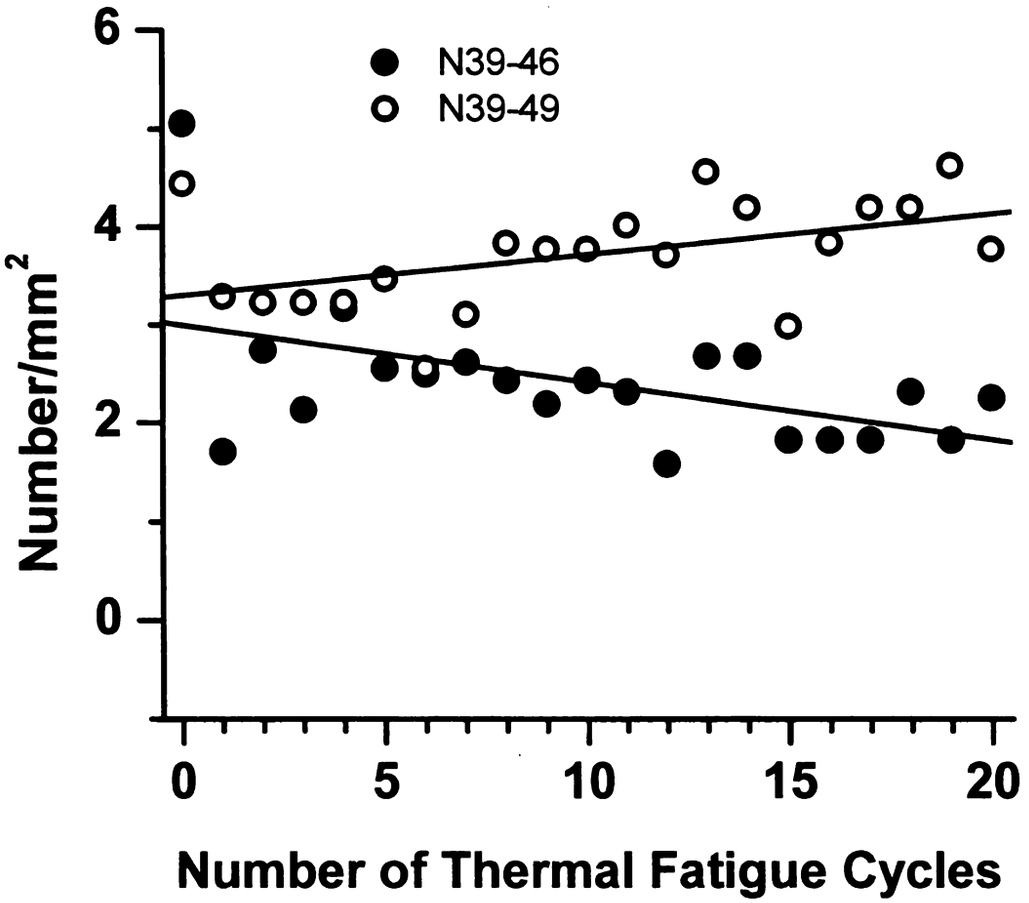

Figure 3.1.2.4c. Sum of Inclusion and Pit Count versus number of thermal fatigue cycles from 0-20 cycles.

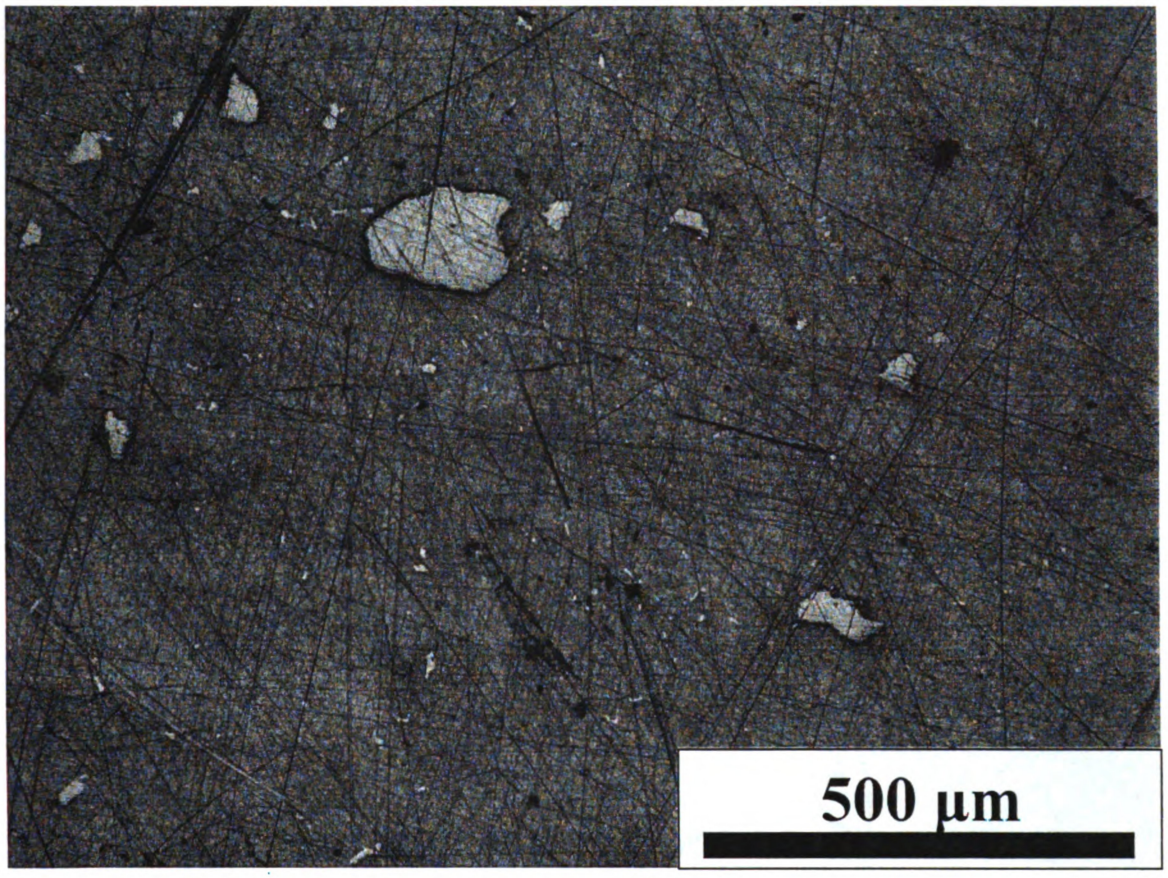

Figure 3.1.2.5a. LAST specimen N39-46, as-received specimen, with inclusions ranging from roughly 20-200 microns observed using optical microscopy.

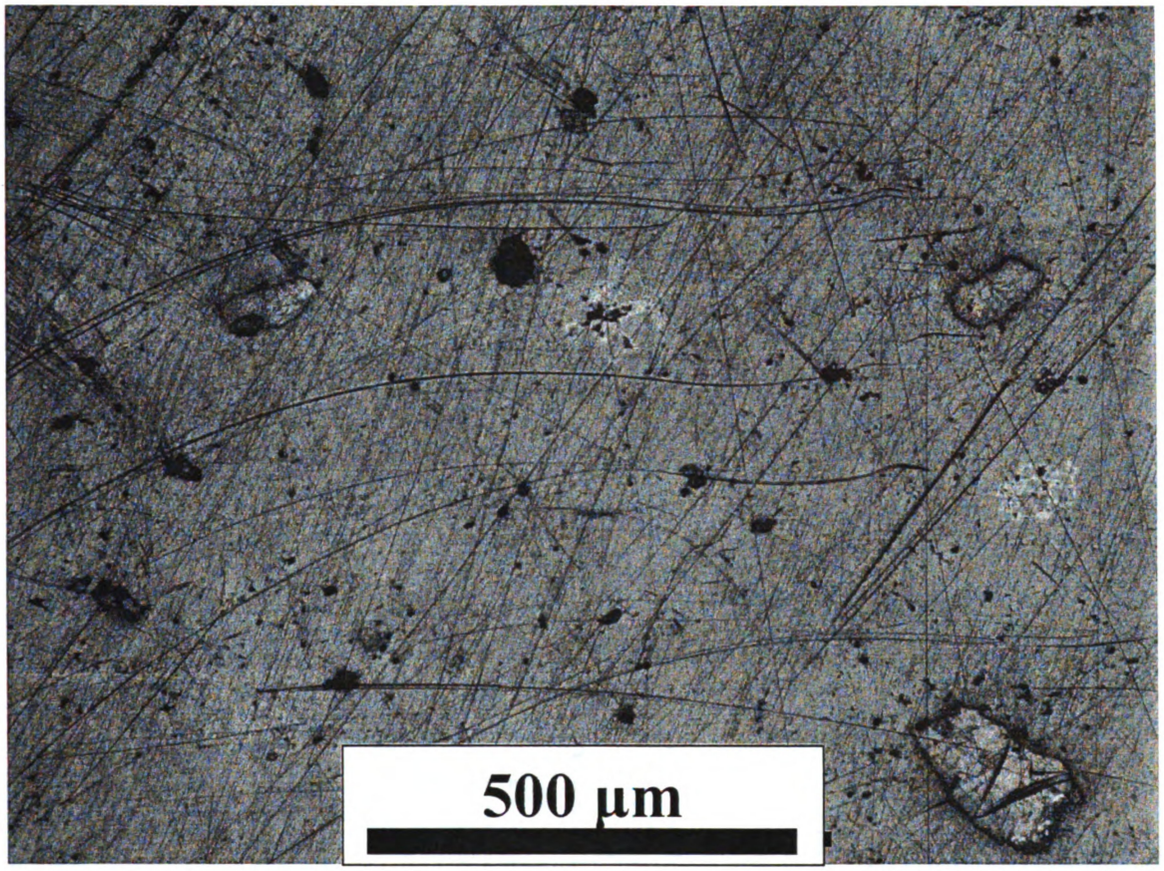

Figure 3.1.2.5b. The surface of LAST specimen N39-46 after 5 thermal cycles. Both inclusions and surface pits are evident.

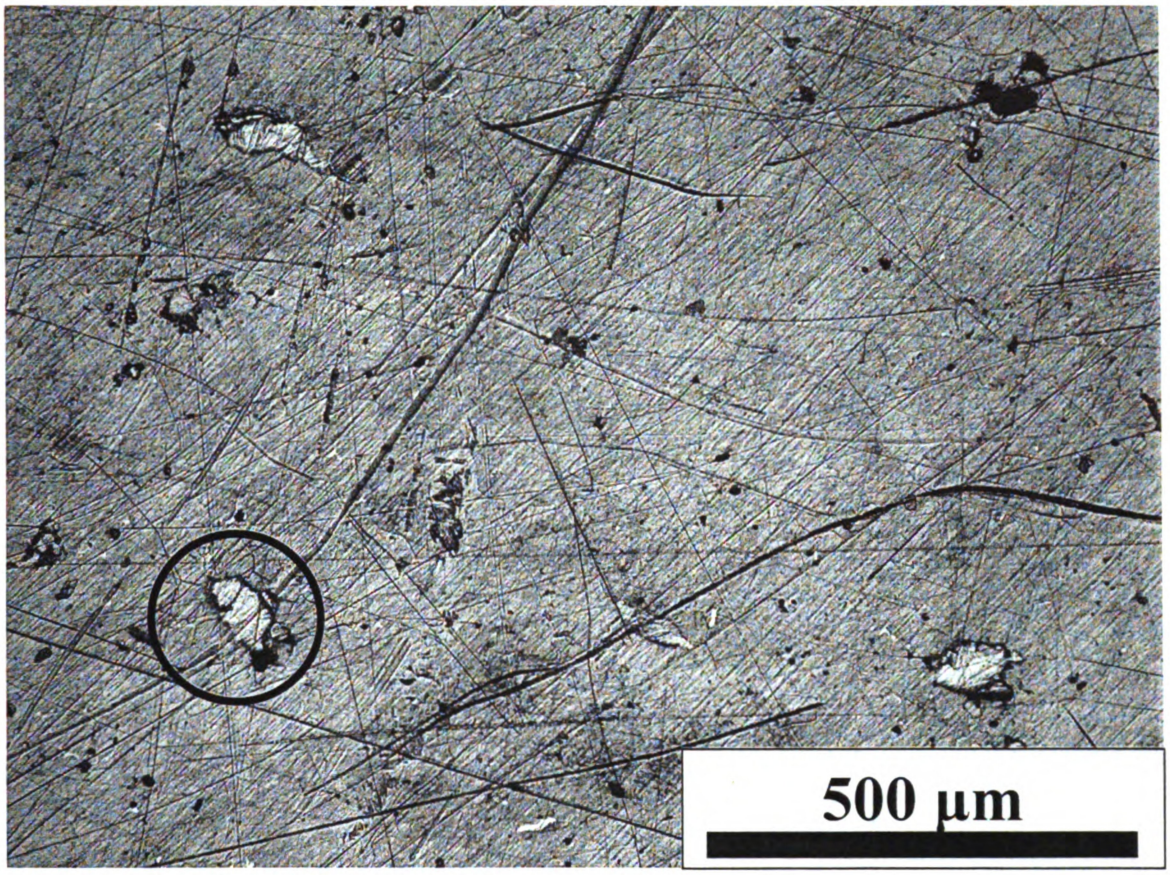

Figure 3.1.2.5c. The surface of LAST specimen N39-46 after 10 thermal cycles. Microcracking (within black circle) is observed around the inclusion.

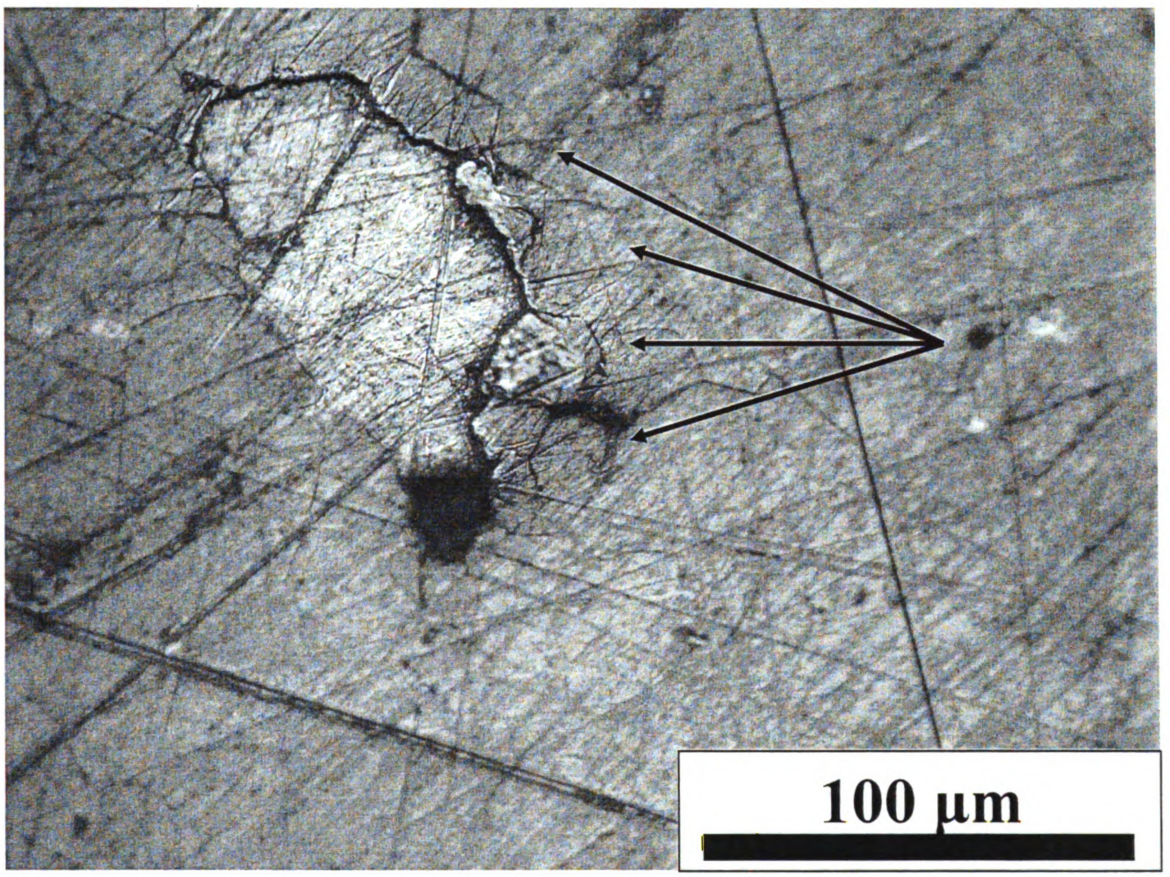

Figure 3.1.2.5d. A higher magnification view of N39-46 after 10 thermal cycles, the arrows highlight microcrack damage surrounding the inclusion caused by thermal expansion anisotropy due to the different thermal expansion coefficients of the inclusion and the LAST matrix.

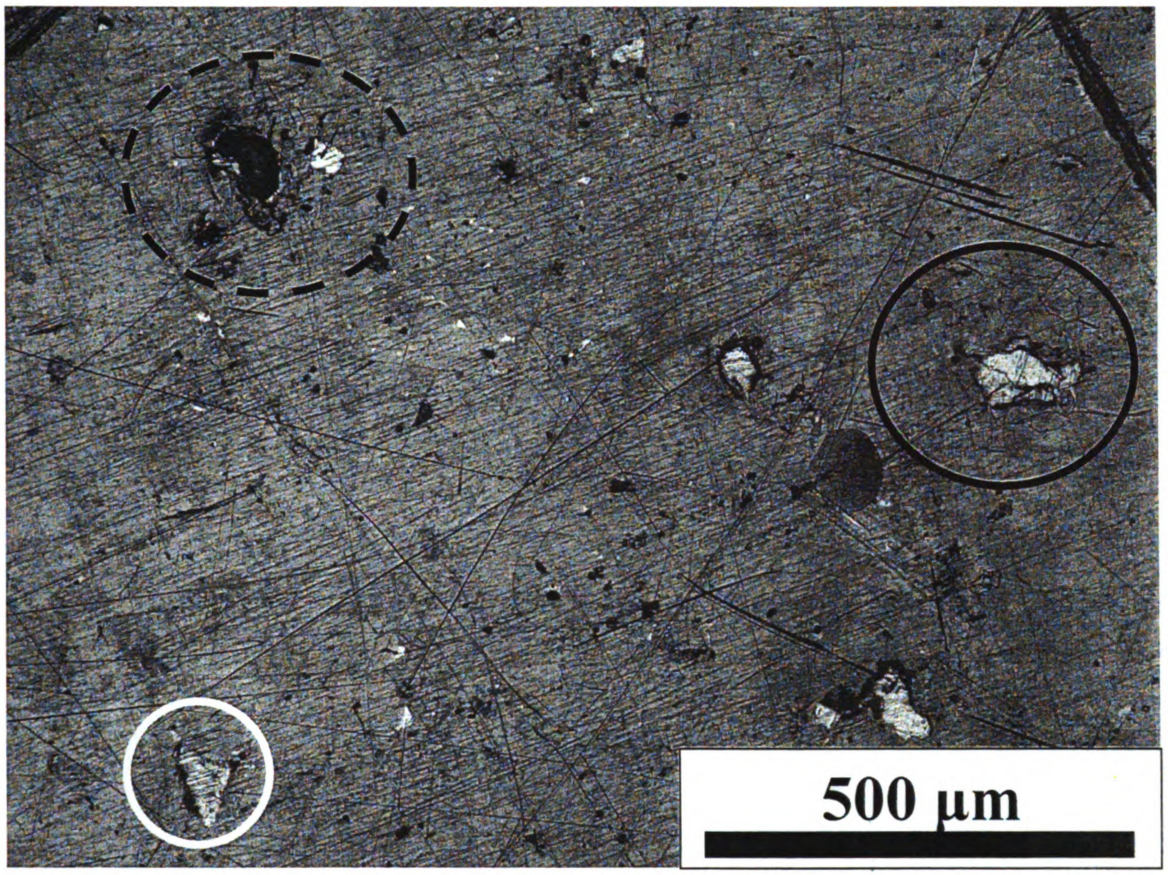

Figure 3.1.2.5e. N39-46 after 12 thermal cycles. The dashed circle shows similar fracture damage surrounding the pit as is found within the matrix surrounding the inclusion in the solid black circle to the right. The inclusion in the white circle can be seen in Figure 3.1.2.5f having suffered further damage during thermal cycling.

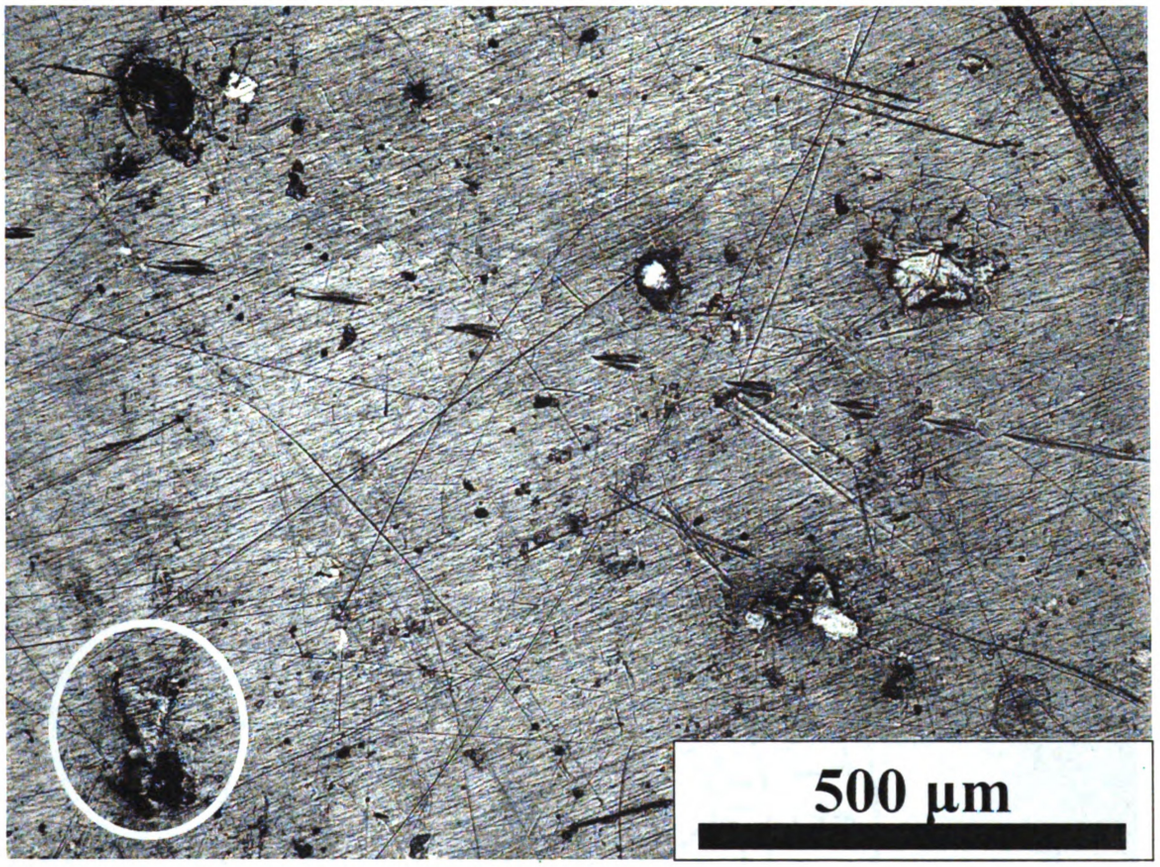

Figure 3.1.2.5f. N39-46 after 15 thermal cycles. Following the lower left inclusion in Figure 3.1.2.5e, it is noticed that spalling occurred at the bottom edge of the inclusion in the white circle within 3 cycles.

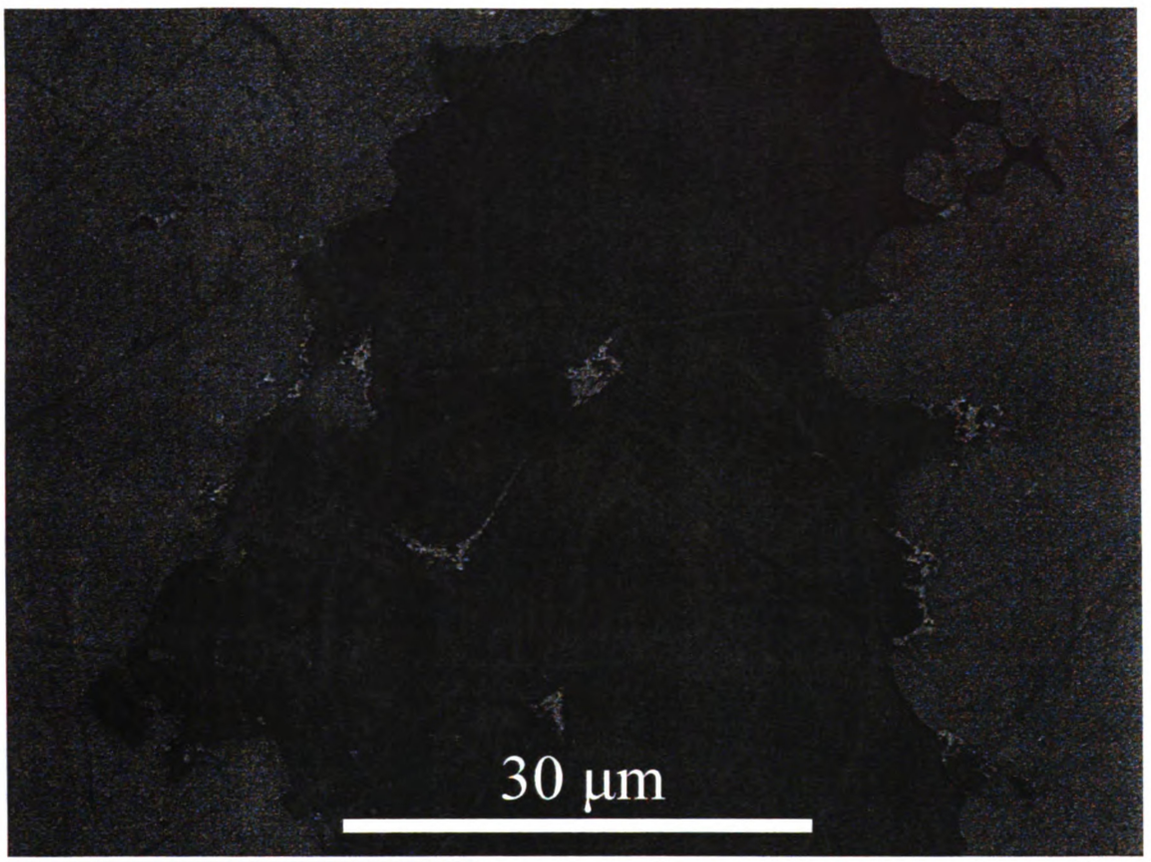

Figure 3.1.2.6a. For as-received LAST specimen N38-10 with an inclusion (dark area) within a lighter-appearing matrix. Light and dark areas are due to atomic number contrast in the SEM.

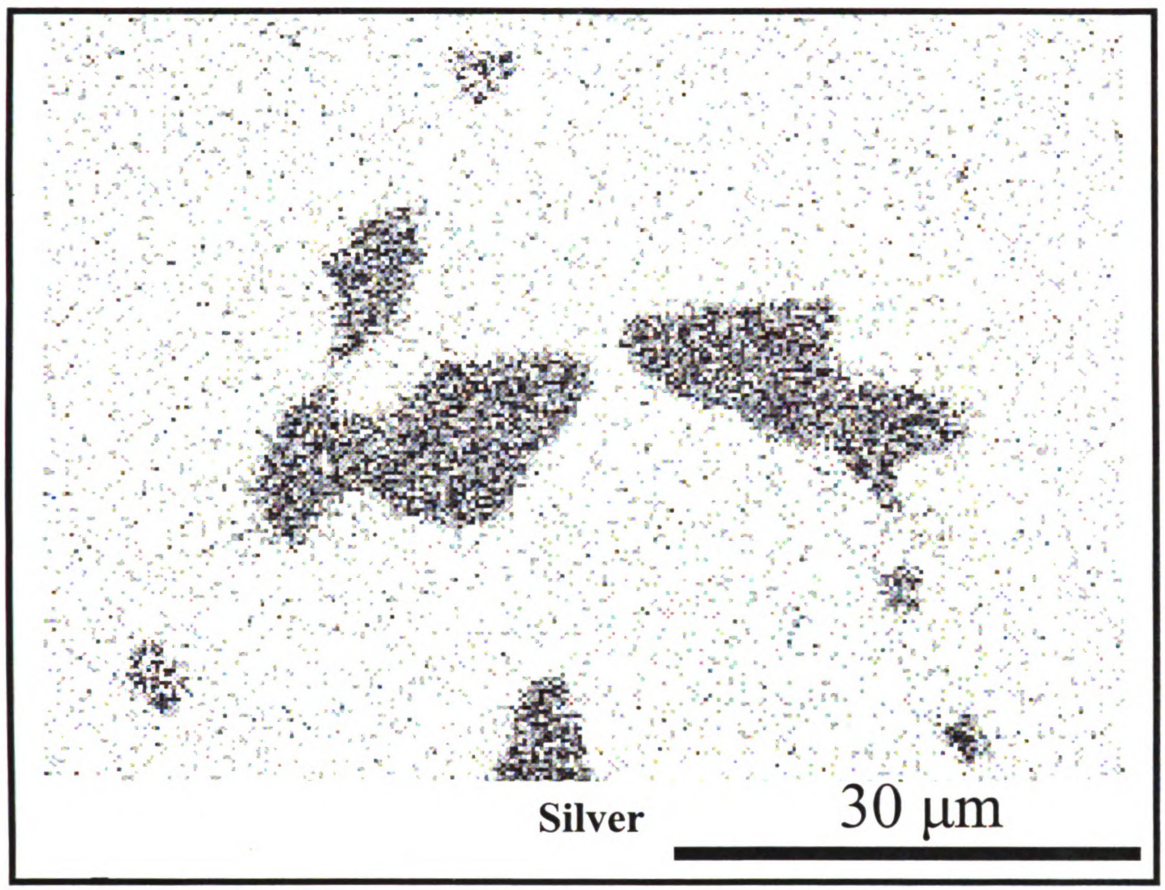

Figure 3.1.2.6b. EDS image of as-received LAST specimen N38-10 with silver rich area within inclusion.

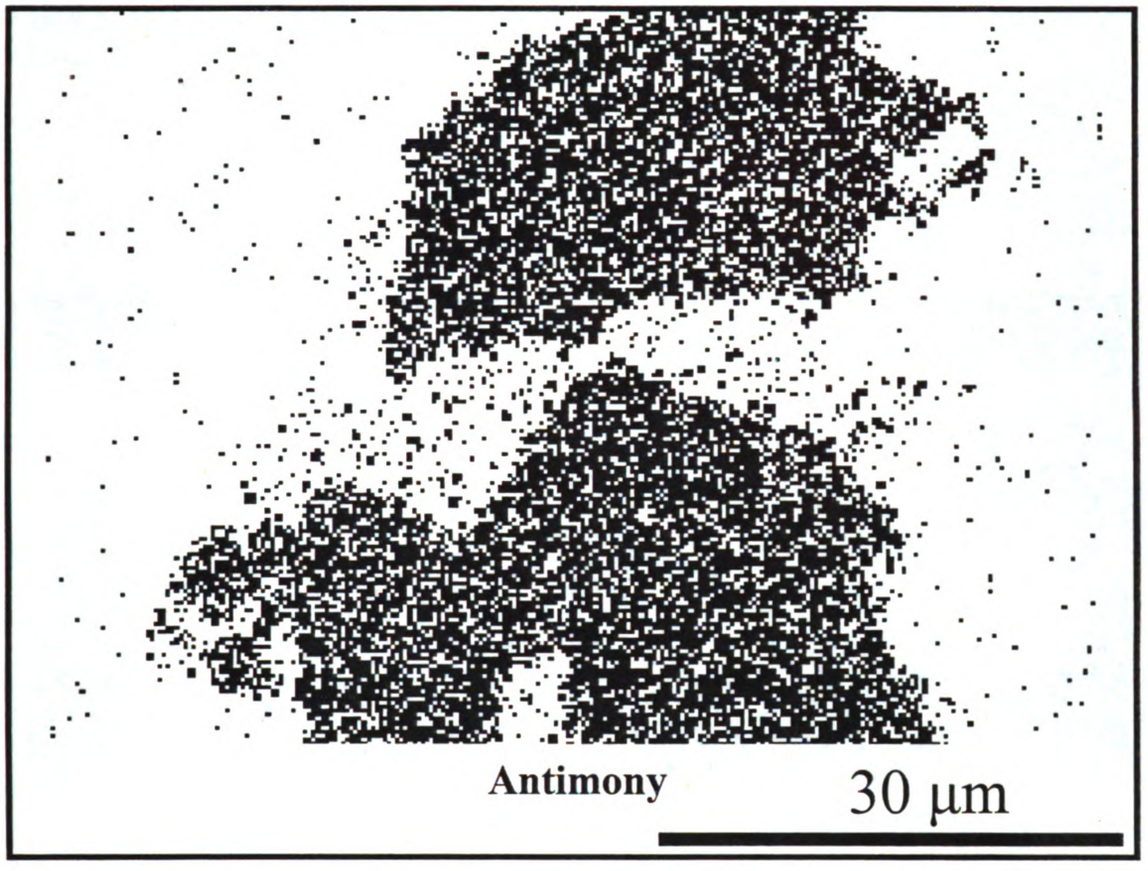

Figure 3.1.2.6c. EDS image for as-received LAST specimen N38-10 with an antimony rich area. The antimony rich region is disjoint from silver-rich regions shown in part (b).

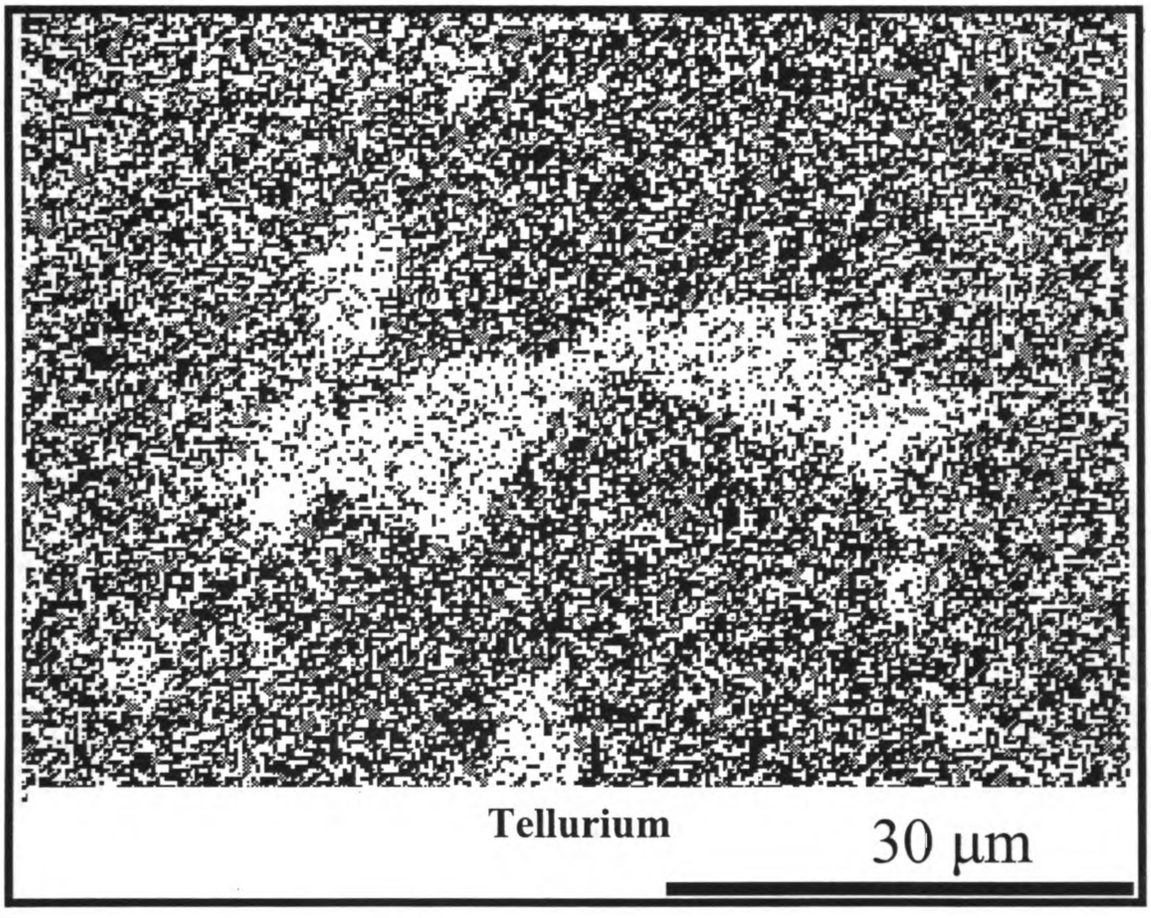

Figure 3.1.2.6d. An EDS image of as-received specimen, N38-10, with a uniform distribution of tellurium in the inclusion, except within silver rich area of Figure 3.1.2.6b.

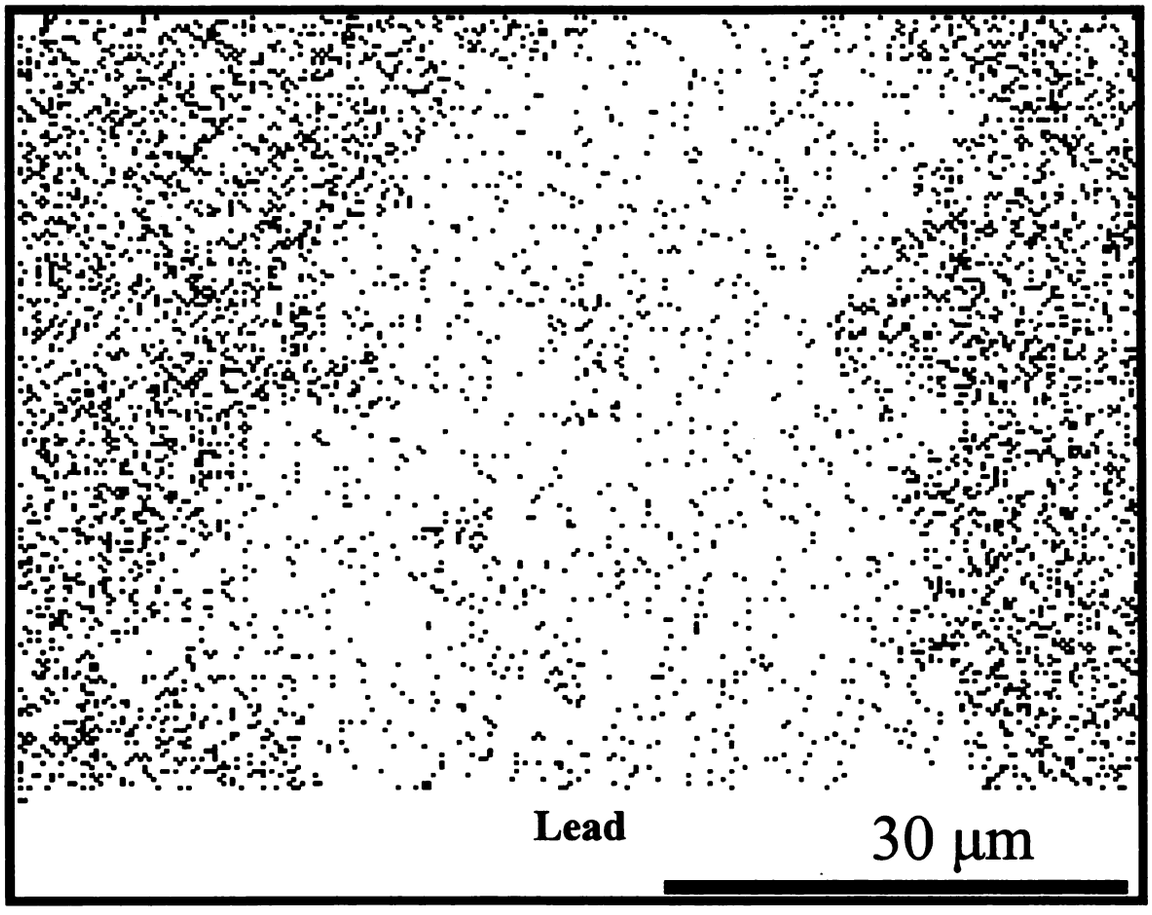

Figure 3.1.2.6e. EDS image of as-received N38-10 specimen indicating the inclusion is lead poor while the surrounding LAST matrix has a uniform and higher concentration of lead.

3.1.3. LASTT Disk Specimen Blistering

Of the 90 LASTT disk specimens that were thermally fatigued, 21 of the specimens (~ 23 %) blistered during thermal cycling (Figure 3.1.3.1.). It was assumed that the blistering of the samples was caused by a decomposition reaction of the LASTT powder during sintering. The LASTT powders were densified in a hot press under high pressure in an evacuated atmosphere. During the sintering process, at an elevated temperature (1000°C or above), a carbonate compound (from the powders contact with the graphite dye) or a metal oxide in the LASTT composition decomposes [Kingery 1975]. The reduction of the metal oxide or carbonate compound during the densification of the powder results in a gaseous byproduct [Alizadeh 2006]. At a high enough temperature and pressure the interconnected pores within the material disassociate and seal the gas within the bulk of the dense material. The blistering occurs in the LASTT disk-shaped specimens during the elevated temperature stage of the thermal cycling (400°C). At a raised temperature, the increased pressure of the decomposition gas in combination with the softening of the material leads to large pores and blistering on the sample surface (Figures 3.1.3.1. – 3.1.3.4) [Kingery 1975].

Blistering only occurred in LASTT samples that were thermally fatigued for 90 or more thermal cycles. The blisters on the specimen's surfaces ranged from 5 mm to 1 cm in diameter and 1-5 mm in height from the original sample surface. Blistering that occurred on only one surface of a specimen, occurred on the surface that contacted the cold plate during thermal cycling. Some of the blisters were so large on the sample's surface the sample cracked at the apex of the blister (Figure 3.1.3.4 and Figure 3.1.3.5a).

An interior inspection of a blistered specimen revealed a void area within the sample, which caused the surface to dimple. The inner surface of the internal void was considerably rougher than the smooth surface of the sample along the fracture (Figures 3.1.3.5b – 2.1.3.5c).

After the LASTT disk specimens were thermally cycled in the large thermal fatigue chamber, the disks underwent biaxial flexural ring-on-ring testing (Section 2.6). All the LASTT specimens with thermal cycle induced blisters resulted in invalid fractures during the ring-on-ring testing (Section 2.6.10, Figure 3.1.3.5a). The ROR fractures of the blistered specimens were considered invalid because the cracks in the samples either initiated at or were impeded by the surface blisters (flaw). As stated in the ROR fracture validity, Section 2.6.10, a crack that initiates from a flaw would result in a diametrial crack across the specimen and would be considered invalid (Figure 3.1.3.5a).

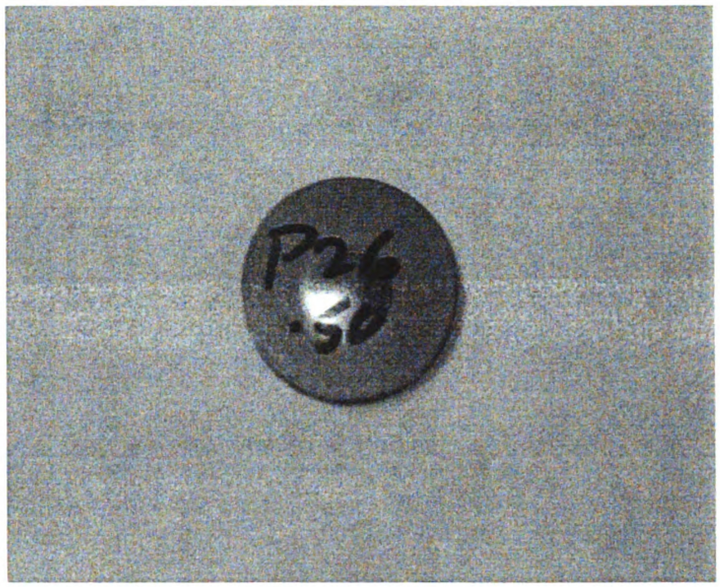

Figure 3.1.3.1. The surface of specimen P26-50 in contact with the **cold plate**. Specimen P26-50 blistered after 120 cycles. The blister dimensions were 1 cm in diameter and 5 mm in height as measured from the original sample surface.

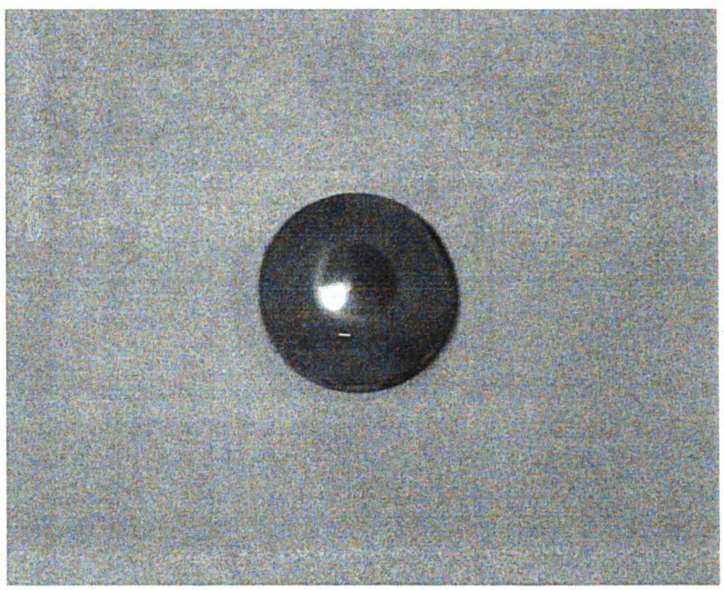

Figure 3.1.3.2. The surface of specimen P26-50 in contact with the **hot plate**. Specimen P26-50 blistered after 120 cycles. The blister dimensions were approximately 8 mm in diameter and 3 mm in height as measured from the original surface of the specimen.

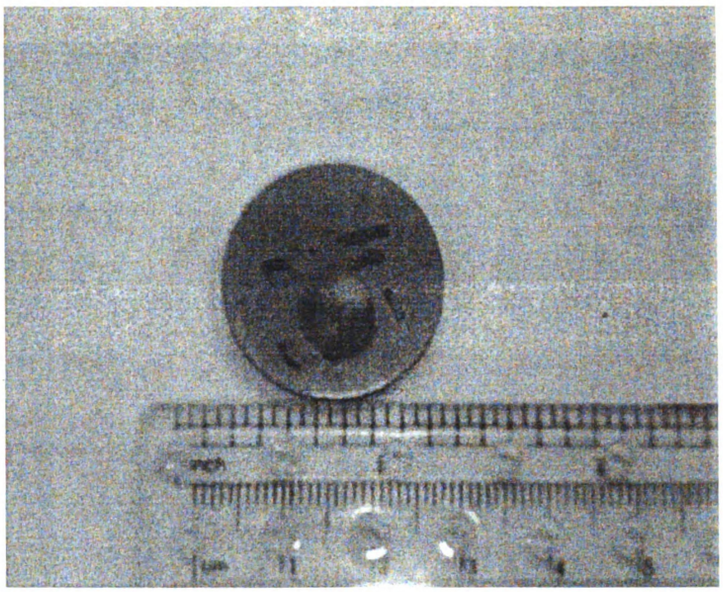

Figure 3.1.3.3. The surface of specimen P32-11 in contact with the **cold plate**. Specimen P32-11 blistered after 150 cycles. The blister dimensions were approximately 7 mm in diameter and 2 mm in height as measured from the original sample surface.

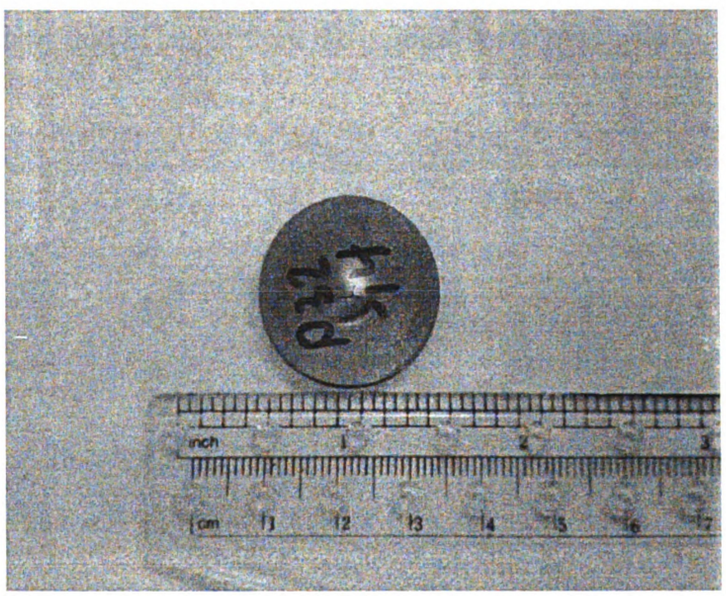

Figure 3.1.3.4. The surface of specimen P32-14 in contact with the **hot plate**. Specimen P32-14 blistered after 150 cycles. The blister dimensions were approximately 6 mm in diameter and 2 mm in height as measured from the original sample surface.

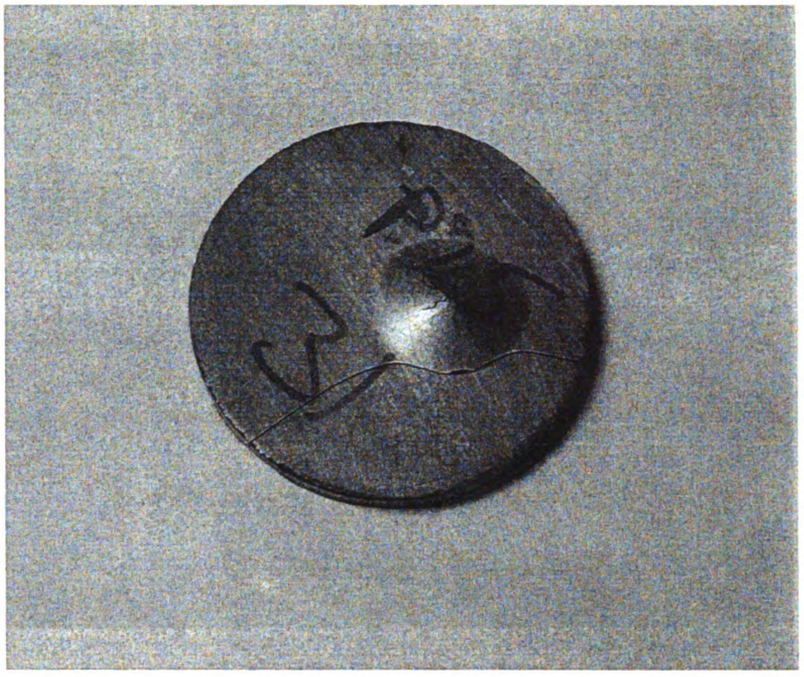

Figure 3.1.3.5a. The surface of specimen P25-31 in contact with the **cold plate** after ring-on-ring fracture testing, which blistered after 90 cycles. The blister dimensions are 1 cm in diameter and 1 mm in height from the original specimen surface.

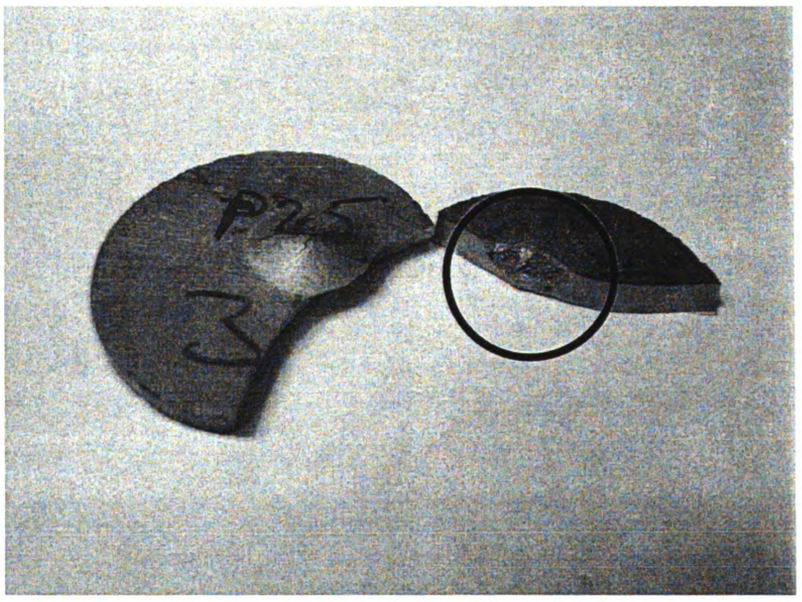

Figure 3.1.3.5b. Interior view of specimen P25-31 on the side which was in contact with the **cold plate**, showing a large void area within the sample with a rough wall compared to the smoother surface of the sample along the fracture, designated by the black circle, which occurred in the sample during blistering after 90 cycles.

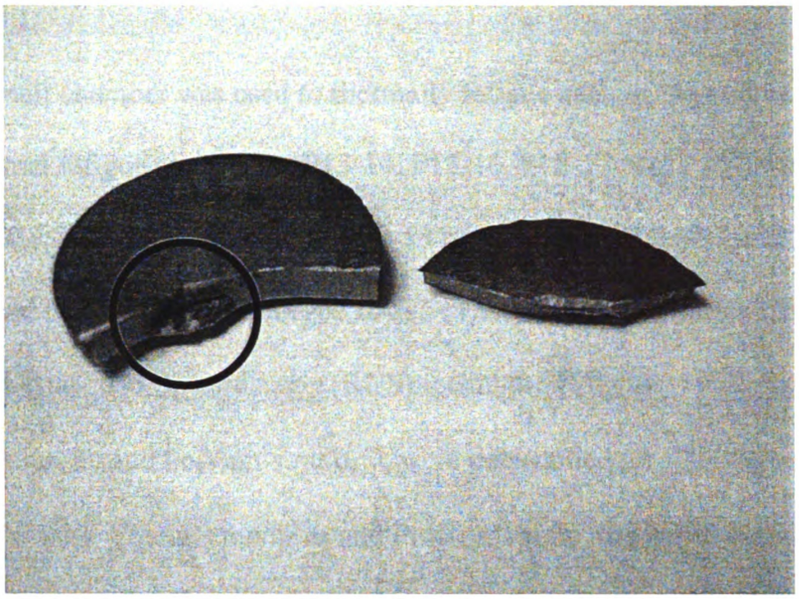

Figure 3.1.3.5c. Interior view of specimen P25-31 on the side which was in contact with the **hot plate**, showing the underside of the void area within the sample which caused the surface to dimple. The inner surface of the internal void was considerably rougher compared to the smooth surface of the sample along the fracture, designated by the black circle, which occurred in the sample during blistering after 90 cycles.

3.2. Elastic modulus measurements in LASTT and LAST specimens

The small chamber was used to thermally fatigue each of the twelve elasticity/thermal fatigue specimens: P15-14, P15-16, P15-17, and P15-19 of p-type LASTT, N37-28, N37-29, N39-50, and N39-53 of reformulated LAST and N28-11, N28-12, N28-14, and N28-16 of initial n-type LAST (Table 3.2.1) [Hendricks 2009]. Using the Resonant Ultrasound Spectroscopy (RUS) technique [Migliori 1997, Ren 2008], the Young's modulus, E, and Poisson's ratio, ν, were determined for the twelve plate-shaped specimens. For both Young's modulus and Poisson's ratio, the initial value (when the number of thermal cycles, N = 0), the value after 200 cycles, as well as the mean, the maximum, and the minimum values are tabulated in Table 3.2.1 and Table 3.2.2.

Table 3.2.1. With respect to the number of thermal fatigue cycles, N, the initial (N=0), the final (N=200), the mean, the maximum, and the minimum values of the Young's modulus, E, for each of the twelve elasticity/thermal fatigue specimens included in this study.

Young's modulus					
Specimen	$E_{N=0}$ (GPa)	$E_{N=200}$ (GPa)	E_{mean} (GPa)	E_{max} (GPa)	E_{min} (GPa)
P15-14	46.8	Fractured at N = 160	46.0 ± 1.0	47.3 (N = 60)	43.4 (N = 150)
P15-16	46.3	46.7	46.4 ± 0.4	46.7 (N = 150)	45.8 (N = 180)
P15-17	46.3	Fractured at N = 190	45.0 ± 5.0	46.5 (N = 100)	26.1 (N = 180)
P15-19	46.4	46.2	46.3 ± 0.2	46.7 (N = 50)	46.0 (N = 120)
N39-50	56.2	55.2	55.5 ± 0.3	56.2 (N = 0)	55.1 (N = 100)
N39-53	57.0	56.6	56.8 ± 0.1	57.0 (N = 0)	56.6 (N = 200)
N37-28	56.5	55.2	56.1 ± 0.4	56.5 (N = 0)	55.2 (N = 200)
N37-29	56.3	55.6	56.0 ± 0.2	56.3 (N = 0)	55.6 (N = 200)
N28-11	53.9	51.8	52.7 ± 1.0	54.0 (N = 10)	50.6 (N = 190)
N28-12	54.1	54.1	54.1 ± 0.03	54.2 (N = 150)	54.0 (N = 190)
N28-14	55.1	54.7	54.8 ± 0.1	55.2 (N = 10)	54.6 (N = 50)
N28-16	53.6	49.5	51.8 ± 1.1	53.6 (N = 0)	49.5 (N = 200)

Table 3.2.2. With respect to the number of thermal fatigue cycles, N, the initial (N=0), the final (N=200), the mean, the maximum, and the minimum values of the Poisson's ratio, υ, for each of the twelve elasticity/thermal fatigue specimens included in this study.

Poisson's ratio					
Specimen	$\nu_{N=0}$	$\nu_{N=200}$	ν_{mean}	ν_{max}	ν_{min}
P15-14	0.265	Fractured at N = 160	0.290 ± 0.04	0.391 (N = 150)	0.262 (N = 10)
P15-16	0.267	0.268	0.269 ± 0.003	0.272 (N = 120)	0.262 (N = 180)
P15-17	0.265	Fractured at N = 190	0.268 ± 0.003	0.271 (N = 130)	0.260 (N = 20)
P15-19	0.256	0.264	0.263 ± 0.002	0.267 (N = 80)	0.256 (N = 0)
N39-50	0.256	0.261	0.260 ± 0.007	0.274 (N = 30)	0.236 (N = 100)
N39-53	0.273	0.269	0.271 ± 0.002	0.275 (N = 150)	0.269 (N = 200)
N37-28	0.271	0.246	0.264 ± 0.009	0.273 (N = 110)	0.246 (N = 200)
N37-29	0.270	0.267	0.269 ± 0.001	0.271 (N = 150)	0.266 (N = 130)
N28-11	0.284	0.274	0.270 ± 0.014	0.284 (N = 0)	0.237 (N = 150)
N28-12	0.274	0.274	0.273 ± 0.001	0.276 (N = 130)	0.270 (N = 50)
N28-14	0.279	0.274	0.276 ± 0.002	0.279 (N = 0)	0.274 (N = 70)
N28-16	0.248	0.208	0.234 ± 0.022	0.279 (N = 70)	0.199 (N = 170)

3.2.1. Young's Modulus of LAST and LASTT Specimens

3.2.1.1. Initial LAST Specimens' Young's Modulus

The initial n-type specimens; N28-11, N28-12, N28-14, and N28-16, were thermally cycled in the small thermal fatigue chamber for 200 cycles. The specimens showed a 10% decline in the Young's modulus with the increase in the number of thermal cycles (Figure 3.2.1.1). Samples N28-11 and N28-16 had the largest decrease in Young's modulus of 4.5 GPa occurring from 100 to 200 thermal fatigue cycles. N28-12 and N28-14 only decreased approximately 1 GPa during the thermal fatigue testing (Figure 3.2.1.1.). From the Young's modulus and Poisson's ratio results (Section 3.2.2) of the initial LAST specimens received from Tellurex Corporation, a reformulation of the LAST specimen composition would be helpful in improving both the thermoelectric properties and the mechanical properties.

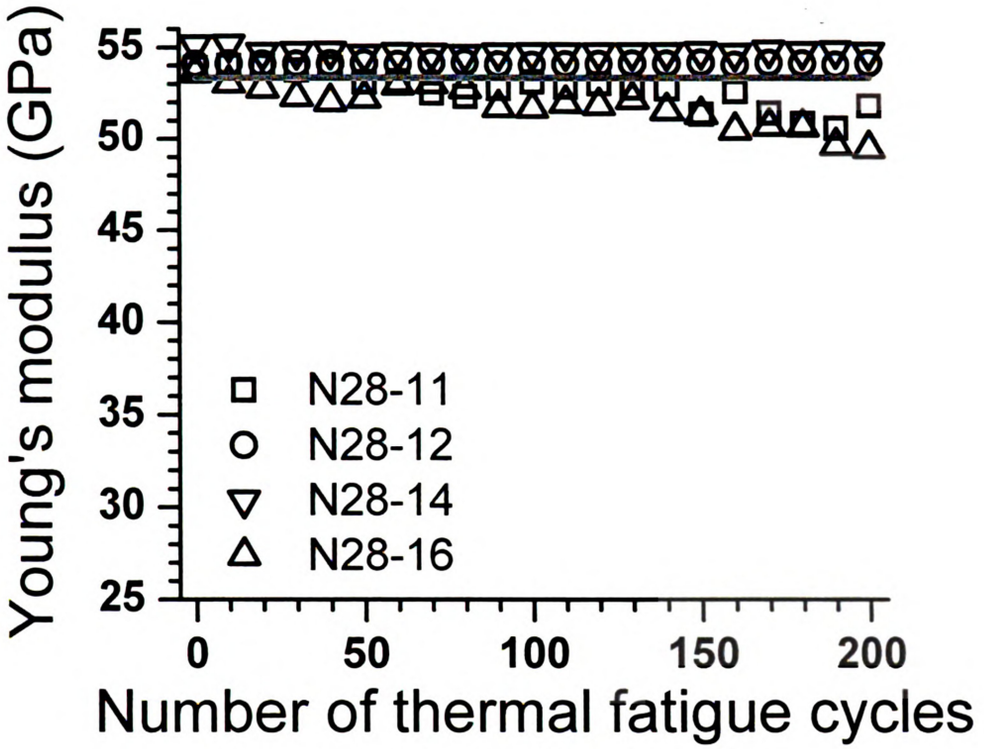

Figure 3.2.1.1. Resonant Ultrasound Spectroscopy (RUS) measurements of the Young's modulus as a function of the number of thermal fatigue cycles for initial n-type (LAST) samples, cycled in the small thermal fatigue chamber.

3.2.1.2. Reformulated LAST Specimens' Young's Modulus

The reformulated LAST specimens, N39-50, N39-53, N37-28, and N37-29 received from Tellurex were processed with a higher composition of lead than the initial LAST specimens (N28). The new LAST composition responded better to the thermal fatigue cycling than the previous n-type sample composition. The reformulated LAST specimens maintained a relatively constant Young's modulis of 56.5 GPa during the 200 thermal fatigue cycles (Figure 3.2.1.2, the light gray horizontal line on the figure graphs depict the initial (zero thermal cycle) average of the four specimens). The drop of the specimens' average modulus over the full 200 thermal cycles was 0.85 GPa. Thus not only was the initial mean of the reformulated n-type higher than the initial n-type specimens (reformatted LAST of mean 56.5 GPa compared to initial LAST mean of 54.2 GPa), but the reformulated LAST also displayed little deviation with the increase of thermal fatigue cycles (Figure 3.2.1.1. and Figure 3.2.1.2., the light gray horizontal line on the figure graphs depict the initial (zero cycle) average of the four specimens).

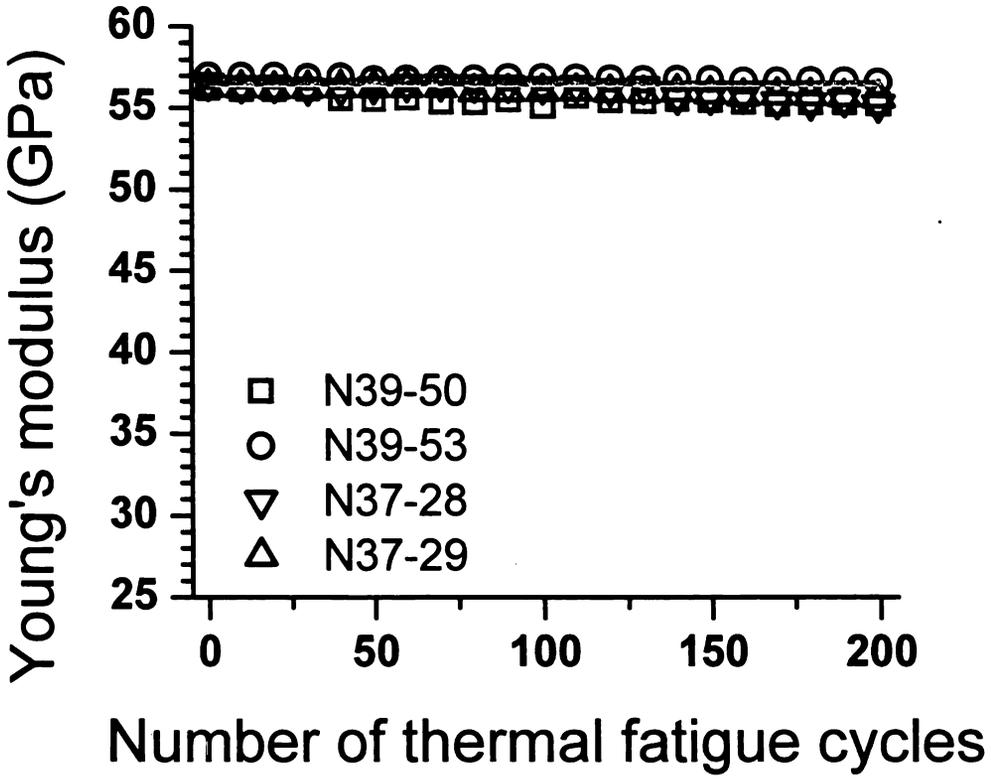

Figure 3.2.1.2. Resonant Ultrasound Spectroscopy (RUS) measurements of the Young's modulus as a function of the number of thermal fatigue cycles for reformulated n-type (LAST) samples, cycled in the small thermal fatigue chamber.

3.2.1.3. LASTT Specimens' Young's Modulus

For the LASTT p-type specimens, except for specimen P15-14 that fractured at N = 160 thermal cycles and specimen P15-17 that fractured at N = 190 thermal cycles, E exhibited small variations as a function of the number of thermal fatigue cycles N for the other 2 specimens included in this study (Figure 3.2.1.3). For example, the as-received Young's modulus of specimen P15-16 was 46.29 GPa, which changed to 46.68 GPa after 200 thermal fatigue cycles, corresponding to a 0.8% increase (Table 3.2.1). The difference between the maximum (N = 150) and minimum (N = 180) values of Young's modulus of P15-16 was only 1.9% (Table 3.2.1). The small changes in E induced by thermal fatigue indicated that the average microcrack size and/or the number density of microcracks did not increase significantly within the 200 thermal cycles for the tested specimens (excluding P15-14 and P15-17).

Two LASTT specimens were fractured prior to completing the 200 thermal fatigue cycle testing. Immediately before fracture, the Young's modulus of P15-14 (N = 150) decreased to 43.38 GPa, approximately 5.7% smaller than the mean value of 46 GPa. Also E of specimen P15-16 decreased to 26.14 GPa at N = 180, nearly 42% smaller than the mean value of 46.4 GPa (Table 3.2.1). The appreciable decrease in Young's modulus for P15-14 and P15-16 implied significant accumulation of microcracking damage which eventually led to the fractures. In contrast, none of the eight LAST specimens failed during thermal cycling in the small thermal fatigue chamber, implying the n-type material may possess a better resistance to thermal fatigue than the p-type material.

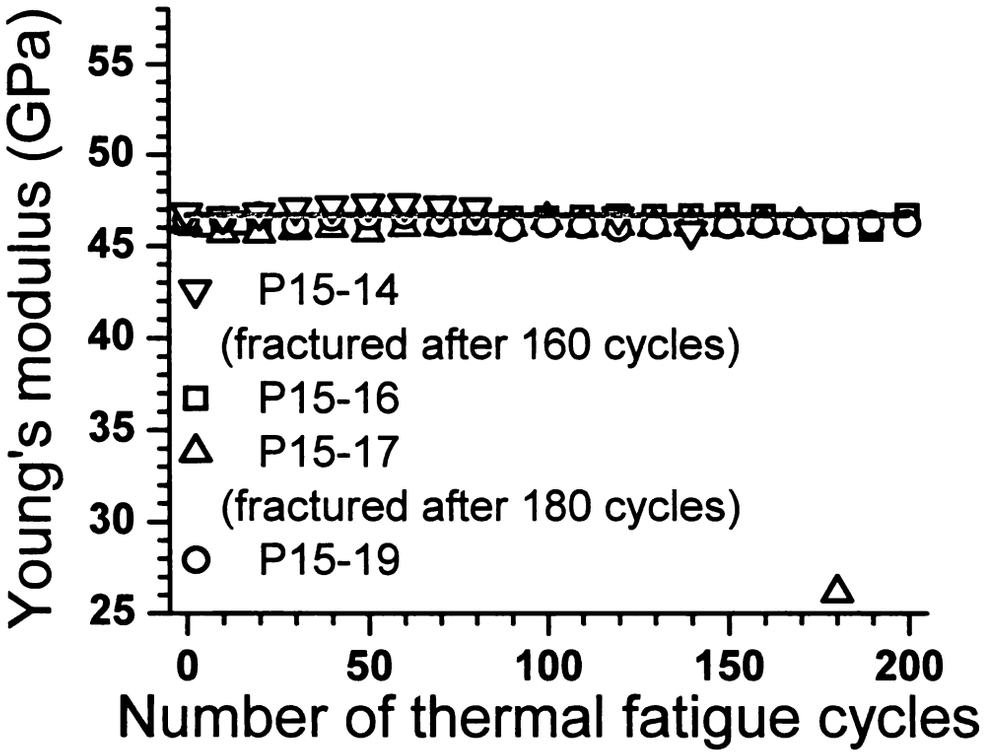

Figure 3.2.1.3. Resonant Ultrasound Spectroscopy (RUS) measurements of the Young's modulus as a function of the number of thermal fatigue cycles for p-type (LASTT) samples, cycled in the small thermal fatigue chamber.

3.2.2. Poisson's Ratio of LAST and LASTT Specimens

3.2.2.1. Initial LAST Specimens' Poisson's Ratio

As with the Young's modulus of the initial n-type LAST composition; N28-11, N28-12, N28-14, and N28-16 showed an erratic and gradual decline in the Poisson's ratio with the increase in the number of thermal fatigue cycles (Figure 3.2.2.1., the light gray horizontal line on the figure graphs depict the initial (zero cycle) average of the four specimens). Samples N28-12 and N28-14 had Poisson's ratio that varied between 0.27 and 0.265 (~2%) during the 200 thermal fatigue cycles. The Poisson's ratios of the two samples did not vary much from 0.27. N28-11 had a larger variation in Poisson ratio but the largest decrease occurred from 0.278 (140 thermal cycles) to 0.238 (150 thermal cycle), a decrease of 14.5%. The lowest and most scattered Poisson ratio values occurred in N28-16. N28-16 began the thermal cycling with the lowest Poison's ratio of the four initial LAST composition (Figure 3.2.2.1.). N28-16 began the testing with a ratio of 0.227 (0 cycles) and ended the testing with a Poisson's of 0.208 (200 cycles). During the thermal cycling of N28-16, the Poisson's ratio varied from as high as 0.26 to as low as 0.19.

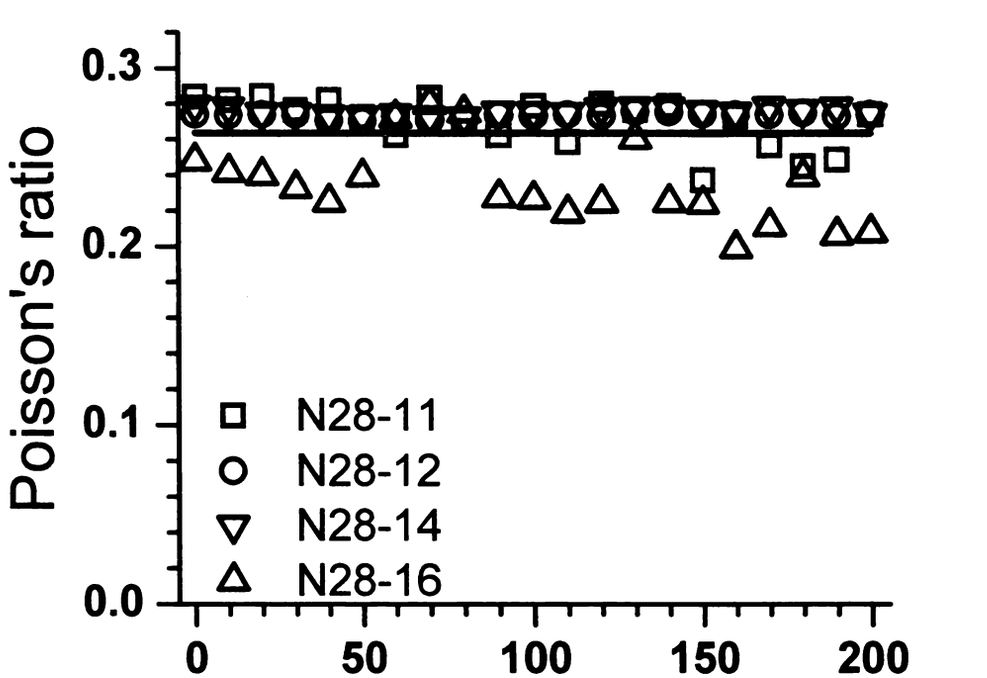

Figure 3.2.2.1. Resonant Ultrasound Spectroscopy (RUS) measurements of the Poisson's ratio as a function of the number of thermal fatigue cycles for initial n-type (LAST) samples, cycled in the small thermal fatigue chamber.

3.2.2.2. Reformulated LAST Specimens' Poisson's Ratio

The reformulated LAST specimens, N39-50, N39-53, N37-28, and N39-29 had a lower zero cycle Poisson's average of 0.268 in comparison to the initial LAST composition average of 0.271 (Figure 3.2.2.2.). The reformulated LAST, however, exhibited small variations as a function of the number of thermal fatigue cycles N.

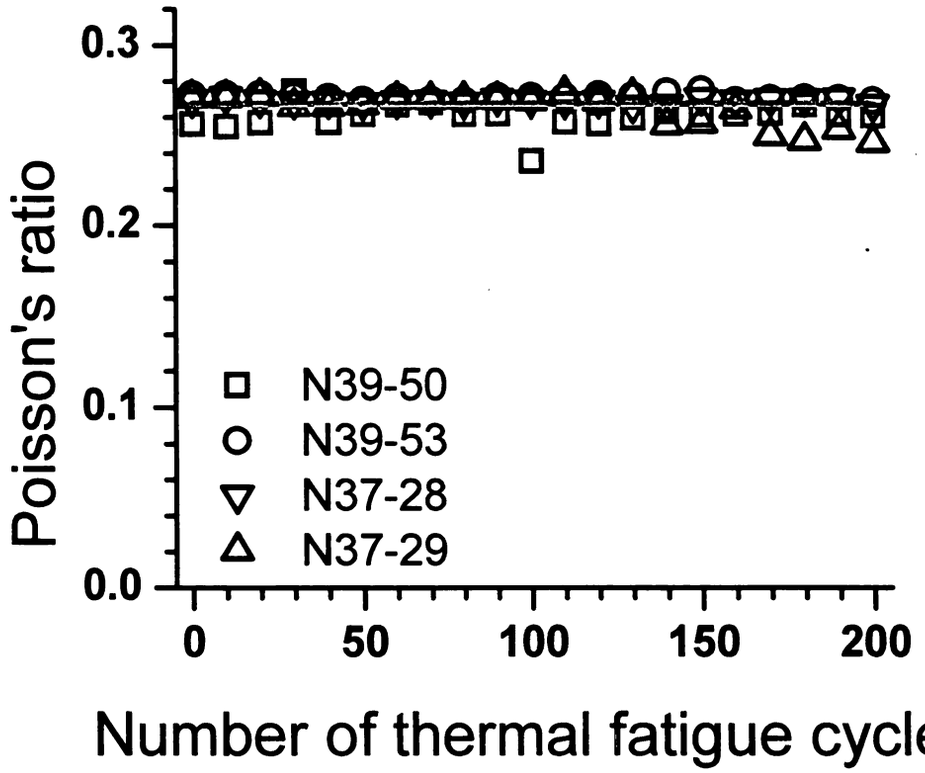

Figure 3.2.2.2. Resonant Ultrasound Spectroscopy (RUS) measurements of the Poisson's ratio as a function of the number of thermal fatigue cycles for reformulated n-type (LAST) samples, cycled in the small thermal fatigue chamber.

3.2.2.3. LASTT Specimens' Poisson's Ratio

As stated in Section 3.2.1.3. for the LASTT specimens, except P15-14 that fractured at N = 160 and specimen P15-17 that fractured at N = 190, E exhibited a 7% (0.256 – 0.271) variation as a function of the number of thermal fatigue cycles N for the other two specimens included in this study (Figure 3.2.2.3). The as-received Poisson's ratio of specimen P15-16 was 0.266, which changed to 0.268 after 200 thermal fatigue cycles, corresponding to a 0.8% change (Table 3.2.2). The difference between the maximum (N = 150) and minimum (N = 180) values of Poisson's ratio of P15-16 was only 2.2% (Table 3.2.2). The small changes in ν induced by thermal fatigue indicated that the average microcrack size and/or the number density of microcracks did not increase significantly within the 200 thermal cycles for the tested specimens (excluding P15-14 and P15-17).

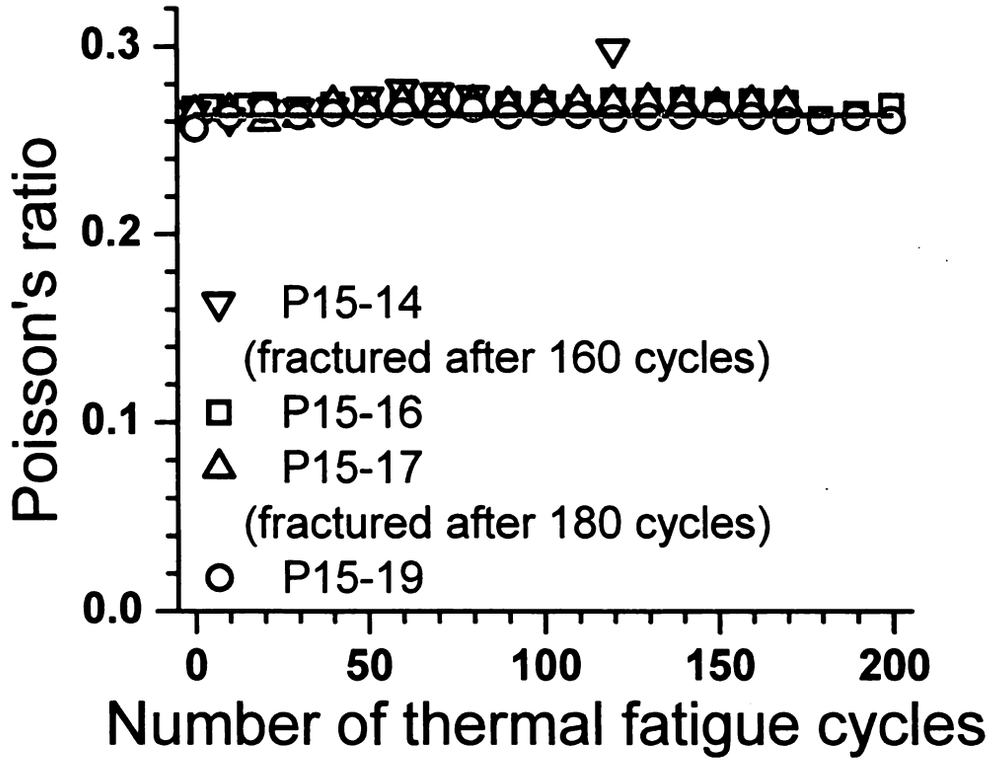

Figure 3.2.2.3. Resonant Ultrasound Spectroscopy (RUS) measurements of the Young's modulus as a function of the number of thermal fatigue cycles for p-type (LASTT) samples, cycled in the small thermal fatigue chamber.

3.3 Fracture strength of as-received and thermally fatigued LAST and LASTT

3.3.1. Fracture Strength

All disc-shaped LAST and LASTT specimens were fractured using the ring-on-ring (ROR) technique [ASTM 1499] following thermal cycling in the large thermal fatigue chamber (Figures 3.3.1-3.3.4). For the zero thermal cycle condition (the as-received specimens) a total of 20 specimens each of LAST and LASTT were fractured in two groups of ten specimens each (Figures 3.3.1-3.3.4). Approximately 60 LASTT and LAST specimens were thermally cycled in the large thermal fatigue chamber for 30, 60, 90,120, 150, or 200 thermal cycles in groups of 10 specimens each, except for the LASTT specimens subjected to 90 thermal cycles. For LASTT specimens that underwent 90 thermal fatigue cycles, two groups of ten specimens each were tested; since the first group tested had a low mean fracture strength (Figure 3.3.1) and a very large scatter (Figure 3.3.2) due to specimen blistering. The fracture strength data and validity of all LAST and LASTT specimens tested in ring-on-ring can be found in Appendix D (LASTT) and Appendix E (LAST).

3.3.1.1. Fracture Strength of as-received and thermally fatigued LASTT

The ROR fracture strength data of the LASTT specimens shows a band of fracture strength values between approximately 25 MPa and 40 MPa for range from 0 to 200 thermal fatigue cycles (Figure 3.3.1, for the numbers in parentheses near the plotting symbols (i,j), the first number "i" indicates the number of valid fractures obtained and the second number "j" indicates the number of specimens fractured for the given thermal shock treatment.). In terms of analyzing the relative spread in the fracture strength data for both the LAST and LASTT specimens included in this study, Weibull statistics could not be applied to the specimens since Weibull statistics would require at least 20 valid fractures at each thermal cycling condition. However, an alternative method to characterize the scatter in the data was performed by using the coefficient of variation, or CV (the standard deviation/mean), which was plotted for the LASTT (Figure 3.3.2) and LAST (Figure 3.3.4) specimens. For the LASTT fracture data, the CV ranged between about 0.1 and 0.2 except for one group of the as-received specimens for which CV $\approx$ 0.3, and both sets of the specimens after 90 thermal cycles where CV $\approx$ 0.36 and 0.45 (Figure 3.3.2).

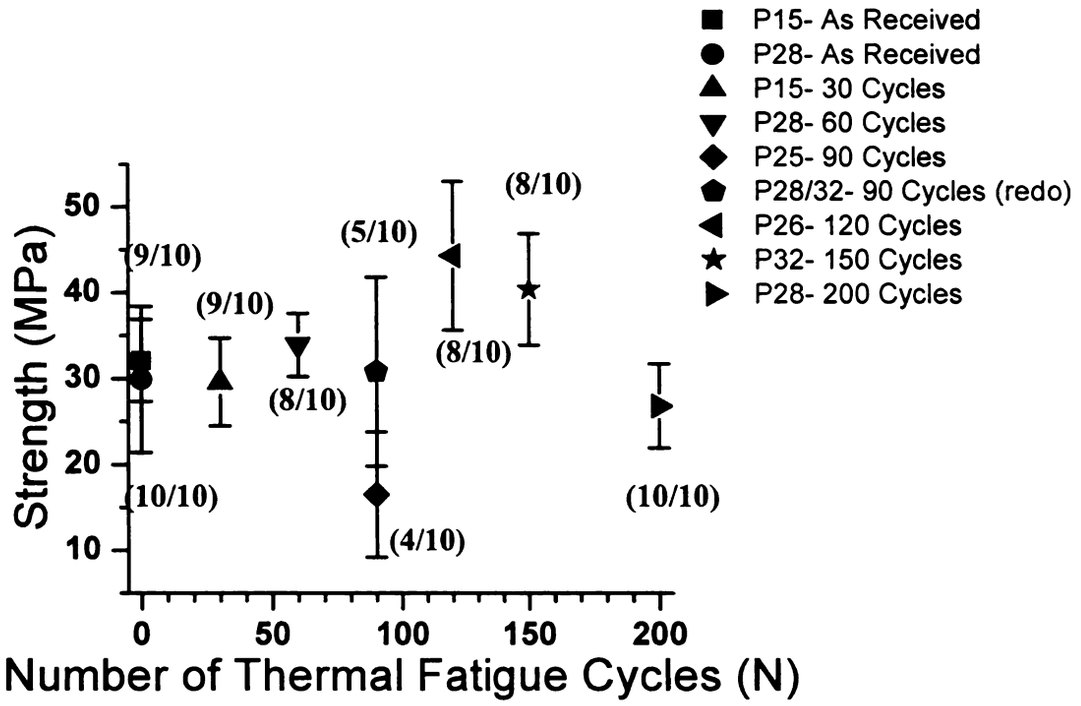

Figure 3.3.1. Ring on Ring (ROR) fracture strength as a function of the number of thermal fatigue cycles for p-type LASTT cycled in the large thermal fatigue chamber. For the numbers in parentheses near the plotting symbols (i/j), the first number "i" indicates the number of valid fractures obtained and the second number "j" indicates the number of specimens fractured for the given thermal shock treatment.

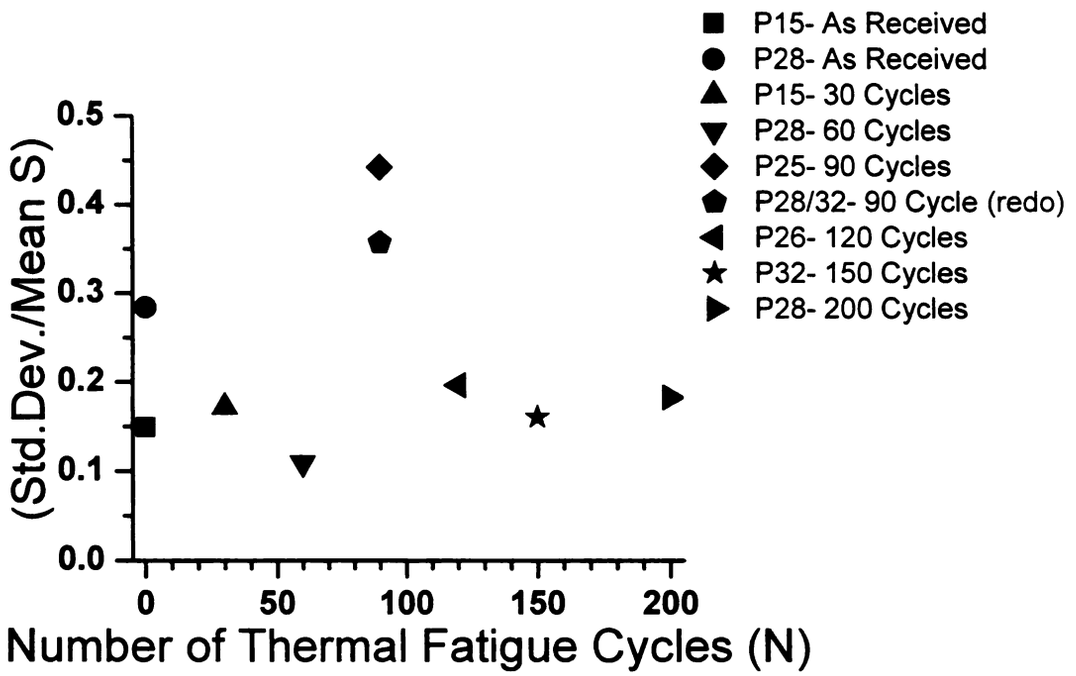

Figure 3.3.2. For the ROR fracture data shown in Figure 3.3.1, the coefficient of variation (standard deviation divided by the mean strength) versus the number of thermal fatigue cycles for the p-type LASTT specimens thermally cycled in the large thermal fatigue chamber.

3.3.1.2. Fracture Strength of as-received and thermally fatigued LAST

For the disc-shaped LAST specimens that were thermally cycled in the large thermal fatigue chamber, the mean ROR fracture strength values averaged between 15 MPa and 29 MPa for the 0 to 200 cycles, with the exception of one group of the as-received specimens, which had a mean strength value of 37 MPa (Figure 3.3.3, for the numbers in parentheses near the plotting symbols (i,j), the first number "i" indicates the number of valid fractures obtained and the second number "j" indicates the number of specimens fractured for the given thermal shock treatment.). The mean fracture strength for LAST was relatively constant between zero thermal cycle and 60 thermal cycles. Although large scatter was observed for 90, 120 and 150 thermal cycle data, a general trend could be found such that the mean strength decreased with an increasing number of fatigue thermal fatigue cycles (Figure 3.3.3). Surprisingly, the mean fracture strength for 200 thermal cycles is approximately 30 MPa, which is comparable to the ROR strength measured following 0, 30 and 60 thermal cycles (Figure 3.3.3). This may imply that the lower mean strengths for the specimens tested after 90, 120 and 150 thermal cycles is due to variations among the specimen batches and perhaps to the number density and size of the inclusions and surface pitting observed on the thermally cycled LAST.

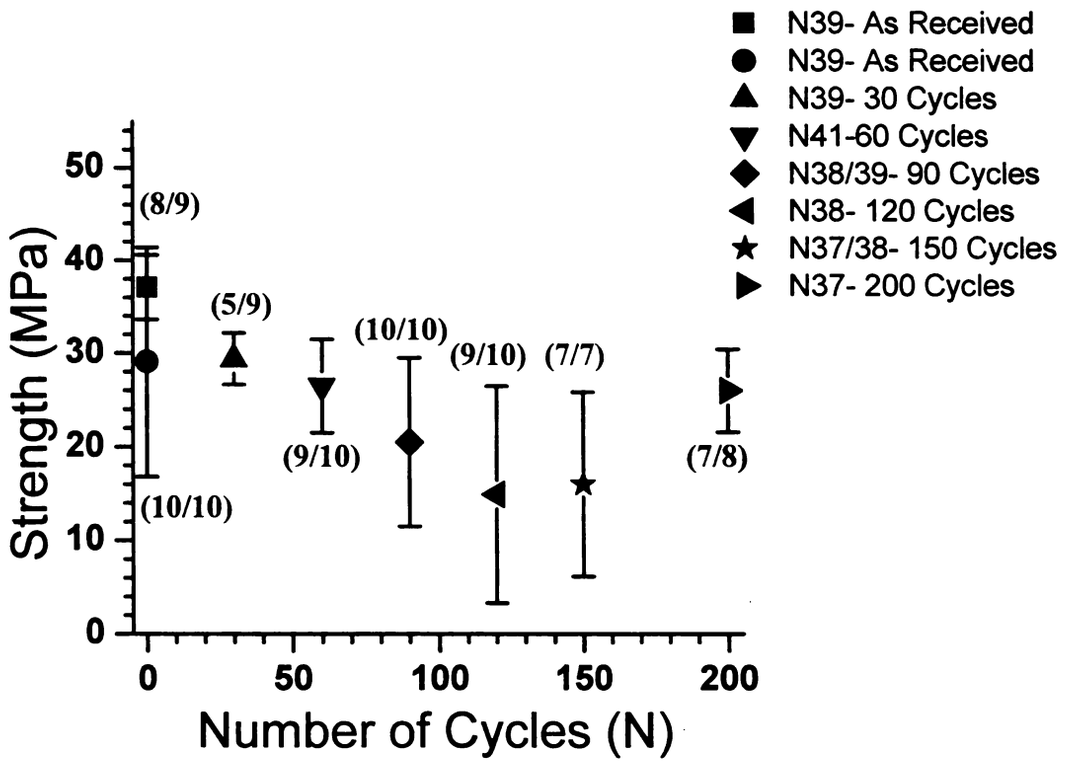

Figure 3.3.3. Ring on Ring (ROR) fracture strength as a function of the number of thermal fatigue cycles for LAST cycled in the large thermal fatigue chamber. For the numbers in parentheses near the plotting symbols (i/j), the first number "i" indicates the number of valid fractures obtained and the second number "j" indicates the number of specimens for fractured for the given thermal shock treatment.

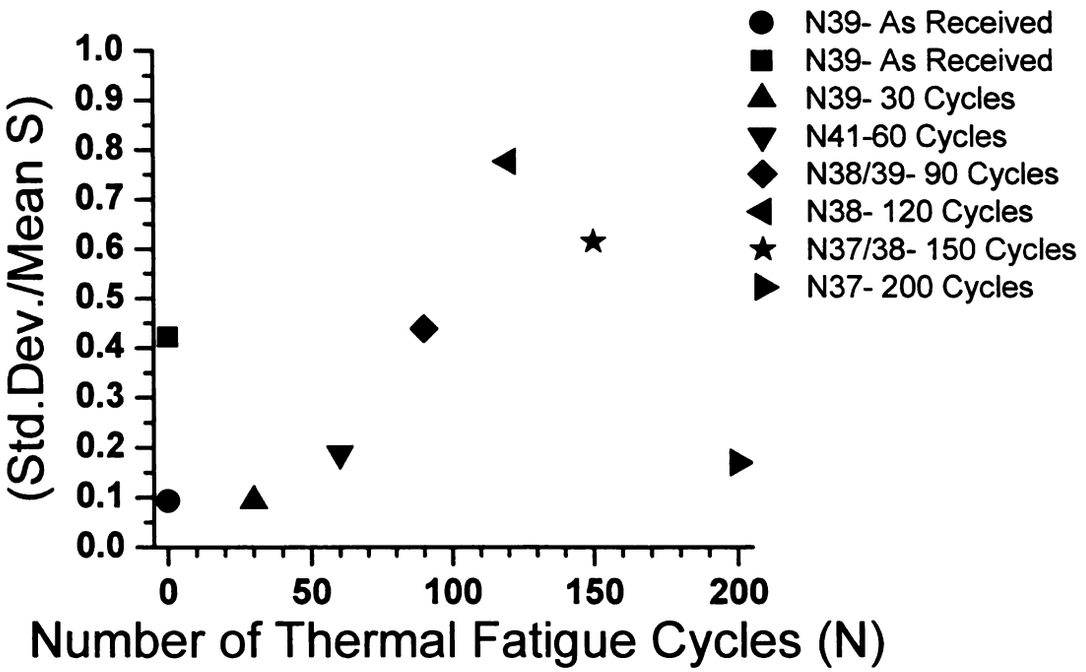

Figure 3.3.4. For the ROR fracture data shown in Figure 3.3.3, the coefficient of variation (standard deviation divided by the mean strength) versus the number of thermal fatigue cycles for the LAST cycled specimens thermally cycled in the large thermal fatigue chamber.

3.3.2. Weibull Statistics for as-received LAST and LASTT

Weibull statistics are used with ceramics, as a function of the material is as strong as the weakest flaw. The Weibull analysis of the LAST and LASTT as-received fracture strength groups is seen as a distribution of strength for the material. A test group of 20 samples or more is necessary to perform the Weibull analysis, and the larger the test set the more reliable the material's failure probability becomes. The higher the Weibull modulus is, the more the uniform flaws are distributed evenly within the material. A high modulus is generally around 10, where a low modulus is about 3.

3.3.2.1. Weibull Statistics for as-received LASTT

The Weibull modulus of the as-received LASTT P15 and P28 specimens show a distinct high strength and low strength trend (Figure 3.3.5). The low strength Weibull modulus had a variable distribution of 2.1 with a characteristic strength of 17.9 ± 6.9 MPa. The high strength Weibull modulus had a variable distribution of 6.1 with a characteristic strength of 32.7 ± 4.5 MPa.

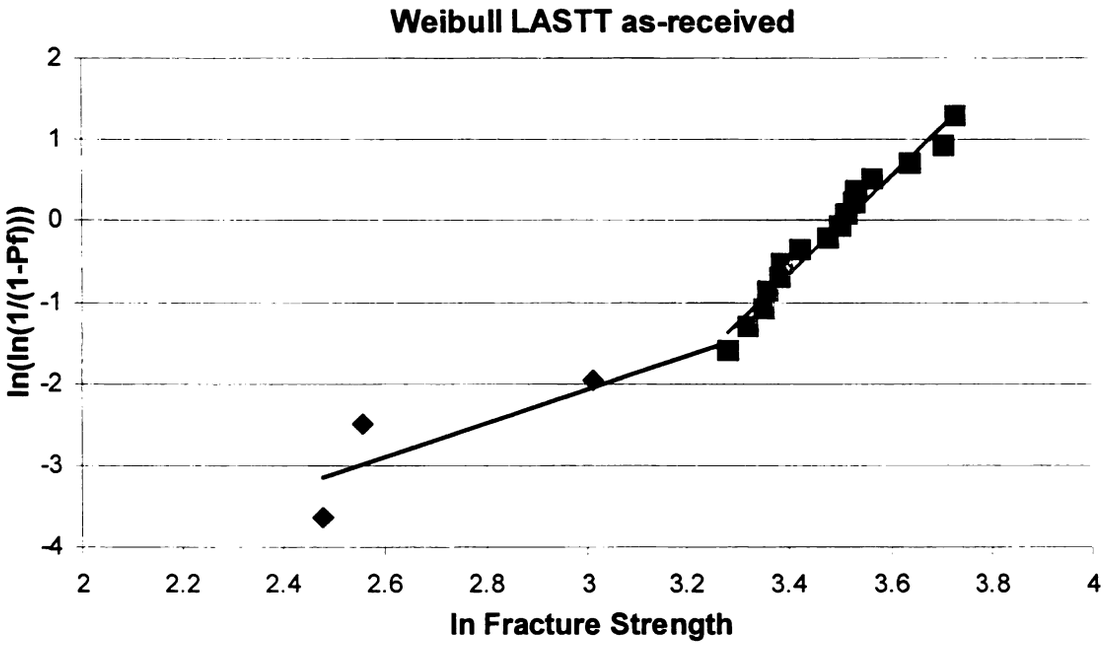

Figure 3.3.5. The Weibull modulus of the as-received LASTT P15 and P28 specimens show a distinct high strength and low strength trend. The low strength Weibull modulus had a variable distribution of 2.1 with a characteristic strength of 17.9 ± 6.9 MPa. The high strength Weibull modulus had a variable distribution of 6.1 with a characteristic strength of 32.7 ± 4.5 MPa.

3.3.2.2. Weibull Statistics for as-received LASTT

The Weibull modulus of the as-received reformulated LAST N39 specimens had a distinct high strength and low strength trend (3.3.6). The low strength Weibull modulus had a variable distribution of 1.4 with a characteristic strength of 19.8 ± 10 MPa. The high strength Weibull modulus had a variable distribution of 8.2 with a characteristic strength of 36.7 ± 3.6 MPa.

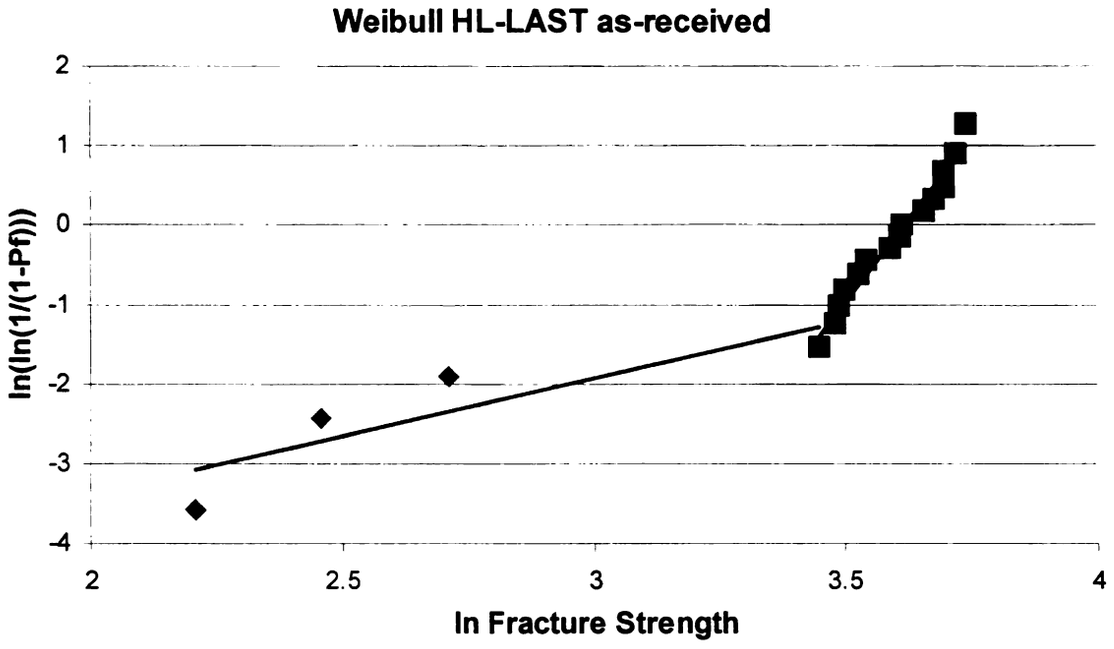

Figure 3.3.6. The Weibull modulus of the as-received high lead LAST N39 specimens show a distinct high strength and low strength trend. The low strength Weibull modulus had a variable distribution of 1.4 with a characteristic strength of 19.8 ± 10 MPa. The high strength Weibull modulus had a variable distribution of 8.2 with a characteristic strength of 36.7 ± 3.6 MPa.

3.3.2.3. Comparative Weibull Statistics for as-received LAST and LASTT

Both the reformulated LAST and LASTT as-received specimens give a similar strength distribution (Figure 3.3.7, the fractions in the parentheses indicate the number of valid fractures in each group over the initial sample size during ring-on-ring testing). When comparing the weibull analysis of the high strength reformulated LAST and LASTT as-received specimens a similar strength distribution for the materials was revealed (Figure 3.3.8). The LASTT Weibull modulus and characteristic strength were slightly lower than the as-received LAST disk specimens tested. The lower strength and modulus could have been attributed to data from samples with large interior flaws that would have lead to surface blistering had the sample been thermally fatigued.

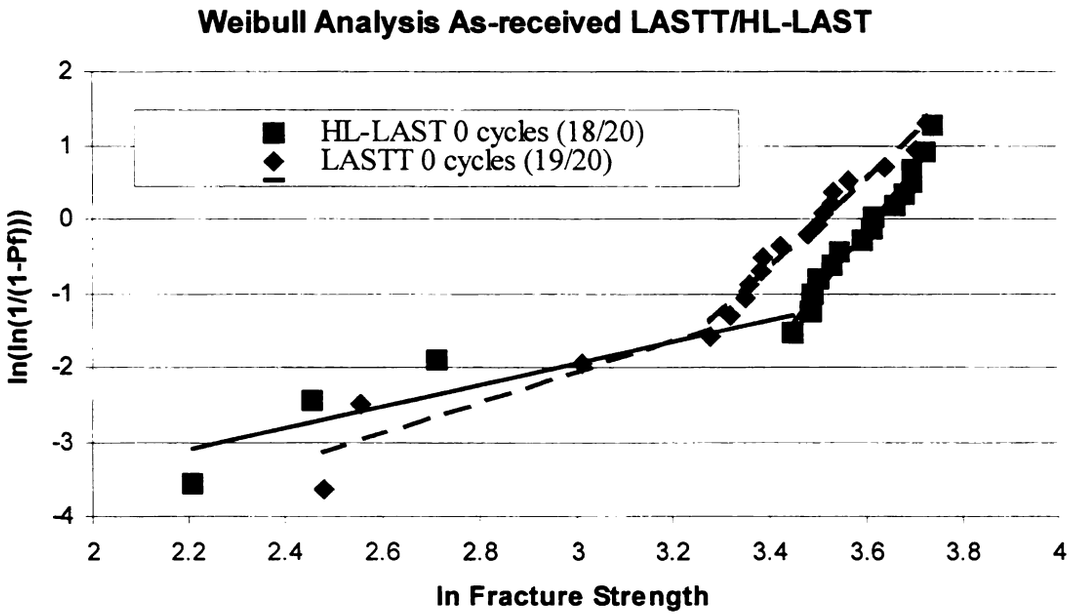

Figure 3.3.7. The weibull analysis compares both high lead LAST and LASTT as-received specimens. It is seen that there is a similar strength distribution for the LAST and LASTT samples. The fractions in the parentheses indicate the number of valid fractures in each group over the initial sample size during ring-on-ring testing.

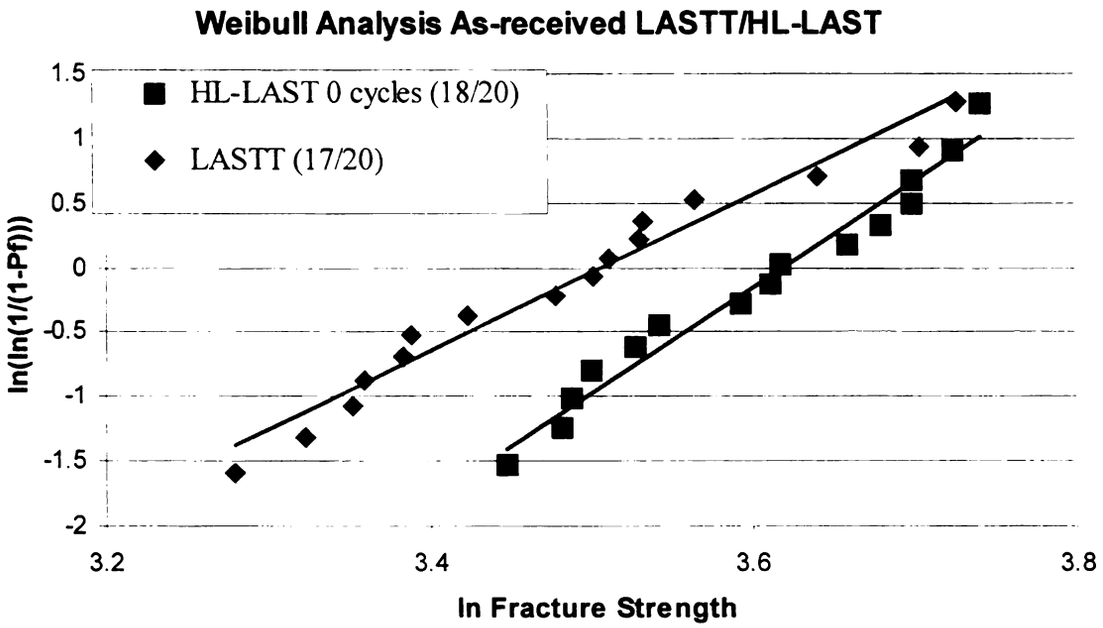

Figure 3.3.8. The weibull analysis shows only the high strength high lead LAST and LASTT as-received specimens. It is seen that there is a similar strength distribution for the LAST and LASTT samples. The fractions in the parentheses indicate the number of valid fractures in each group over the initial sample size during ring-on-ring testing.

3.4 Specimen surface finish and impact on this study

Prior to strength testing, a specimen's surfaces typically are polished to a mirror-like finish that corresponds to polishing with grit sizes of about one micron or less. Fracture testing earlier in this study indicated that if as-received LASTT specimens were polished to a mirror finish, their strength increased to about 40 – 50 MPa [Ren, Unpublished SERDP].

However, when thermoelectric modules are fabricated commercially, considerations of time and expense make it extremely unlikely that each surface of each thermoelectric leg would be polished to a mirror-like surface finish. Therefore, every one of the LAST and LASTT specimens reported on in this study had surfaces in the "as-received condition", which refers to the 400 grit surface finish each of the disc and plate specimens had when the specimens were received from Tellurex Corporation. Thus, the as-received specimen surface finish represents a more realistic surface condition for TE module fabrication rather than polishing to a mirror-like finish.

4. Summary and Conclusions

Hot pressed n-type LAST and p-type LASTT specimens were produced by Tellurex Corporation (Traverse City, MI) from the powder processing of cast ingots. Two types of specimens were produced for thermal fatigue testing. Disk-shaped specimens (25 mm in diameter, 2.5 mm thick, Figure 2.1.1) were thermally fatigued in a large thermal fatigue chamber and fractured in biaxial flexural ring-on-ring testing (Figure 2.6.9). Fracture strength data was obtained from the biaxial strength testing using a fixture fabricated a Michigan State University (Section 2.6). Parallelepiped plate-like specimens (12 mm x 10 mm x 2.5 mm, Figure 2.1.2) were thermally fatigued in a small thermal fatigue chamber and the elastic moduli of the specimens were determined using Resonant Ultrasound Spectroscopy (Figure 2.5.1). The Young's modulus and Poisson's ratio of the thermally cycled specimen was analyzed from the RUS data (Section 2.5).

The large thermal fatigue chamber was a pressure vessel 11 cm in diameter and 24.5 cm in length, with a 300-Watt, 120 V resistance heater used with a water-cooled copper cold plate 15.2 cm x 8.9 cm x 0.7 cm for thermal fatiguing 10 disk-shaped specimens simultaneously (Figures 2.3.12 and 2.3.13). The large chamber was fabricated and assembled by the Michigan State University Physics Shop approximately twelve years prior to the start of the thermal fatigue work described here. The small thermal fatigue chamber was a 30.5 cm x 30.5 cm x 2 cm sheet of clear Plexiglas with a rubber sheet gasket and a 26 cm diameter x 29 cm tall high-pressure glass bell jar as a pressure vessel. The chamber was equipped with a 75 Watt, 120 V, resistance heater and a 15.2 cm x 8.9 cm x 1.3 cm water-cooled copper cold plate capable of thermal cycling 2 plate-

shaped specimens. In both the large and the small thermal fatigue chambers, a fibrous zirconia ceramic blanket material insulated the sides of the specimens (large chamber Figure 2.3.11, small chamber Figure 2.3.19). Fei Ren at Michigan State University manufactured the small chamber for thermal fatigue testing. The specimens and the ceramic insulation were then sandwiched between the hot plate and the cold plate, creating a temperature gradient through the specimen thickness. The cold plate temperature was maintained at 40°C, while the hot plate temperature was cycled between 50°C and 400°C for a preselected number of thermal cycles.

Both the large and small fatigue chambers were sealed, evacuated with a mechanical pump and purged three times with argon gas. The thermal fatigue testing was performed in a flowing argon environment to minimize oxidation of the specimens. For the small chamber, the cold plate was cooled to a constant temperature water bath. For the large thermal fatigue chamber the cold plate was cooled by a solid state chiller.

In this study, inclusions approximately 50 to 75 microns in diameter were observed on the as-received LAST specimen surfaces. An EDS analysis indicated that the inclusions were generally lead poor, but had disjoint sub-regions within the inclusions that were rich in either silver or antimony (Figures 3.1.2.6a – 3.1.2.6e). All of the LAST specimens that were thermally cycled in either the small or the large thermal fatigue chambers showed surface pitting and a decrease in the number density of inclusions, which implies that the inclusions spalled off the surfaces during thermal fatigue. An EDS analysis indicated the chemistry of the inclusions are different than the average chemistry of the bulk material. Thus the spalling of the surface inclusions may be due to a mismatch in thermal expansion coefficient between the LAST matrix and the inclusions.

Twenty-one of the 90 LASTT disk-shaped specimens thermally cycled in the large thermal fatigue chamber blistered (Figure 3.1.3.1). The blistering in the samples was believed to have been the result of a decomposition reaction of a metal oxide in the LASTT powder during densification. The decomposition reaction resulted in a gas that became trapped at an elevated temperature (~1000°C) when the specimens' pores sealed. The blistering occurred in the LASTT disk-shaped specimens during the elevated temperature stage (400°C) of thermal cycling. The pressure from the expansion of the trapped gas and the increased softness of the material at the elevated temperature formed the blisters. The blisters on the specimens' surface were 5 mm to 1 cm in diameter and from 1 mm to 5 mm in height from the original specimen surface (Figures 3.1.3.1. - 3.1.3.4). The LASTT specimens with surface blisters were classified as giving invalid ring-on-ring fracture data (Section 2.6.10).

All LAST and LASTT specimens tested prior to thermal cycling and all specimens fatigued in either the large or small thermal fatigue chambers had an "as-received" surface finish (which was the 400 grit surface finish present when the specimens were received from Tellurex Corporation). This as-received surface finish was selected for both strength and elastic modulus testing since it was assumed that the as-received specimen surfaces was a more realistic surface finish for TE module legs than the mirror-like surface finish typically used in strength testing.

The elasticity/thermal fatigue testing of the initial LAST specimens resulted in decreases in the Young's modulus as large a 4.5 GPa, as well as a 14.5% decrease in the Poisson's ratio with the increase in the number of thermal fatigue cycles (Figure 3.2.1.1 and Figure 3.2.2.1). The elasticity/thermal fatigue testing on the reformulated LAST and

LASTT showed that the Young's modulus and Poisson's ratio were relatively insensitive to thermal fatigue cycling varying only about 2% in value, except for two specimens: P15-14 which fractured after 160 thermal cycles and P15-17 which fractured after 180 thermal cycles (Figures 3.2.1.2 – 3.2.1.3 and Figures 3.2.2.2 – 3.2.2.3). This indicates that the "average" microcrack length and/or number of microcracks do not increase appreciably during thermal cycling in the small thermal fatigue chamber (Section 3.2).

The ring-on-ring (ROR) fracture strength for both the as-received (not thermally fatigued) LAST and LASTT is comparable to ROR strengths measured on commercially available Bi_2Te_3 [Wereszczak 2009]. However there is no data available in the open literature for the strength or elasticity changes due to thermal fatigue of Bi_2Te_3 or any other thermoelectric material.

The ring-on-ring fracture for LASTT (p-type) shows a band of fracture strength values between approximately 25 MPa to 40 MPa for up to 200 thermal fatigue cycles (Figure 3.3.1), thus the fracture strength of LASTT did not degrade significantly during thermal cycling in the large thermal fatigue chamber. The LAST fracture data shows a band of strength values between about 15 MPa and 38 MPa for 0 to 200 thermal fatigue cycles (Figure 3.3.3).

The n-type LAST and p-type LASTT materials thermal fatigued in this study had mechanical properties comparable to those of commercially available Bi_2Te_3. The elastic moduli of the reformulated LAST and LASTT materials varied roughly 2% during the 200 thermal fatigue cycles. The fracture strengths were relatively constant for the n-type material at 30 MPa and 35 MPa for the p-type material with an increase in the 200 thermal fatigue cycles. The moderately constant fracture strength and elastic moduli of

the thermoelectric materials in this study were assumed to have occurred because the microcrack density and/or microcrack size did not increase from 0 to 200 thermal fatigue cycles.

5. Future Work

With an extension of time and funding there were several avenues of work that would have been pursued in the further development and testing of LAST and LASTT thermoelectric materials. If additional LAST and LASTT specimens were available, one could further investigate both the mechanical properties (elastic moduli, fracture strength, Weibull modulus) and the anomalies of the blistering and inclusions, which developed in the samples.

Elastic modulus measurements for thermally cycled specimens were complicated involving running the thermal chamber and testing the samples using Resonant Ultrasound Spectroscopy. A single 200-cycle run in the small thermal chamber took over two weeks and was only capable of fatiguing two samples simultaneously. An increase in the number of test specimens would result in a more accurate estimate of the LAST and LASTT Young's modulus and Poisson's ratio.

A larger test group of LAST and LASTT disk-shaped specimens cycled in the large thermal chamber and fracture tested in the ring-on-ring apparatus would allow for Weibull statistics to be applied in determining the scatter of the mean sample fracture strengths for all thermal fatigue cycle groups. However, Weibull statistics require a sample size of at least 20 valid fractures for each cycle group for the fracture testing analysis. To accomplish 20 valid fractures for each LAST and LASTT 30, 60, 90, 120, 150 and 200 thermal cycle group, an additional 10-15 samples would need to be cycled and fracture tested for each thermal cycle group.

Further investigation of the inclusions in the LAST samples and the bloating of the LASTT specimens could be performed. Thermal cycling and microstructural investigation under a larger scale would be possible. LAST inclusions would be observed on several additional samples during the thermal cycling process and the evolution of pitting on the specimens' surfaces compared. Since it was assumed that a processing issue during mechanical alloying of the raw LAST powder caused the inclusions, it would be important to see if variations in the ball milling time would have any change on the inclusion density and size within the samples.

A larger number of LASTT test specimens would determine if the bloating within the initial LASTT disk-shaped specimen thermal cycling was caused by a processing condition for a particular hot pressed specimen, group of specimens or the LASTT powder or if instead the LASTT material is prone to bloating.

Appendix A. Standard Operation Procedure for Large Thermal Fatigue Experiment with the Prototype Thermal Fatigue Chamber (Fei Ren), this standard operating procedure gives the ability to properly load and operate the large thermal fatigue chamber used in the thermal cycling of the wafer LAST and LASTT specimens.

1. Sample Preparation:

1.1 Measure the diameter with a micrometer and the thickness with a caliper of the specimens from at least three locations.

1.2 Weigh specimens using a digital balance.

1.3 Record the dimensions and mass in the log book.

1.4 Note any apparent defects (cracks, chips, scratches, porosities, etc.) on the samples.

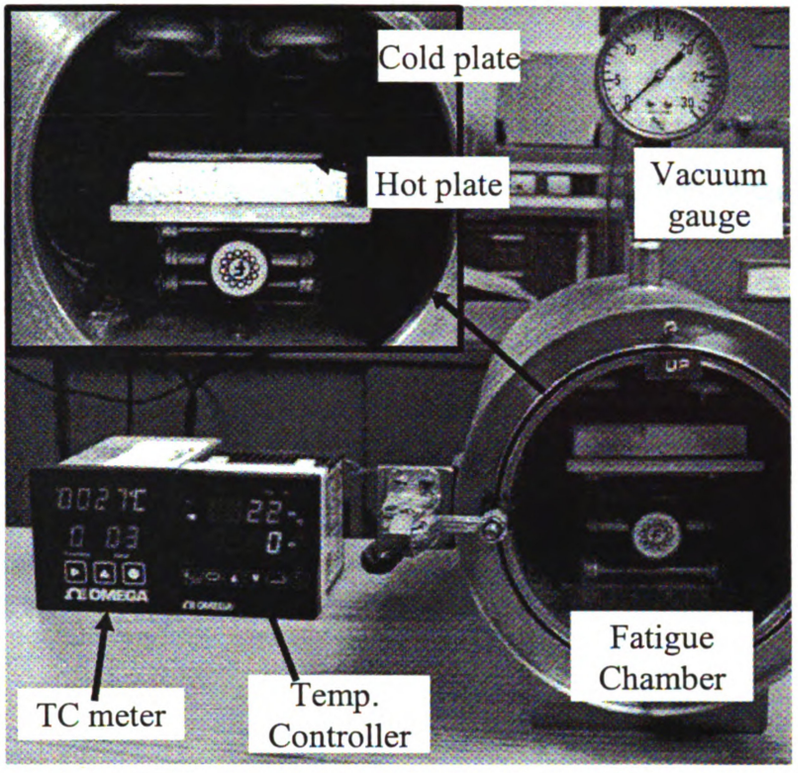

Figure A1. Front view of the thermal fatigue chamber system.

2. Loading the Samples:

2.1 Carefully place the pre-cut felt insulation on top of the hot plate (*do not disturb the thermal couples).

2.2 Place the sample(s) inside the insulation felt. Record the positions of the samples in the notes section of the log book.

2.3 Place the hot plate assembly in the thermal fatigue chamber and align with the cold plate.

2.4 Raise the specimen stage until the samples are just touching the cold plate. Do not over tighten the samples against the cold plate, which might cause the samples to fracture.

2.5 Apply vacuum grease onto the O-ring of the front cover. Put the front cover in place and tighten the screws to form a good seal.

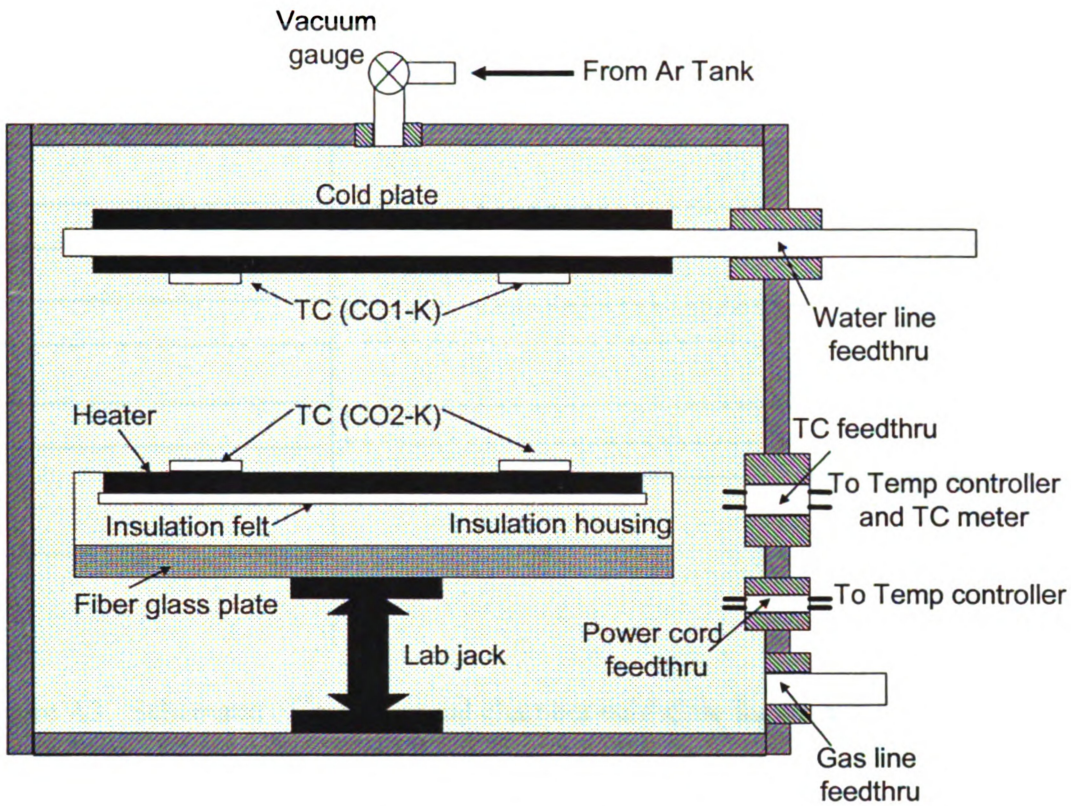

Figure A2. Schematic of the thermal fatigue chamber.

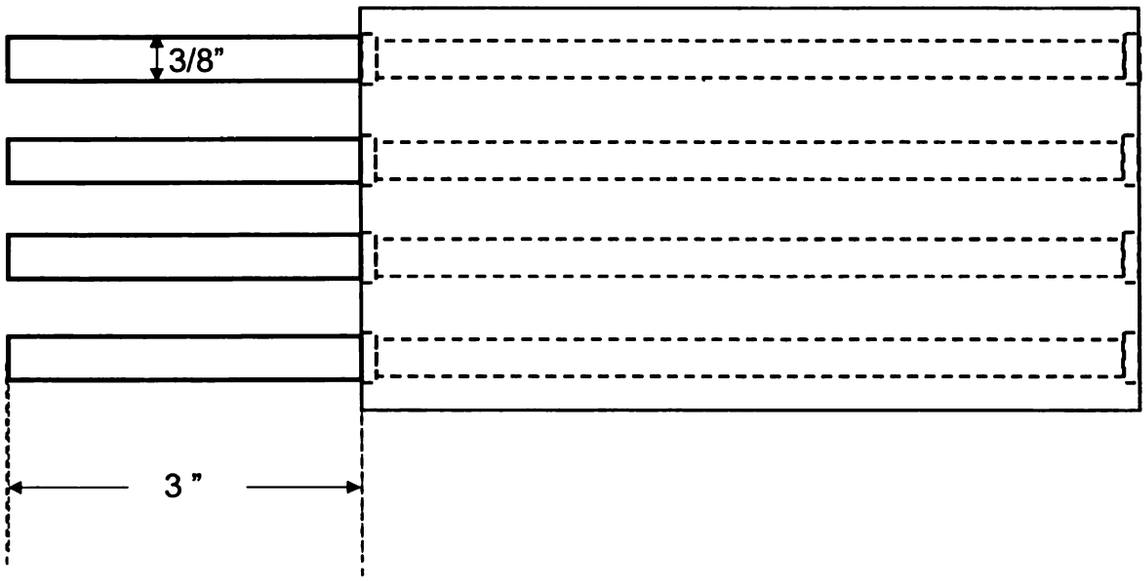

Figure A3. Schematic of large thermal chamber cold plate for construction by MSU physics shop.

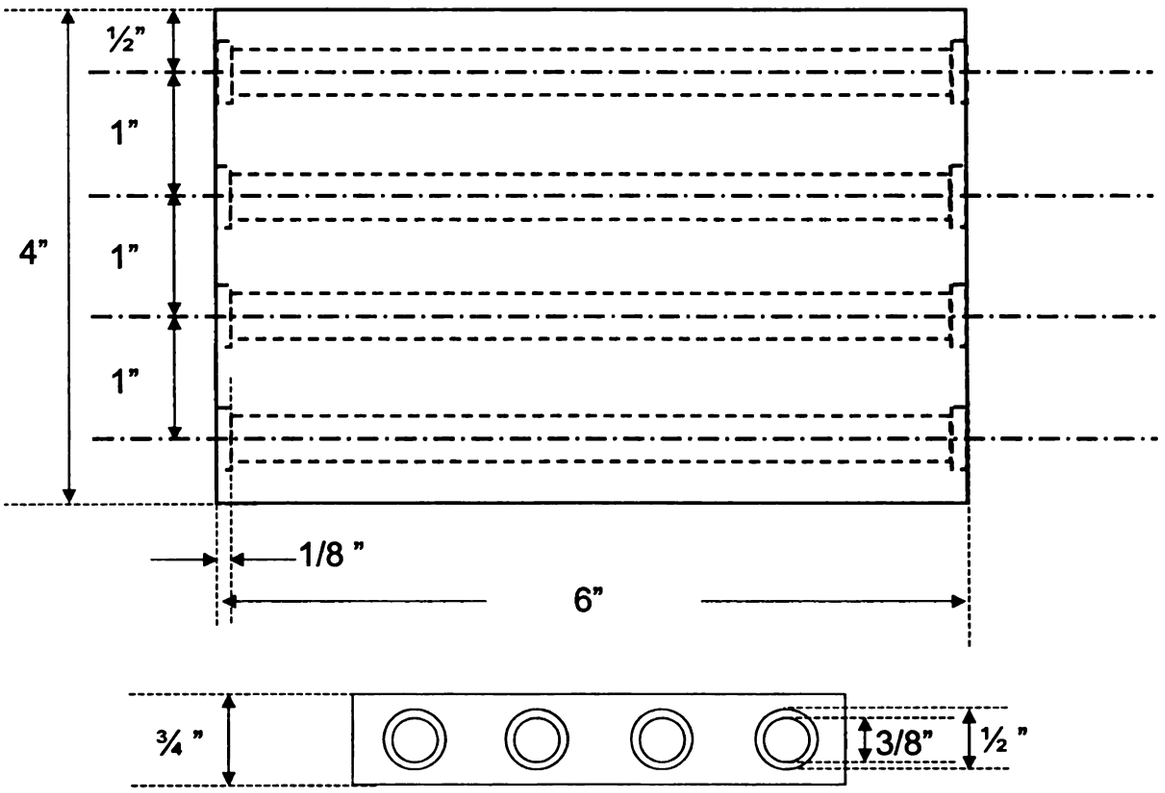

Figure A4. Detailed schematic of large chamber cold plate.

3. Pumping/purging the chamber:

3.1 Plug in the power cord of the vacuum pump into the surge protector.

3.2 Close the valve on the top of the chamber, which connects to the Ar tank.

3.3 Connect the quick-disconnect adapter to the vacuum pump.

3.4 Turn on the pump.

3.5 While the vacuum pump is on, tighten down the screws on the front cover of the thermal fatigue chamber.

3.6 Turn off the vacuum pump when the vacuum gauge reads 30 psi.

3.7 Switch the quick-disconnect adapter to the bubbler (The valve of the bubbler should be closed!).

3.8 Open the valve on the Ar tank counter-clockwise. Open the valve on the top of the fatigue chamber to purge the chamber with Ar gas. When the vacuum gauge reads zero psi, open the bubbler valve slightly to check the Ar pressure in the chamber (Ar bubbles should be coming out from the bubbler).

3.9 Repeat steps 3.3 to 3.8 for another two times.

3.10 Leave the Ar running for the rest of the experiment. One can adjust the regulator on the Ar tank to maintain a small continuous Ar flow as indicated by bubbling in the bubbler.

4. Thermal Cycle Fatigue Experiment:

4.1 Turn on the chiller. Note: The temperature is currently set at 38.5°C to achieve a cold side temperature of 40°C at the cold plate. It may take some time for the chiller to reach the set temperature; one may turn on the chiller before pumping the chamber to save time.

4.2 Turn on the power for the heater, thermal couple meter, and temperature controller.

4.3 Check the temperature readings on the thermal couple meter and the temperature controller, which should be close to room temperature.

4.4 Turn on the computer.

4.5 Open the program "Green Series LL100" – thermocouple #1

4.5.1 Choose "Multi-monitor Tool" then "Start monitor"

4.5.2 Choose "Front communication" and "COM3" serial port, and then click "Execute".

4.5.3 In the "Trend setup" step, choose the parameters to monitor and set corresponding scales. Note: the current setting includes:

Parameter	**Scale**	**Color**
Current temperature (PV)	0 – 600°C	Blue
Programmed temperature (CSP)	0 – 600°C	Red
Output power	0 – 100 %	Green

4.5.4 Choose "Multi-monitor" → "Start trend display".

4.6 Open the program "CN606" –thermocouples #2 – #8

4.6.1 Click "Run"

4.6.2 Type the file path and file name in the field labeled "SavePath"

4.6.3 Check the box "Datalogger".

4.7 On the temperature controller UP550E, choose the desired program using the "Pt No." arrows; and then press and hold the "Run" button for ~ 2 secs to start the program. Note: currently program #1 is in use, which cycles between 50°C and 400°C for 30 cycles.

5. Shutting down the Experiment/Removing the samples:

5.1 Turn off the Ar tank and close the valve on the top of the fatigue chamber.

5.2 Close the valve of the bubbler. Disconnect the quick-disconnect adapter from the bubbler.

5.3 Turn off the bubbler.

5.4. In the "Multi-monitor" program, choose "Multi-monitor" → "Stop trend display", one will be asked to save the temperature profile. Exit the program.

5.5 In the CN606 program, the temperature profiles will be saved automatically. Exit the program.

5.6 Turn off the power for the heater, thermal couple meter, and temperature controller.

5.7 Remove the screws on the front cover of the chamber and remove the cover.

5.8 Lower the stage approximately 1 ½ -2"down. Remove the sample stage from the chamber. Remove the precut felt insulation from the stage without disturbing the samples. Remove the samples.

6. Temperature controller UP550E – set program pattern using Green Series LL100 (for advanced operations, refer to the product manual).

6.1 Open the program "Green Series LL100" and select "Program Pattern Setting Tool"

6.2 Select "UP550"

6.3 To make a new temperature profile → choose "new"; to modify existing profile → choose "Open user file"; to modify profile on the temperature controller → choose "Uploading from controller".

6.4 In the main menu, there are three options: (Note: do NOT change the current setting unless necessary!)

6.4.1 *Program condition setting*: These settings work fine for thermal cycling experiment required by SERDP and should NOT be changed unless necessary (refer to the manual).

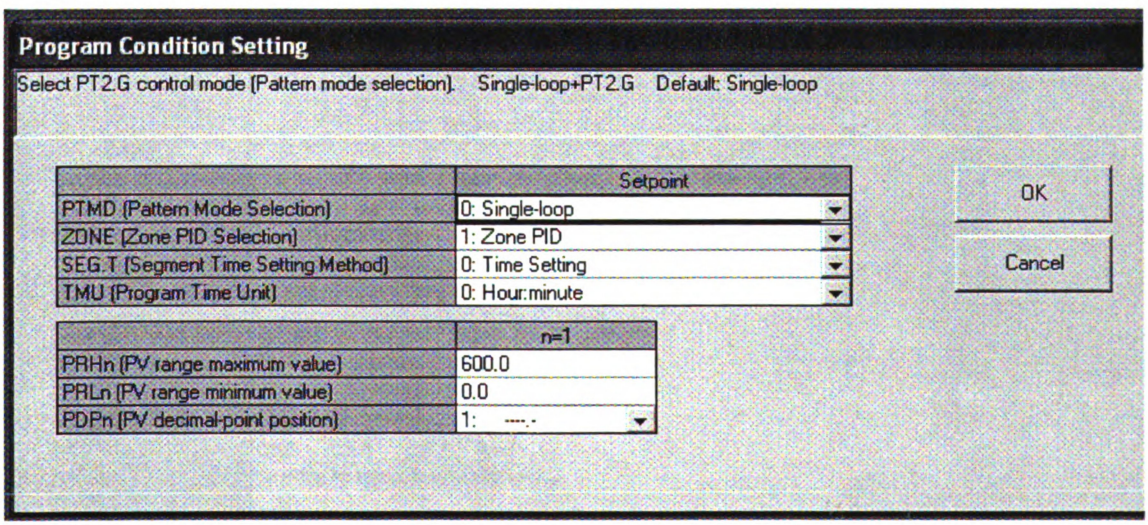

6.4.2 *Pattern start setting*: the current program is set to repeat 29 times (a total number of 30 cycles) between segment 1 and segment 4. To change these settings, type in desired numbers in the fields labeled as: "RCY" for number of repetitions, "RST" repetition start segment, and "REN" repetition end segment.

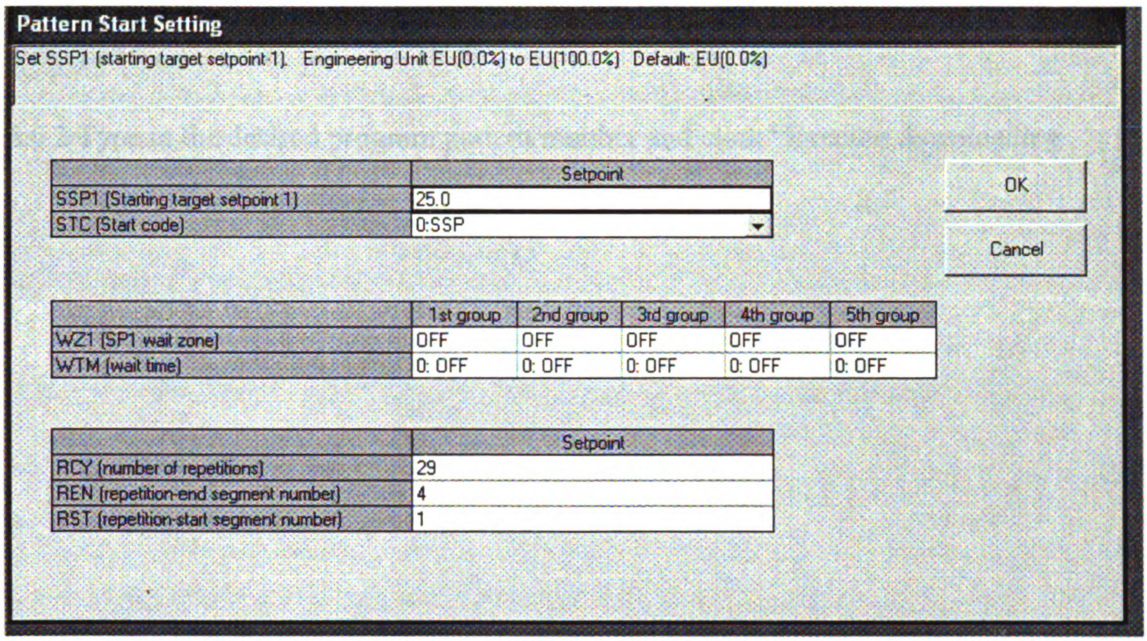

6.4.3 *Program pattern setting*: To change the program of the hot plate, type in the temperature and time in the lower portion of the window for each segment. A temperature-time profile will appear automatically.

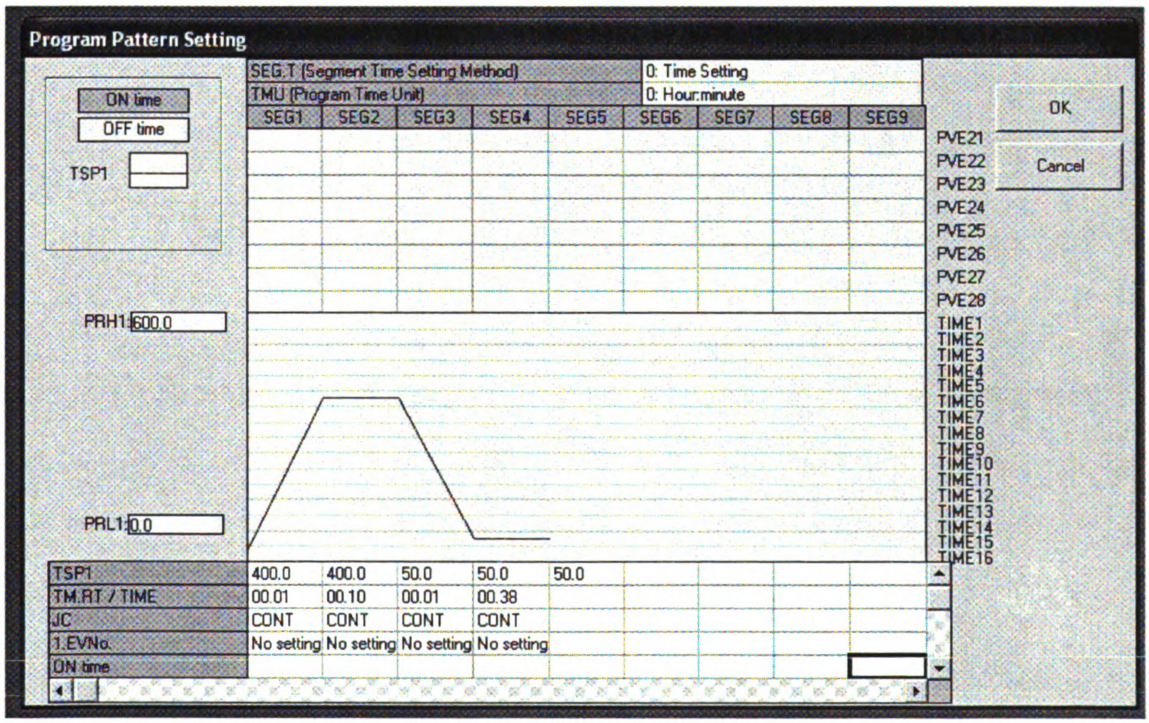

6.5 Save the new/edited program(s) on the computer.

6.6 Choose "Communication" → "Download to controller":

6.6.1 Select "Communication through front panel", "Serial communication", and "COM3".

6.6.2 Type in the desired program pattern number and click "Execute downloading

Appendix B. Standard Operation Procedure for Thermal Fatigue Experiment with the Prototype Thermal Fatigue Chamber (Dan Kleinow and Fei Ren 12-16-2008). This standard operating procedure gives the ability to properly load and operate the small thermal fatigue chamber used in the thermal cycling of the parallelepiped LAST and LASTT specimens.

1. Sample Preparation:

1.1 Measure the length, width, and thickness of the specimens with a caliper at three different locations.

1.2 Weigh specimens using a digital balance.

1.3 Record the dimensions and mass in the log book.

1.4 Note any apparent defects on the samples.

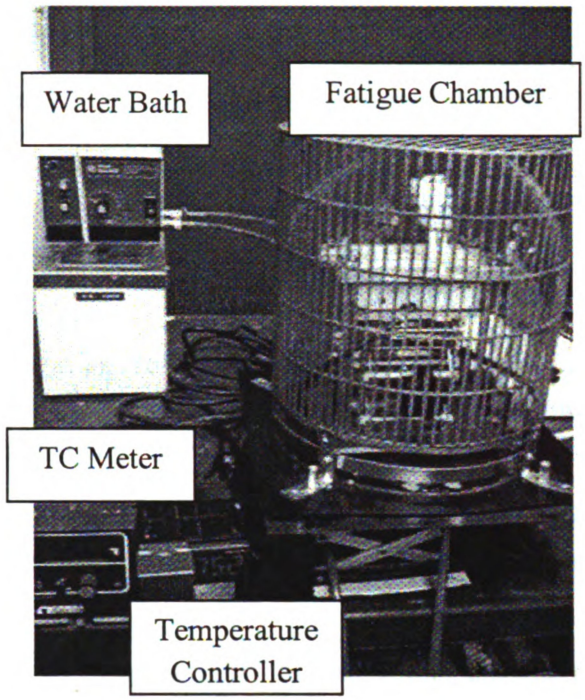

Figure B1. Small thermal fatigue chamber with cold plate chiller and thermocouple controller and thermocouple meter.

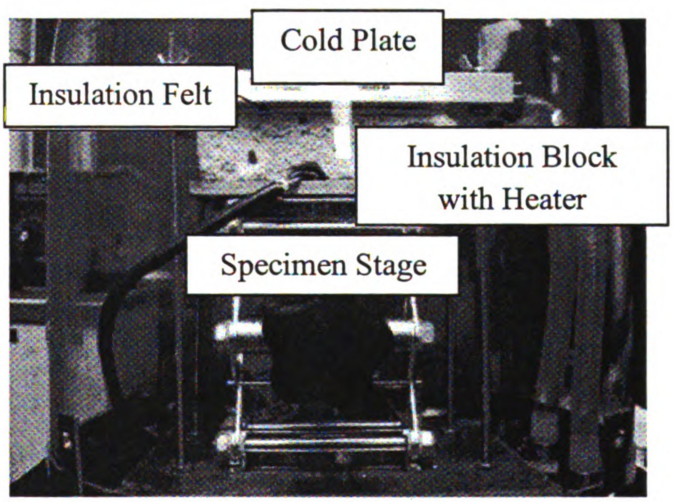

Figure B2. Small thermal chamber hot plate assembly in position under the cold plate.

2. Mounting the Samples:

2.1 Lower the specimen stage 1 ½" from the bottom of the cold plate.

2.2 Carefully place the pre-cut felt insulation on top of the hot plate (*do not disturb the thermal couple). Good to have more details on the refractory felt insulation. Pre-cut to what dimensions? What refractory material is the insulation felt? What thickness? What vendor and

2.3 Place the sample(s) on inside the insulation felt. The felt is cut so that there is a hole that is the same dimensions as the specimen? Record the positions of the samples (if more than one sample is being tested) in the notes section of the log book.

2.4 Raise the specimen stage until the samples are just touching the cold plate. Do not over tighten the samples against the cold plate, which might cause the samples to fracture.

2.5 Place the glass bell jar firmly against the rubber mat and inside the metal band and the "L" brackets. Using a flat head screw driver, loosen the screw at the back of the platform if the metal band is too tight.

2.6 Using a flat head screw driver, tighten the screw at the back of the platform until the metal band is firmly tight around the glass dome.

2.7 Place the metal cage on top of the glass bell jar. The metal cage must be in place during the experiment since it is a safety barrier if the bell jar implodes during the evacuation/purging procedure. (the metal cage is only held on due to gravity)

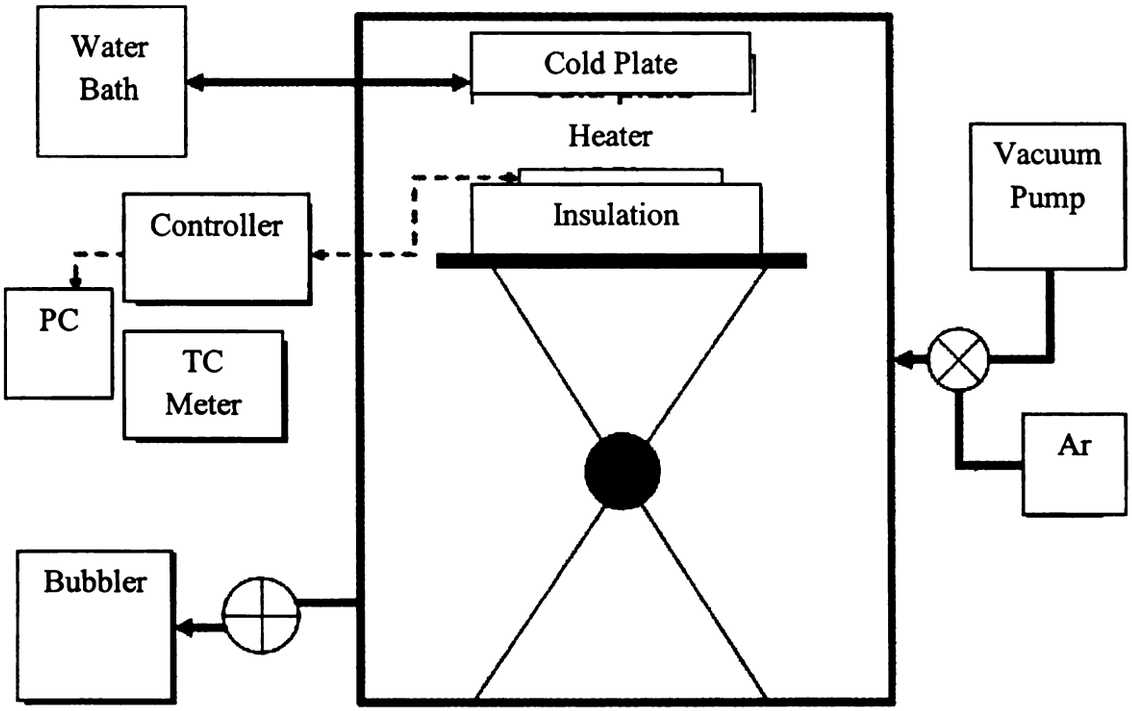

Figure B3. Schematic of the thermal fatigue system.

3. Pumping/purging the chamber:

3.1 Plug in the power cord from the vacuum pump into the surge protector.

3.2 Close the valve in the outlet line of the chamber. To prevent water back-filling, remove the outlet line from the bubbler. (Bubbler liquid is water. How much water is put into the bubbler beaker and what size beaker is used for the bubbler?)

3.3 Connect the quick-disconnect adapter in the inlet line of the chamber to the vacuum pump.

3.4 Turn on the power switch.

3.5 While the vacuum pump is on, tighten down the four hexagonal nuts on the chamber platform at each L bracket using an Allen wrench and a 5/16" socket wrench. (When the vacuum has pumped all of the air out of the chamber, it will begin to make a noise that sounds like shaking a spray paint can).

3.6 Turn off the vacuum pump and disconnect the pump from the chamber.

3.7 Connect the quick-disconnect adapter in the inlet line of the chamber to the Ar tank.

3.8 Open the valve on the Ar tank counter-clockwise. Purge the fatigue chamber with argon gas at a purge of 10 KPa, which takes approximately 2 minutes. (The tank will make little or no sound when the chamber has been filled).

3.9 Repeat steps 3.3 to 3.9 for another two times.

3.10 Leave the chamber connected to the Ar tank after the third purging step.

3.11 Place the outlet line of the chamber into the bubbler and open the valve in the outlet line.

3.12 Adjust the regulator on the Ar tank to maintain a small continuous Ar flow as indicated by bubbling in the bubbler.

4. Thermal Cycle Fatigue Experiment:

4.1 Turn on the power to the surge protector for the heater, water bath, thermal couple meter, and temperature controller which will power up the components immediately.

4.2 Adjust the temperature of the water bath (it is currently set at 40°C). (Temperature is set manually by an indicator knob on the water bath).

4.3 Check the temperature readings on the thermal couple meter and the temperature controller using the external temperature controller and thermocouple meter, which should be close to room temperature.

4.4 Turn on the computer.

4.5 Open the program "Multi-Comm-CN8200.MCS".

4.5.1 User Name: user Password: user

4.5.2 From the top menu select: options→Logging

4.5.3 Enter the date the experiment is being conducted.

4.5.4 Then, from the top menu select: Controller → Start Recipe

What is one wants to change the maximum temperature at which the fatigue cycle is run?

5. Shutting down the Experiment/Removing the samples: (Emergency shutdown and "normal" shutdown)

Emergency shutdown procedure:

In the case of an emergency, the emergency shutdown is done by turning of the surge protector which runs the small thermal fatigue chamber (hot plate, temperature controller, thermocouple meter, chiller).

Shutdown procedure when the experimental run is complete:

When the experiment is finished, the temperature controller which connects the hot plate thermocouple to the computer should read "STBY" (standby). This indicates that the experiment has completed its set number of cycles.

5.1 Close the regulator on the Ar Tank and use the quick connect fitting to disconnect the Ar tank from the chamber.

5.2 Close the valve in the outlet line and remove the outline line from the bubbler.

5.3 Remove the metal bird cage from the bell jar. Use a flat head screw driver to loosen the screw at the back of the platform. Loosen the hexagonal nuts on the platform at each L bracket using an Allen wrench and a 5/16" socket wrench. Lift the glass dome up from the platform.

5.4 Lower the stage approximately 1 ½ -2"down. Remove the precut zirconia felt insulation from the stage without disturbing the samples. Remove the samples.

5.5 Unplug the vacuum pump from the power strip.

Log Book:

Two tables need to be filled out when conducting the thermal fatigue experiment.

The first table:

Date/Operator/sample #/ Number of cycles/ Note

*In the Note section, record the position of the samples relative to the thermal couple.

The second table:

Sample #/ Number of cycles/ Mass/ Thickness/Length/

Appendix C. Bluehill ROR-BFT Test Protocol Software Standard Operating Procedure (SOP) for the proper programming, loading and testing methods for Ring-on-ring fracture testing. The Appendix has the step by step process for programming the computer used to run the Instron machine with the ring-on-ring apparatus, as well as the testing procedures to properly prepare and run the Instron and Bluehill safely.

Creating a New Test Method

1. Click on the "Method" icon from the Bluehill Home screen.

2. Click "New" icon

3. Next, choose the test type for the method that you want to create from the pull down menu, and click on create.

4. Click the "Save As" icon and save the method with a name unique to what the method will be used for.

5. Next, go through all of the navigation bar items on the left of the screen and make changes to the parameters in the test method. You have the opportunity to set up the information about samples, the controls of the experiment, the output tables, graphs, and reports. You also have the ability to set up the method as a prompted test.

6. You are now ready to use the test method to run specimen tests.

7. Click the "Print" icon if you want a copy of the method parameters that you set up.

8. When you are finished click the "save & close" icon on the lower right side of the screen.

Running a Test

1. To begin, turn the power on for both the Instron computer and the Instron machine.

2. Open the Bluehill Instron program from the computer program list and from the Bluehill home screen click on the "Test" icon. If prompted to by the Bluehill program, press the EEEI button located on the Instron control panel to allow a connection between the computer and the Instron.

3. Choose a test method file containing the test parameters that you want to use to run your tests. You can choose from a recently used method or "Browse" through the computer files for other methods. You can read a description of the method file by clicking once on the file name, and choose the method file by double clicking on it or clicking the next button.

4. Next enter the name and choose a location for the sample data file.

5. If you choose a prompted test, then follow the instructions until the testing is complete. If you choose an unprompted test, enter all of the required inputs to run the tests (loading rate, number of samples, maximum load, compression/tension loading) .

6. Mount a Specimen in the Ring-on-ring Biaxial Flexural Testing Cage and lower the loading rod to the preload position (loading rod ball and loading fixture hemispherical cavity align).

7. Once the specimen has been loaded click Next on the right hand blue side bar.

8. Next the program asks for a name and description for the sample, this is done before each sample is tested in the Instron. Ensure to refer to each specimen properly as the names cannot be changed in the program once testing has begun.

9. Before initiating each test for each specimen the Balance Load and Reset Gauge Length buttons, located at the top of the Bluehill page, must be clicked. This will zero the gauge length and load for the Instron machine for each specimen. The Gauge Load may not hold at zero Newtons, but a variation of ± 10 N is allowable. If the variation is larger than ± 10 N than the load must be reset again.

10. The ring-on-ring testing is initiated by again clicking the Next arrow located on the right hand blue side bar.

11. The ring-on-ring test must be stopped manually by clicking the STOP button on the left hand blue side bar. The testing is stopped once the specimen fractures. It is known that the specimen has fractured because the specimen will make a pop sound and the loading on the specimen will drop sharply (seen on the Bluehill testing graph).

12. Once the program has been stopped, the program will prompt for a comment on the testing, this is where a brief summary of the testing for the sample may be included (cataloging of information such as valid or invalid fractures and/or program problems). The Next button on the left hand blue side bar can again be clicked, prompting for a new sample to be prepared for testing.

13. The Load rod can then be raised from the ring-on-ring cage and the tested sample removed. A new sample can then be loaded into the cage and instructions 5-13 can be repeated until all specimen have been tested.

14. Once the testing is complete, click on "finish" to end the test. An output file for the experiment will be saved under the name and at the location given at the beginning of the experiment.

Entering specimen specification

1. Open Bluehill Instron software from the computer main window. A window showing Bluehill Main Menu will appear with icon of Test, Method, Report, Admin, User, Help and Exit.

2. Click Method, then choose a method that has been created and open it.

3. Click the Method tab and edit the following parameters: General (Method and Sample); Specimen (Dimensions); Control; Results and Report then save as (create a new file name).

Appendix D. Ring-on-ring biaxial flexural data for all LASTT specimens tested. The Tables in this appendix contain all measurements and validity for all LASTT specimens tested for 0, 30, 60, 90, 120, 150, and 200 thermal fatigue cycle using ring-on-ring technique. A brief description for specimens with an invalid or premature fracture can be found under the specimens corresponding table.

v - Poisson's Ratio
Ds - Diameter of small ring (mm)
DL - Diameter of large ring (mm)

Table D1. P15: As-received

Specimen	Diameter (mm)	thickness (mm)	Peak load (N)	v	Ds	DL	Strength (MPa)	Fracture
P15-27	25.43	2.52	390	0.27	20	10	30.7	Valid
P15-28	25.43	2.50	520	0.27	20	10	41.6	Valid
P15-29	25.43	2.54	440	0.27	20	10	34.1	Valid
P15-30	25.42	2.50	370	0.27	20	10	29.6	Valid
P15-31	25.42	2.54	370	0.27	20	10	28.7	Valid
P15-32	25.42	2.49	180	0.27	20	10	14.5	Invalid
P15-33	25.42	2.51	350	0.27	20	10	27.7	Valid
P15-34	25.40	2.51	480	0.27	20	10	38.1	Valid
P15-35	25.41	2.54	380	0.27	20	10	29.5	Valid
P15-36	25.42	2.51	360	0.27	20	10	28.5	Valid

-P15-32 was an invalid fracture, propagating through a pre-existing crack in the sample during ring-on-ring testing.

Table D2. P28: As-received

Specimen	Diameter (mm)	thickness (mm)	Peak load (N)	v	Ds	DL	Strength (MPa)	Fracture
P28-24	25.55	2.47	145	0.27	20	10	11.9	Valid
P2P28-25	25.52	2.50	161	0.27	20	10	12.9	Valid
P28-26	25.53	2.52	338	0.27	20	10	26.6	Valid
P28-27	25.53	2.50	255	0.27	20	10	20.4	Valid
P28-28	25.45	2.51	416	0.27	20	10	33.2	Valid
P28-29	25.45	2.48	397	0.27	20	10	32.4	Valid
P28-30	25.47	2.46	489	0.27	20	10	40.6	Valid
P28-31	25.51	2.50	427	0.27	20	10	34.2	Valid
P28-32	25.50	2.53	427	0.27	20	10	33.5	Valid
P28-33	25.50	2.45	422	0.27	20	10	35.3	Valid

Table D3. P15: 30 Thermal Fatigue Cycles

Specimen	Diameter (mm)	thickness (mm)	Peak load (N)	v	Ds	DL	Strength (MPa)	Fracture
P15-38	25.41	2.53	303.4	0.27	20	10	23.68	Valid
P15-39	25.41	2.54	349	0.27	20	10	27.03	Valid
P15-40	25.43	2.50	351.7	0.27	20	10	28.11	Valid
P15-41	25.42	2.51	434.9	0.27	20	10	34.38	Valid
P15-60	25.40	2.53	410.7	0.27	20	10	32.17	Valid
P15-61	25.40	2.53	346.3	0.27	20	10	27.12	Valid
P15-62	25.42	2.53	292.6	0.27	20	10	22.91	Valid
P15-63	25.42	2.52	408.1	0.27	20	10	32.21	Valid
P15-64	25.43	2.52	488.6	0.27	20	10	38.56	Valid
P15-65	25.44	2.54	268.5	0.27	20	10	20.85	Invalid

- P15-65 was an invalid fracture, propagating from an edge flaw on the sample during ring-on-ring testing.

Table D4. P28: 60 Thermal Fatigue Cycles

Specimen	Diameter (mm)	thickness (mm)	Peak load (N)	v	Ds	DL	Strength (MPa)	Fracture
P28-8	25.43	2.46	432	0.27	20	10	35.8	Valid
P28-9	25.44	2.50	231	0.27	20	10	18.5	Invalid
P28-10	25.41	2.49	416	0.27	20	10	33.7	Valid
P28-11	25.45	2.48	0.0	0.27	20	10	0.0	Invalid
P28-18	25.50	2.45	454	0.27	20	10	38.0	Valid
P28-19	25.49	2.45	352	0.27	20	10	29.4	Valid
P28-20	25.50	2.49	454	0.27	20	10	36.6	Valid
P28-21	25.52	2.48	354	0.27	20	10	28.9	Valid
P28-22	25.52	2.48	459	0.27	20	10	37.5	Valid
P28-23	25.54	2.48	381	0.27	20	10	31.1	Valid

-P28-9 was an invalid fracture, the crack propagated through pre-existing facial damage outside of testing ring in the sample during ring-on-ring testing. Sample P28-11 was invalid as it had fractured during thermal cycling and could not be biaxial tested.

Table D5. P25: 90 Thermal Fatigue Cycles

Specimen	Diameter (mm)	thickness (mm)	Peak load (N)	v	Ds	DL	Strength (MPa)	Fracture
P25-24	25.45	2.45	314	0.27	20	10	26.3	Valid
P25-25	25.46	2.43	72	0.27	20	10	6.1	Invalid
P25-26	25.49	2.43	263	0.27	20	10	22.2	Invalid
P25-27	25.46	2.47	172	0.27	20	10	14.2	Invalid
P25-28	25.47	2.45	94	0.27	20	10	7.8	Invalid
P25-30	25.52	2.56	164	0.27	20	10	12.5	Invalid
P25-31	25.48	2.48	164	0.27	20	10	13.4	Invalid
P25-32	25.47	2.51	271	0.27	20	10	21.6	Valid
P25-33	25.41	2.57	129	0.27	20	10	9.8	Valid
P25-34	25.48	2.58	110	0.27	20	10	8.3	Valid

-P25- (25, 26, 27, 28, 30, 31) were considered invalid fractures, the fractures propagated through a pre-existing crack in the sample during ring-on-ring testing.

Table D6. P28/32: 90 Thermal Fatigue Cycles (REDO)

Specimen	Diameter (mm)	thickness (mm)	Peak load (N)	v	Ds	DL	Strength	Fracture
P32-18	25.39	2.44	481	0.27	20	10	40.6	Valid
P32-19	25.38	2.49	180	0.27	20	10	14.6	Valid
P32-20	25.39	2.45	86	0.27	20	10	7.2	Invalid fracture- Fracture propagated through blister
P32-25	25.37	2.47	507	0.27	20	10	41.6	Valid
P32-27	25.41	2.48	137	0.27	20	10	11.1	Invalid fracture- Fracture propagated through blister
P32-28	25.39	2.39	102	0.27	20	10	9.0	Invalid fracture- Fracture propagated through blister
P32-29	25.40	2.44	266	0.27	20	10	22.5	Invalid fracture- Fracture propagated through blister
P32-31	25.32	2.50	228	0.27	20	10	18.3	Invalid fracture- Fracture propagated through blister
P28-44	25.45	2.43	330	0.27	20	10	27.9	Valid
P28-45	25.44	2.47	357	0.27	20	10	29.4	Valid

-P32- (20, 27, 28, 29, 31) were considered invalid fractures, the fractures propagated through blisters which occurred in the samples during thermal cycling.

Table D7. P26: 120 Thermal Fatigue Cycles

Specimen	Diameter (mm)	thickness (mm)	Peak load (N)	v	Ds	DL	Strength (MPa)	Fracture
P26-34	25.46	2.46	486	0.27	20	10	40.2	Valid
P26-35	25.50	2.41	435	0.27	20	10	37.5	Valid
P26-36	25.47	2.41	553	0.27	20	10	47.8	Valid
P26-45	25.47	2.47	360	0.27	20	10	29.5	Valid
P26-46	25.49	2.49	0	0.27	20	10	0.0	Invalid
P26-47	25.48	2.44	642	0.27	20	10	53.9	Valid
P26-50	25.47	2.46	0	0.27	20	10	0.0	Invalid
P26-52	25.45	2.48	660	0.27	20	10	53.6.	Valid
P26-53	25.47	2.43	601	0.27	20	10	50.8	Valid
P26-54	25.48	2.42	478	0.27	20	10	41.0	Valid

-P26-46 and P26-50 were considered invalid fractures, the fractures propagated through blisters which occurred in the samples during thermal cycling.

Table D8. P32: 150 Thermal Fatigue Cycles

Specimen	Diameter (mm)	thickness (mm)	Peak load (N)	v	Ds	DL	Strength (MPa)	Fracture
P3P32-5	25.40	2.48	373	0.27	20	10	30.4	Valid
P32-6	25.40	2.42	529	0.27	20	10	45.4	Valid
P32-7	25.38	2.41	462	0.27	20	10	40.0	Valid
P32-8	25.38	2.39	542	0.27	20	10	47.5	Valid
P32-11	25.41	2.50	177	0.27	20	10	14.2	Invalid
P32-12	25.41	2.44	142	0.27	20	10	12.0	Invalid
P32-14	25.42	2.53	303	0.27	20	10	23.8	Invalid
P32-15	25.35	2.53	596	0.27	20	10	46.6	Valid
P32-16	25.38	2.45	411	0.27	20	10	34.4	Valid
P32-17	25.40	2.42	446	0.27	20	10	38.3	Valid

-P32-11, P32-12 and P32-14 were considered invalid fractures, the fractures propagated through blisters which occurred in the samples during thermal cycling.

Table D9. P28: 200 Thermal Fatigue Cycles

Specimen	Diameter (mm)	thickness (mm)	Peak load (N)	v	Ds	DL	Strength (MPa)	Fracture
P28-34	25.50	2.43	89	0.27	20	10	7.6	Valid
P28-35	25.50	2.47	86	0.27	20	10	7.1	Valid
P28-36	25.51	2.51	306	0.27	20	10	24.4	Valid
P28-37	25.50	2.44	279	0.27	20	10	23.5	Valid
P28-38	25.51	2.45	336	0.27	20	10	28.1	Valid
P28-39	25.50	2.46	387	0.27	20	10	32.0	Valid
P28-40	25.53	2.50	381	0.27	20	10	30.5	Valid
P28-41	25.51	2.47	403	0.27	20	10	33.2	Valid
P28-42	25.51	2.46	271	0.27	20	10	22.4	Valid
P28-43	25.45	2.45	239	0.27	20	10	20.0	Valid

Appendix E. Ring-on-ring biaxial flexural data for all Reformulated LAST specimens tested. The Tables in this Appendix contain all size and strength measurements and validity for all LAST specimens tested for 0, 30, 60, 90, 120, 150, and 200 thermal fatigue cycle using ring-on-ring technique. A brief description for specimens with an invalid or premature fracture can be found under the specimens corresponding table.

v - Poisson's Ratio
Ds - Diameter of small ring (mm)
DL - Diameter of large ring (mm)

Table E1. N39: As-received

Specimen	Diameter (mm)	thickness (mm)	Peak load (N)	v	Ds	DL	Strength (MPa)	Fracture
N39-10	25.37	2.49	491	0.27	20	10	39.6	Valid
N39-11	25.38	2.54	467	0.27	20	10	36.3	Valid
N39-12	25.40	2.55	78	0.27	20	10	0.0	Invalid
N39-13	25.39	2.52	397	0.27	20	10	31.4	Valid
N39-14	25.36	2.51	507	0.27	20	10	40.4	Valid
N39-15	25.35	2.56	486	0.27	20	10	37.2	Valid
N39-16	25.36	2.58	491	0.27	20	10	37.0	Valid
N39-17	25.37	2.53	422	0.27	20	10	33.2	Valid
N39-18	25.36	2.53	529	0.27	20	10	41.5	Valid
N39-19	25.37	2.52	0	0.27	20	10	0.0	Fractured before testing

-N39-12 was an invalid fracture, propagating through a pre-existing crack in the sample during ring-on-ring testing. N39-19 fractured during thermal cycling, prior to the ring-on ring testing.

Table E2. N39: As-received

Specimen	Diameter (mm)	thickness (mm)	Peak load (N)	v	Ds	DL	Strength (MPa)	Fracture
N39-20	25.35	2.50	424	0.27	20	10	34.0	Valid
N39-21	25.45	2.50	145	0.27	20	10	11.7	Valid
N39-22	25.33	2.51	411	0.27	20	10	32.7	Valid
N39-23	25.29	2.53	416	0.27	20	10	32.5	Valid
N39-24	25.34	2.53	515	0.27	20	10	40.4	Valid
N39-25	25.45	2.51	489	0.27	20	10	38.8	Valid
N39-26	25.34	2.51	529	0.27	20	10	42.1	Valid
N39-27	25.33	2.49	427	0.27	20	10	34.6	Valid
N39-28	25.34	2.50	113	0.27	20	10	9.1	Valid
N39-33	25.47	2.50	188	0.27	20	10	15.1	Valid

Table E3. N39: 30 Thermal Fatigue Cycles

Specimen	Diameter (mm)	thickness (mm)	Peak load (N)	v	Ds	DL	Strength (MPa)	Fracture
N39-34	25.34	2.44	360	0.27	20	10	30.3	Valid
N39-35	25.35	2.49	148	0.27	20	10	12.0	Invalid
N39-36	25.34	2.48	56	0.27	20	10	4.6	Invalid
N39-47	25.38	2.51	379	0.27	20	10	30.1	Valid
N39-48	25.37	2.53	86	0.27	20	10	6.7	Invalid
N39-55	25.40	2.51	309	0.27	20	10	24.5	Valid
N39-56	25.38	2.51	395	0.27	20	10	31.5	Valid
N39-57	25.37	2.51	381	0.27	20	10	30.4	Valid
N39-58	25.41	2.50	169	0.27	20	10	13.6	Invalid

- N39- (35, 36, 48, 58) were invalid fractures, initiating from edge flaws in the samples during ring-on-ring testing.

Table E4. N41: 60 Thermal Fatigue Cycles

Specimen	Diameter (mm)	thickness (mm)	Peak load (N)	v	Ds	DL	Strength (MPa)	Fracture
N41-1	25.38	2.49	360	0.27	20	10	29.2	Valid
N41-2	25.42	2.49	443	0.27	20	10	35.9	Valid
N41-3	25.37	2.49	188	0.27	20	10	15.2	Invalid
N41-5	25.38	2.50	328	0.27	20	10	26.3	Valid
N41-6	25.36	2.52	330	0.27	20	10	26.1	Valid
N41-7	25.37	2.53	330	0.27	20	10	25.9	Valid
N41-8	25.37	2.52	387	0.27	20	10	30.6	Valid
N41-10	25.41	2.49	263	0.27	20	10	21.3	Valid
N41-11	25.38	2.52	309	0.27	20	10	24.5	Valid
N41-12	25.37	2.51	239	0.27	20	10	19.1	Valid

- N41-3 was an invalid fracture, initiating from an edge flaw in the sample during ring-on-ring testing

Table E5. N38/39: 90 Thermal Fatigue Cycles

Specimen	Diameter (mm)	thickness (mm)	Peak load (N)	v	Ds	DL	Strength (MPa)	Fracture
N38-38	25.34	2.53	78	0.27	20	10	6.1	Valid
N38-39	25.35	2.55	403	0.27	20	10	31.0	Valid
N38-45	25.34	2.46	140	0.27	20	10	11.6	Valid
N38-49	25.34	2.52	379	0.27	20	10	29.9	Valid
N38-51	25.33	2.60	354	0.27	20	10	26.3	Valid
N38-53	25.41	2.39	277	0.27	20	10	24.2	Valid
N38-54	25.35	2.46	193	0.27	20	10	16.0	Valid
N39-1	25.39	2.49	118	0.27	20	10	9.5	Valid
N39-2	25.36	2.56	362	0.27	20	10	27.7	Valid
N39-3	25.36	2.59	306	0.27	20	10	22.8	Valid

Table E6. N38: 120 Thermal Fatigue Cycles

Specimen	Diameter (mm)	thickness (mm)	Peak load (N)	v	Ds	DL	Strength (MPa)	Fracture
N38-15	25.37	2.55	86	0.27	20	10	6.6	Invalid
N38-16	25.39	2.51	89	0.27	20	10	7.1	Valid
N38-17	25.35	2.51	338	0.27	20	10	26.9	Valid
N38-20	25.36	2.56	105	0.27	20	10	8.0	Valid
N38-23	25.34	2.55	169	0.27	20	10	13.0	Valid
N38-24	25.39	2.57	97	0.27	20	10	7.3	Valid
N38-25	25.38	2.47	333	0.27	20	10	27.4	Valid
N38-26	25.35	2.50	46	0.27	20	10	3.7	Valid
N38-29	25.36	2.52	440	0.27	20	10	34.8	Valid
N38-32	25.38	2.55	75	0.27	20	10	5.8	Valid

-N38-15 was an invalid fracture, propagating through a pre-existing crack in the sample during ring-on-ring testing.

Table E7. N37/38: 150 Thermal Fatigue Cycles

Specimen	Diameter (mm)	thickness (mm)	Peak load (N)	v	Ds	DL	Strength (MPa)	Fracture
N37-56	25.34	2.52	282	0.27	20	10	22.3	Valid
N37-57	25.35	2.52	124	0.27	20	10	9.8	Valid
N37-61	25.36	2.50	357	0.27	20	10	28.7	Valid
N38-5	25.41	2.50	56	0.27	20	10	4.5	Valid
N38-9	25.38	2.51	223	0.27	20	10	17.8	Valid
N38-13	25.38	2.49	301	0.27	20	10	24.3	Valid
N38-14	25.36	2.51	54	0.27	20	10	4.3	Valid

-Samples N38-10 and N38-11 were not included in the testing as they were received too damaged to test from Tellurex Inc.

Table E8. N37: 200 Thermal Fatigue Cycles

Specimen	Diameter (mm)	thickness (mm)	Peak load (N)	v	Ds	DL	Strength (MPa)	Fracture
N37-15	25.33	2.55	322	0.27	20	10	24.8	Valid
N37-16	25.32	2.52	403	0.27	20	10	31.8	Valid
N37-18	25.36	2.53	266	0.27	20	10	20.8	Valid
N37-20	25.32	2.59	86	0.27	20	10	6.5	Invalid
N37-21	25.32	2.54	373	0.27	20	10	29.0	Valid
N37-23	25.35	2.42	277	0.27	20	10	23.8	Valid
N37-24	25.33	2.45	362	0.27	20	10	30.3	Valid
N37-25	25.32	2.37	236	0.27	20	10	21.1	Valid

-N37-20 was an invalid fracture, the crack propagated through a pre-existing crack in the sample during ring-on-ring testing.

References

[Alizadeh 2006] P. Alizadeh, M. Yousefi, B.E. Yekta, N. Ghafoorian, F. Molaie, "Sintering Behavior of SiO2-CaO-MgO (Na2O) Glass-Ceramics System". Ceramics International 33 [5] (2007): 767-771.

[Androulakis 2007] J. Androulakis, C. Lin, H. Kong, C. Uher, C. Wu, T. Hogan, B.A. Cook, T. Caillat, K.M. Paraskevopoulos, M.G. Kanatzidis, Spinodal Decomposition and Nucleation and Growth as a Means to Bulk Nanostructured Thermoelectrics: Enhanced Performance in $Pb_{1-x}Sn_xTe$–PbS, J. Am. Chem. Soc., 129 (31): 2780-2788, 2007.

[ASTM 1499] ASTM 1499-03 Standard Test Method for Equibiaxial Flexure Strength, 2004.

[Barbier 1992] E. Barbier, F. Thevenot, "Electrical resistivity in the titanium carbonitride-zirconia system". J. Mat. Sci. 27 (1992): 2383-2388

[Barsoum 1997] M. W. Barsoum, Fundamentals of Ceramics, McGraw-Hill, New York, 1997.

[Barsoum 2003] M.W. Barsoum, Fundamentals Of Ceramics. New York: Taylor & Francis Group, 2003.

[Bradt 1978] J.J. Cleveland, R.C. Bradt, Grain size dependence of spontaneous cracking in ceramics, J. Amer. Ceram. Soc., **61[11-12]**: 478-481, 1978.

[Bradt 1993] R.C. Bradt, M. Ashizuka, T.E. Easler, H. Ohira, Statistical aspects of the thermal shock damage and the quench-strengthening of ceramics, in *Thermal Shock Behavior and Thermal Fatigue of Advanced Ceramics,* eds. G.A. Schneider and G. Petzow, Kluwer Academic Publishers, the Netherlands, pp. 447-458, 1993.

[Budiansky 1976] B. Budiansky, R.J. O'Connell, Elastic moduli of a cracked solid, Int. J. Solids Structures, **12**: 81-97, 1976.

[Campbell 2008] F.C. Campbell. Elements of Metallurgy and Engineering Alloys. ASM International, Materials Park, OH, 2008.

[Case 1981] E.D. Case, J.R. Smyth, Fracture energy of monoclinic Gd_2O_3, J. Mater. Sci. **16**: 3215-3217, 1981.

[Case 1983] E.D. Case, "Microcrack Healing During The Temperature Cycling Of Single Phase Ceramics", *Fracture Mechanisms of Ceramics- Volume 5: Surface Flaws, Statistics, and Microcracking*. Bradt, R.C., Evans, A.G., Hasselman, D.P.H., Lange, F.F. Plenium Press, New York, NY, 1983. 507-530.

[Case 1993] E. D. Case, Y. Kim, W. J. Lee, 1993, Cyclic Thermal Shock in SiC whisker reinforced alumina and in other ceramic systems, Proceedings of the Thermal Shock Behavior and Thermal Fatigue of Advanced Ceramics, G.A. Schneider and G. Petzow, Editors, Kluwer Academic Publishers, the Nederlands, 393-406.

[Case 1993a] E.D. Case, Y. Kim, 1993, "The Effect of Surface-Limited Microcracks on the Effective Young's Modulus of Ceramics, I. Theory," Journal of Materials Science, 28: 1885-1900.

[Case 1993b] E. D. Case, Y. Kim, and W. J. Lee, 1993, "Cyclic Thermal Shock in SiC whisker reinforced alumina and in other ceramic systems," Proceedings of the Thermal Shock Behavior and Thermal Fatigue of Advanced Ceramics, G.A. Schneider and G. Petzow, Editors, Kluwer Academic Publishers, the Nederlands, 393-406.

[Case 1995] E. D. Case, 1995, Thermal Fatigue in Ceramics, Proceedings of the 1995 SEM Spring Conference on Experimental Mechanics, Society for Experimental Mechanics, Inc., Bethel, CN, 264-271.

[Case 2002] E. D. Case, 2002, "The Saturation of Thermomechanical Fatigue in Brittle Materials", a chapter in Thermo-Mechanical Fatigue and Fracture, WIT Press, Southampton, UK, editor, Prof. M. H. Alibadi, pp. 137 – 208

[Chiu 1992] C.C. Chiu, E.D. Case, Prediction of a thermal shock damage map for ceramics, J. Mater. Sci. 27: 1553-1559, 1992.

[Chung 1989] H.T. Chung, B.C. Shin, H.G. Kim, "Grain-Size Dependence of Electrically Induced Microcracking in Ferroelectric Ceramics". J. Am. Ceram. Soc. 72 [2], (1989): 327-29

[Cleveland 1978] J.J. Cleveland, and R.C. Bradt, Grain size dependence of spontaneous cracking in ceramics, J. Amer. Ceram. Soc., 61[11-12]: 478-481, 1978.

[Davidge 1968] R.W. Davidge, D.J. Green, The strength of two-phase ceramic/glass materials, J. Mater. Sci., 3: 629-634, 1968.

[Fang 2004] D. Fang, B. Liu, "Fatigue Crack Growth in Ferroelectric Ceramics Driven by Alternating Electric Fields". J. Am. Ceram. Soc. 87 [5], (2004): 840-846

[Favvas 2008] E.P. Favvas, A. Ch. Mitropoulos, What is Spinodal Decomposition, J. Eng. Sci. and Tech. Review 1 (2008): 25-27.

[Gogotsi 2006] Y. Gogotsi. Nanomaterial Handbook. Taylor and Francis Group, Boca Raton, FL, 2006: 740.

[Green 1983] D.J. Green, "Microcracking Mechanisms In Ceramics", Fracture Mechanisms of Ceramics- Volume 5: Surface Flaws, Statistics, and Microcracking. Bradt, R.C., Evans, A.G., Hasselman, D.P.H., Lange, F.F. Plenium Press, New York, NY, 1983. 457-478.

[Harris 2008] K.D. Harris, P.P. Edwards. Turning Points in Solid-State, Materials and Surface Science. Royal Society of Chemistry, 2008.

[Hasselman 1969] D.P.H. Hasselman, Unified theory of thermal shock fracture initiation and crack propagation in brittle ceramics, J. Amer. Ceram. Soc., **52**: 600-604, 1969.

[Hendricks 2009] T. Hendricks, T. Hogan, E. D. Case, N. Karri, J. D'Angelo, C. Wu, F. Ren, A. Morrison, and C. Cauchy, Advanced Soldier-Based Thermoelectric Power Systems Using Battlefield Heat Sources, submitted, MRS Fall 2009 Proceedings.

[Hogan 2007] T. P. Hogan, A. Downey, J. Short, J. D'Angelo, C-I Wu, E. Quarez, J. Androulakis, F. P. Poudeu, J. Sootsman, D-Y Chung, M. G. Kanatzidis, S. D. Mahanti, E. Timm, H Schock, Fei Ren, J. Johnson, E. D. Case, 2007, Nanostructured Thermoelectric Materials and High Efficiency Power Generation Modules, Journal of Electronic Materials, 36[7] 704-710.

[Ivon 2000] A.I. Ivon, V.R. Kolbunov, I.M. Chernenko, "Effects of Thermal Cycling and Subsequent Heat Treatment on the Electrical Conductivity of a VO_2-Based Ceramic". Inorganic Materials 36 [1], (2000): 88-89

[Jile 1994] D. Jiles. Electronic Properties Of Materials. Chapman and Hall. 2-6 Boundary Row, London, UK. 1994: 129-141.

[Kaliakin 2002] V.N. Kaliakin, Introduction to Approximate Solution Techniques, Numerical Modeling, and Finite Element Methods, Marcel Dekker, Inc, New York, 2002.

[Kanatzidis 2003] M.G. Kanatzidis, S.D. Mahanti, T.P. Hogan. Chemistry, Physics, and Materials Science of Thermoelectric Materials: Beyond Bismuth Telluride. Kluwer Academic/Plenum Publishers, New York, New York, 2003.

[Kasap 2006] S.O. Kasap, Electronic Materials and Devices. 3rd Ed., McGraw-Hill Companies, Inc. New York, New York, 2006: 285-392.

[Katigiri, 1994] N. Katigiri, Y. Hattori, T. Ota and I. Yamai, Grain size dependence of thermal shock resistance in $KZr_2(PO_4)_3$ ceramic, J. Ceramic Soc. of Japan, **102**: 715-718, 1994.

[Kim 1993a] Y. Kim, E. D. Case, 1993, "The Effect of Surface-Limited Microcracks on the Effective Young's Modulus of Ceramics, II. Theory, as Applied to Indentation Crack Systems," Journal of Materials Science 28: 1901-1909.

[Kim 1993b] Y. Kim, E. D. Case, S. Gaynor, 1993, "The Effect of Surface-Limited Microcracks on the Effective Young's Modulus of Ceramics, III. Experiment," Journal of Materials Science 28: 1910-1918.

[Kingery 1975] W.D. Kingery, H.K. Bowen, and D.R. Uhlmann, Introduction To Ceramics. John Wiley & Sons, INC. New York, New York, 1975:504-505.

[Kittel 2005] C. Kittel. Solid State Physics. 8th Ed., Wiley. 2005: 132-182.

[Laws 1987] N. Laws, J.R. Brockenbrough, The effect of micro-crack systems on the loss of stiffness of brittle solids, Int. J. Solids Structures, **23** (9): 1247-1268, 1987.

[Lee 1989] W. J. Lee, E. D. Case, 1989, Cyclic Thermal Shock in SiC Whisker Reinforced Alumina Composites, Mater. Sci. and Eng. A119: 113-126.

[Lee 1990] W. J. Lee, E. D. Case, 1990, Thermal Fatigue in Polycrystalline Alumina, Journal of Materials Science, 25[12]: 5043-5054.

[Lee 1990] W.J. Lee, E.D. Case, Thermal fatigue in polycrystalline alumina, J. Mater. Sci., **25**: 5043-5054, 1990.

[Lee 1992] W. J. Lee, E. D. Case, 1992, Comparison of Saturation Behavior of Thermal Shock Damage for a Variety of Brittle Materials, Materials Science and Engineering, A154:1-9.

[Li 2006] S.S. Li, Semiconductor Physical Electronics. 2nd Ed., Springer Science + Business Media, LLC, 233 Spring Street, New York, NY, 2006: 176-178.

[Liao 2010] C.N. Liao, C.Y. Chang, H.S. Chu, "Thermoelectric properties of electrically stressed Sb/Bi-Sb-Te multilayered films." J. App. Phy. 107 (2010), 066103-1 - 3

[Liu 1994] S.Y. Liu, I.W. Chen, "Plasticity-induced Fatigue Damage in Ceria-Stabalized Tetragonal Zirconia Polycrystals". J. Am. Ceram. Soc. 77 [8], (1994): 2025-35

[Luo 1997] J. Luo, R. Stevens, The role of residual stress on the mechanical properties of Al_2O_3-5 vol% SiC nano-composites, J. European Ceram. Soc., **48**: 1565-1572, 1997.

[Martin 2009] J. Martin, L. Wang, L. Chen, G.S. Nolas, "Enhanced Seebeck coefficient through energy-barrier scattering in PbTe nanocomposites." Physical Review B 79. 17 March 2009: 115311-1 – 115311-5.

[Matsudaira 2009] T. Matsudaira, Y. Matsumura, "Effect of microstructure on the fatigue behavior of aluminum titanate ceramics". J. Mater. Sci. 44, (2009): 1622-1632

[Mekkelbost 2009] T. Mekkelbost, H.L. Lein, P.E. Vullum, R. Holmestad, T. Grande, M.A. Einarsrud, "Thermal and mechanical properties of $LaNbO_4$-based ceramics". Ceramics International 35 (2009): 2877-2883

[Migliori 1997] A. Migliori and J. L. Sarrao, *Resonant Ultrasound Spectroscopy: Applications to Physics, Materials Measurements, and Nondestructive Evaluation*, (Academic Press, New York, 1997).

[Mikama 2009] M. Mikama, S. Tanaka, K. Kobayashi, "Thermoelectric properties of Sb-doped Heusler Fe_2Val Alloy." J. Alloys and Compounds 484 (2009), 444-448

[Navratil 2010] J. Navratil, F. Laufek, T. Plechacek, J. Plasil, "Synthesis, crystal structure and thermoelectric properties of the ternary skutterudite $Fe_2Pd_2Sb_{12}$." J. Alloys and Compounds 493 (2010), 50-54

[Nolas 2001] G.S. Nolas, J. Sharp, H.J. Goldsmid, Thermoelectrics: basic principles and new materials developments. Springer Science + Business Media, LLC, New York, NY, 2001: Chap. 1,4.

[Ohira 1988] H. Ohira, R.C. Bradt, Strength distributions of a quench-strengthened aluminosilicate ceramic, J. Amer. Ceram. Soc., **71[1]**: 35-41, 1988.

[Ozin 2009] G.A. Ozin, A.C. Arsenault, L. Cademartiri. Nanochemistry: A Chemical Approach to Nanomaterials. Royal Society of Chemistry, 2008.

[Pollock 1991] D.D. Pollock, Thermocouples: theory and properties. CRC Press, Inc., Boca Raton, Florida, 1991:

[Porter 2004] D.A. Porter, K.E. Eastling. Phase Transformation in Metals and Alloys. Taylor and Francis Group, Boca Raton, FL, 2004.

[Reed-Hill 1994] R.E. Reed-Hill, R. Abbaschian, Physical Metallurgy Principles, 3rd Ed., PWS Publishing Company, Boston, MA, 1994:

[Ren 2008] F. Ren, E. D. Case, J. R. Sootsman and M. G. Kanatzidis, H. Kong, C. Uher E. Lara-Curzio and R. M. Trejo, C. Uher, 2008, The high temperature elastic moduli of polycrystalline PbTe measured by resonant ultrasound spectroscopy" Acta Materialia, 56, 5954 – 5963.

[Ren Unpublished] F. Ren and E. D. Case, unpublished data, included in progress report to SERDP.

[Salvador 2009] J.R. Salvador, J. Yang, X. Shi, H. Wang, A.A. Wereszczak, "Transport and mechanical property evaluation $(AgSbTe)_{1-X}(GeTe)_X$ (X= 0.80, 0.82, 0.85, 0.87, 0.90)." J. Solid State Chem. 182 (2009), 2088-2095

[Schaftenarar 2008] H.P.C. Schaftenarar, Theory and Examples of Spinodal Composition in a Variety of Materials, Scheikude Utrecht University, 2008.

[Schilling 1991] M. Schilling, U. Merkt, "$YBa_2Cu_3O_x$ – Microstructures On Semiconductor Substrates". IEEE Transactions On Magnetics 27 [2], (1991): 1630-33.

[Sinha 2003] A.K. Sinha. Physical Metallurgy Handbook. McGraw-Hill Companies, Inc., 2003: 6.15-6.28.

[Soboyejo 1995] W. Soboyejo, D. Brooks, L.C. Chen, "Transformation Toughening and Fracture Behavior of Molybdenum Disilicide Composites Reinforced with Partially Stabilized Zirconia". J. Am. Ceram. Soc. 78 [6], (1995): 1481-1488

[Sootsman 2009] J.R. Sootsman, J. He, V.P. Dravid, C.P. Li, C. Uher, M.G. Kanatzidis, "High thermoelectric figure of merit and improved mechanical properties in melt quenched PbTe-Ge and PbTe-$Ge_{1-X}Si_X$ eutectic and hypereutectic composites." J. App. Phy. 105 (2009), 083718-1 – 8.

[Sze 1981] S.M. Sze. Physics of semiconductor devices. John Wiley & Sons, INC. New York, New York, 1981:7-50, 304, 799.

[Sze 2007] S.M. Sze, K.K. Ng, Physics of semiconductor devices. 3rd Ed., John Wiley & Sons, INC. New York, New York, 2007: 187.

[Takahashi 2010] S. Takahashi, H. Muta, K. Kurosaki, S. Yamanaka, "Synthesis and thermoelectric properties of silicon- and manganese-doped $Ru_{1-X}Fe_XAl_2$." J. Alloys and Compounds 493 (2010), 17-21

[Todd 2004] R.I. Todd, B. Derby, Thermal stress induced microcracking in alumina-20% SiCp composites, Acta Mater., 52[6] 1621 – 1629, 2004.

[Wachtman 2009] J. B. Wachtman, W. Roger Cannon, M. J. Mattheson, Mechanical Properties of Ceramics, Second Edition, John Wiley and Sons, New York, 2009, pp. 112 - 113.

[Westram 2009] I. Westram, H. Kungl, M.J. Hoffmann, J. Rodel, "Influence of crystal structure on crack propagation under cyclic electric loading in lead-zirconate-titanate". J. Eur. Ceram. Soc. 29 (2009): 425-430

[Wilson 1993] B. A. Wilson, E. D. Case, 1993, Comparison of Mechanical Fatigue with Thermal Fatigue in Ceramics, Scripta Metallurgica et Materialia, 28: 1571-1576.

[Yamai 1993] I.Yamai, T. Ota, "Grain Size-Microcracking Relation for $NaZr_2(PO_4)_3$ Family Ceramics". J. Am. Ceram. Soc. 76 [2], (1993): 487-91.